Final Report

BARGE IMPACT TESTING OF ST GEORGE ISLAND CAUSEWAY BRIDGE GEOTECHNICAL INVESTIGATION

UF Project No.: 4910 4554 016-12 (00030893)

Contract No.: BD545, PRWO # 5

Submitted to:

Mr. Richard Long
Research Center
Florida Department of Transportation
Tallahassee, FL 32399-0450

Project Manager: Henry Bollmann

Principal Investigator: Michael McVay
Co Authors: Scott Wasman
Paul Bullock

December 2, 2005

1.Report No.	2. Government Accession No.	3. Recipient's Catalog No.

Barge Impact Testing of St. George Causeway Bridge Geotechnical Investigation	5. Report Date September 2005
	6. Performing Organization Code
7. Author(s) Michael McVay, Scott Wasman and Paul Bullock	8. Performing Organization Report No. 4910 4554 016-12
9. Performing Organization Name and Address University of Florida Department of Civil and Coastal Engineering 365 Weil Hall / P.O. Box 116580 Gainesville, FL 32611-6580	10. Work Unit No. (TRAIS)
	11. Contract or Grant No. BD545, RPWO #5
12. Sponsoring Agency Name and Address Florida Department of Transportation Research Management Center 605 Suwannee Street, MS 30 Tallahassee, FL 32399	13. Type of Report and Period Covered Draft Final Report
	14. Sponsoring Agency Code

15. Supplementary Notes

Prepared in cooperation with the Federal Highway Administration

16. Abstract

This study reports on the insitu investigation, site stratigraphy, field monitoring, data reduction and subsequent time domain analysis of soil-structure interaction at St. George Island Causeway Pier 1S and 3S subject to barge impacts. The insitu investigation involved Standard Penetration Testing, Electric Cone Penetration Testing, Dilatometer Testing and Pressuremeter Testing. The insitu testing was used to identify soil stratigraphy, engineering properties (i.e., strength, & moduli), as well as axial T-z and lateral P-y nonlinear soil-pile spring behavior. The field instrumentation included soil total stress and pore pressure gages in front and behind the embedded pile cap as well as a fully instrumented (strain gages along length) pile attached to the lead row of the Pier 1S group (5 x8 layout). The pier was struck multiple times with a Jumbo barge at different velocities resulting in varying peak loads (100^{kips}, 800^{kips}, 900^{kips}). The resulting pile cap displacements, soil pressures, and pile moment & shears, as well as dynamic soil-pile resistance was obtained for each impact. The field impact data suggests that significant inertia and damping resistance from the soil occurs besides static resistance for barge impact.

The field tests were subsequently modeled with both LS-DYNA and FB-MultiPier in time domain analyses. The soil-pile damping resistance was characterized through viscous dampers as identified by Smith & El Naggar. In the case of Smith, the ultimate lateral soil resistance, Pu, was multiplied recommended Smith Damping, Js (0.1) for granular soil and the layer thickness. Group reduction factors, i.e., P-y multipliers were used for both the static as well as damping resistance. The predicted deflections, pile head shears, and soil resistance agreed reasonably with the field measurements. Analyses of Pier 1S & 3S revealed that at peak load, anywhere from sixty to seventy percent of the resistance may be attributed to damping and inertia. The latter suggests that time domain analysis may result in greater resistance (vs. current AASHTO) as well as more accurate analysis of bridge response to vessel impacts. However, further laboratory and field-testing are warranted for soil damping characterization.

17. Key Words	18. Distribution Statement
Soil-Structure Interaction, Pile Groups, Vessel Collision, Full Scale, Damping, Inertia, Time Domain Analysis, P-y, T-z, LS-DYNA & FB-MultiPier	No restrictions. This document is available to the public through the National Technical Information Service, Springfield, VA, 22161

19. Security Classif. (of this report)	20. Security Classif. (of this page)	21. No. of Pages	22. Price
Unclassified	Unclassified		

Form DOT F 1700.7 (8-72)

SI* (MODERN METRIC) CONVERSION FACTORS

APPROXIMATE CONVERSIONS TO SI UNITS

Symbol	When You Know	Multiply By	To Find	Symbol
	LENGTH			
in	inches	25.4	millimeters	mm
ft	feet	0.305	meters	m
yd	yards	0.914	meters	m
mi	miles	1.61	kilometers	km
	AREA			
in^2	square inches	645.2	square millimeters	mm^2
ft^2	square feet	0.093	square meters	m^2
yd^2	square yards	0.836	square meters	m^2
ac	acres	0.405	hectares	ha
mi^2	square miles	2.59	square kilometers	km^2
	VOLUME			
fl oz	fluid ounces	29.57	milliliters	ml
gal	gallons	3.785	liters	l
ft^3	cubic feet	0.028	cubic meters	m^3
yd^3	cubic yards	0.765	cubic meters	m^3
NOTE: Volumes greater than 1000 l shall be shown in m^3.				
	MASS			
oz	ounces	28.35	grams	g
lb	pounds	0.454	kilograms	kg
T	short tons (2000 lb)	0.907	megagrams	Mg
	TEMPERATURE (exact)			
°F	Fahrenheit temperature	5(F-32)/9 or (F-32)/1.8	Celcius temperature	°C
	ILLUMINATION			
fc	foot-candles	10.76	lux	l
fl	foot-Lamberts	3.426	candela/m^2	cd/m^2
	FORCE and PRESSURE or STRESS			
lbf	poundforce	4.45	newtons	N
psi	poundforce per square inch	6.89	kilopascals	kPa

APPROXIMATE CONVERSIONS FROM SI UNITS

Symbol	When You Know	Multiply By	To Find	Symbol
	LENGTH			
mm	millimeters	0.039	inches	in
m	meters	3.28	feet	ft
m	meters	1.09	yards	yd
km	kilometers	0.621	miles	mi
	AREA			
mm^2	square millimeters	0.0016	square inches	in^2
m^2	square meters	10.764	square feet	ft^2
m^2	square meters	1.195	square yards	yd^2
ha	hectares	2.47	acres	ac
km^2	square kilometers	0.386	square miles	mi^2
	VOLUME			
ml	milliliters	0.034	fluid ounces	fl oz
l	liters	0.264	gallons	gal
m^3	cubic meters	35.71	cubic feet	ft^3
m^3	cubic meters	1.307	cubic yards	yd^3
	MASS			
g	grams	0.035	ounces	oz
kg	kilograms	2.202	pounds	lb
Mg	megagrams	1.103	short tons (2000 lb)	T
	TEMPERATURE (exact)			
°C	Celcius temperature	1.8C + 32	Fahrenheit temperature	°F
	ILLUMINATION			
lx	lux	0.0929	foot-candles	fc
cd/m^2	candela/m^2	0.2919	foot-Lamberts	fl
	FORCE and PRESSURE or STRESS			
N	newtons	0.225	poundforce	lbf
kPa	kilopascals	0.145	poundforce per square inch	psi

* SI is the symbol for the International System of Units. Appropriate rounding should be made to comply with Section 4 of ASTM E380.

(Revised August 1992)

DISCLAIMER

"The opinions, findings and conclusions expressed in this publication are those of the authors and not necessarily those of the Florida Department of Transportation or the U.S. Department of Transportation."

Prepared in cooperation with the State of Florida Department of Transportation and the U.S. Department of Transportation.

TABLE OF CONTENTS

page

LIST OF TABLES

Table page

LIST OF FIGURES

Figure page

CHAPTER 1
INTRODUCTION

1.1 Background

It has been identified that at least one serious vessel collision occurs with a bridge every year (Larsen, 1993). For example, in September 2001, a barge collided with the Queen Isabella Causeway Bridge in South Padre Texas collapsing 3 spans. Subsequently, in May 2002, an errant barge tow struck the interstate I-40 Bridge in Webbers Falls, Oklahoma, resulting in the loss of fourteen lives.

Many of the early bridges in Florida were designed with minimal vessel impact loading considerations. However with the collapse of the Sunshine Skyway Bridge in Tampa in the early 1980s, the consideration of a vessel impact loading or extreme event became a priority in Florida. Based on the latter, as well work in Europe, Asia, etc., the American Association of State Highway and Transportation Officials (AASHTO) developed and adopted vessel impact design guidelines (AASHTO, 1991).

The current AASHTO guidelines compute equivalent static load acting on a bridge based on the calculated kinetic energy (mass, and velocity) of a moving barge for a given waterway. The relationship between equivalent static load and kinetic energy of a moving barge is based on barge crush experiments conducted in Germany. Since the loading is an equivalent static force, other dynamic forces, i.e., inertia and damping are not considered. Depending on duration of impact, particle velocities, accelerations, and

size or zone of soil mass, dynamic resistance may be significant. Of interest are dynamic resistances provided by the soil-structure interaction below the vessel impact zone.

1.2 Objective

To better characterize the vessel impact loading on a bridge, as well as the soil-structure interaction during the impact, the Florida Department of Transportation (FDOT) decided to monitor a full-scale barge-bridge impact. The St. George Island Causeway Bridge (Florida State Road 300) near Apalachicola, Florida (USA) was selected for this study because of its size, shape and foundation layout. Specifically, the main pier was a reinforced concrete structure, composed of a pile cap, two large square pier columns, and a lateral stiffened shear wall. The width of each pier column at the point of a potential barge impact was 6 ft. The mud-line footing consisted of a single concrete pile cap (21 ft. wide, 39 ft. long, 5 ft. thick), underlain by a concrete tremie seal (24 ft. wide, 42 ft. long, and 6 ft. thick) with forty steel HP 14x73 piles down to elevation –60 ft.

Since 70% or more of the vessel impact loading was expected to be transferred to the foundation (not superstructure), the foundation (piles) and the adjacent soil had to be monitored during the vessel collision. This study reports on the soil conditions (layering, properties, etc.) adjacent to Pier 1S, from insitu testing, as well as the change in soil stresses, pile shears, moments, and displacements, within the foundation during multiple barge impacts. From the pile shears calculated along an instrumented pile, the cyclic dynamic soil resistance curves were developed for individual soil layers. Subsequently, the impact loading was modeled with the FB-MultiPier time-domain analysis based upon the recorded impact force vs. time along with the back computed dynamic soil resistance curves. A comparison of pile and cap displacements, pile head shears, and soil pressures

along the pile cap were subsequently undertaken. Conclusions and recommendations (improvements to FB-MultiPier) follow.

1.3 Scope of Work

To accomplish the objectives, the following tasks were performed: a) insitu soils testing (SPT, CPT, and PMT) around Pier 1S, b) Installation of soil monitoring and pile instrumentation, c) Pile and Soil Monitoring during the barge impact testing, d) Reduction of soil and pore water stresses, calculation of pile shears along the length, and subsequent development of dynamic soil resistance curves, and e) Comparison of measured and predicted (FB-MultiPier) displacements, shears, etc. A discussion of individual tasks follows.

1.3.1 InSitu Soil Testing

Minimal soil information was available for both Pier 1S and 3S, which required the development of an insitu testing program. Because the Pier 1S cap was below both the sea level and mudline, all work had to be performed from a barge at the site. Four types of insitu tests were performed around Piers 1S and 3S to assess soil stratification and soil properties: Standard Penetration (SPT), Cone Penetration (CPT), Marchetti Dilatometer (DMT), and Cone Pressuremeter (CPMT) Tests. The SPT and CPT were used for classification. The cone pressuremeter (CPMT) and Marchetti Dilatometer (DMT) were used to assess initial lateral stresses, as well as developed of standard, i.e., default P-y curves. In addition, the SPT drill rig was used at Pier 1S to install the instrumented pile and to place the lateral soil stress and pore pressure gages.

1.3.2 Pile Instrumentation and Soil Monitoring

Significant in understanding the soil-structure interaction during a barge impact, is the behavior of the supporting piles and associated pile cap. To assess deformations and

shears within the piles, an instrumented pile of similar stiffness had to be placed through the seal concrete, driven into the soil to a depth greater than 40' and attached (fixed head) to the pile cap. The instrumented pile consisted of an 8.6" steel pipe, with rebar and concrete grout placed within it to replicate the stiffness of H piles under Pier 1S. Attached to the sides of the reinforcing cage of this composite pile were pairs of strain gages at various elevations. At the center of the composite pile was a slope inclinometer casing with an accelerometer string to monitor motion of the pile during impact. To validate the moment-curvature as well as instrumentation gage factors, etc., a test section of the pile was loaded in the laboratory under 3-point flexural testing.

To monitor soil stresses in front of and behind of the pile cap and seal, 6 lateral stress and pore pressure cells were installed with the SPT drill rig. The cells, manufactured by Geokon, were capable of monitoring changes in pore pressure and total lateral stress during the dynamic event, i.e., barge impact.

1.3.3 Barge Impact Tests

The barge impacted Pier 1S and Pier 3S multiple times. Soil-structure interaction (i.e., instrumented pile, and soil stress and pore pressure) gages were placed around Pier 1S. Multiple barge impacts were recorded to Pier 1S with speeds varying from 0.86 to 3.97 mph. Data was collected with a 46 channel National Instruments Data Acquisition System recording 2000 samples per second. Three impacts were fully recorded at Pier 1S: P1T1, P1T6 and P1T7. The first, P1T1 had the lowest maximum impact force, 102 kips, but the other two had peak forces of 882 kips (P1T6) and 864 kips (P1T7), respectively. In addition, P1T6 had a second peak of 250 kips, after 0.5 sec which was attributed to the tug directing and pushing the barge striking its rear. Data during each event was collected and subsequently analyzed.

1.3.4 Experimental Data Reduction

Based on the strain data, accelerometer data, etc., recorded for each barge impact, the deflections, and bending moments along the instrumented pile were back calculated as a function of time. Based on the bending moments along the length of the model pile at a given increment in time, the dynamic soil resistance, i.e., P (force/length) vs. lateral deflection, y, for individual soil layers was found. Note these curves are cyclic (i.e., positive and negative values), and represent the total dynamic soil resistance, i.e. static, damping, and inertia. Of interest is the shape of the dynamic soil resistance curves vs. traditional P-y curves used in the static analysis.

Also of interest were the dynamic resistances, or soil-structure interaction, of both the pile cap, and seal embedded 11 ft in shelly sands. Changes in soil stresses, i.e., resistance, were recovered on both the front and rear of the cap and seal concrete as a function of time. The latter were modeled in FB-MultiPier with nonlinear springs attached to the piles within the pile cap.

1.3.5 Predicted vs. Experimental Results

Using the soil layering and properties from insitu testing (i.e. CPT, SPT, PMT, etc.), as well as the measured impact force vs. time, time domain dynamic analyses, FB-MultiPier, and LSDYNA were performed on Pier 1. Both analyses used the experimental dynamic resistance measured from the experimental pile. That is, the dynamic resistance included both the static and damping resistance from the soil-structure interaction. Of interest were the comparison of measured and predicted time history of pile cap, as well as the distribution of forces within the piles, and separation of static from dynamic resistance (i.e., inertia and damping). Since the experimental data included deflected

shape, moments and shears along the length of the pile, the latter were compared at multiple time steps (i.e., maximum applied impact force, cap displacements, etc.).

Chapter 4 also presents a discussion of Consolazio (2005) prediction of Pier 3S response using FB-MultiPier. The pier was supported by a small 8-pile group of battered prestressed concrete piles with an above water cap, representative of many approach piers in Florida. Since the group did not have an instrumented pile along its length, the static soil properties (i.e. T-z, and P-y) were obtained from nearby insitu data (Chapter 2), and the viscous damping based on El Naggar and Novak (1996) (Chapter 4). Analyses of Pier 3S as well as 1S, suggest that anywhere from 60 to 70% of a pier's resistance at peak barge loading occurs from dynamic (inertia and damping) resistance.

CHAPTER 2
FIELD INVESTIGATION AND INSTRUMENTATION

2.1 InSitu Equipment

For this research, a 40 ft x 100 ft, center-hole barge, Figure 2.1, along with an air compressor, a welder, a fuel tank, a water tank, a wheeled crane, a tugboat and a crew of two, was rented from H.G. Harders & Son, Inc. in Panama City, FL for two weeks. FDOT District 3 provided a CME 75 drill rig, Figure 2.2 along with driller and three helpers, to perform Standard Penetration Test (SPT) borings and set casing to the mudline for the CPT Rig. The drill crew also installed the push-in lateral stress cells and helped construct the instrumented mini-pile, used to monitor soil-structure interaction during the barge impact. The drill rig worked off of the bow of the barge on a 4 ft wide deck grating installed by Mr. Gerald Brazil from FDOT Maintenance in Defuniak Springs.

Figure 2.1 40 ft x 100 ft Spud Barge at Pier 3S

Figure 2.2 Drill Rig and CPT Rig at Pier 1S

The State Materials Office (SMO) provided a Hogentogler Cone Penetrometer Rig (20 ton thrust), test equipment, with operators to perform Cone Penetration Test (CPT) soundings, Marchetti Dilatometer Test (DMT) soundings, and Cone Pressuremeter Test (CPMT) soundings. The CPT rig worked through a center hole 2 ft in diameter located 26 ft from the bow of the barge.

2.2 InSitu Tests

To model (FB-Pier, LS-Dyna, etc.) soil-structure interaction, the soil stratigraphy (layering) and mechanical properties (strength, compressibility, etc.) adjacent to Piers 1S and 3S are needed. In addition, since, a number of insitu tests, i.e., CPMT (cone pressuremeter), and DMT, have published algorithms for automatic P-y curve generations, the latter were used to compare with the mini-pile P-y results. For layering and strength assessment, the SPT and CPT were used whereas, to assess compressibility

(e.g.,, subgrade modulus), initial stresses and over consolidation ratios, the pressuremeter (CPMT) & DMT were used.

All of the Soundings/borings were located next to Pier 1S and 3S, or as close as allowed with barge, and the fender system at Pier 1S. Figures 2.3 and 2.4 show location plans of the soundings and borings performed adjacent to Piers 1S and 3S respectively. Table 2.1 lists the details of each sounding or boring, including the elevations of the mudline and the maximum penetration. Boring or sounding locations were obtained by triangulating measured distances from reference points on each pier. Differential GPS location did not prove accurate enough to verify the separation between adjacent soundings and/or borings.

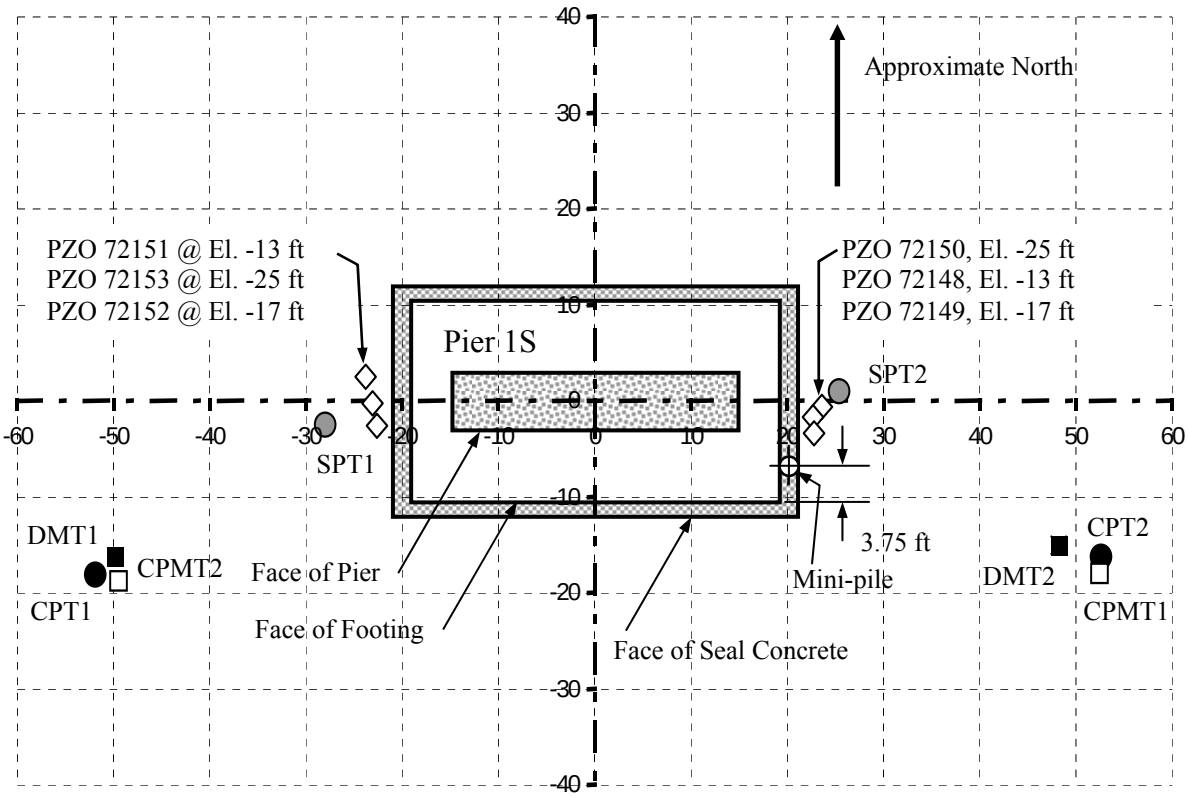

Figure 2.3 Location Plan for Pier 1S Borings, Soundings, and Instrumentation

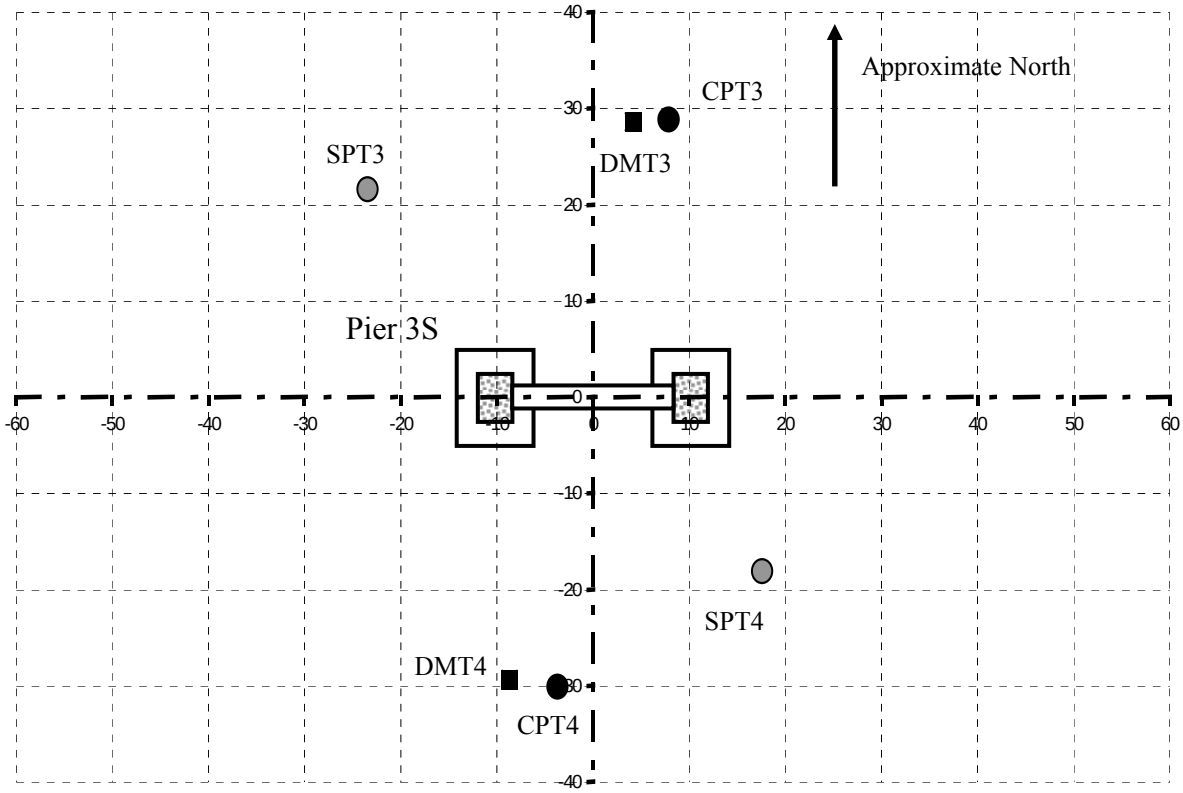

Figure 2.4 Location Plan for Pier 3S Borings, Soundings, and Instrumentation

Table 2.1 Sounding/Boring Dates and Elevations

Sounding/Boring	Date Started	Date Finished	Mudline Elevation ft, msl	First Test Elevation ft, msl	Final Test Elevation ft, msl
SPT1	11/03/03	11/04/03	- 7.33	-7.83	-92.33
SPT2	11/05/03	11/04/03	-11.50	-18.50	-92.00
SPT3	11/12/03	11/12/03	- 8.67	-18.67	-89.17
SPT4	11/13/03	11/13/03	- 7.92	-13.42	-89.92
CPT1	11/03/03	11/03/03	- 9.75	-20.37	-61.55
CPT2	11/05/04	11/05/04	-12.63	-15.63	-59.26
CPT3	11/12/03	11/12/03	- 8.07	-16.98	-58.65
CPT4	11/12/03	11/12/03	- 7.04	-16.45	-61.07
DMT1	11/04/03	11/04/03	-10.08	-16.47	-58.43
DMT2	11/05/03	11/05/03	-12.76	-10.19	-52.18
DMT3	11/12/03	11/12/03	-10.50	-15.09	-55.77
DMT4	11/13/03	11/13/03	- 6.92	-16.93	-57.61
CPMT1	11/07/03	11/07/03	-15.58	-22.15	-43.73
CPMT2	11/11/03	11/11/03	-10.00	-24.05	-48.65

2.3 Site Stratigraphy and Soil Properties

Based on SPT1 and SPT2 (Fig. 2.3) recovered samples, the soil layering shown in Figure 2.5(a) was developed for Pier 1S. Evident from the figure, the soils are predominately cohesionless down to an elevation of –36ft under which there is stiff clay underlain by dense sand. Figure 2.5(b) shows a plot from CPT1 located near Pier 1S (Fig. 2.3). Based on each insitu device, soil description (i.e., classification), strength, and compressibility were assessed. For instance, Table 2.2 gives the estimated soil properties for each layer from individual SPT, CPT and DMT data near Pier 1S. Of interest, are the mean and coefficient of variability (COV) of the various layer data. Shown in Table 2.3 are the final selected strength and compressibility of soil layers near Pier 1S. The vertical shear failure (i.e., axial skin friction on the pile) in the last column of Table 2.3 was obtained from the unit skin friction values obtained from the CPT data (Fig. 2.5 (b)). The latter is used by FB-Pier and LS-Dyna for their axial T-z spring models. Note, due to fixed head pile conditions, lateral loading (i.e., barge impact) will generate significant axial forces within the pile group and must be modeled. In addition, skin friction between the pile cap, seal and soil is characterized with the skin friction values given in column 12 of Table 2.3.

Shown in Figure 2.6 (a) is a typical Pressuremeter Test (Elev. –27.15 ft) from the CPMT device. Using Robertson, et al. (1985), recommended procedures, the P-y curves given in Figure 2.6 (b) were obtained for each pressuremeter test at elevations - 27.15ft (i.e. Fig. 2.6(b)), -32.15ft, -37.05ft, -41.95ft, and –43.85ft. Evident from Fig. 2.6(b), the upper soil layers (Fig. 2.5(a)) are much softer and weaker than the bottom stiff (Navg =30) sand layer. Of interest is the P-y curves given in Fig. 2.6(b) versus the measured P-y curves from the instrumented mini-pile during the barge impact, as well as the default

P-y curves in FB-Pier using strength and compressibility properties given in Table 2.3. Note the axial unit skin friction, column 13 of Table 2.3, were based on the unit sleeve friction measured from CPT3&4, shown in Fig. 2.4. The latter are important when modeling battered piles as was the case of Pier 3S.

2.4 Instrumented Mini-Pile

It was readily recognized that the distribution of shear forces transmitted to the piles, cap, etc. were of great interest during the barge impact of Pier 1S. However, Pier 1S had a 5 ft thick concrete cap underlain by a 6 ft thick concrete seal, both constructed using quartz "river rock" aggregate. Contact of the HP 14 x 73 steel piles to the soil occurred well below the mudline, i.e. Elev. –20, eliminating potential instrumentation of the HP piles. In order to estimate the pile bending and shear forces along the length of the piles (i.e. back computing P-y curves), the research envisioned installing two instrumented 4 inch diameter “mini-piles” through the footing. However, subsequent analyses using FB-Pier indicated that the intended mini-piles deflected excessively with poor bending agreement with the H-piles. After successive analyses with FB-Pier, a 8.625” steel pipe, i.e., ZW drill casing with a steel reinforcement cage, and high-strength grout was settled upon, Figure 2.8. Figure 2.9 shows the FB-Pier moment and deflection of the leading and trailing rows of H-piles compared to the redesigned mini-pile at a lateral load of 1,200 kips. Due to cost of pile, instrumentation, etc., only one mini-pile was installed in the lead row of Pier 1S.

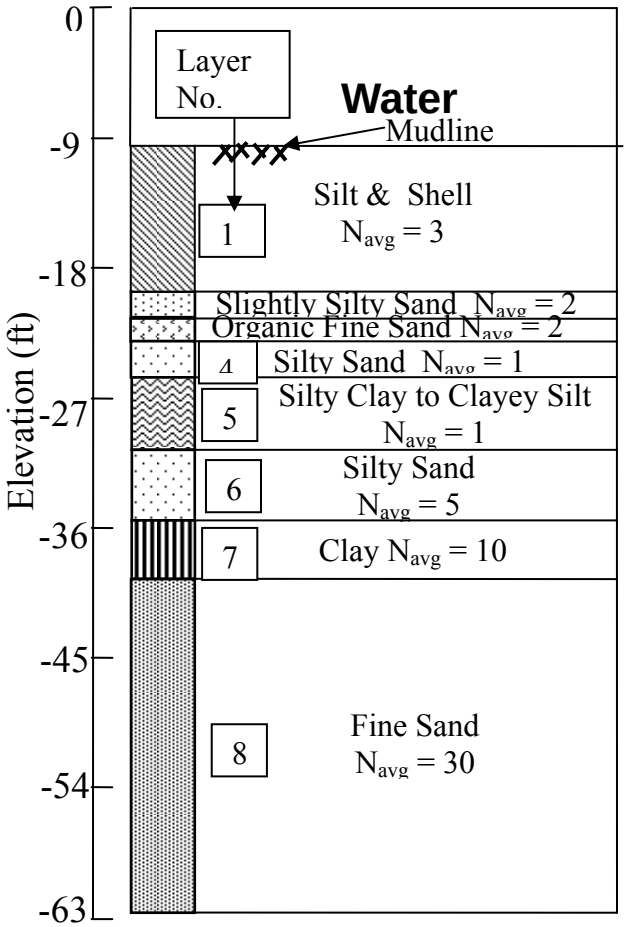

a) SPT Blow Count and Layering

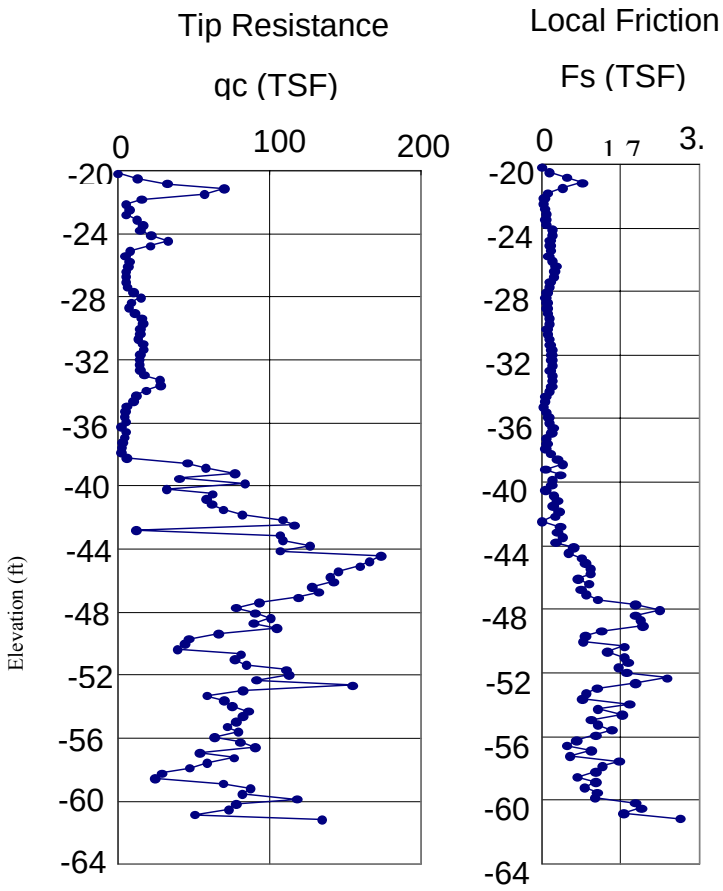

b) CPT Data

Figure 2.5 Pier 1S Layering and Insitu Data

Table 2.2 Soil Properties from Different Insitu Tests

Soil Layer	SPT [a]					CPT [b]					DMT [c]			
	N_{avg} ---	ϕ_{avg} (deg)	γ_{avg} (pcf)	S_{uavg} (psf)	k_{avg} kcf	ϕ_{avg} (deg)	γ_{avg} (pcf)	S_{uavg} (psf)	k_{avg} (static) kcf	k_{avg} (cyclic) kcf	ϕ_{avg} (deg)	γ_{avg} (pcf)	S_{uavg} (psf)	Ko_{avg} ---
1	3	27	95									99	104	0.45
2	2	27	100			41	120					99		0.41
3	2		100				110					103	574	1.1
4	1	27	100			33	120				33	109		
5	1		95	250				444	866	346		99	300	0.66
6	5	28	101		12	31	120				28	106		
7	10		100	375				403	866	346		99	334	0.56
8	30	33	127		28	41	125				33	124		

[a] $\phi = 53.881 - 27.6034 * e^{-0.0147*N}$. (Peck et.al, 1974); $S_u = 0.06NP_a$ (Terzaghi and Peck, 1968); k from Hababagahi and Langer, 1984

[b] ϕ from Robertson & Campanella, 1983; S_u from q_c and S_u relationship, EPRI 1990; k (static & cyclic) from S_u, Reese & Wang, 1993

[c] $\phi = 31^o + 1/((0.236/K_D) + 0.066)$, Marchetti, 1997; $S_u = 0.22(0.5K_D)^{1.25} * \sigma'_{vo}$ & $K_o = (K_D/1.5)^{0.47} - 0.6$, Marchetti, 1980

Table 2.3 Soil Properties Assigned to Each Soil Layer, Pier 1S

Layer	Soil Type	SPT N	Elev. (ft)	(a) ϕ_{avg} (deg)	Unit Weight γ (pcf)	(b) Subgrade k (kcf)	(c) Undr. Strength (psf)	Strain at 50%	(d) Shear Modulus (ksi)	Poisson's Ratio	(e) Vert. Shear Fail. (psf)
1	Loose Silt and Shell	3	9-20	27	97	43	104	0.02	0.632	0.3	840
2	Slightly Silty Sand	2	20-21	34	106.3	35	NA	NA	1.075	0.3	564
3	Organic Fine Sand	2	21-22		104.3	NA	574	0.02	0.145	0.37	480
4	Silty Sand	2	22-25	31	109.6	51	NA	NA	2.043	0.3	564
5	Silty Clay to Clayey Silt	3	25-30		97	NA	331.3	0.02	0.096	0.2	840
6	Silty Sand	5	30-35	29	109	77	NA	NA	4.730	0.3	1374
7	Clay	10	35-40		99.5	NA	370.7	0.07	0.095	0.35	1629
8	Fine Sand	30	40-63	35	125.3	224	NA	NA	23.276	0.37	1269

(a) Based on SPT
(b) Based on SPT and CPT
(c) Based on CPT
(d) Based on DMT and CPT
(e) Based on CPT

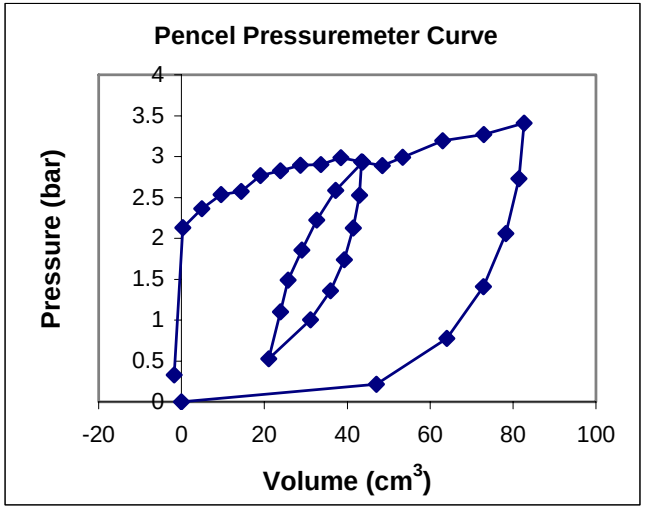

a) Pressuremeter Data: Elev. –27.15 ft

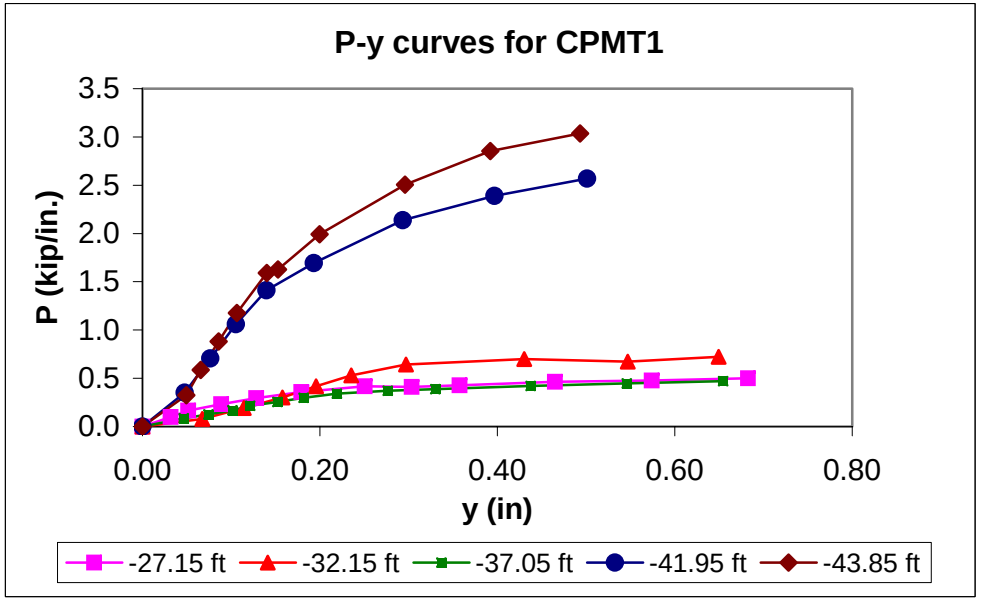

b) Computed P-y Curves from Pressuremeter Data

Figure 2.6 CPMT1 Pressuremeter Results

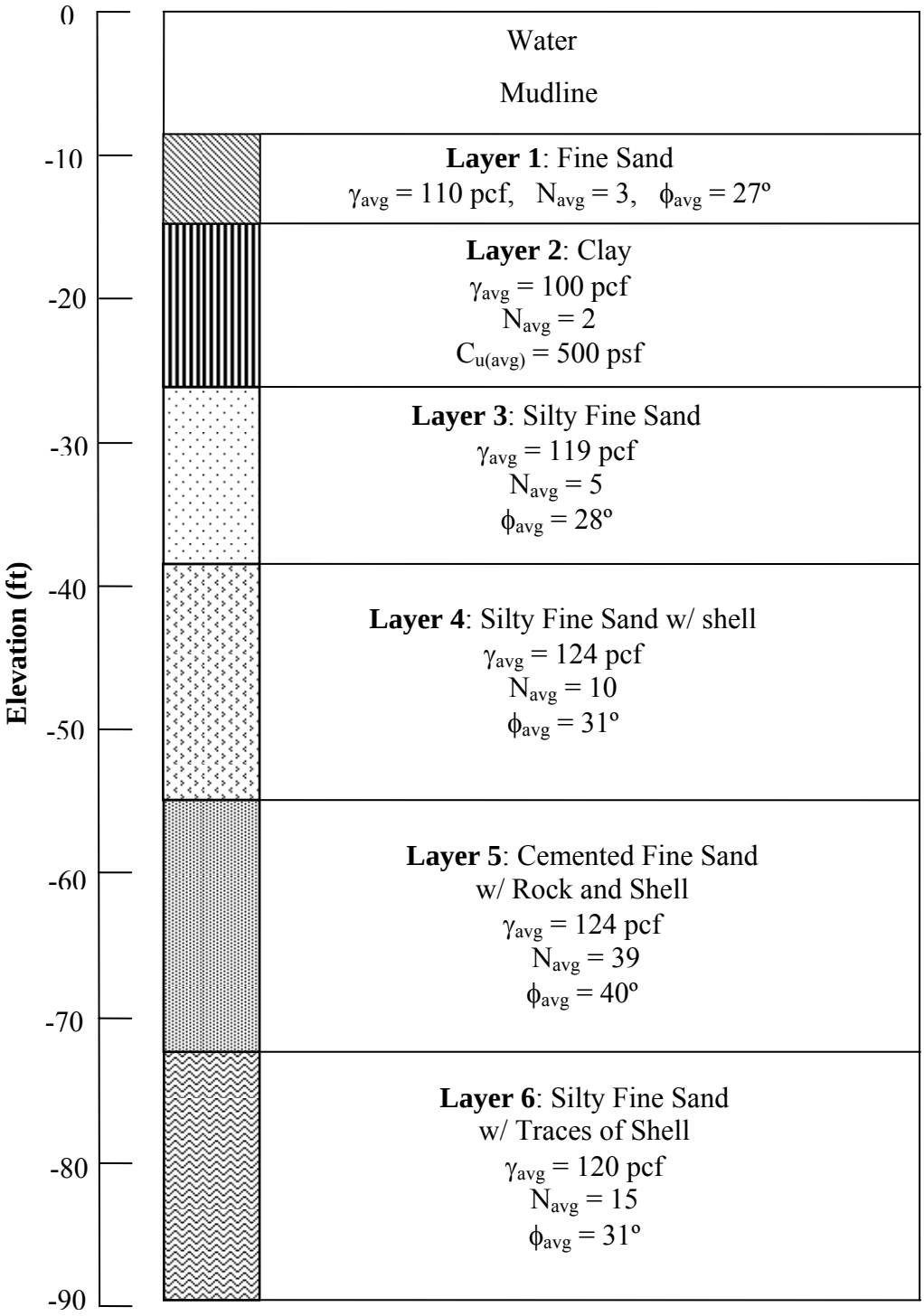

Figure 2.7 Pier 3S Soil Stratigraphy

Table 2.4 Soil Properties Assigned to Each Soil Layer, Pier 3S

Layer	Soil Type	SPT	Elevation (ft)	ϕ_{SPT} (deg)	ϕ_{CPT} (deg)	Unit Weight (pcf)	(a) Subgrade (pci)	(b) Undr. Stregth (psf)	Strain at 50%	(c) Shear Mod. (ksi)	Poisson's Ratio	(d) Vert. Shear Fail. (psf)
1	fine sand	3	-8.0 to -15.5	27		110	20			0.375	0.2	280.2
2	clay	2	-15.5 to -26.4			100	9.8	500	0.02	0.139	0.25	488
3	silty fine sand	5	-26.4 to -38.8	28		119	39			0.675	0.3	320
4	silty fine sand w/ shell	10	-38.8 to -55.0		31	124	45			3.000	0.35	2260
5	cemented fine sand w/ rock & shell	39	-55.0 to -73.0		40	124	85			8.000	0.4	2300
6	silty fine sand w/ traces of shell	15	-73.0 to -89.0	31		120	60			4.000	0.3	2100

(a) Based on SPT and CPT
(b) Based on CPT
(c) Based on DMT and CPT
(d) Based on SPT and CPT

values based on CPT3 and CPT4

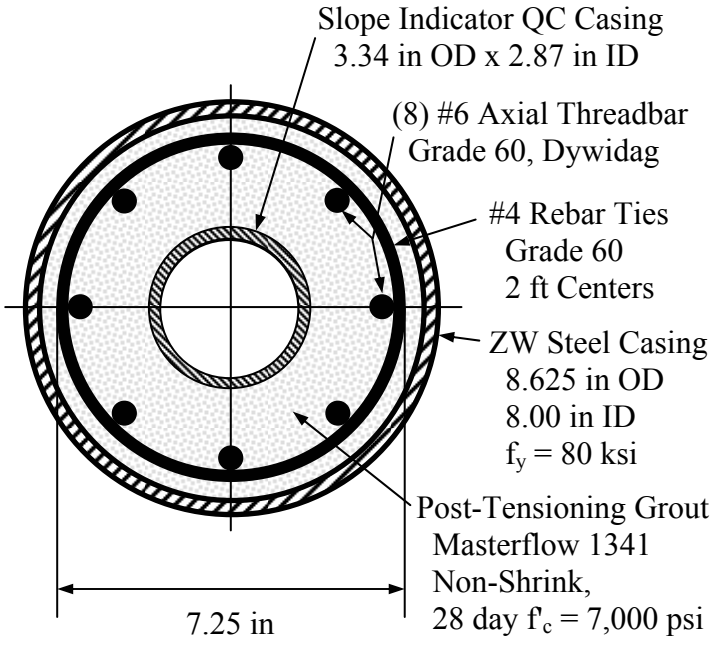

Figure 2.8 Revised Cross-Section of ZW Mini-Pile

At the center of the ZW mini-pile (Fig. 2.8) is a 3.34" PVC casing to house accelerometers along the length of the pile to monitor lateral accelerations, velocities and displacements of the pile. To ascertain moments, shears and soil stresses acting in the pile, 11 pairs of strain gages were placed within the mini-pile, Figure 2.10. Since significant changes in shear and soil resistance were expected near the footing/seal, higher density of gages were used in the shallower depths, Fig. 2.10. Due to diameter of the mini-pile (8.625"), the strain gages could not be attached to the inside of pile without cutting and rewelding, which would result in residual stresses. Attaching the gages to the outside of the pile was ruled out due to the driving process, saltwater, etc. Consequently, it was decided to use Vishay's 350 Ω, model EGP-5-350 concrete strain gages in a quarter bridge, tied to the reinforcing steel in opposing pairs, Figure 2.11. The latter gages were used very successfully in monitoring stresses in prestressed concrete piles during driving (McVay, 2002).

a)

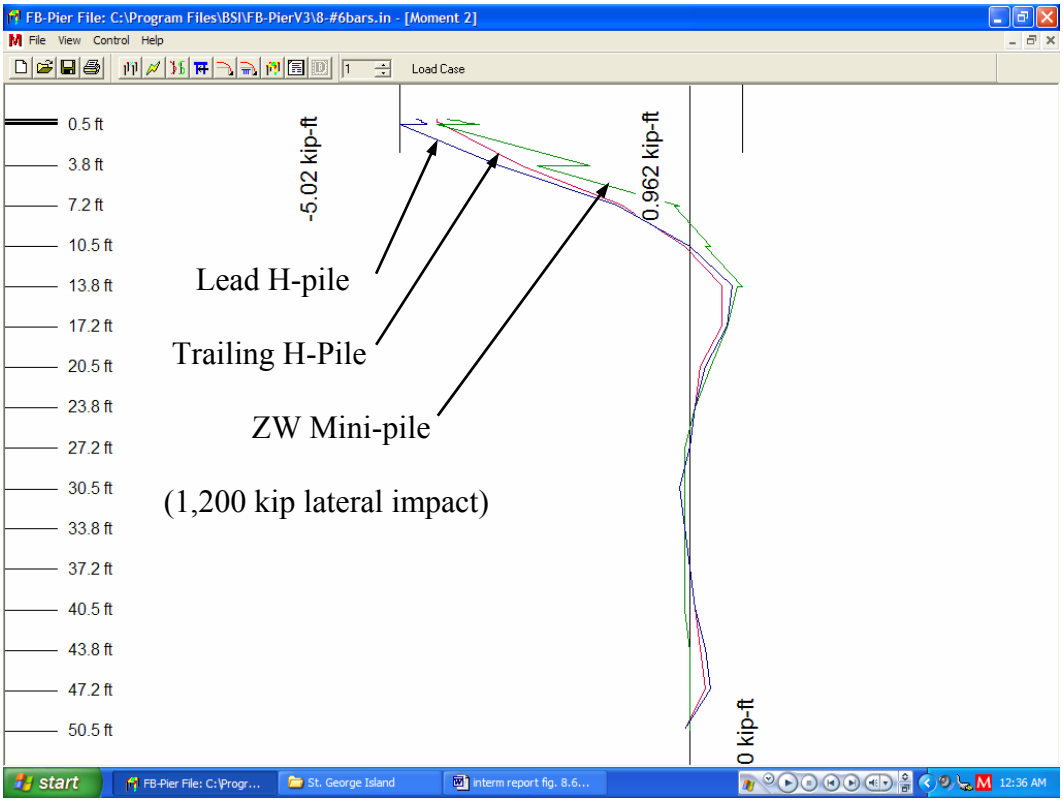

b)

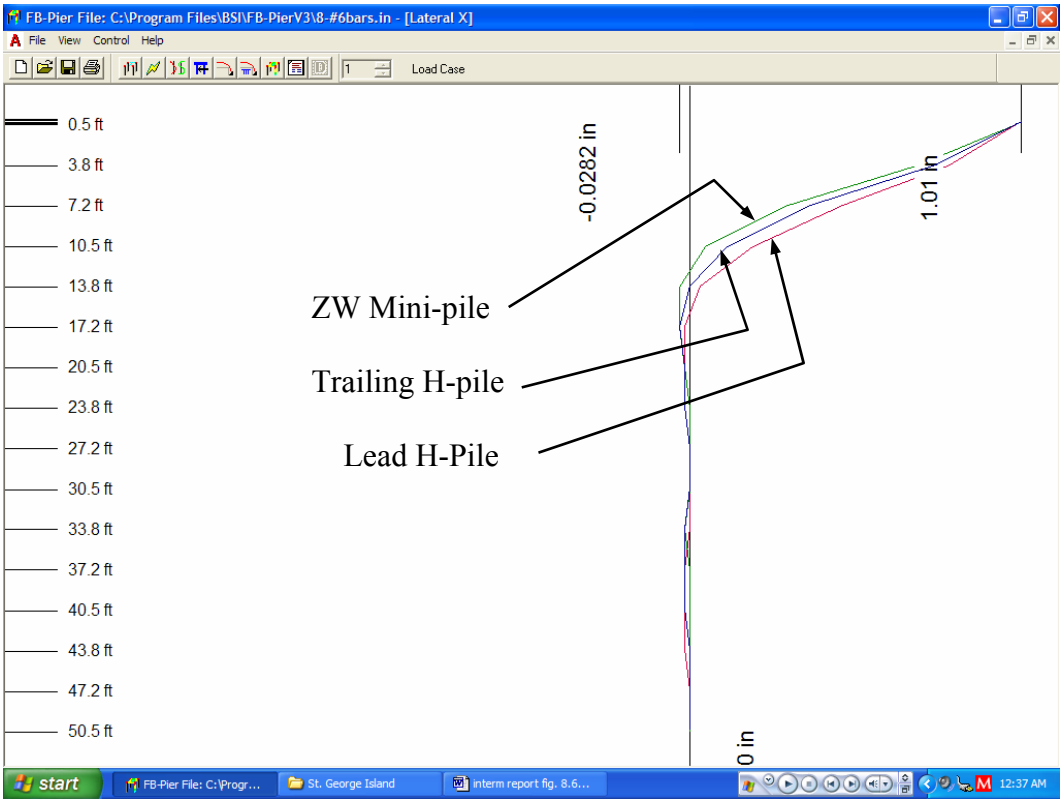

Figure 2.9 FBPier Prediction of Pile a) Moment and b) Deflection for ZW Mini-pile

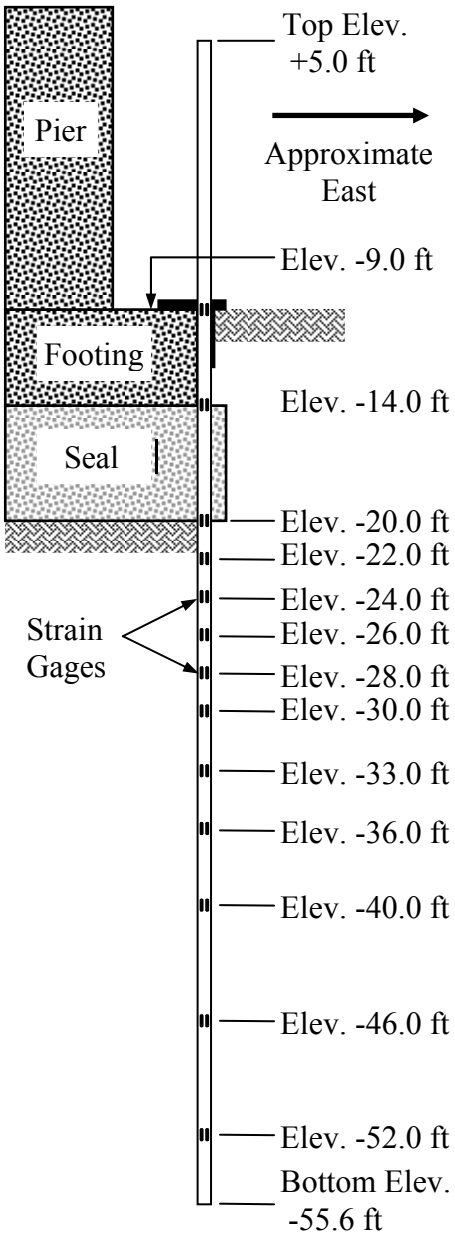

Figure 2.10 Section Elevation of As-Built ZW Mini-Pile

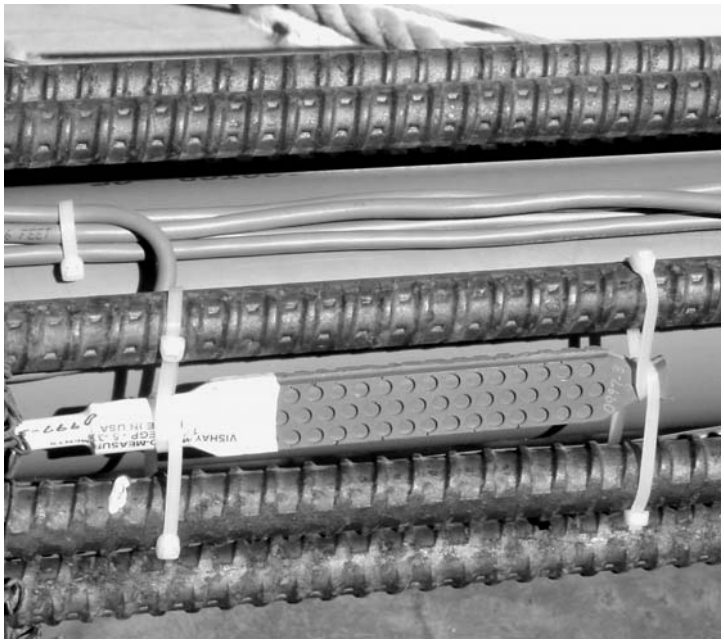

Figure 2.11 Vishay Model EGP-5-350 Embedment Strain Gage

Coring a 9-in-diameter hole for the ZW mini-pile, through four layers of steel reinforcement and 11 ft of concrete with quartz aggregate, required expensive coring equipment beyond the scope of this project. Therefore, the location of the mini-pile was moved to the trailing face of the pier, as shown in Figure 2.10, where it would penetrate only the 6-ft-thick seal and no reinforcing steel. A bracket, constructed of 6 in x 6 in x ½ in steel angles, bolted to the pier footing by a diver using ten ¾ in x 7 in Hilti concrete studs, was used to attach the top of the mini-pile to the pile cap. The location of mini-pile was equidistant between the outer two H-piles in the trailing row of Pier 1S and 1.8 ft center to center from the row. The fender system prevented installation nearer to the pier centerline.

Installation of the mini-pile required five days, November 17-21, 2003. Equipment breakdowns delayed the installation, and 50 knot winds moved the barge 10 ft overnight, snapping the ZW casing just above the footing bracket. A diver replaced the damaged

casing, and the site work was completed within the planned 3-week schedule. Figure 2.12a shows the placement of ZW steel casing (i.e. mini-pile) and 2.12b shows the rebar cage being installed in the mini-pile.

Figure 2.12 a) Placing ZW Casing b) Placing Mini-Pile Rebar Cage

2.4 Soil Total Stress and Pore Pressure Gages

During the installation of the mini-pile, UF also installed six push-in lateral stress cells, Figures 2.13a and 2.13b, to monitor changes in the pore pressure and total horizontal stresses at Pier 1S. Since the greatest soil stress changes were expected in the soil adjacent to the cap and seal concrete, the instrumentation was placed 1.5 to 2.8 ft from and facing the

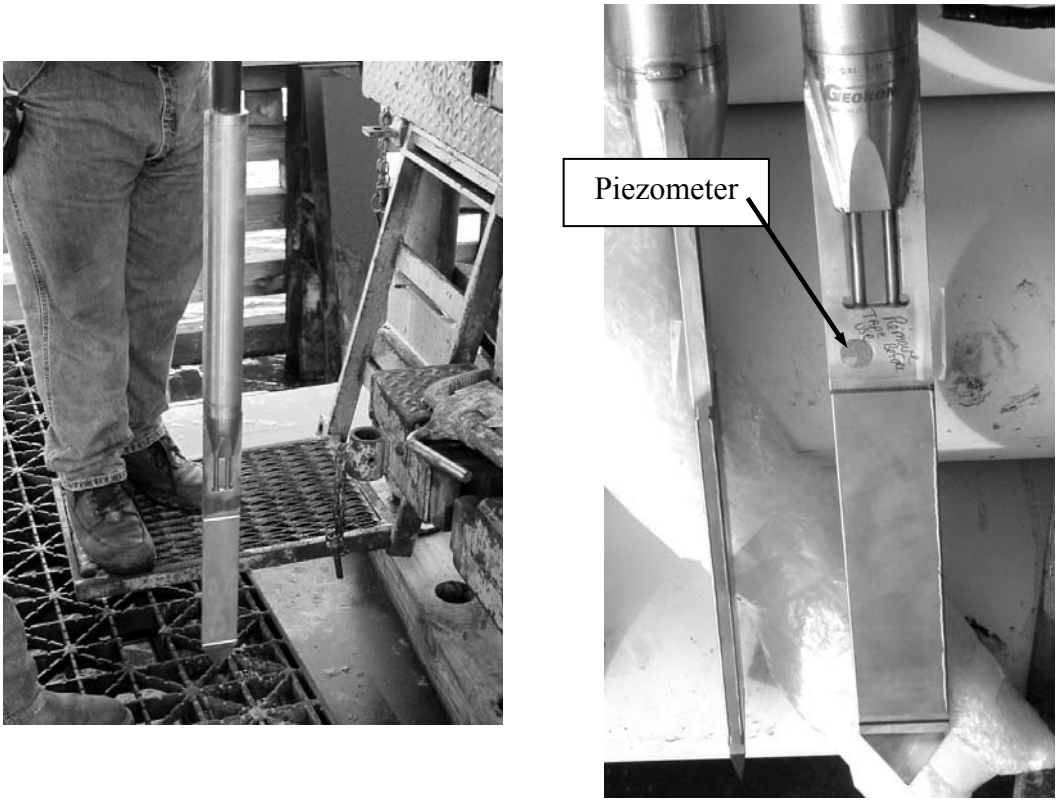

Figure 2.13 a) Push-in Stress Cell b) Piezometer

cap & seal, at three locations on both the East and West sides of Pier 1S. Figure 2.3 provides the locations and centerline elevations of the installed cells. UF purchased the push-in cells (model 4830) from Geokon, Inc. Both the total stress cells and the piezometers have a full scale range of 150 psi and provide 5 volts output at full scale. Shown in Figure 2.13 b, the piezometers located just above the stress cell have a stainless steel filter stone with a 0.75 in diameter. The total stress cells had dimensions of 2 in width x 8.25 in length x 0.25 in thickness. The drill rig pushed the cells (see Figure 2.13) down to the target elevation using AWJ rods. After the push, the driller disconnected the rods from a reverse thread coupler 5 ft above the cell, leaving the cell and 5 ft of rod in place. A diver helped orient the cell as it penetrated the mudline and then installed the instrumentation cables in PVC piping run over to the pier for protection.

2.5 Laboratory Testing of Mini-Pile

To develop the mini-pile's P-y curves, as well as validate FB-Pier's representation of the mini-pile for later dynamic analyses, the moment curvature relationship of the composite pile had to be determined. Given the complexity of the pile (i.e. steel shell, concrete, and grade 60 dywidag bars, Fig 2.8), it was decided to cast an identical 5-ft-section of the mini-pile during field grouting, and test it later at UF's structures lab, Figure 2.14. The test section also included two strain gages embedded in the concrete grout at the center (2.5' in from ends) equally spaced above and below the neutral axis. In addition, three 6" cylinder specimens and three 2" cube specimens of the high strength grout in the mini-pile were collected from the field and tested at UF for modulus and compressive strength.

At the University of Florida Structure's Lab, a 3 point flexural beam test was setup with a concentrated load applied upward at the center of the 5-ft-section, Figure 2.15, and steel threaded bar as tie downs or reaction at each end. Each threaded bar, two at each end, i.e. straddling the mini-pile, were connected to 200 kip tie down points in the lab's floor. The load, Fig. 2.15, was applied using an Enerpac hydraulic jack with a manual hydraulic pump and a pressure gage. Wooden bearing seats and steel plates, Fig. 2.13 and 2.15, were used to apply the load uniformly to the round mini-pile section at both the supports and the hydraulic jack. The load was measured using a Houston Scientific 200 kip load cell placed between

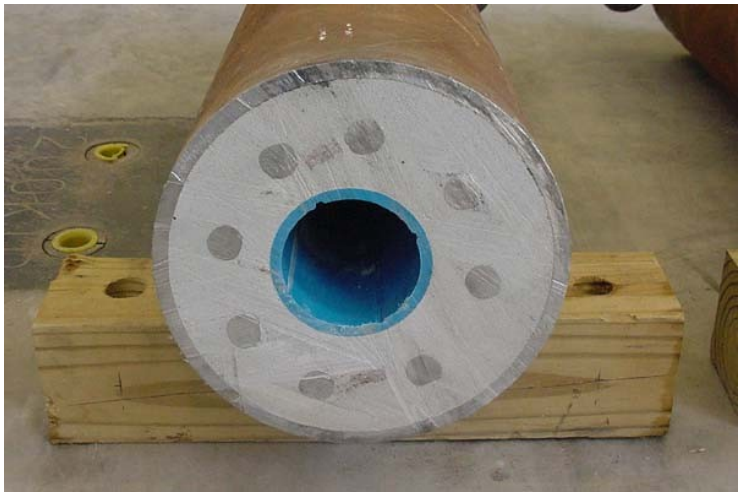

Figure 2.14 Five Foot Test section of Mini-pile

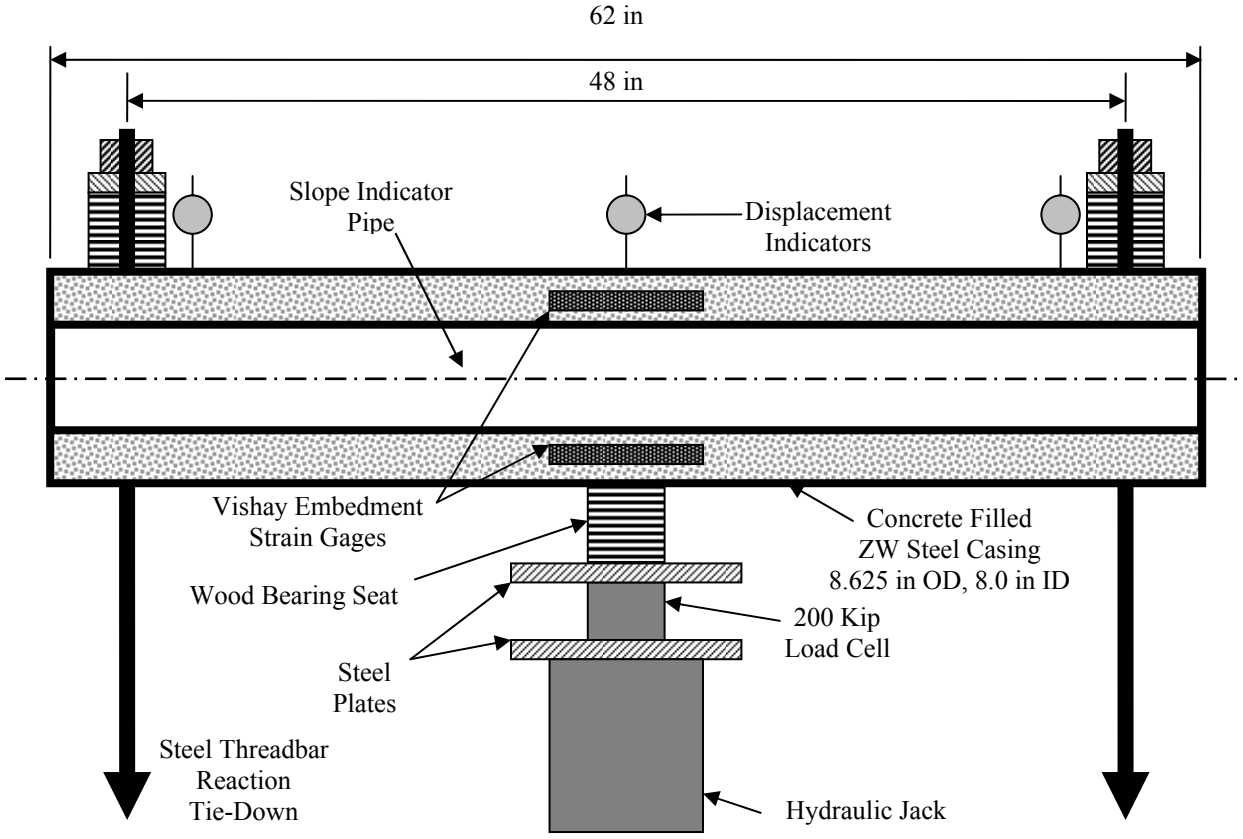

Figure 2.15 Laboratory Composite Pile Test Setup

the jack and the wooden bearing seat. Chicago Dial Indicator (CDI) electronic displacement indicators, Fig. 2.15 & 2.16, were placed at the ends and the center point of the top of the mini-pile and attached to a stable reference beam. At the start of the test, a

seating load of 1,000 lbs was applied for approximately 5 minutes followed by 1,000 lbs load increments up to 40,000 lbs. The displacements of the dial indicators were monitored and recorded for approximately 2 minutes after the application of each 1,000 lb load increment. The strains and applied load were monitored and recorded using a laptop computer running Labview with a PCMCIA data acquisition card (6036E) and SCXI Conditioning Modules from National Instruments (NI). During the test, the Labview program provided real-time plots of the load versus strain from each gage. The hydraulic pump pressure was also recorded to compare with the load cell measurement.

Figure 2.16 Laboratory Mini-Pile Test

Following the test, the beam was cut in half (Fig. 2.14) at the strain gage locations to identify visible signs of grout cracking as well as verify orientation and location of the strain gages (i.e. radial distance to gages).

Based on length between reactions and loading point, the moments at the center of test section (location of strain gages) were computed for each load step. Using radial distance from the neutral axis of the composite section and the bending strains, the curvature of the pile at the strain location was computed for each load increment. Shown in Figure 2.17 is the experimental moment curvature relationship for the composite pile. Also shown in the figure is FB-Pier predicted moment curvature relationship of the pile assuming the steel shell acts as reinforcement instead of concrete confinement. Note, the moment curvature relationship of the mini-pile is required to evaluate the field P-y curves of the soil. That is, the strain gages give the curvature at multiple locations along the pile, Fig. 2.10,

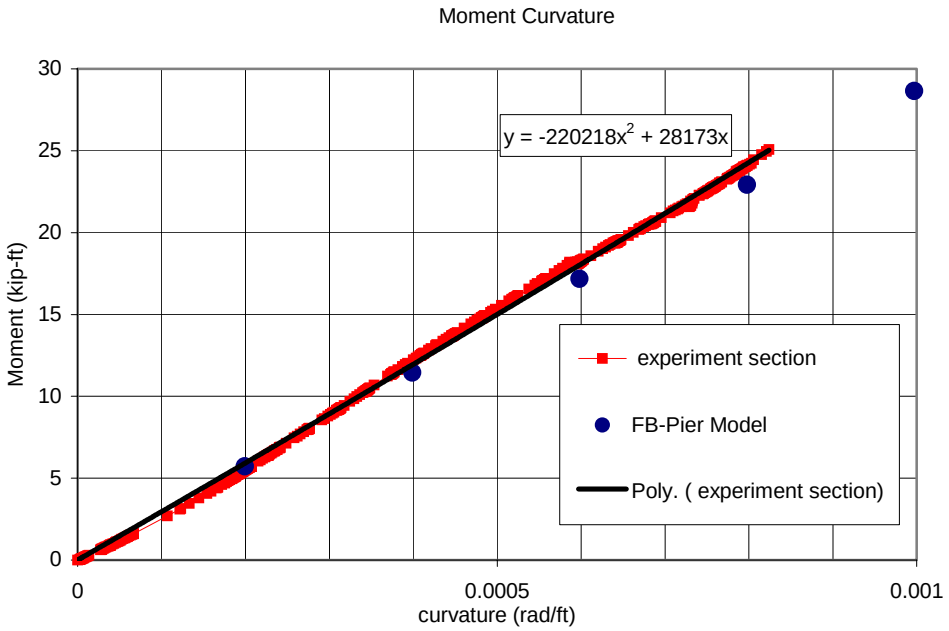

Figure 2.17 Moment Curvature Relationship for Mini-Pile

from which the bending moments, Fig. 2.17, are found. Differentiating the bending moment distribution twice at a specific location gives the soil resistance, P, of a P-y plot.

CHAPTER 3
PIER 1S SOIL-STRUCTURE RESPONSE WITH BARGE IMPACT

3.1 Testing Program

Barge impact testing was performed on Piers 1S and 3S at the St. George Island Bridge. As indicated in Chapter 2, only Pier 1S was equipped with soil-structure instrumentation to monitor the impact below the mud-line. Presented in this chapter are the soil and pile results for Pier 1S for three of those impacts, P1T1, P1T6 and P1T7. All of these impacts occurred without the superstructure (i.e. bridge deck, etc.) in place. A discussion of data reduction (pile displacements, soil dynamic resistance, P-y curves etc.) and distribution of forces (pile, cap, etc.) follows. The results of the soil-structure interaction (i.e. soil-pile resistance, cap pressures, etc.) will be used in Chapter 4 for FB-Pier and LS-Dyna modeling. A brief description of Pier 1S, vessel type and data acquisition system, is given prior to showing the measured results.

3.1.1 Pier Description

Pier 1S was built in the 1960's and was not designed for a specified vessel impact loading. At that time the AASHTO design code did not address vessel impact. The pier members were reinforced concrete and consisted of two tapered pier columns with pier cap, and a lateral shear wall just above the waterline. The width of each pier at the barge contact point was 6 ft. Attached to the pier in the impact zone were four clevis-pin load cells connected to a reinforced concrete block (Consolazio et al., 2004) used to measure the impact forces on the structure.

The mud-line footing consisted of a single concrete pile cap (21 ft wide, 39 ft long, by 5 ft thick), Figure 3.1. Beneath the pile cap was a concrete tremie seal (24 ft wide, 42 ft wide, 6 ft thick), with forty driven steel HP 14x73 piles to an elevation -62 ft. A layout of the pile cap, seal, and piles are shown in Figure 3.1. Attached to the pile cap, inserted through a drilled hole in the tremie seal was the mini-pile (Figs. 2.8 & 2.10).

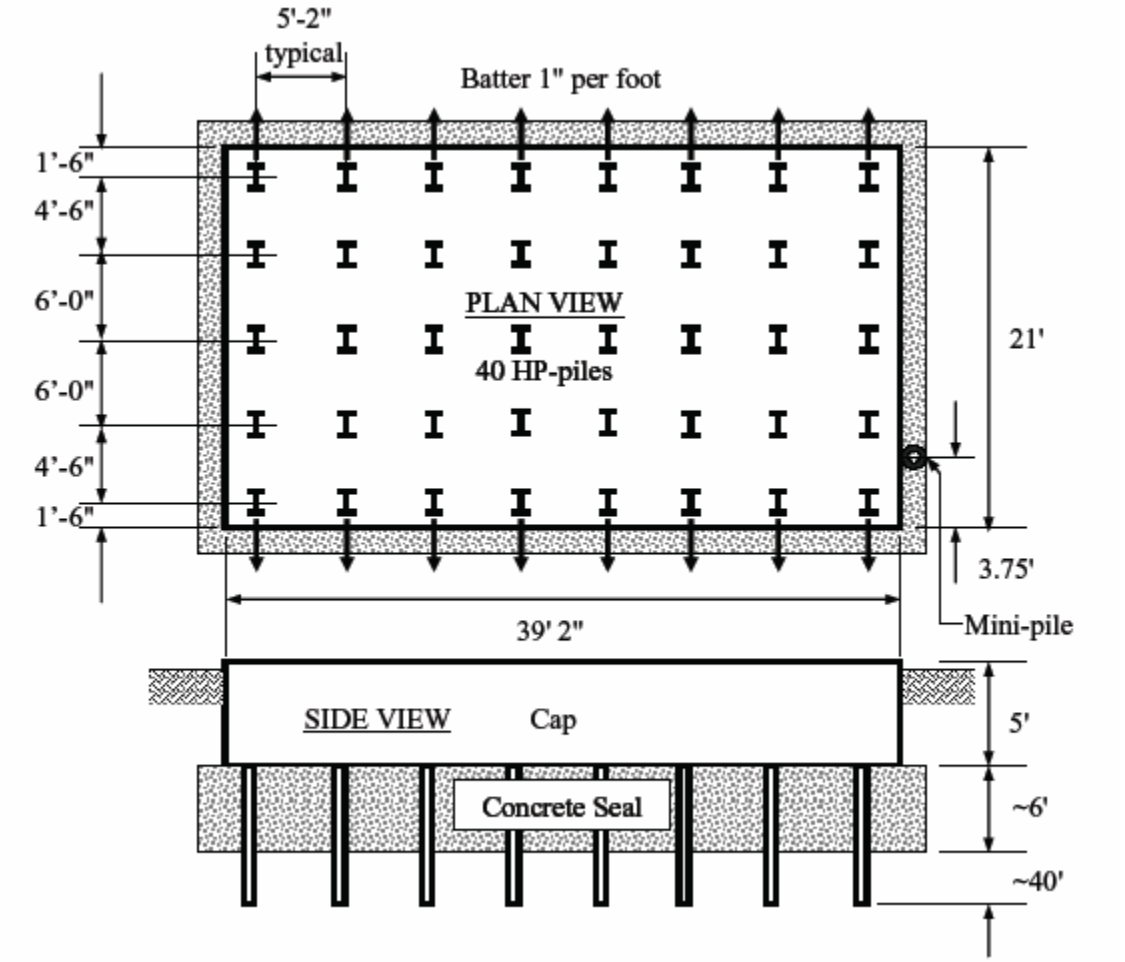

Figure 3.1 Pier 1S Plan and Elevation

3.1.2 Vessel Description

The deck barge used for the impact testing was leased from Boh Brothers Construction, Inc., the construction contractor of the new St. George Island Bridge, as well as the demolition contractor of the old St. George Bridge. The barge was 151.5 ft

long, 50 ft wide, 12 ft deep, and weighed approximately 344 tons when empty. This specific barge was selected because 1) it was representative of a jumbo barge; 2) it was already onsite, thus eliminating mobilization and transportation costs; and 3) with the wide head log, it allowed for multiple undamaged impact locations.

3.1.3 Data Acquisition System

The data acquisition system (Fig. 4.2) consisted of a laptop computer, along with a PCMCIA data acquisition card (6036E) and two SCXI Modules from National Instruments (NI). The four SCXI-1520 Strain Input Modules provided 26 channels (32 max) for strain gages buffered for nearly simultaneous digital measurement. The SCXI-1102, 32 channel Analog Input Module, provided 6 channels for stress cells and 8 channels for accelerometers. A LabView Virtual Interface (VI) was written later to convert the raw voltages to strains and accelerations. The data was stored in ASCII format and later transferred to Excel spreadsheets for filtering and analysis.

The raw voltage from the soil monitoring instruments; soil total stress gages and pore pressure gages, and the instrumented mini-pile with accelerometers was sampled at 2000 samples per second over a period of 60 seconds after being triggered. Note, it was important to continue sampling after the impact to monitor any delayed rebound in the pier as well as any dissipation of the excess pore pressure in the soil. A change in pore pressure indicates if the soil behaves as a drained or undrained soil.

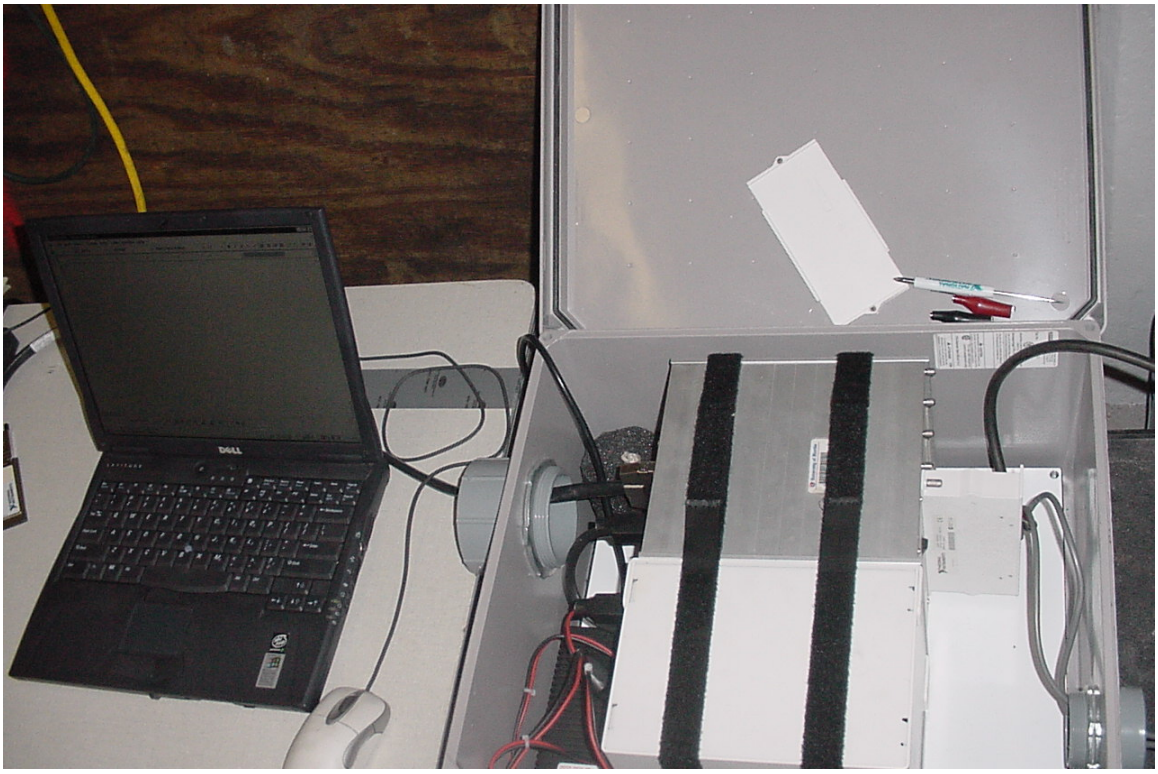

Figure 3.2 Data Acquisition System

3.1.4 Data Acquisition Equipment Location During Impact

Each of National Instrument's SCXI Modules were housed in sealed enclosures (Fig. 3.2), to provide protection from impact debris and salt water spray. Each module was attached to a shock absorbent pad within the enclosure (Figure 3.2), to prevent vibration disturbances.

Due to limited space at the pier for placement of the equipment during the testing, a portion of the fender system was left in place to serve as a platform for the data acquisition equipment during the impact tests. The cables for the soil total stress and pore pressure gages were housed in PVC piping extending from the mudline, up the side of the pier and over to the working platform. The cables from the mini-pile (strain gages and accelerometers) were routed around the PVC piping from the pier to the working platform, Figure 3.3.

The data acquisition was initially set to be triggered from infrared optical break beams attached to the pier and located at the front or bow of the barge. However, due to interference from a portable power supply, the optical trigger did not perform consistently and consequently, a manual trigger was installed in order to capture the data.

Figure 3.3 Fender System and Working Platform

3.1.5 Monitored Vessel-Pier Impacts

In the planning stages of the tests, LS-Dyna simulation of barge – pier impacts were performed to determine representative barge velocities vs. impact forces. Based on the latter study, it was decided to vary barge velocities between 0.86 and 3.97 knots and to thus limit impact forces to 1000 kips or less in order to prevent pier collapse.

Shown in Table 3.1 is a summary of the recorded barge speed, weight and peak impact force that were captured with the UF Geotechnical Instrumentation. Note that for the tests the barge carried an additional payload of two 55 ft long prestressed concrete bridge superstructure units salvaged from the demolition, see Fig. 3.4. The barge and payload had a total weight of 626 or 604 tons, Table 3.1. The impact tests were performed at different times of the day, consequently, the channel current direction and velocity was a factor that affected the barge impact location and final impact velocity. Tugboats were used to accelerate the barge while a ringer barge was used to control the direction of the barge. This approach was shown to limit the maximum speed to 4 knots; however this controlled approach did result in very satisfactory tests.

Table 3.1 Summaries of Impact Tests Parameters and Results

Test Series	Test Number	Impact Speed (knots)	Barge Weight (tons)	Peak Impact Load (kips)
P1	P1T1	0.86	626	102
	P1T6	3.97	604	882
	P1T7	3.92	604	864

Figure 3.4 Deck Barge with Payload

3.2 Experimental Results

As identified in Section 3.1.3, Data Acquisition, all of the data (i.e., strain, stress, etc.) was recorded at 2000 samples/second to ensure that all soil-structure response was captured. However, at such frequencies, the likelihood of capturing noise (i.e., generators, welders, etc.) was also probable. To remove extraneous noise from the impact signals, the data was subsequently filtered with Fast Fourier Transform (FFT). Generally, the latter involved removing high frequency (> 500 Hz) noise. However, in the case of piezoelectric accelerometers, which involve DC coupling, both low and high frequency filtering was employed. The resulting (frequency domain) data was transformed back to a time domain (inverse FFT) and analyzed. The following pile displacements, loads, soil pressures, etc. are based on the filtered data. A complete description, i.e. recording of the filtered impact data is given in Appendix B.

3.2.1 Applied Loads

Pier 1S was struck by the barge multiple times, with full soil-structure behavior captured for three of these events, Table 3.1. Shown in Figure 3.5 are the dynamic pier loads as a function of time as recorded from the barge striking the concrete impact block. The maximum recorded dynamic loads for each of the events, Fig. 3.5 were 102, 882 and 864 kips.

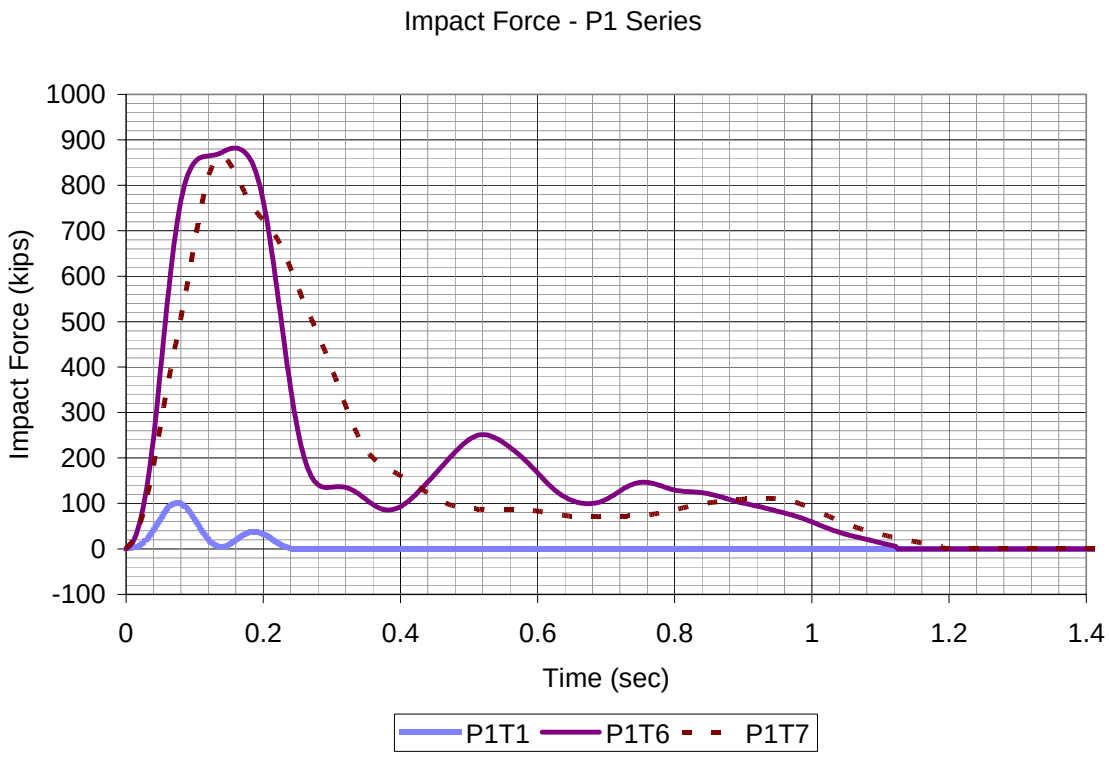

Figure 3.5 Impact Force for P1 Series

The smallest load application, P1T1, was used to check the data collection trigger, as well as the storing functions of the data acquisition system. The impact duration from this test was no more than 0.24 sec. Evident for this impact were the two load peaks. The latter could possibly be attributed to the structure (i.e. pier, pile cap, and piles) separating and re-striking the barge (slower velocity) during the event.

Even though P1T7 had a slightly smaller peak dynamic force (864 kips) than P1T6 (882 kips), it produced the highest energy (integral of F x velocity) transfer from the barge to the pier and was the impact test studied in detail. Also, it is evident that the impact force of P1T6 was more complicated than P1T7. P1T7's force time response suggests that the barge rammed the pier, and both were moving together, i.e. barge developing a constant force (80kips) between 0.5 and 0.8 sec, Fig. 3.5. However, in the case of P1T6, there was another peak force (250 kips) at 0.5sec, which was thought to be the tug striking the rear of the barge. Note, that the tug, Fig. 3.4, disengaged the barge only seconds (2-4) before impact.

For the later FB-Pier and LS-Dyna modeling (Chapter 4), impact P1T7 was modeled with only the dynamic Force vs. Time plot given in Figure 3.5. Of interest is the distribution of dynamic forces (inertia, damping, and static) acting within the system for various times (i.e., peak applied force, 0.15sec, or at maximum cap displacements, 0.25 sec). The pile-soil inertia, damping, and static forces were assessed from the pile strain gage data, whereas the soil-cap static, inertia and damping forces were determined from the soil pressure gages in front and behind the pile cap and seal. Unfortunately, the shear forces beneath and alongside the pile cap and seal could not be measured directly, however they were estimated based on the shear forces measured adjacent to the piles using the strain gage data.

3.2.2 Analysis of Strains

Thirteen strain gage pairs were cast within the mini pile, Fig 2.10, at multiple elevations. The voltages from each gage were monitored for each impact (Table 3.1) and saved to a file. Subsequently, the voltage readings for each gage (2000/sec) were converted to strain, ε, using the equation:

$$\varepsilon = \frac{4\Delta V}{G.F. * E} \qquad \text{Eq. 3.1}$$

Where ε = strain

ΔV = voltage output

G.F. = gage factor

E = excitation voltage

Next, the data was filtered (FFT, signal less than 500 Hz), and plotted as a function of time. For instance, the filtered strain gage data at the top of the mini-pile (Elev. –20 ft) for impact P1T7 are shown in Figure 3.6. The two strains, from each side of the mini-pile, represent the compression (positive) and tension (negative) stresses from bending and axial resistance at Elev. –20 ft. Evident, from the figure, the bending has a higher component of the stresses than the axial (average) term.

To estimate the lateral soil resistance (Force/length: P-y), the bending moments have to be separated from the axial behavior. Generally, the bending moments are linearly related to the total strains, unless the section cracks (i.e., concrete filled pipe, Fig. 2.8). In the latter case, the bending strains have to be related the curvature of the section which in turn is related to the moments within the pile at a specific elevation and time. Equations, Eq. 3.2 and Eq. 3.3, were used to calculate the bending strains from the total strains, which were subsequently used to determine the curvature of the cross-section at a specific elevation and time. Note, the equation relating curvature to bending strain, Eq. 3.3, is a function of the distance, r to the location of the gages. Note, all strains were measured at the perimeter of the steel-reinforcing cage, Fig. 2.8.

$$\varepsilon_b = \frac{\varepsilon_1 - \varepsilon_2}{2} \qquad \text{Eq. 3.2}$$

$$\phi = \frac{\varepsilon_b}{r} \qquad \text{Eq. 3.3}$$

Where ε_1 and ε_2 are lead and trail strains, respectively

r = radius of pile where strain is measured

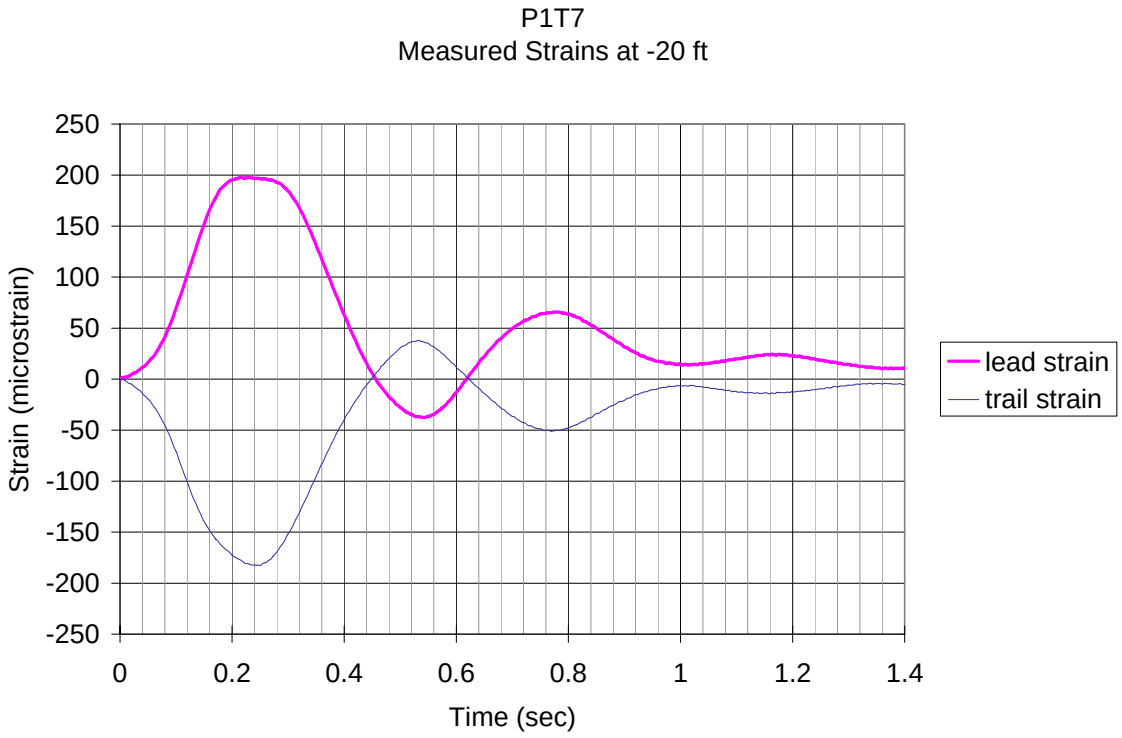

Figure 3.6 Paired Strains at -20 ft for P1T7

3.2.3 Dynamic Soil-Pile Resistance and P-y Curves

In order to develop the soil-pile resistance (P, force/length, vs. Y- lateral displacement) the lateral translation of the pile at a specific elevation as a function of time must be determined. The lateral displacements, Y, were determined by integrating (twice) the curvature as a function of depth for a specific time. First, the curvature was calculated from Eq. 3.3 as a function of depth for a given time (e.g., 0.025 sec intervals).

Note, since the strains were measured at points along the pile and not continuously, it was required to fit polynomials (least squares) to the data. Through single integration of curvature polynomial, the rotation, θ (angle), of a cross-section was found:

$$\theta = \frac{dy}{dz} = \int \varphi \, dz + C_1 \qquad \text{Eq. 3.4}$$

Next, integration of the rotation, θ (angle) Eq. 3.4, as a function of depth results in lateral displacement, y, as a function of depth, z, for a specific time, t,

$$y = \int \theta \, dz + C_2 \qquad \text{Eq. 3.5}$$

For evaluation of Eqs. 3.4 and 3.5, the constants C_1 and C_2, are required. Based on the negligible curvature of pile at -52 ft and downward, the following integration assumptions were used to assess the constants, C_1 & C_2:

Rotation

When z = -52 ft, θ = 0 rads

Displacement

When z = -52 ft, y = 0 ft

Figure 3.7 shows the results of the double integration of the curvature to obtain lateral pile displacements, y, as a function of depth, z, for multiple time steps. The deflected shapes of the mini-pile are for impact P1T7, plotted at 0.025 sec time intervals.

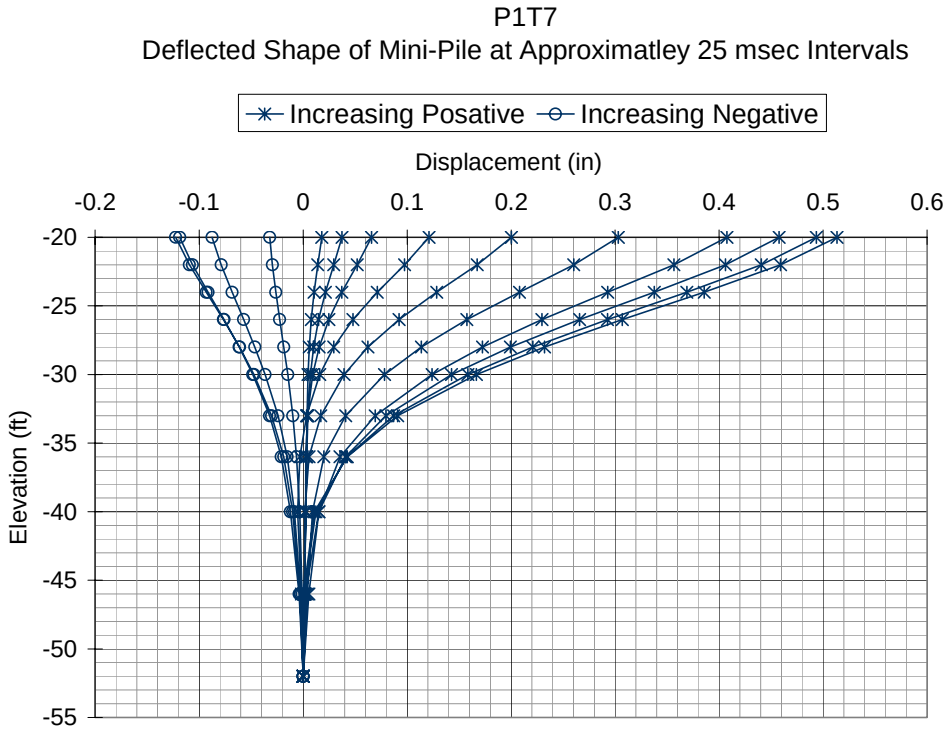

Figure 3.7 Deflected Shapes of Mini-Pile for P1T7

Of interest is a comparison of the lateral deflection of the piles versus other points on the cap, pier, etc. as a function of time for impact P1T7. Shown in Figure 3.8 are the measured displacements at the top of the shear wall, Elev. +6.0 ft, and the back calculated displacements of the mini-pile head, i.e., Elev. -20.0 ft (Fig. 3.7), as a function of time. The displacements at the shear wall, i.e., Elev. +6.0 ft, were the average response from integrating multiple accelerations records near the shear wall (Consolazio et al., 2005). Evident due to the similarity of period, and the rigidity of the pile cap, and seal, the difference in peak displacement was attributed to rotation about the center of pile cap-seal location. Specifically, due to the difference in elevations (i.e., 27 ft = 324 in.), a rotation of 0.00031 rad (0.05 deg) at the pile cap-seal would account for difference of 0.1 in. in lateral displacements of the two points.

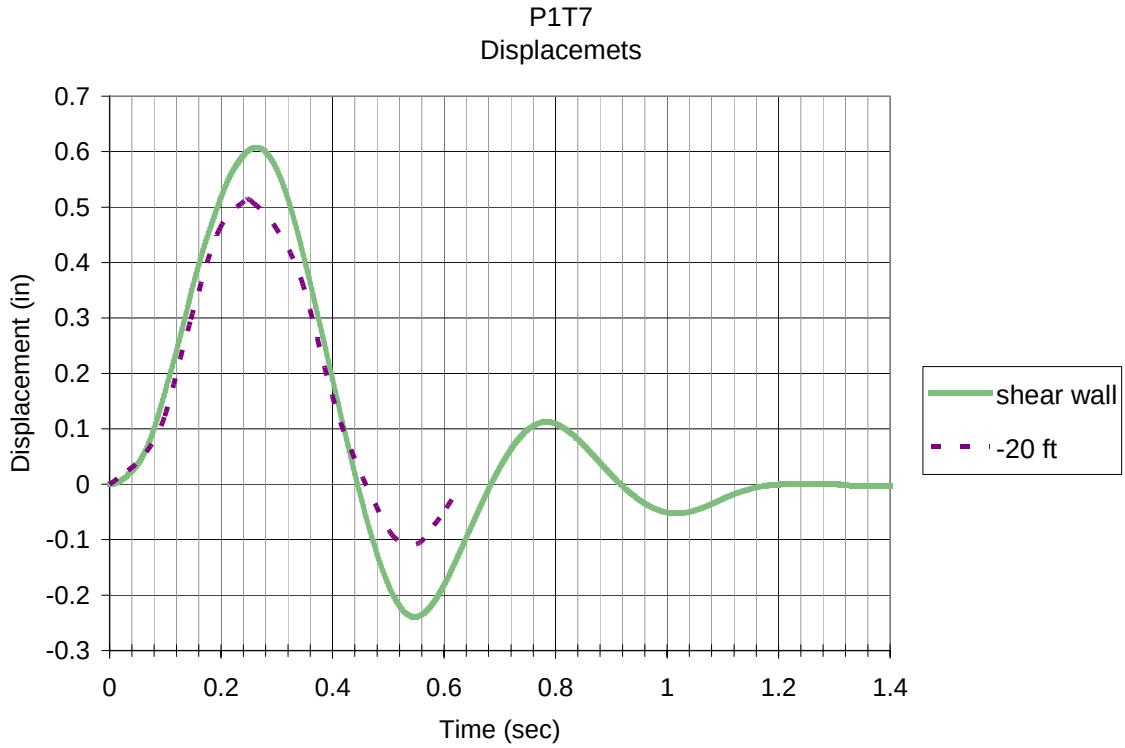

Figure 3.8 P1T7 Displacements

Having established the lateral deflections, y, as a function of time along the pile, the soil resistance, P (Force/length) for a given displacement, y, was needed. The soil resistance, P, may be obtained from double differentiation of the moment distribution along the length of the pile at a specific time. However, also of special interest are the shear forces, at the top of piles as a function of time. Specifically, Chapter 4 focuses on the different dynamic resistance (inertia, damping and static) provided to the pile cap-seal (piles, soil, etc.). Note, current AASHTO design only accounts for static resistance in vessel collision analysis.

Using the moment curvature relationship developed in section 2.6, the bending moments along the pile were determined from the curvatures, Eq. 3.3, for multiple time steps. Note, the moments could only be established at the 13 locations of strain gages,

Fig. 2.10, on the pile. Consequently, as with rotation and displacement analyses, polynomial equations were fit (least squares) to the moment points along the mini-pile. Each polynomial fit at a specific time was based on the shape of the moment distribution within the pile. Presented in Figure 3.9 are examples of the moment distributions plots along the pile length for test P1T7 at two different times, i.e., the peak lateral displacements (positive & negative) of the mini-pile's head.

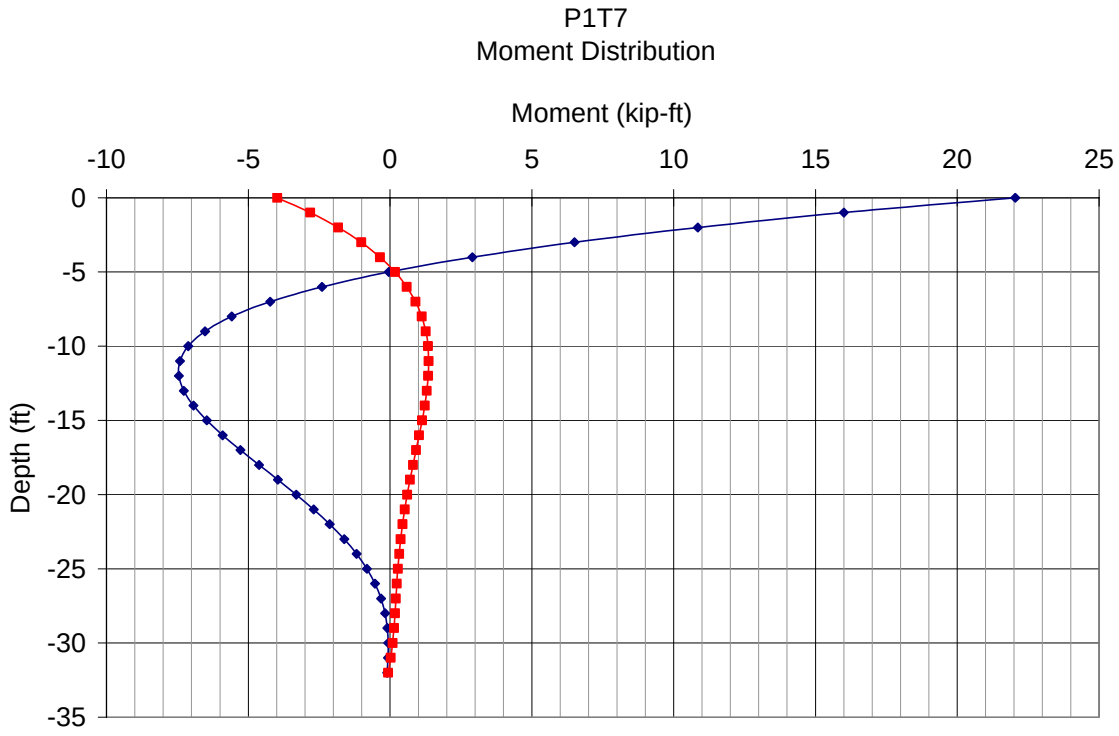

Figure 3.9 Moment Distributions at Peak Displacements in Mini-Pile for P1T7

Next, the shear force, V, within the mini pile was found by differentiating each moment distribution along the pile at specific times. For instance, Figure 3.10 depicts the shear force distribution, V, within the mini-pile for test P1T7 at peak lateral displacements, Fig. 3.7 (positive and negative) of the mini-pile. The shear (Fig. 3.10), moment (Fig. 3.9), and soil distribution, begin at the bottom of the seal concrete, i.e.,

Elev. –20 ft. Evident from Fig. 3.7, a maximum pile head shear of 6.5 kips was transferred from the pile cap-seal to an individual pile at a pile top displacement of 0.52".

Also of special interest was the pile head shear as a function of time. Shown in Figure 3.11 are shear forces as a function of time (0.025 sec increments). Interestingly, the maximum pile head shear, 8.5 kips occurs at 0.15 sec after impact, not at 0.25 sec where the maximum pile head displacements occurs, i.e., Fig. 3.8. The latter suggests

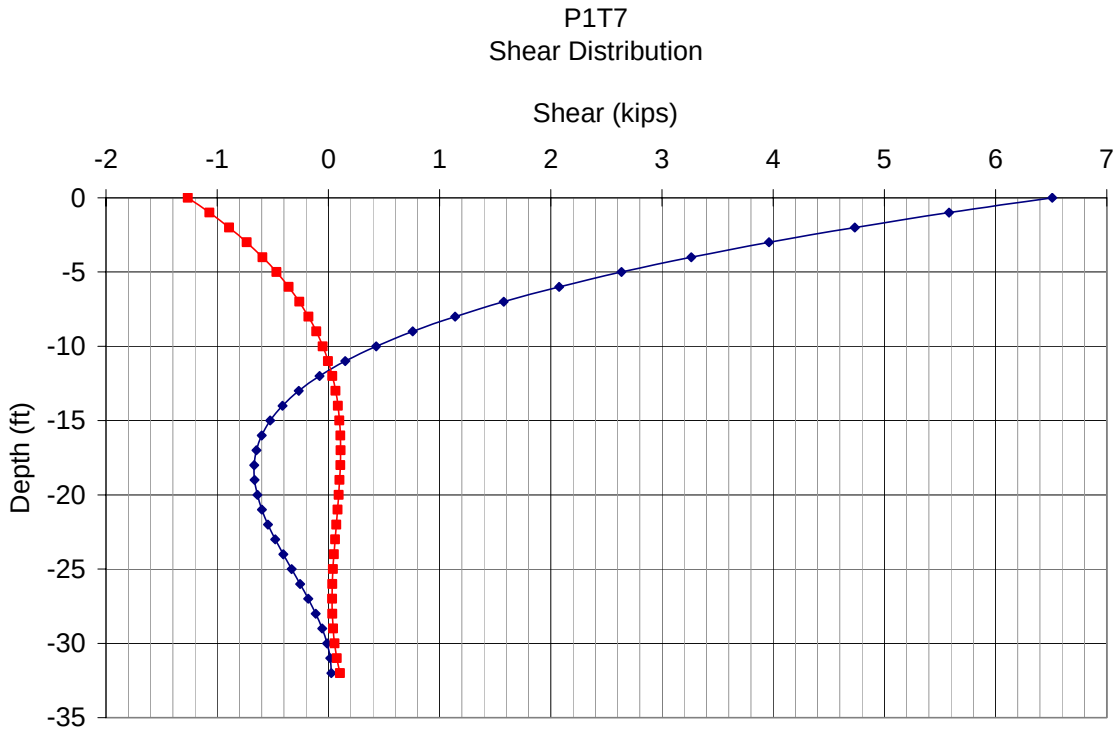

Figure 3.10 Shear Distributions at Peak Displacements in Mini-Pile for P1T7

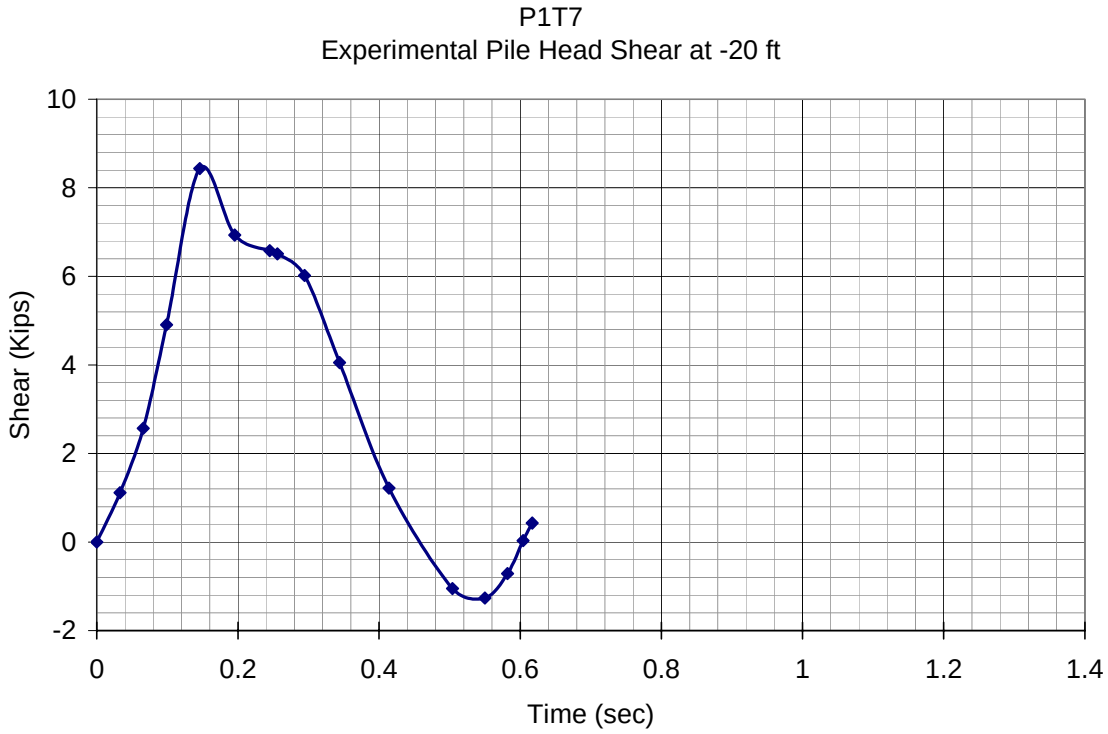

Figure 3.11 Pile Head Shear in Mini-Pile as Function of Time for P1T7 Impact

that other dynamic forces besides static resistance ($k\ y$) are developing. It should be remembered that the shear forces shown in Fig. 3.11 represents the total dynamic forces, i.e. the sum of inertia ($m\ \ddot{y}$), damping, ($c\ \dot{y}$), and static, ($k\ y$) resistance. Evident from Fig 3.8 at 0.15 sec, the velocity at Elev. –20ft is a maximum (i.e., $\dot{y} = \frac{d\,y}{d\,t}$), or significant damping resistance is developing, whereas the acceleration ($\ddot{y} = \frac{d^2 y}{d\,t^2}$) is small (change in slope ≅ 0) or inertia forces are negligible, and the static resistance ($k\ x$) is approximately half of the value at peak displacements, i.e., 0.25 sec. At 0.25 sec, or at the peak lateral displacements, Fig. 3.8, the static resistance is a maximum (i.e., $k\ y$), the damping, ($c\ \dot{y}$),

is negligible (i.e., velocity is zero), and the inertia force, ($m\ddot{y}$), is small. Consequently of special interest is the separation of dynamic forces (i.e., inertia, damping, & static) from the soil and the piles.

The total dynamic soil resistance, P (force/length), along the length of the mini-pile at a particular time was obtained by differentiating the shear distribution, V (Fig. 3.10), with respect to depth (i.e., $P = d\,V/\,dz = d^2\,M/\,dz^2$). For instance, Figure 3.12 shows the soil resistance, P for P1T7 corresponding to peak deflection times (i.e., 0.25 sec & 0.55 sec) of the mini-pile, Fig. 3.7. Again, P (force/length) represents the total dynamic force (inertia: $m\ddot{y}$, damping: $c\dot{y}$, and static: $k\,y$) transmitted from the pile to the soil at a specific time and depth.

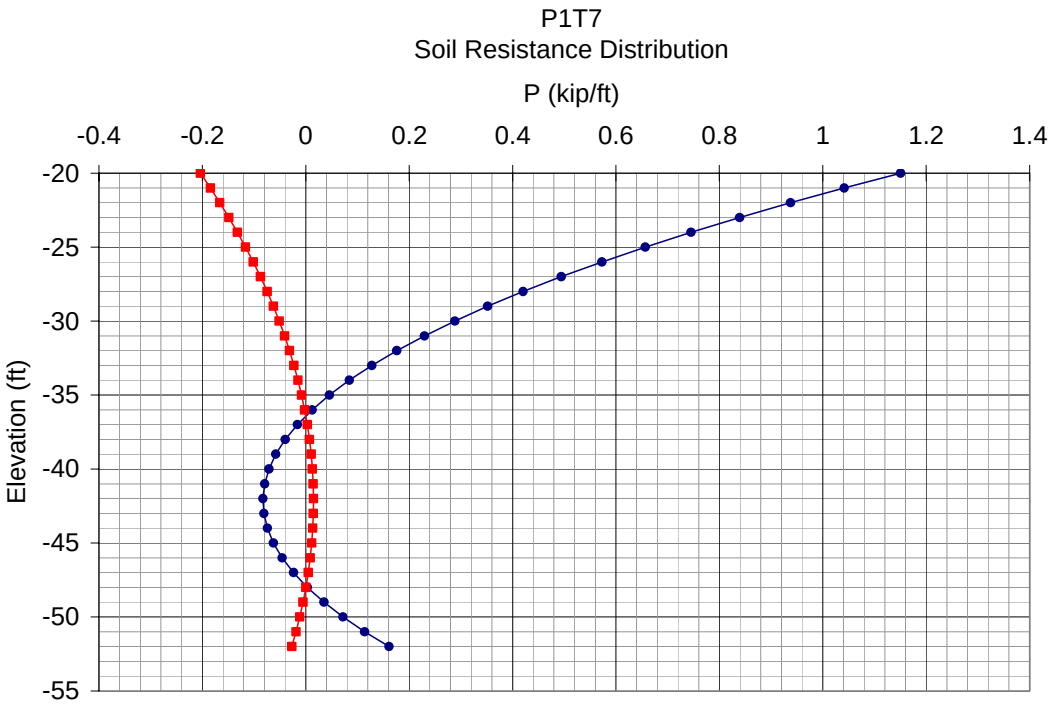

Figure 3.12 Peak Soil Resistance Distributions for P1T7

Next, for a specific depth, the dynamic soil resistance, P, was plotted as a function of displacement. The latter required that the shear distribution as a function of time (e.g., Fig 3.11) be differentiated at a specific depth at multiple times and plotted against pile displacements from Fig. 3.7 for the same depth and time. Shown in Figure 3.13 is a typical dynamic soil resistance vs. displacement at the pile head (Elev. –20 ft) of the mini-pile. Of interest is the shape and magnitude of the soil resistance curve. Evident is that the peak soil resistance occurs at a displacement of 0.3 in. or at a time of 0.15 sec (Fig 3.8) for which pile velocities and damping are high. However, at 0.5 in. displacement or time 0.25 sec (Fig. 3.8), the damping forces are negligible (velocity, $\dot{y} \mapsto 0$) and the soil static resistance (i.e., $k\ y$) is fully mobilized. Obviously, at peak

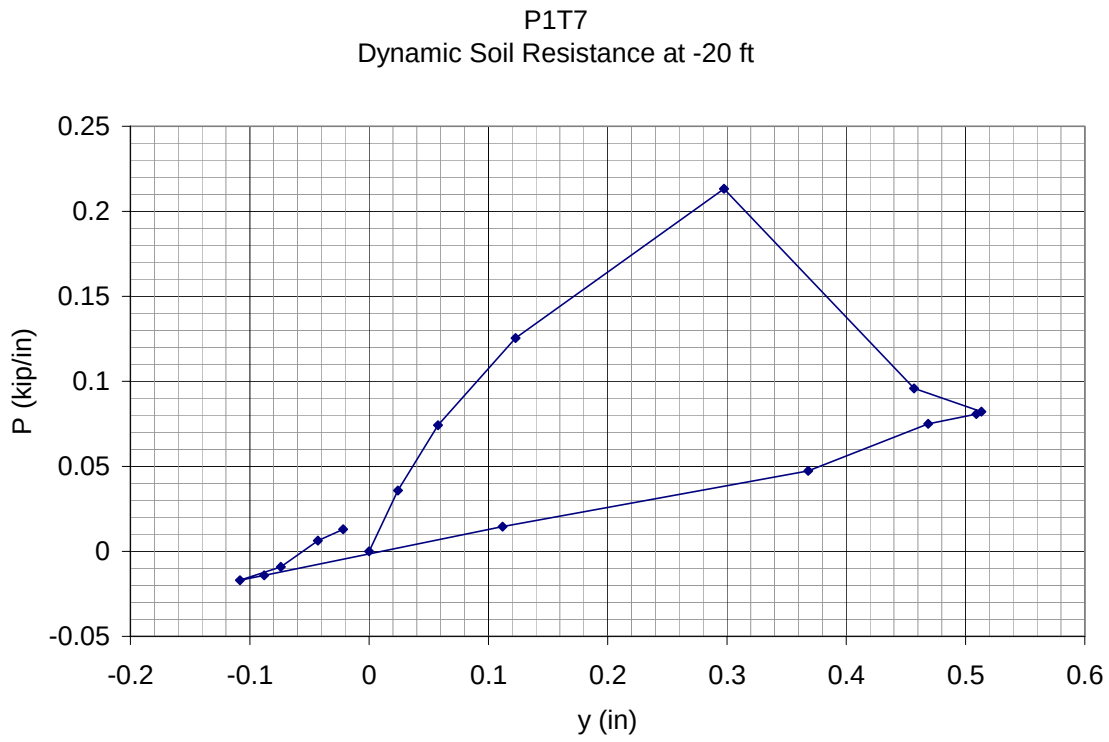

Figure 3.13 Typical Back Computed Dynamic Soil Resistance for P1T7

dynamic loading, 0.15sec - Fig. 3.5, the major dynamic soil resistance may be attributed to damping, which is currently not considered in the AASHTO design.

Next of interest is a comparison of the static soil resistance, P-y, as determined from insitu testing (Chapter 2) with the measured dynamic soil resistance. For Pier 1S there were multiple DMT and PMT tests conducted on the East and West side of the Pier (i.e., Fig. 2.3, Table 2.1). Based on the insitu tests, soil layering, Fig. 2.5 was identified. Evident from Fig. 2.5 there are 5 layers between Elev. –20ft and –25ft; however from Insitu testing on both sides of cap-seal, the layers were sloping. Shown in Fig. 3.14 are the computed P-y soil resistances at multiple depths (Elev. –20ft to –25 ft) from both Dilatometer and Pressuremeter Data from both sides of the pier. Note that each curve is for an individual test performed at a specific elevation. The "Average Back Computed" value represents the mean of the dynamic soil resistance (e.g., Fig. 3.11) from the experimental mini-pile from Elevation –20ft to –25ft. Evident from the insitu and measured resistance, Fig. 3.14, there is some variability in the maximum static soil resistance (0.02 kip/in. to 0.19 kip/in) due to soil layering and spatial variability (east vs. west); however the mean of the insitu data (0.09 kip/in) is close to the measured dynamic soil resistance, 0.075 kip/in from the mini-pile at a lateral deflection of 0.4 in. Whereas, at the peak dynamic resistance, 0.12 kips/in. at 0.25 in. to 0.03 in. of lateral displacement (occurs at 0.15 sec -Fig. 3.8), the average static P-y resistance is only 0.065 kips/in (Fig. 3.12). Consequently approximately half of the dynamic resistance is due to static resistance and the other half may be attributed to soil damping.

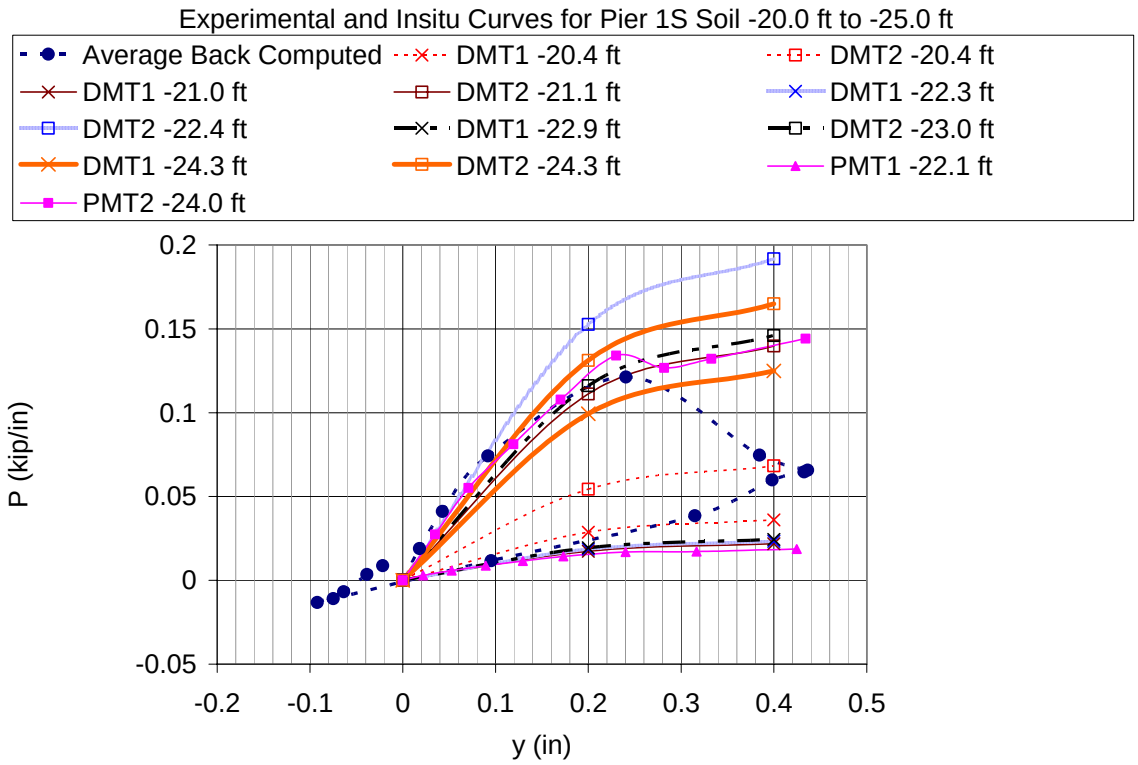

Figure 3.14 Dynamic and Static Soil Resistance Curves at Elev. -20 ft to 25 ft

3.2.4 Soil Stress Gages

Besides pile-soil resistance, the pile cap/seal-soil resistance is also of great interest. Since the soil-pile cap/seal forces are also dynamic in nature, they may include inertia, damping, and static resistance. To assist in assessing the dynamic soil forces in the vicinity of the pile cap-seal, lateral stress cells, Fig. 2.3, were placed on both the east and west side of the cap at various depths. Note, these devices are total stress cells and monitor the forces that the cap and seal would sense. Also, the devices only measure changes in stresses, i.e., not the existing insitu lateral stress currently in the ground, but the change in stress from pile-cap motion or even possibly soil mass motion due to the barge impact.

Shown in Figures 3.15 and 3.16 are the changes in the total lateral soil stresses at Elev. -13.0 ft, -17.0 ft, and -25.0 ft on the east and west side of Pier 1S which represent the front and back of the pile cap – seal during the impact. The first two elevations are the response in the silt, sand layers with shell, Fig. 2.5 (layers 1-3) that surrounds the cap and seal. The highest stress change (Elev. –25ft) occurs within layer 4 (Fig. 2.5) that corresponds to a stronger silty sand layer. The response displayed in Figs. 3.15 and 3.16 are classic passive and active soil pressures that would be observed in front and behind a retaining wall. For instance, Fig. 3.15 displays the increase in soil pressure, i.e., passive stress state, acting in front of a wall as the wall moves into the soil, whereas, Fig. 3.16

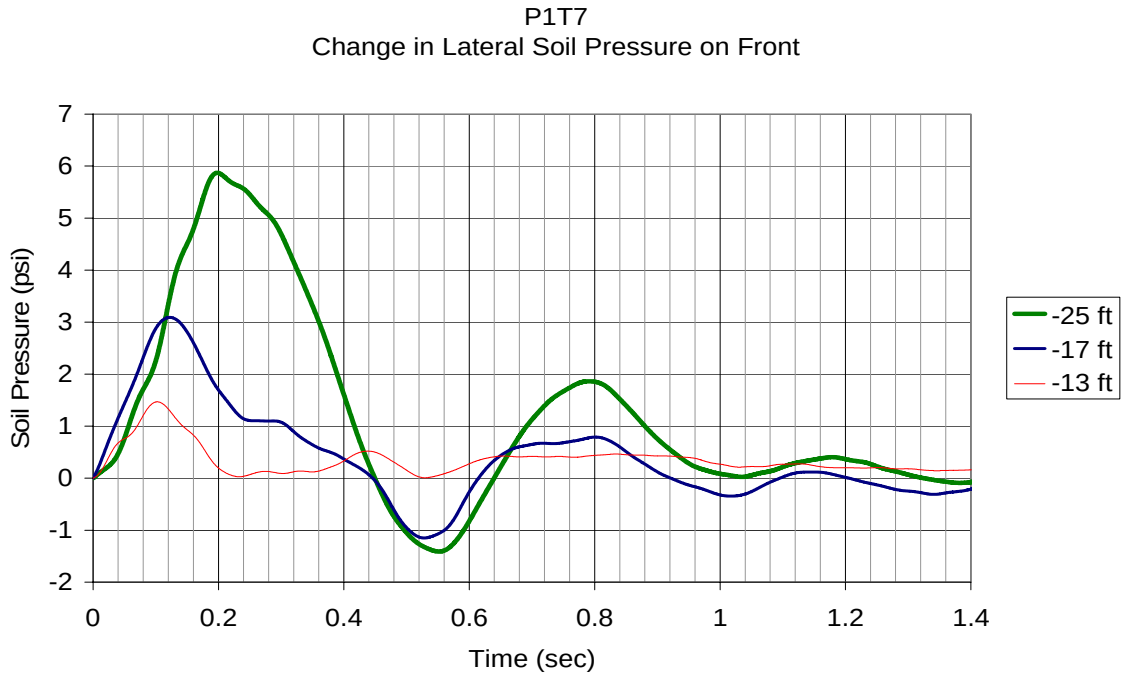

Figure 3.15 Changes in Lateral Soil Pressure on Front

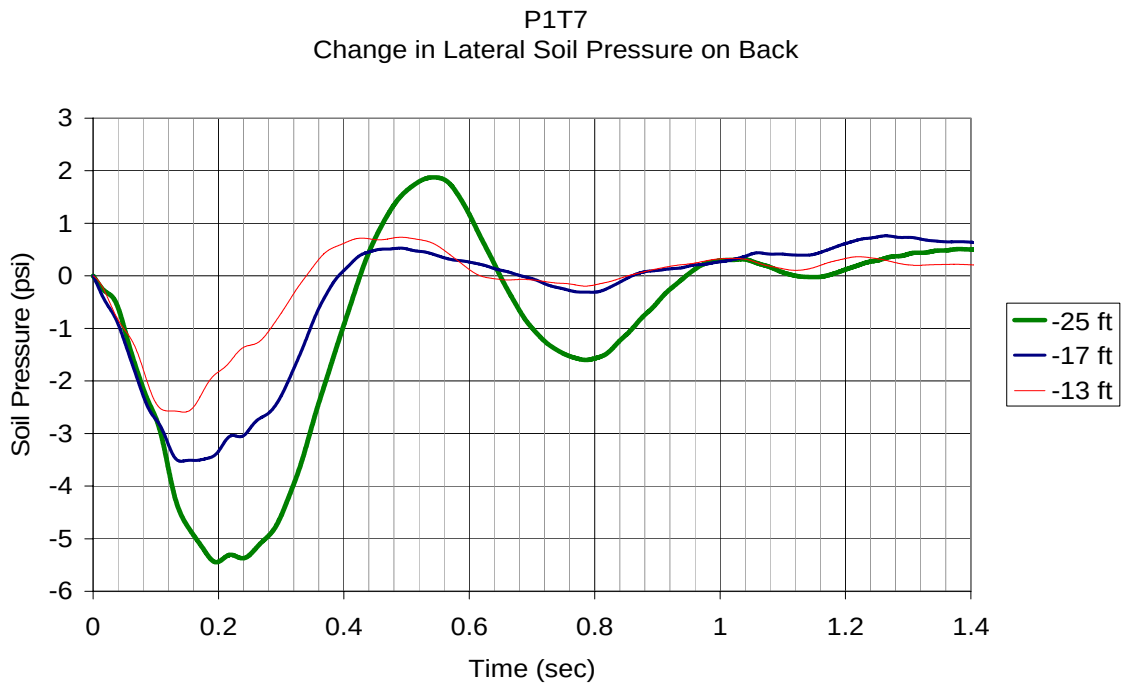

Figure 3.16 Changes in Lateral Soil Pressure on Back

shows the decrease in soil pressure, i.e., active stress state, as the wall moves away from the soil mass. Also, the increase in lateral stress change with depth, Figs. 3.15 and 3.16, may be attributed to the higher vertical stresses with depth, i.e., the horizontal stress is usually characterized as a constant (e.g., active and passive pressure coefficients, Ka, Kp) times the vertical stress at a given depth.

Next, the resultant lateral stress, σ_R (Fig. 3.17), i.e., the sum of the lateral stress on the lead and trail side of cap and seal was obtained. Note, this is possible, since the lead and trail sides of the cap and seal have the same areas. Finally, the resultant lateral stress, σ_R, was multiplied by the surface area of the cap and seal faces to give the resultant dynamic forces, Fig. 3.18, acting on the cap and seal as a function of time for barge impact P1T7.

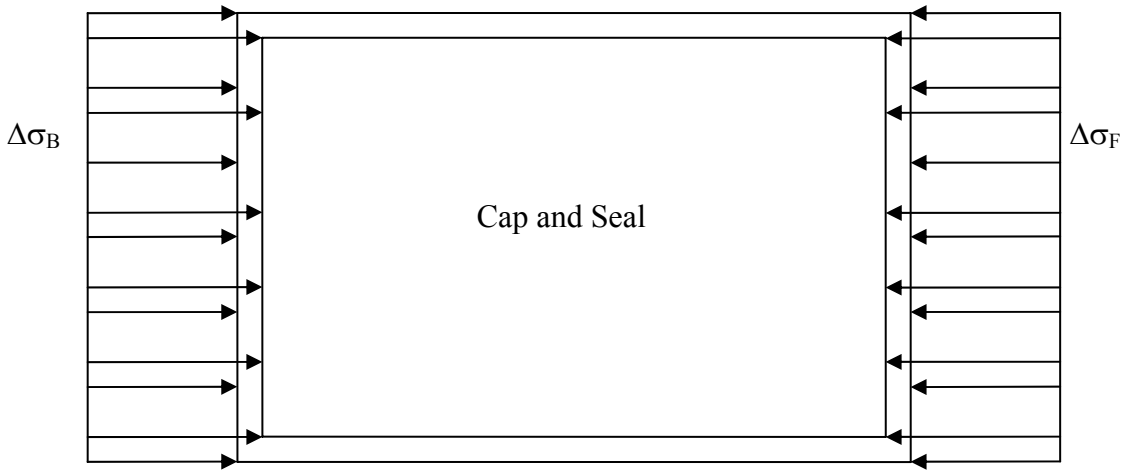

$\sigma_R = \Delta\sigma_F - (-\Delta\sigma_B)$

Figure 3.17 Lateral Stresses on Cap and Seal

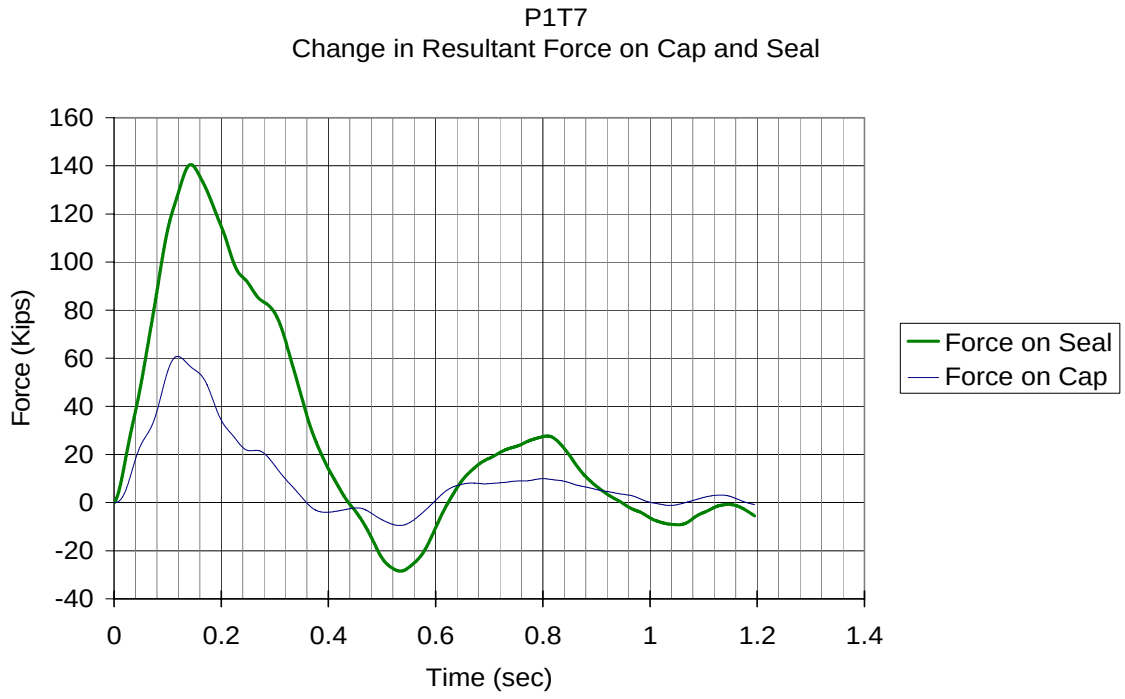

Figure 3.18 Resultant Forces on Cap and Seal for P1T7

As was found with the soil resistance at pile-soil interfaces, Figs. 3.13 & 3.14, the peak dynamic total resistance on the pile cap and seal, Fig. 3.18, occurs between 0.15 sec to 0.2 sec, which occurred at the peak impact load, Fig. 3.5, with the highest pile cap-seal velocities, Fig. 3.8, or damping. At peak lateral displacement, time 0.25 sec, for which static soil resistance, $k\ y$, is a maximum, the pile cap-seal velocity is zero (damping resistance – negligible), Fig. 3.8, and soil cap-seal resistance, Fig. 3.18 was smaller.

Inertia soil forces may contribute to the pile cap-seal resistance in one of two ways. First the soil mass around the pile cap-seal could oscillate as a result of the barge impact, which in turn would generate a resistance ($m\ \ddot{y}$) on the pile cap-seal. Generally, if the latter were to occur, the soil mass system should exhibit a significantly different period of motion than the pier/cap/pile system due to its significantly different stiffness. However, the resultant soil-pile cap-seal force at 0.44 sec, Fig 3.16, was zero, which corresponds exactly to when the pile cap displacements are zero, (i.e., Fig 3.8 – 0.44 sec), suggesting that no oscillation of soil mass with the pile cap-seal occurred. The second way that soil inertia forces could contribute to the piles or pile cap-seal resistance was if the soil mass around the piles or pile cap-seal were to travel with the pier/pile/cap/seal system, i.e., as attached. The latter will be investigated in detail in Chapter 4 through dynamic numerical analyses.

3.2.5 Pore Pressure Gages

Pore pressure changes in the soil adjacent to the lead and trailside of the cap and seal were also measured during barge impacts. The gages, Fig 2.13b, were part of the total stress cell instruments, Fig. 2.14a, used to measure horizontal stress changes adjacent to pile cap and seal, Section 3.2.4. The pore pressure reaction in the soils around

the pile cap and seal would aide in identifying if soil behaved in a drained or undrained response and identifies the appropriate static P-y resistance. Specifically, if the soil around the pile cap and seal exhibited little if any pore pressure change, then the soil should be modeled with a Reese and O'Neill granular P-y model which employs an angle of internal friction, ϕ. However, if soil exhibited pore pressure change, then the soil should be characterized with a cohesive P-y model (e.g., Matlock), which employs a total strength parameter, Su

Figure 3.19 presents the pore pressure responses (front & back pile cap) at Elev. – 13 ft in the soil for P1T7 barge impact. Evident from the figure, the soil in front of the cap (i.e., lead) exhibited little if any pore pressure change, representative of a granular material. The gage behind the cap (trail side) did exhibit an initial drop in pore pressure as expected for a fine-grained soil (i.e., low permeability) undergoing a decrease in total stress (cap moving away from soil) and a subsequent increase in stress (cap moving toward) the soil. However, because of the rapid dissipation of pore pressure, less than 5 sec, the physical size of the zone of fine-grained material must be small. Since none of the other (4 sensors) showed little if any pore pressure change, it was decided to model the silty-sand with shell around the pile cap and seal as granular, i.e., Reese & O'Neill P-y model. The measurements of the pore pressure response as a function of time for each test and sensor is presented in Appendix B.

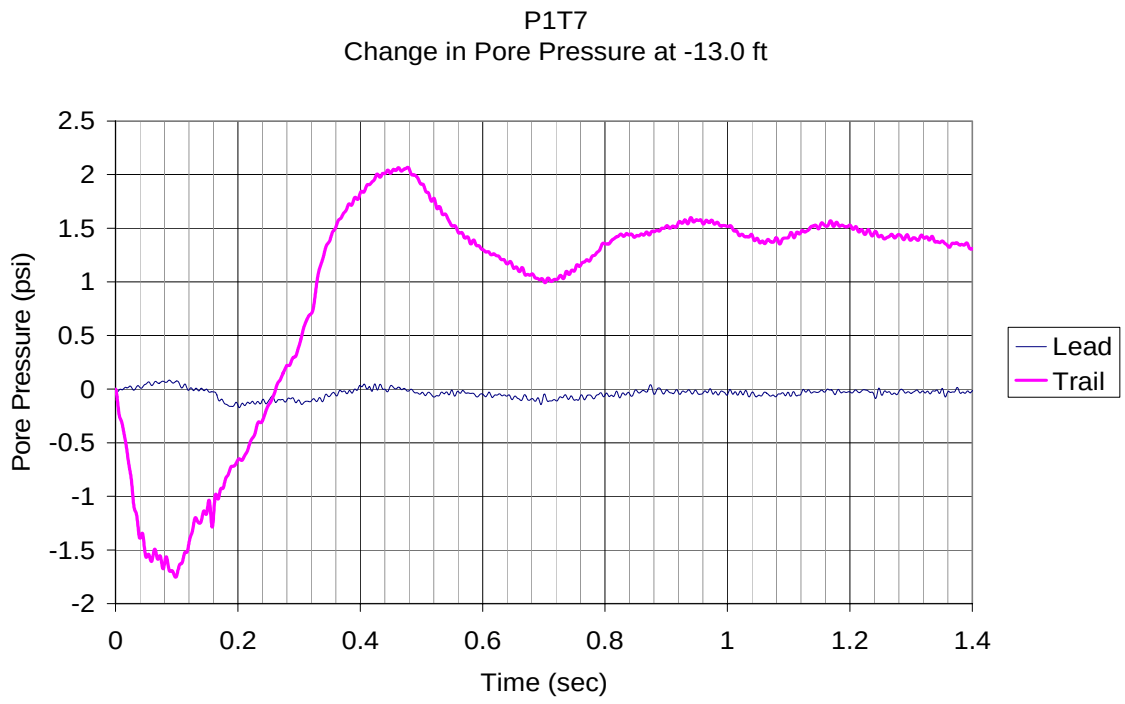

Figure 3.19 Changes in Pore Pressures

3.2.6 Accelerometers

In the center of the mini-pile, Fig 2.8 was a 2.87" ID PVC casing in which lateral accelerometers were placed to monitor velocities and displacements along the length of the pile with time. The accelerometers, which were borrowed from Applied Foundation Testing, were developed to monitor large slope, or wall movements. Unfortunately a review of the data using various filters, etc. resulted in velocities (integration of acceleration) and displacements (integration of velocity), that were considered unreliable for P1T7. The latter was attributed to the small measured velocities and displacements, versus the sensitivity of the devices (5% of full range – 1000gs). All of the acceleration data for each test is given in Appendix B.

CHAPTER 4
NUMERICAL MODELING OF PIER 1S VESSEL IMPACT

4.1 Introduction

The barge impact tests on Pier 1S were modeled with finite element programs FB-MultiPier and LS-DYNA. LS-DYNA is routinely used by the military, car manufactures, and barrier designers to simulate crashes (automotive or vehicles into walls, etc.). LS-DYNA employs an explicit solution strategy, i.e., no equilibrium checks, which require very small time steps for stability. BSI recently released FB-MultiPier, the next generation of FB-Pier, which incorporates an implicit dynamic solution strategy (i.e., iterating within each time step until equilibrium is achieved) and was developed to model the whole bridge both linearly as well as nonlinearly under static and dynamic vessel impact. Of interest, is a validation of the numerical codes through comparison to each other, i.e., resulting pile deflected shapes, shears, and forces.

Also of strong significance is a comparison of the numerical predicted behavior and the experimental measured response, e.g., pile displacements, shears, as well as dynamic forces in the system as a function of time. Since this analysis is performed in the time domain, inertia and damping resistance will be quantified over current AASHTO practice, i.e., static analysis. For the latter analysis, the need to consider soil mass in the analysis, as well as the associated damping viscous parameters will be investigated.

Note, similar soil parameters were used in both (FB-MultiPier & LS-DYNA) finite element simulations; however the pile cap and seal were modeled with brick elements in

LS-DYNA and with shell and truss elements in FB-MultiPier. The following sections present the modeling as well as comparisons between the experimental results and the programs.

4.2 FB-MultiPier Analyses

4.2.1 Soil Layering and Properties

The soil profile used for the Pier1S simulation is shown in Fig. 4.1. It consists of eight inter-bedded cohesionless and cohesive soil layers. Each layer was characterized as either cohesionless (i.e., sand, etc.) or cohesive (i.e., clay) based on its strength assessment as well as its behavior (i.e., drained or undrained) during the impact event. The layer boundaries in Figure 4.1 are the same as Figure 2.5, which were determined from SPT, CPT, and DMT testing.

Soil Properties needed for the axial and lateral soil-structure interaction is given in Table 2.3, based on combined insitu testing, Table 2.2. Material properties of the instrumented mini-pile are described in Section 2.4, as well as the lengths and tip elevations of all piles. The pier structure properties, such as Modulus of Elasticity and compressive strength, were determined from lab tests on the core samples obtained from the pier.

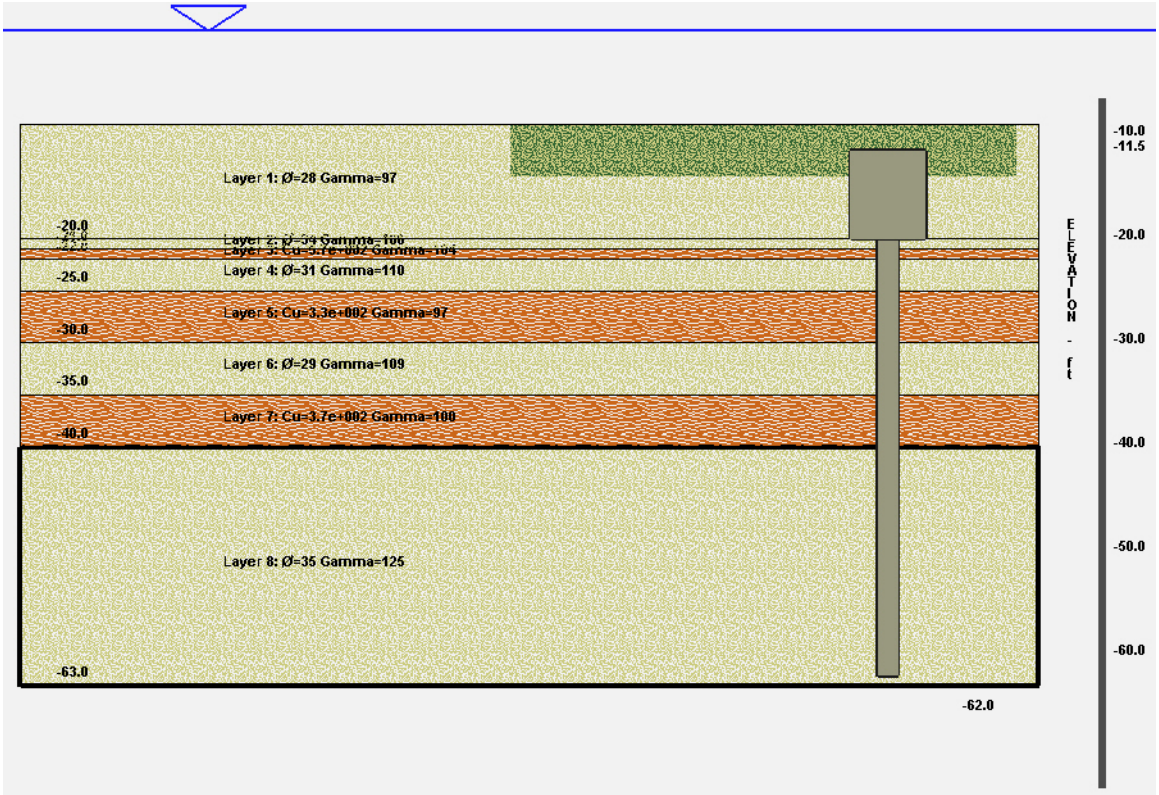

Figure 4.1 Pier1S Soil Profile-FB-Pier

4.2.1.1 Lateral P-y Characterization

Since the pile cap and seal were embedded approximately 11 ft in the sandy-shell material, Fig. 4.1, and FB-Multipier models the pile cap as a 2D surface (i.e., shell element) of zero thickness, it was decided to increase the diameters of the lead row piles, Fig. 4.2, over this depth to capture the cap and seal's added soil resistance. Note, the P-y resistance, i.e., force per unit length along the pile, is based on the width or diameter of the object. The latter approach was only done to the lead row piles in order to characterize the soil resistance on both ends of the pile cap and seal. Since the analysis employed P-y multipliers (0.8, 0.4,…etc.) to model group interaction, the multipliers

were kept fixed during the cyclic event, i.e., the 0.8 multiplier was always applied to the enlarged pile row, Fig. 4.2.

Since the pier had 6' of tremie concrete below the cap, it was readily recognized that the seal concrete provided rotational restraints to the piles and would result in a much deeper shear transfer from the piles to the soil, as well as point of fixity and rotation. To accomplish the latter, it was decided to introduce cross-bracing, Fig. 4.2, between the piles. The bracing was attached between the pile cap nodes and points along the pile representing the bottom of the tremie seal (Elev. –20ft). The bracing was given concrete properties, i.e., modulus, and strength.

FB-MultiPier models the soil using nonlinear soil springs, i.e., lateral, P-y and vertical, T-z, at nodes equally spaced along the length of the piles as well as nodes on the cap elements. Since skin friction information for the bottom and sides of the cap and seal was not available for the soil layer 1, Fig. 4.1, it was decided to use the conventional P-y curves, suggested by Reese, Cox, and Koop (1974) for sand to represent all the shear transfer in this layer. The necessary P-y parameters, i.e., unit weight and angle of internal friction, were obtained from Table 2.3, with a typical curve shown in Figure 4.3. The FB-Pier User Manual (2005) describes the use of degrading or gap formation in the P-y response. Since, the sandy shell is below the water table, it was expected that no gaps between pile and soil would develop. However, due to the development of some pore water pressure within layer 1, Fig. 3.19, it was decided to degrade the P-y resistance in successive cycles due to loss of effective stress. A degradation value of 0.3 was employed. Figure 4.3 shows the first and second loading cycles for layer 1 at elevation –11.5ft.

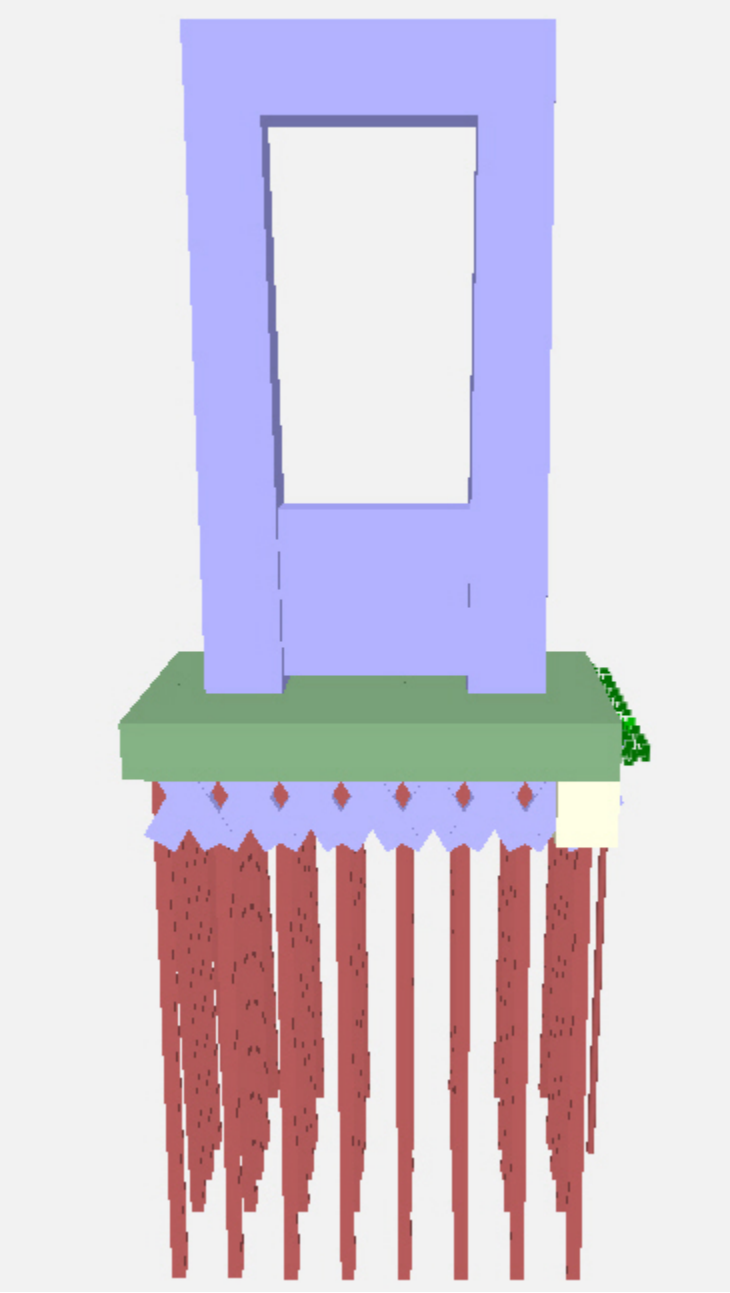

Figure 4.2 FB-Pier Depiction of Pier 1S

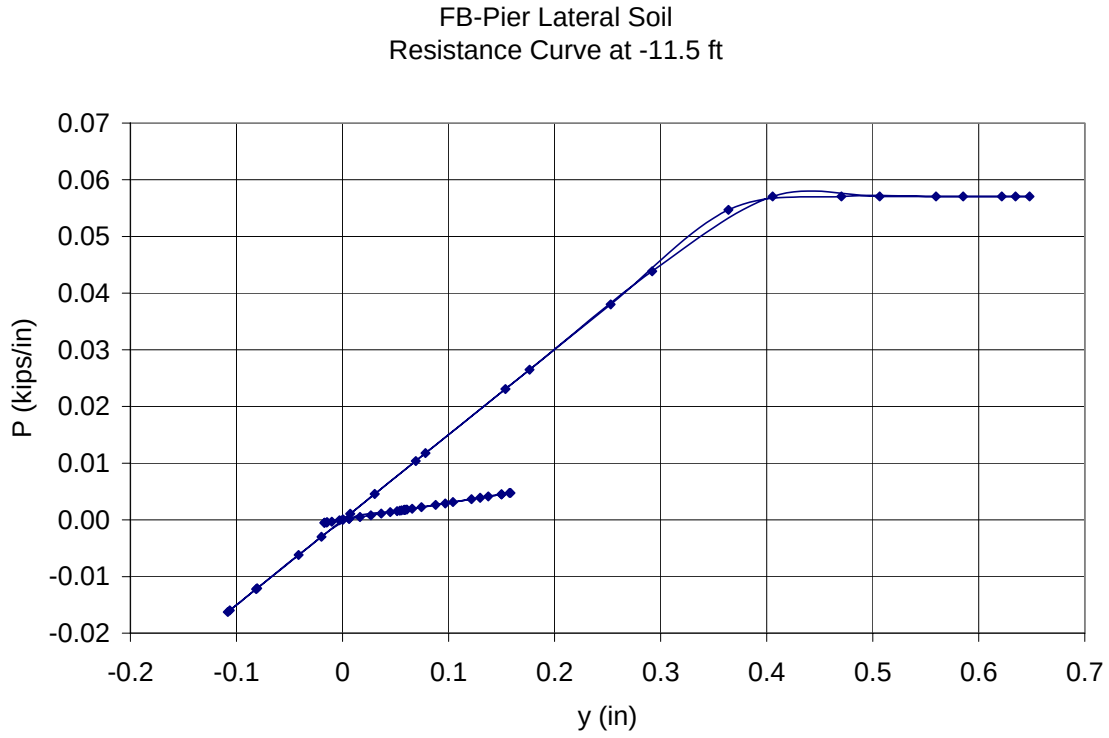

Figure 4.3 Example P-y Curve for Layer 1, Elev. –11.5ft

4.2.1.2 Damping

As identified in Chapter 3, significant soil resistance associated with damping was measured on the instrumented pile. Along the length of the piles, the latter was characterized with the dynamic (i.e., static and damping) soil resistance measured from the instrumented pile, e.g., Figs. 3.13 and 3.14 for each soil layer beneath the pile cap seal (Elev. –20ft). However in the case of the pile cap and seal, the uses of viscous dampers or dashpots were employed, since FB-MultiPier supports the use of dashpots at or above the pile cap in a dynamic analysis.

The damping on the pile cap and seal may be due to both material and radiation type damping characterizing both the near and far field response. A number of studies on

damping of deep foundations systems have been reported in the literature. For instance, Gazetas and Dobry (1984) developed a plane strain model for radiation damping which agreed well with the more rigorous research done by Novak, 1978, and Roesset, 1980. Their material damping was based on a damping ratio as a function of the induced shear strain and the soil's modulus, k. For typical damping ratios of 20% to 25% and a soil modulus determined from the P-y curve, viscous damping values, in the range of 1 kip sec/in to 6 kip sec/in, were computed.

In pile driving software, e.g., WEAP (Wave Equation Analysis of a Pile), axial damping is significant and may be characterized with Smith damping or,

$$R_d = j_s R_u v \qquad \text{Eq. 4.1}$$

where R_d is the damping resistance force, j_s is the smith damping factor, R_u is the static resistance of the soil, and v is the particle velocity at the soil-pile interface. Evident herein, the viscous damping factor, c, is obtained through the product of smith damping factor and R_u, the soil's axial resistance. WEAP recommends a Smith damping factor, j_s, between 0.1 sec/m and 0.6 sec/m depending on soil type (i.e., low value for sand high value for clay). For this analysis, one could assume that the R_u was equivalent to the ultimate lateral resistance for a single pile, i.e., P_u times the thickness of the cap or layer. Using the latter approach, a viscous damping constant, c, of 3.5 kip sec/in would be computed at an elevation of -11.5 ft for granular soil for an H pile.

El Naggar and Novak (1996) modeled harmonic response at the pile heads and developed dynamic P-y curves from a computational model, Brown et al., 2001. The near field and far field soil behavior was modeled with nonlinear springs, linear springs, and dashpots, respectively. The near field soil behavior was represented with hysteretic

nonlinear P-y curves in series with frequency dependant dampers. The far field was represented with linear soil springs in parallel with viscous dampers representing radiation damping. Using a complex stiffness approach, the computational model was rewritten into a real and an imaginary part. The imaginary part of the complex stiffness represents the damping as a result of the energy dissipation within the soil and was shown to be frequency dependent (El Naggar, Novak, 1996). The damping constant was shown to be a function of soil type, the static soil resistance, the corresponding displacements, diameter of the pile, and frequency of motion. Considering a range of soil constants and varying frequencies, damping constants in the range of 4 kip sec/in to 10 kip sec/in, was calculated.

What is evident is that, the literature supports a range of viscous damping, c, values (1 kip sec/in to 10 kip sec/in) with a typical value of 3.5 kip sec/in. Also, of concern is the viscous damping for a group of piles, specifically one which includes both a pile cap and seal. One approach is to consider the group as a large single pile with a width of 278". Using the latter with Smith Damping (c = js x Ru) with Ru set equal to Pu from a P-y curve (278" diameter) times the thickness of a layer (11ft), viscous damping of 50 kip sec/in is obtained. Another approach is to use the same concept of multipliers for group interaction for soil stiffness (i.e., 0.8, 0.4, etc.) for damping resistance. Using 0.8 x 3.5 kip sec/in x number of piles in 1^{st} row plus 0.4 x 3.5 kip sec/in x number of piles in 2^{nd} row, etc. which when summed equals 45.5 kip sec/in. It should be noted that this approach will also identify the distribution of the damping in the front and back of the pile cap and seal (lead and trail rows), which is approximately 20 kip sec/in or

approximately 45% of the total damping within the top 11' of the pile cap seal system. The latter approach is employed for this analysis.

4.2.1.3 Soil Gapping

Based on the dynamic soil resistance measured in the instrumented pile, e.g., Fig. 3.13 and 3.14, it was decided to introduce soil gapping in layers 2 through 8, in the FB-MultiPier match with the LS-DYNA. The gapping was determined to only be effective in the layers where the dynamic curves were input, -20.0 ft to -30.0 ft.

4.2.1.4 Axial Model

It is not readily evident that the axial soil-structure resistance has significant impact on the lateral response of a pile group. However, for a fixed head group, approximately 50% of the lateral resistance (McVay, 1996) is due to a transfer of vertical shear in the pile cap to axial pile-soil structure interaction.

For FB-MultiPier and the LS-DYNA simulation, the axial soil structure interaction is accomplished with nonlinear axial, T-z, springs acting along the length of each pile. A typical axial T-z curve for side friction used in FB-Pier is presented in Figure 4.4, which was assigned based on soil layering, Fig. 4.1. The model used for all soil layers in the profile was that for driven piles (FB-Pier User Manual) which were developed with the insitu soil properties determined from CPT-1 and CPT-2 data and PL-AID software program. The FB-MultiPier requires the soil's Poisson's ratio, ν, the initial shear modulus, G_i, and the vertical shear failure, T_f, and are given in Table 2.3

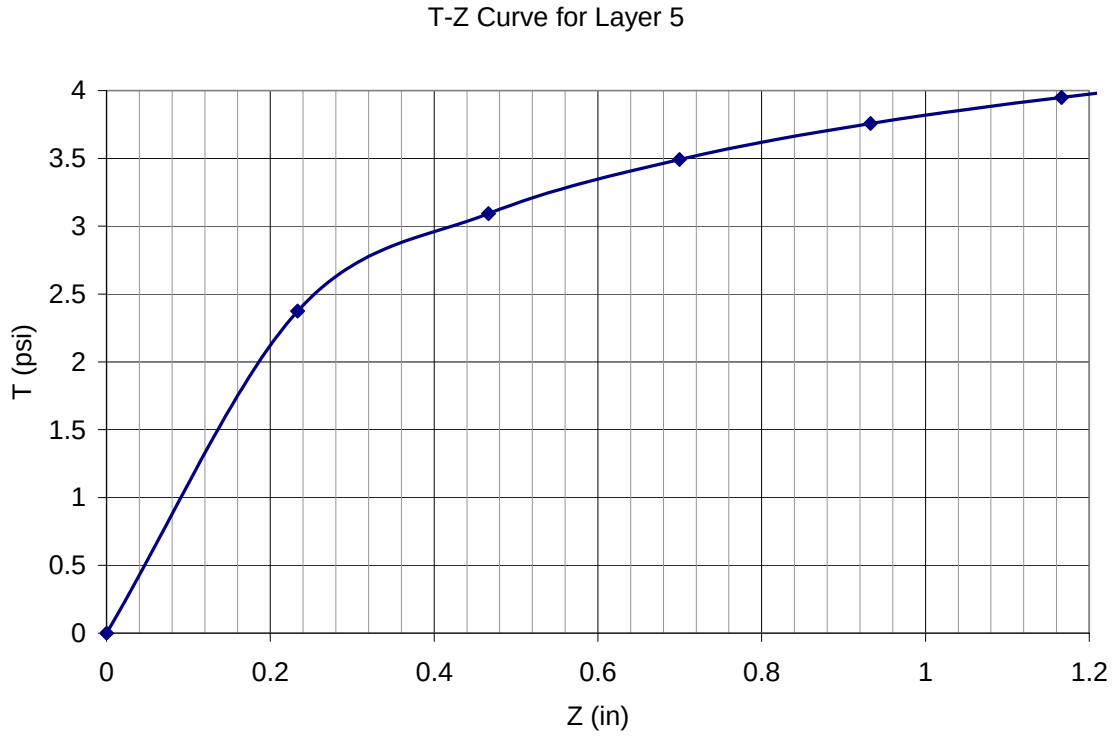

Figure 4.4 T-z Curve used in FB-MultiPier

The tip resistance acting on the bottom of each pile was modeled with an axial Q-z curve based on bearing properties of layer 8. The required properties were the ultimate tip resistance, Q_u, Poisson's ratio, ν, and initial shear modulus, G_i of the soil. These values were also determined from CPT-1 and CPT-2 data with the PL-AID software.

4.2.2 Comparison of FB-Pier and Experimental Results

The soil-structure response from the barge striking Pier 1S under P1T7 impact, Fig. 3.5, was studied with FB-MultiPier. Note, FB-MultiPier has the option of inputting load time histories to a node on the structure or pile. For this analysis, a node just above the shear wall location, representing the concrete block load cell was used in this analysis.

4.2.2.1 Displacements

Presented in Figure 4.5 is a comparison of the predicted (FB-MultiPier) and measured displacements at the shear wall elevation as well as the bottom of the seal concrete (Elev. -20ft). Evident, the shear wall and top of the seal concrete have very similar frequencies with slight difference in peak displacement amplitudes. The latter may be attributed to a slight rotation of the pier-cap system. Note, both the measured and predicted displacements are close (<15%) in both amplitude and frequency. Also note with progressive cycles, the period of the response is lengthening. The latter may be due to either an increase in mass or a reduction in stiffness as shown by the following equation:

$$T = 2\pi\sqrt{\frac{m}{k}} \qquad \text{Eq. 4.1}$$

Where m = soil mass

k = soil stiffness

The elongation of the predicted response, Fig. 4.5, may be attributed to the degraded P-y response, Fig. 4.3, with successive cycles due to the buildup of excessive pore pressure or loss of effective stress.

Besides degradation in stiffness, the addition of mass associated with the soil in the footprint of the piles would also increase the period of the structure, Eq. 4.1. The latter mass was analyzed with FB-MultiPier by adding additional mass to the reinforced concrete extra members representing the tremie seal concrete, Fig. 4.2. The mass was increased by 50% through changing the concrete's unit weight from 130 pcf to 195 pcf. Shown in Figure 4.6 are the predicted vs. measured cap displacements from increasing the soil mass. Evident from the figure, the period of the shear wall and cap has been

increased. The latter may be attributed to the cap acceleration and associated inertia forces as shown in Figure 4.7. Note the acceleration, or inertial resistance is mobilized much quicker than the velocity or damping resistance. In addition, after 0.16 sec the acceleration is negative which results in a negative inertial force causing the cap to continue in the positive x direction, i.e., lengthening the period, which doesn't appear to agree with the measured response, Fig. 4.6. Also evident from Fig. 4.7, the velocity is the highest at 0.15 sec or at the largest dynamic loading, Fig. 3.5 providing significant damping resistance. Consequently, figures 4.6 and 4.7 suggest there is no need to model the added soil mass between the piles or around the pile cap for inertia; however resistance from damping must be considered. Further analysis will neglect added soil mass.

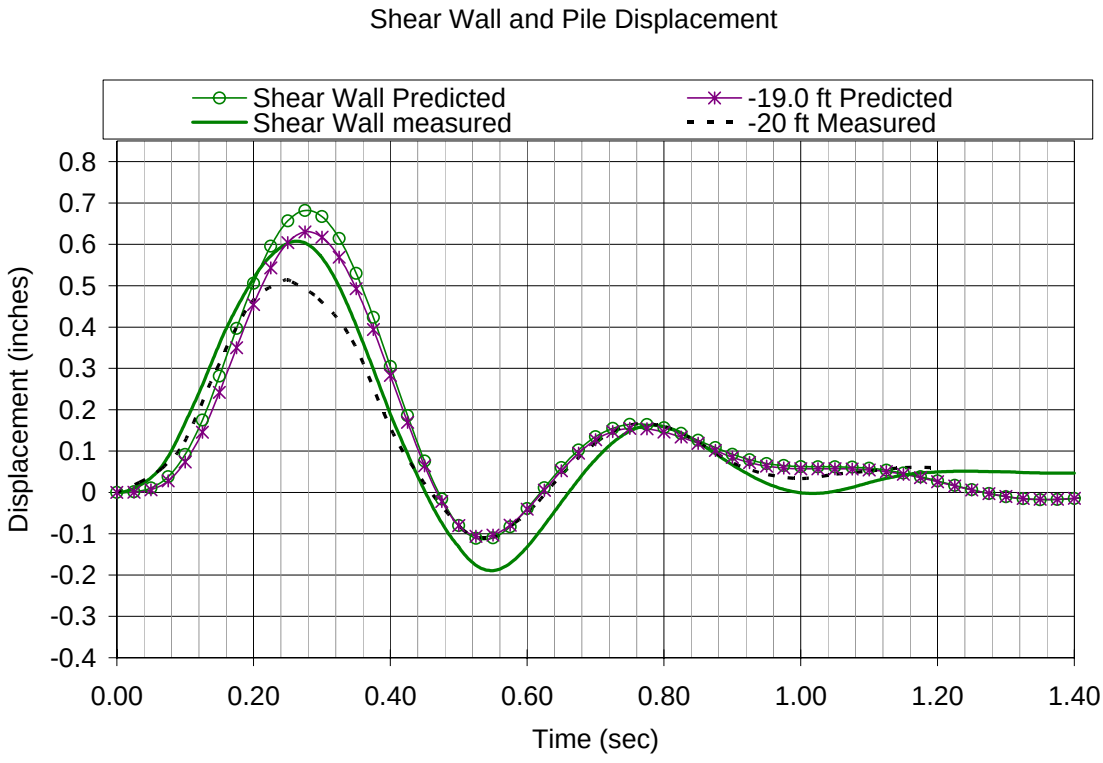

Figure 4.5 FB-MultiPier Predicted and Measured Displacements

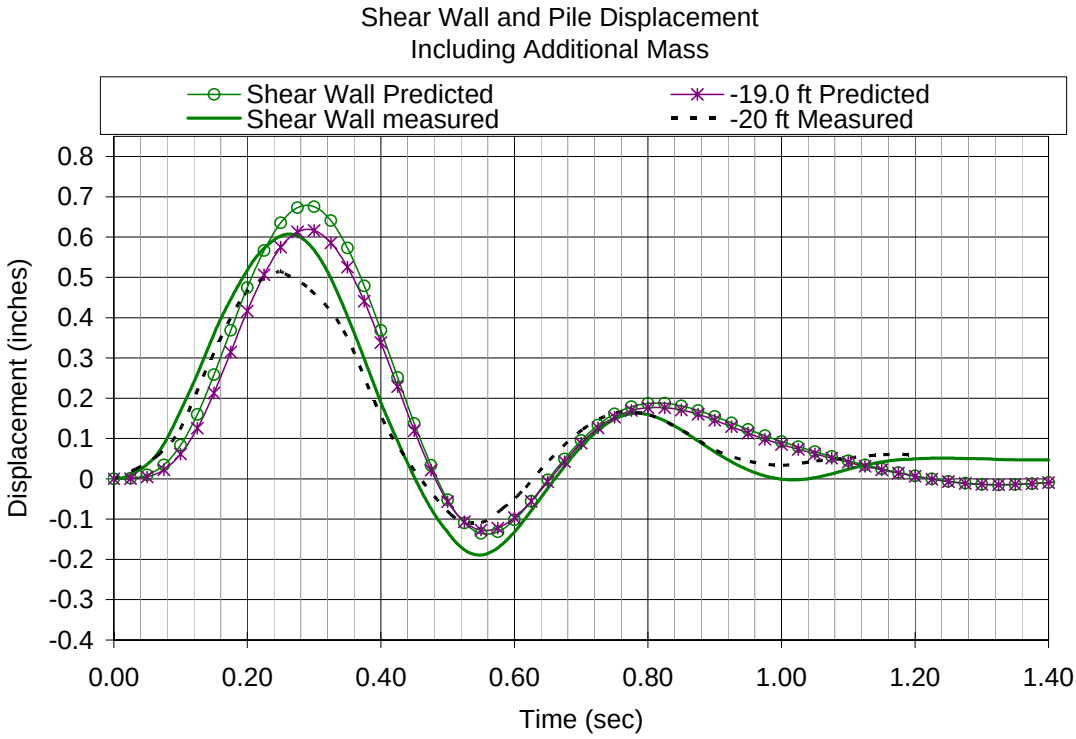

Figure 4.6 FB-Pier Displacements - Additional Mass

A comparison of the deflected shape of the experimental pile from FB-MultiPier and the measured response is presented in Figure 4.8 at maximum lateral displacement, 0.25sec after impact. In general the predicted pile shape agrees with the measured response with depth. The obvious difference is the point of zero lateral displacement. For the measured response, this occurs at approximate Elev. -42.0 ft, while the FB-MultiPier response occurs at Elev. -38 ft. This difference was attributed to the use of traditional P-y curves below Elev. -30.0 ft. In addition, it should be noted that the damping resistance was handled with an increased P-y resistance, which is a function of displacement instead of velocity for viscous resistance.

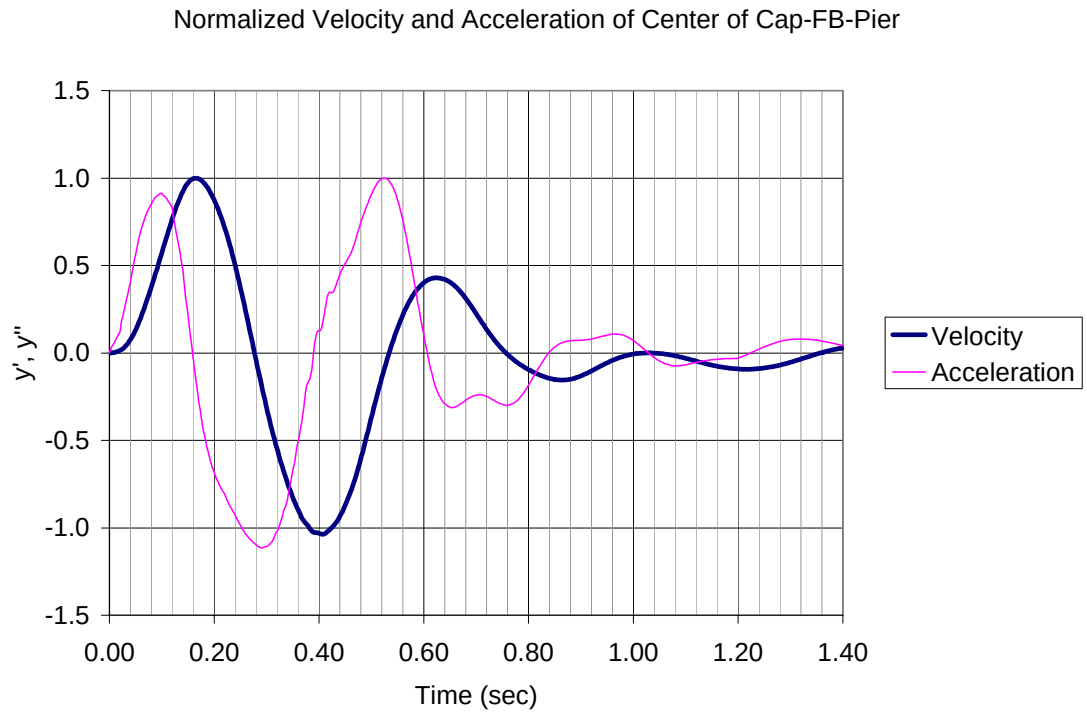

Figure 4.7 Acceleration and Velocity of Pile Cap

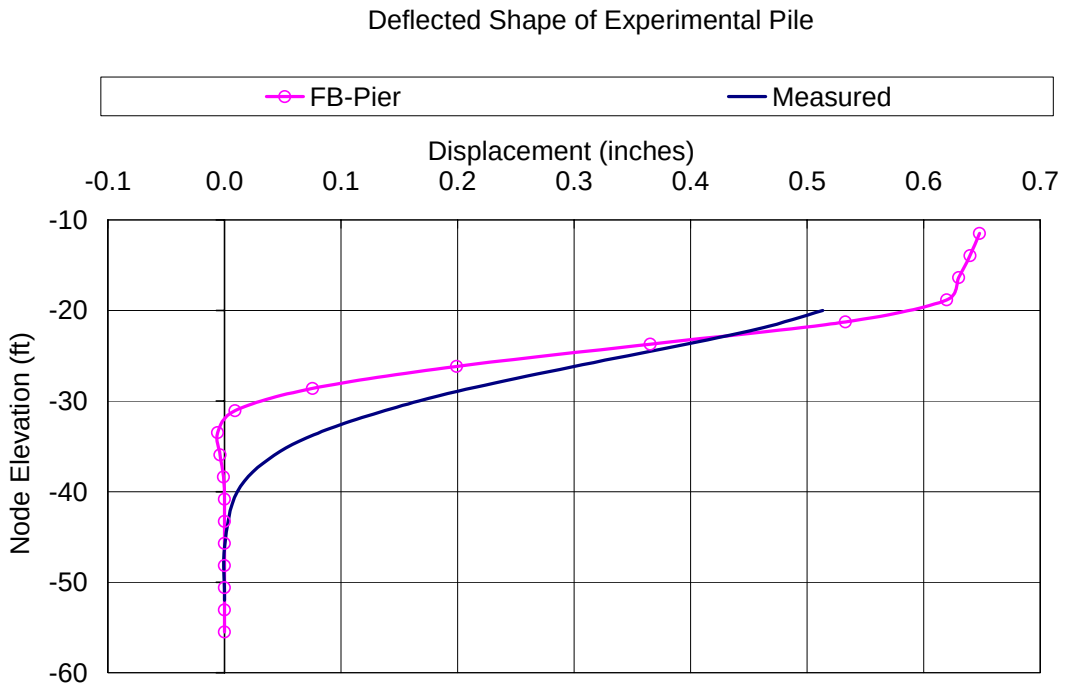

Figure 4.8 Deflected Shape of Experimental Pile

4.2.2.2 Resistance Forces

Shown in Figure 4.9 are the measured and predicted dynamic soil resistance acting on the front and rear of the pile cap and seal as a function of time. The measured response is the sum of the seal and cap forces identified in Fig. 3.18. The predicted forces were found from FB-MultiPier as follows: 1) Static – the sum of all spring forces within the footprint of the pile cap and seal times the effective area ratio [end areas / (end areas + bottom area + side area)]; 2) Damping – 45% of total damping resistance which was attributed to just the end effects (i.e., piles within lead and trail rows, see section 4.2.1.2). Subsequently, the static and damping resistance were summed, Fig. 4.9, to give total cap and seal dynamic resistance.

Evident from Fig. 4.9, the amplitude of the measured and predicted total forces agrees fairly well; however the time of maximum occurrence are slightly different for the measured (0.15 sec) and predicted (0.2 sec) resistance. The latter suggests a greater portion of the soil resistance should be attributed to damping instead of static resistance. Specifically at 0.17sec, pile cap and seal velocity is high (Fig. 4.7) which develops the high damping resistance, Fig. 4.9. To replicate the measured response, the static soil resistance could be reduced, and the damping force increased. One way to reduce the static resistance on the cap would be to remove the enlarged pile elements in the front of the cap (Fig. 4.2).

Note, the force plot of Figure 4.9 does not include the frictional forces from the soil acting on the surface of the pile cap and seal. FB-MultiPier has no provisions for directly modeling such resistance. All soil-structure resistance is measured with P-y springs within the volume of pile cap and seal. The latter was investigated with LS-DYNA through the use of brick elements to characterize the cap & seal with nonlinear skin

friction springs attached to the bottom and sides of the cap and seal. In addition, the P-y springs on the front and back of the cap & seal were based on the H pile dimensions, not the enlarged section, Fig. 4.2.

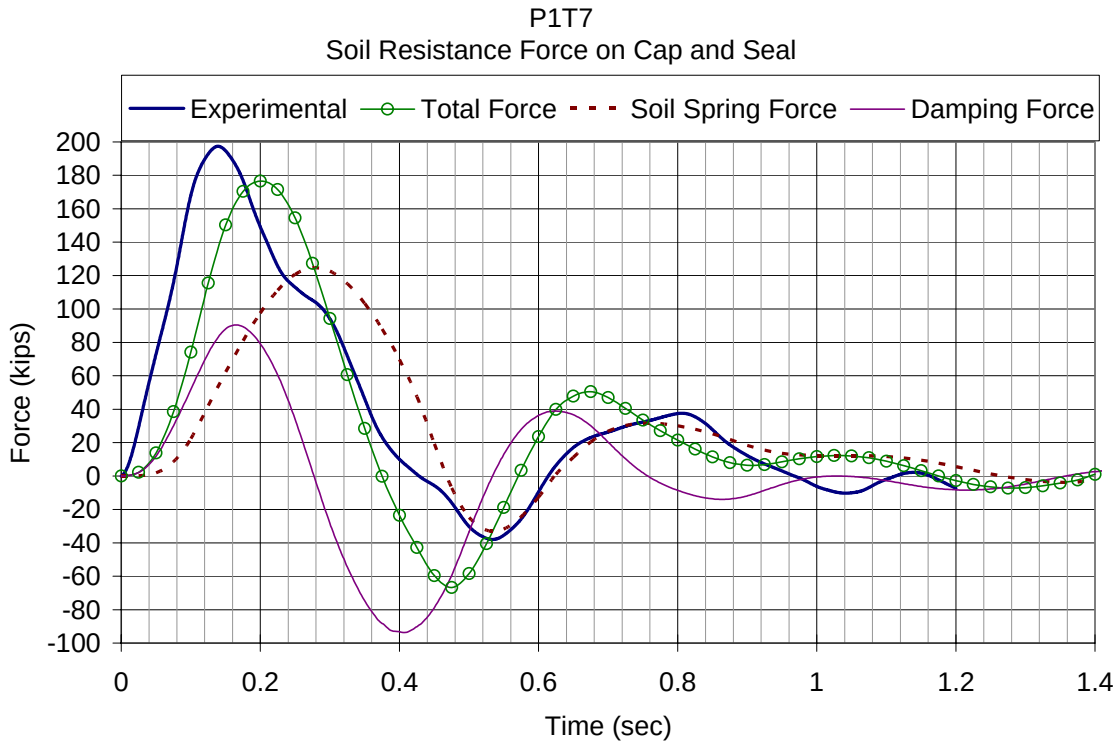

Figure 4.9 Lateral Soil Force on Cap and Seal

A comparison of the predicted vs. measured shear force at Elev. –20 ft in the experimental pile (see Fig 3.11) is presented in Figure 4.10. It is evident that the agreement between measured and predicted peak amplitude and time history is quite good. It should be noted that the peak response, 8.5 kip, occurs at 0.15 sec, which is the same time for peak impact force, Fig. 3.5 and peak cap velocity, Fig. 4.7. Note, the pile-soil damping resistance for this system was characterized with dynamic P-y curves, Fig. 3.13. However, it is recommended that future characterization split out dynamic

damping resistance from the static resistance (i.e., ky) through viscous dashpots attached along the length of each pile with viscous damping values, c, identified for each layer by soil type.

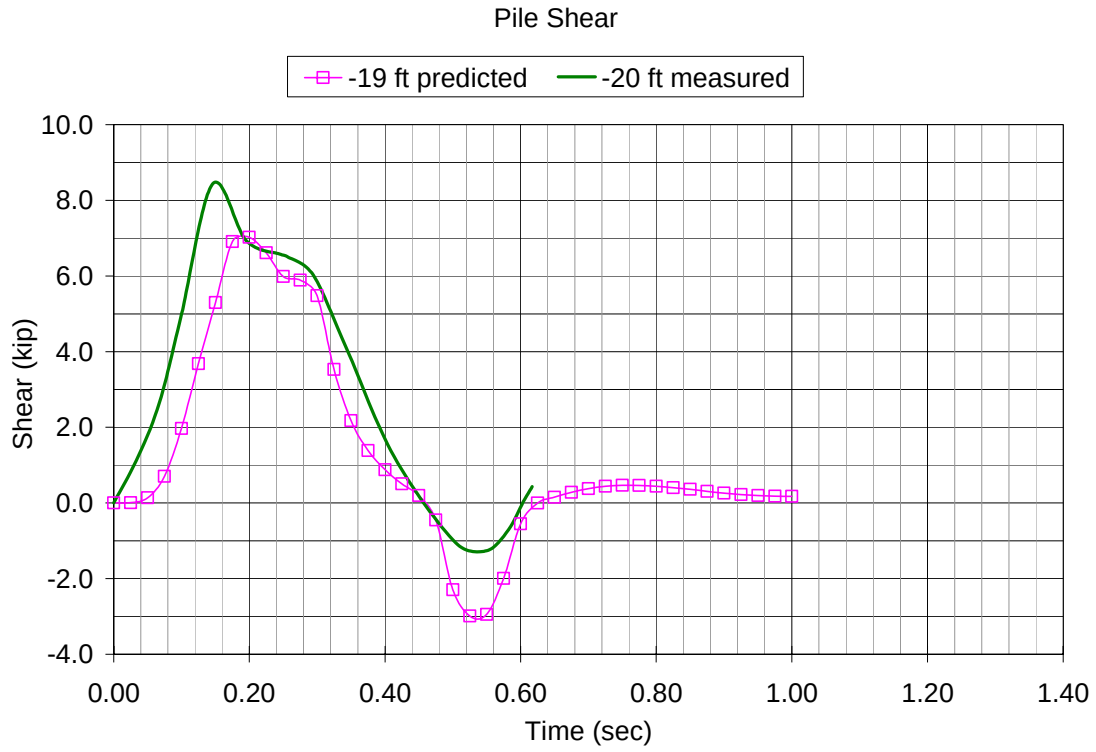

Figure 4.10 Experimental Pile Head Shear

Shown in Figure 4.11 is each of the predicted forces acting on the pile cap as a function of time as well as the applied dynamic load. Evident from the figure, the initial resistance was provided by inertia, followed by damping, and then static resistance. Note, the pile head shear in Fig. 4.11 was primarily due to damping at 0. 17 sec (Figs. 3.13 & 3.14), corresponding to a displacement of 0.3in. At the peak load (864 kips, time of 0.15 sec), 70 % of the total resistance was provided by inertia and damping forces.

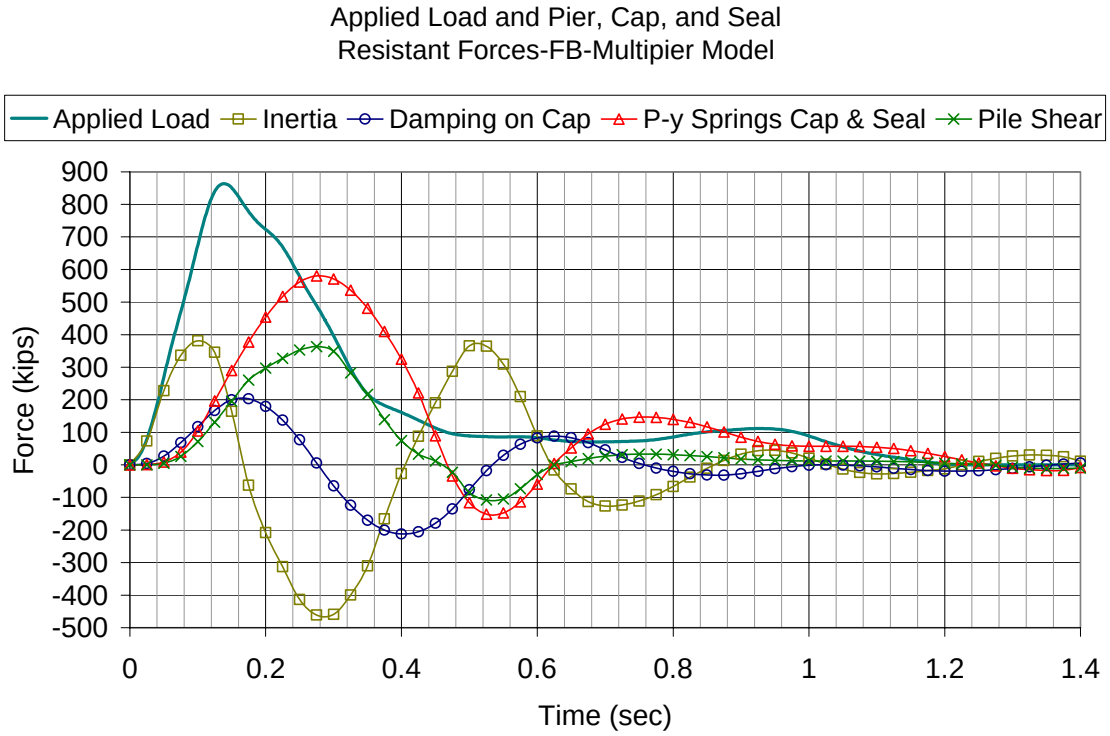

Figure 4.11 Total Forces Acting on the Pile Cap: Inertia, Damping, and Static Resistance

4.2.3 Discussion of FB-MultiPier Analysis of Pier 3S

Also of strong interest were the dynamic forces, i.e., inertia and damping for Pier 3S, which had no embedded pile cap, but 8 battered 20" prestressed concrete piles with an above waterline cap, i.e., representative of typical approach piers. Consolazio (2005) constructed an FB-MultiPier model of Pier 3S using the soil profile given in Fig. 2.7, based on soil properties in Table 2.4 from insitu field test data (SPT, CPT, and DMT).

Since the piles were not instrumented, experimental (measured) dynamic soil resistance curves were not available, as was the case for Pier 1S. Consequently, to characterize the lateral static soil resistance, conventional P-y curves, i.e, Reese, Cox, and Koop (sand) and Matlock (clay), were used based on soil properties given in Table 2.4.

In addition, damping was characterized with dashpots placed along the length of each pile. Each dashpot required a viscous damping value, c (force- time/length). The viscous damping value was calculated from the complex stiffness approach described by El Naggar and Novak, 1996, discussed in Section 4.2.1.2. Soil layer 1 (Fig. 2.7), had a viscous damping constant of approximately 1.8 kip-sec/in, layer 2 had value of 0.088 kip-sec/in, and layer 3 had a viscous damping value of 3 kip-sec/in. The damping was distributed based on the number of pile elements within each soil layer. For instance, if a pile had 5 nodes within the layer and the layer had a viscous damping value of 3 kip-sec/in, then each node within the layer would have a damping value of 3/5 kip-sec/in.

The impact event chosen for analysis was P3T3 due to the magnitude of the load as well as the energy contained with the event. The peak impact load measured for P3T3 was 512 kips (Consolazio, 2005) and occurred at approximately 0.09 sec.

Figure 4.12 presents a comparison of the predicted foundation resistance for P3T3 from FB-MultiPier (Consolazio, 2005). At peak lateral loading (512 kips) which occurred at time 0.09 sec, the static resistance (i.e., spring force, Fig. 4.12) was 190 kips, whereas the dynamic resistance (inertia and damping) was 322 kips, accounting for approximately 63% of the total resistance in the system. Note, the dynamic resistance included the sum of soil damping, and pile inertia. As with P1T7 analysis of Pier 1S, Section 4.2.2.2, which had approximately 70% dynamic resistance, the soil-structure dynamic resistance is significant and is rate dependent.

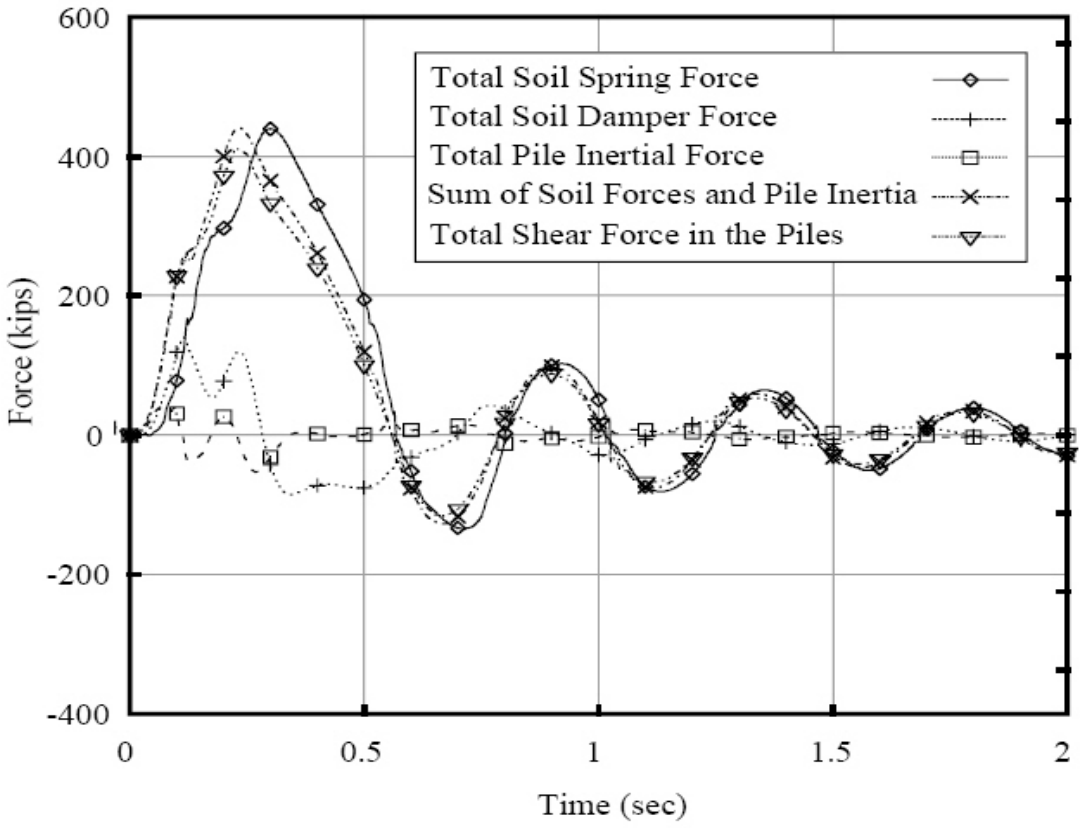

Figure 4.12 P3T3 FB-MultiPier Foundation Force Comparisons

4.3 LS-DYNA and FB-Pier Match Models

4.3.1 LS-DYNA Pier and Pile Model

The pier and foundation system modeled in LS-DYNA consisted of more than a thousand 3 dimensional brick elements (see Fig. 4.13) used in characterizing the piers, shear beam, pile cap and tremie concrete. The piles were characterized with beam elements and the soil-pile interaction was represented with nonlinear P-y and T-z springs.

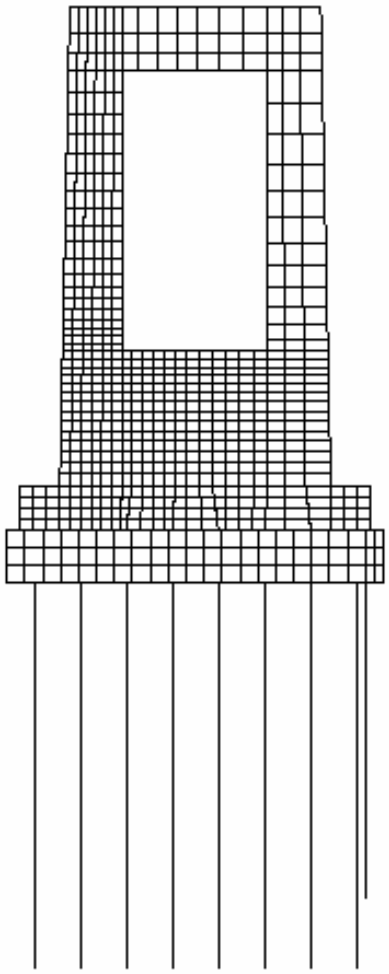

Figure 4.13 LS-DYNA Depiction of Pier 1S

Since the actual volume of seal and cap concrete is represented by the brick elements, soil springs and dashpots could be connected at the actual soil depths, Figure 4.14 representative of soil layering, center of gravities, etc. The cap and seal were each split into 5 sections of brick elements (see Fig. 4.14) on the front and back face of the cap & seal to capture the potential gradients between the 5 columns of H piles in each row. Lateral P-y and Axial T-z soil curves were applied at the nodes along each pile length. Damping was not applied to the pile nodes between Elevations -20.0 ft to -30.0 ft since

they were modeled with the dynamic P-y curves (include static and dynamic resistance, Fig 3.13). The presence of damping in the soil layers below this elevation was not considered due to the negligible response measured below this depth.

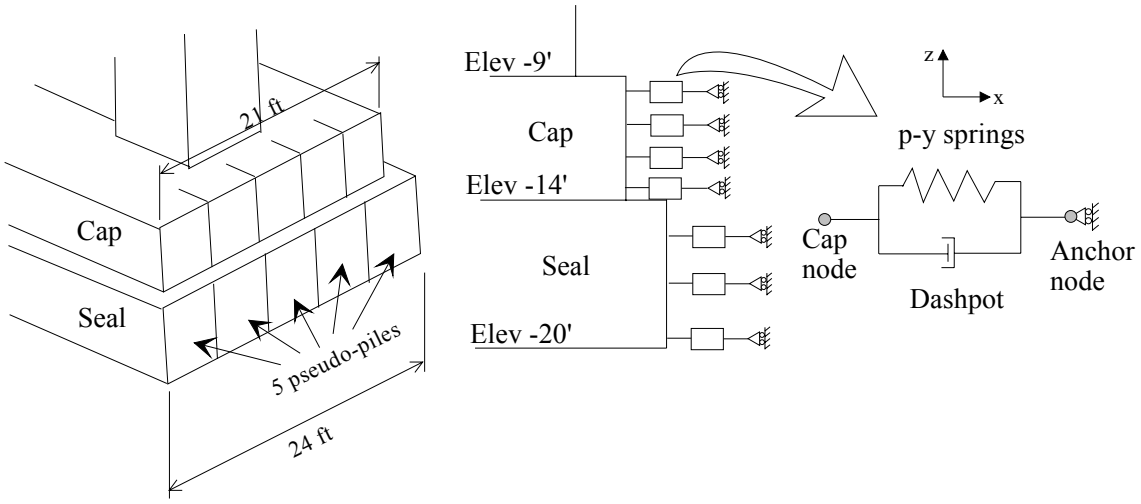

Figure 4.14 Cap and Seal Elements with Spring and Dashpot Arrangement

4.3.1.1 Lateral Soil Model

Attached to the brick nodes along the front and back of the cap (Elev. -9.0 ft to -14.0 ft), and seal (Elev. -14.0 ft to -20.0 ft) were P-y springs and dashpots (see Fig. 4.14) representing the soil. The latter soil springs (Elev. -9ft to -20ft) in the vicinity of the pile cap and seal were modeled with Reese, Cox, and Koop P-y curves for H piles which were approximately 35% of the resistance from the enlarged lead row piles, Fig. 4.2. From Elev. -20.0 ft to -32.0 ft (layers 2-5), the soil was modeled with the measured dynamic soil resistance curves, Chapter 3 (Eq. Fig. 3.13). Layers 6 (Elev. -32.0 ft to -35.0 ft) and layer 8 (Elevation -40.0 ft to -63.0 ft) were characterized with the default Reese, Cox, Koop criteria for sand, and layer 7 was modeled with Matlock's criteria for soft clay

below the water table. Hysteretic soil behavior in the form of soil gapping was used for all soil layers beneath the concrete tremie (i.e., layers 2 and beyond).

The P-y curves in front and behind the cap and seal had to be degraded with successive cycles to model remolding, pore pressure buildup etc. Unfortunately, LS-DYNA does not have a cyclic degradation option like FB-MultiPier, Fig. 4.3. To model the degradation in LS-DYNA, the soil static resistance was modeled with two springs in parallel, Figure 4.15. The first was the traditional static P-y curve (called Degraded P-y = 0.3 x original P-y), the second was a time dependent Maxwell linear spring (Fig. 4.15). The Maxwell spring was active for 0.45 sec of impact after which it was not present. The stiffness of the Maxwell spring was selected to result in the same energy as the original P-y curve when summed with the degraded P-y energy.

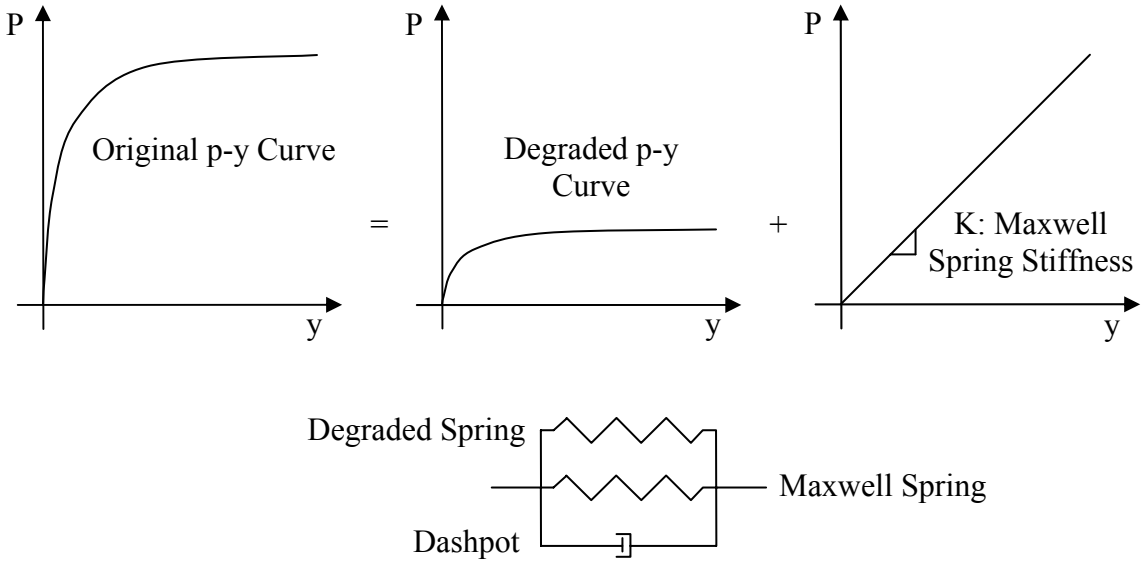

Figure 4.15 Soil Model for Cyclic Degradation

4.3.1.2 Axial Soil Model

Attached to the nodes along each pile were vertical T-z springs characterizing the axial load transfer from the piles to the surrounding soil. The nonlinear springs required each soil layer's Shear Modulus and ultimate skin friction as identified in Table 2.3. Attached to the tip of each pile were nonlinear springs, Q-z, requiring the ultimate tip resistance of the bearing soil layer.

4.3.1.3 Skin Friction Model on Cap and Seal

An advantage of using the brick elements for the cap and seal was that soil springs and dashpots representing the skin friction on the pile cap and seal could be considered. Based on the CPT data (Chapter 2), it was decided to use the bilinear T-z curve (e.g., Fig. 4.4) used to characterize axial pile resistance for the cap and seal friction. Note, the skin friction is generally mobilized at much smaller displacements, e.g., 0.1 inches (see Fig. 4.4) vs. the P-y lateral spring approach, Fig.4.16. The bilinear skin friction springs were applied to both the sides and the bottom of the pile cap & seal system.

Degradation was also applied to the skin friction springs, based on the assumption of remolding due to cyclic shear strain and pore pressure buildup. The latter was accomplished with a static degraded bilinear spring (0.3 x original curve) in parallel with a linear time dependent Maxwell spring. The Maxwell spring was active for 0.45 sec of impact after which it was not present. The stiffness of the Maxwell spring was selected to result in the same energy as the original T-z curve when summed with the degraded T-z energy.

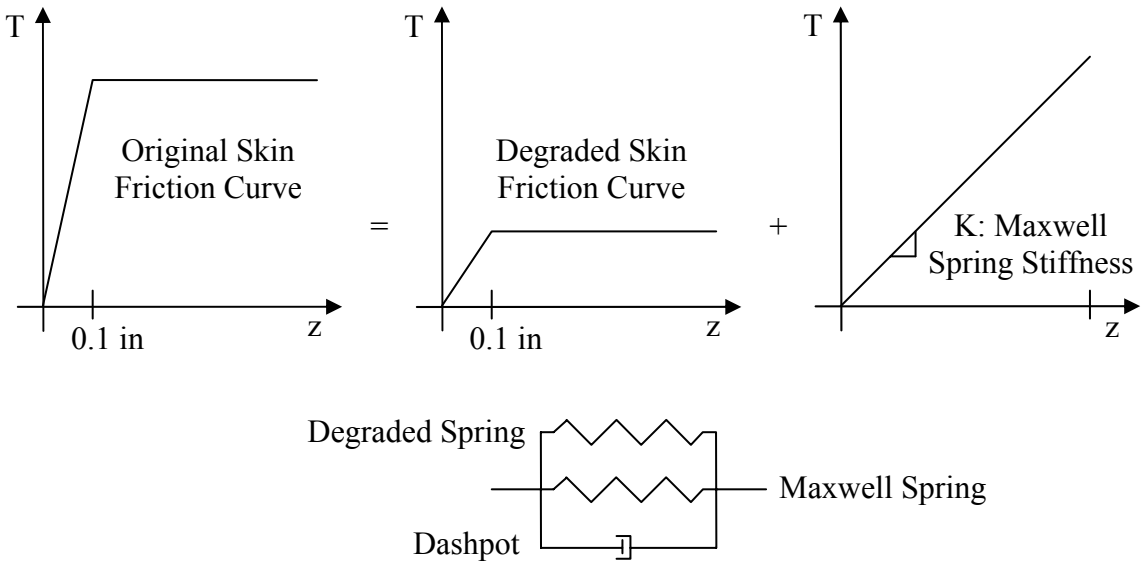

Figure 4.16 Soil Model for Skin Friction Degradation

As with the spring-dashpot elements used in the lateral soil model for the front and back of the cap and seal, spring-dashpot elements were also placed along the sides and the bottom of the cap and seal. The magnitude of the spring force was assessed from the unit skin friction times the surface area that it acted over.

4.3.1.4 Damping

The damping was modeled with dashpots, Figs. 4.15 and 4.16, at each node along the front and back of the cap and seal and at the nodes along the bottom surface of the cap. For similarity in total damping resistance between the FB-MultiPier and LS-DYNA analyses, a total of 39 kip sec/in viscous damping was applied to the cap and seal with approximately 45% of total resistance applied to the front and back of the cap & seal.

4.3.2 FB-Pier Model

An alternative FB-MultiPier model was constructed with the primary focus of comparing FB-MultiPier results with LS-DYNA. This model was intended for research purposes only with the intention of comparing the results of the software programs. Of

specific interest was the significance of modeling the pile cap and seal with 3D brick elements with associated skin friction springs vs. FB-MultiPier shell element for pile cap, truss members characterizing the tremie seal concrete, and P-y springs representing soil resistance.

To accomplish a direct comparison the same input parameters for the soil and structure employed in the LS-DYNA analysis were used in the FB-MultiPier model. Following is a description of the FB-Pier model.

4.3.2.1 Lateral Soil Model

As discussed in Section 4.2, a limitation of FB-Pier is that it does not allow the user to model the cap and seal with 3D brick elements. Therefore, the soil around the lead and trail row of piles, -9.0 ft to -20.0 ft, was modeled with P-y curves used on the front and back of the cap and seal of LS-DYNA, as described in Section 4.3.1.1.

The soil layers beneath the seal down to an Elev. Of –32.0 ft were modeled with the dynamic (static and damping) P-y curves measured on the experimental pile and used in the LS-DYNA model. Below this elevation, the soil P-y curves were again the default P-y curves based on soil strength and unit weight identified in section 4.3.1.1.

4.3.2.2 Axial Soil Model

The axial soil-pile force transfer was through bilinear T-z springs behavior described in section 4.3.1.2. The T-z springs, which were applied at the nodes along the length of each pile required ultimate skin friction and shear modulus, G, for each soil layer. The values identified in Table 2.3 were employed.

4.3.2.3 Skin Friction on Pile Cap and Seal

Since the FB-MultiPier employs a zero thickness shell element to model the pile cap, and beam members for the seal, the soil resistances within the footprint of both were

characterized with lateral P-y springs. To represent the skin friction springs along the side and bottom of the brick elements, section 4.3.1.3, user defined P-y springs were input from Elev. –11.5 ft to –20.0 ft as follows. The sum of all skin spring forces along side and bottom of the cap and seal at multiple displacements were divided by the number of piles (30) and number of pile nodes within Elev. –11.5 ft to –20.0 ft and placed at each node along the piles within the footprint of cap and seal.

4.3.2.4 Damping

The viscous damping applied to the cap through the use of dashpots totaled 39 kip sec/in. The viscous dashpots were attached to thirteen nodes across the front of the cap, as with the FB-MultiPier model shown in Fig 4.2. Consequently, each dashpot employed a viscous constant, c, of 3 kip sec/in. As with section 4.3.1.4, approximately 45% of damping resistance was associated with the front and rear of the pile cap and seal.

4.3.3 Comparison of LS-DYNA and FB-MultiPier Results

Presented in the following figures are the displacement and force responses in LS-DYNA and FB-MultiPier for the models described in the previous sections. The responses are compared to the measured experimental response in the figures as well.

4.3.3.1 Comparison of Displacement Responses

Figure 4.17 is a comparison of the predicted displacements and experimental displacement at the shear wall, +6.0 ft. There is good agreement among all three displacements up to approximately 0.40 sec. This suggests that the inertia, damping, and static forces in the models were distributed on the system similar to the actual forces, which acted on the system in the experiment. This is different from the results of the primary FB-Pier model (Section 4.2.2). The difference was attributed to the changes to

the lateral soil springs representing skin friction as well as the reduction of the soil stiffness adjacent to the lead row of piles.

Following 0.40 sec, the negative peak displacements in the models occur earlier (shorter period) and the magnitudes are less than that experimentally measured. The divergence between the predicted and experimental period is due to high soil stiffness, k, which is inversely proportional to the time between peaks (Eq. 4.2). Another indication of the high soil stiffness is reflected in the predicted displacement being less than the measured. It is not necessarily the original soil stiffness value that determined this result, but the degraded soil stiffness. This value is a function of the degraded soil factor and consequently the effect on the displacement is a function of both parameters.

At 0.55 sec the displacements from the models begin to diverge and it is clear that their periods are shorter than the observed period of the shear wall. In addition to the shorter period, the displacements are less than the measured, illustrating the effect of the higher soil stiffness, see Eq. 4.2. The difference between LS-DYNA and FB-MultiPier was attributed to Maxwell spring in LS-DYNA, Figs. 4.15 & 4.16, which disappears (i.e., loss of stiffness) vs. no degrading P-y curve, Fig. 4.3 wasn't applied (i.e., P-y curve was user supplied, couldn't cover multiple cycles). Up to the 2nd cycle, the comparison between LS-DYNA and FB-MultiPier were quite close.

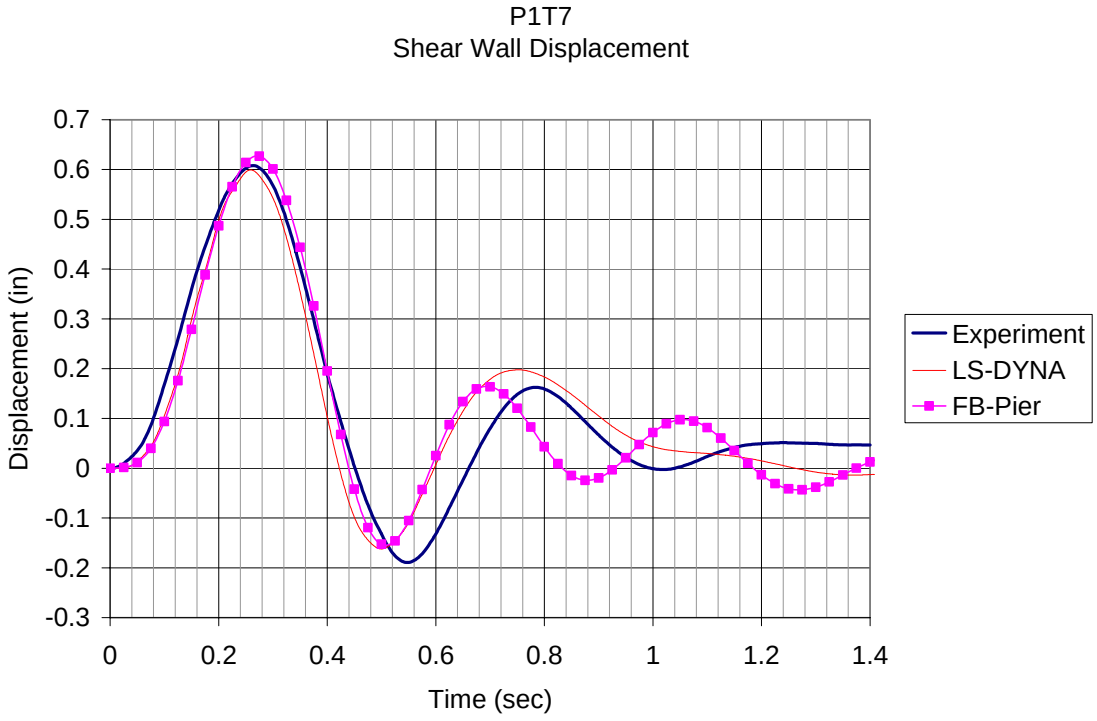

Figure 4.17 Predicted and Measured Shear Wall Displacements

Shown in Figure 4.18 is the experimental pile deflected shape at 0.25 sec vs. the predicted LS-DYNA and FB-MultiPier experimental pile shape. Generally, the predicted shape agrees the measured experimental response. It is evident that from Elev. -15ft to –50ft, both LS-DYNA and FB-MultiPier compare favorably. However, from Elev. –10ft to –20ft, LS-DYNA shows more relative displacement than the FB-MultiPier response. The latter was attributed to the use of beam elements in a truss layout (see Fig. 4.2) to characterize the seal concrete in FB-MultiPier vs. LS-DYNA's 3D brick element, which allowed shear distortion.

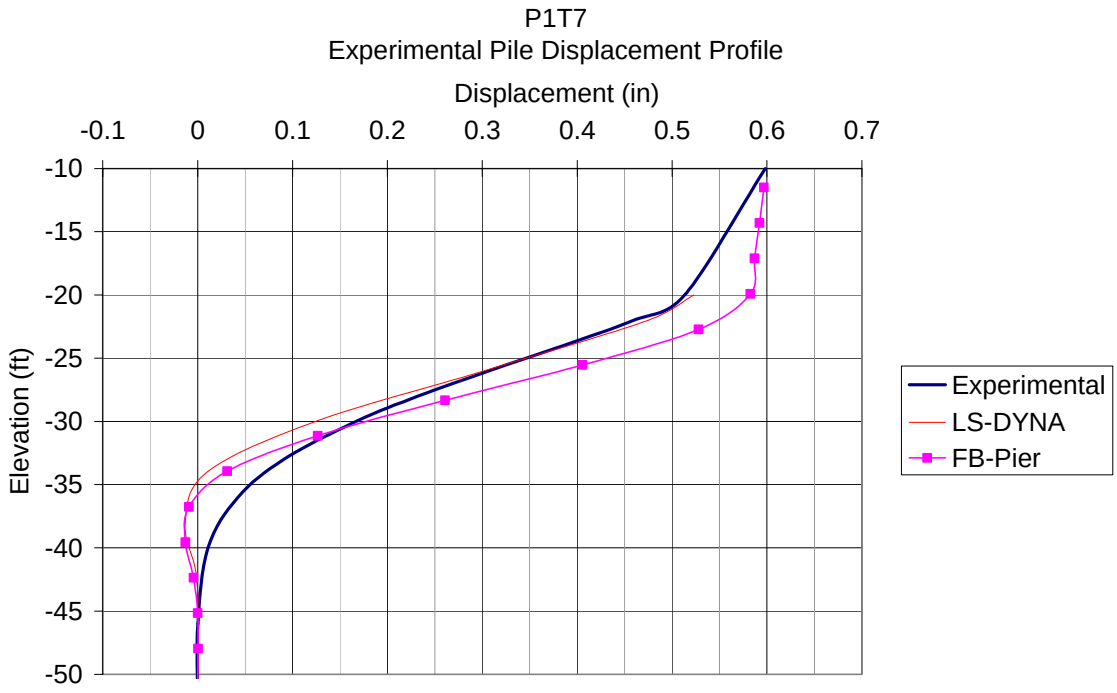

Figure 4.18 Predicted and Measured Experimental Pile Displacement, 0.15 sec

4.3.3.2 Comparison of Force Responses

Presented in Figure 4.19 is the experimental pile head shear vs. LS-DYNA and FB-MultiPier Pile head shear as a function of time. Note, the pile head shear includes the inertia, damping and static resistance. Evident is the measured and predicted response have similar amplitudes and periods up to 0.8 sec with the exception of the amplitude at 0.5 sec, which shows lower shears for the experimental response. LS-DYNA and FB-MultiPier response are quite similar up to 0.8 sec whereupon the LS-DYNA period response is longer. The latter was again attributed to the degrading stiffness of LS-DYNA vs. limitation of FB-MultiPier's user supplied P-y curves. Overall, the comparisons between LS-DYNA and FB-MultiPier are quite acceptable.

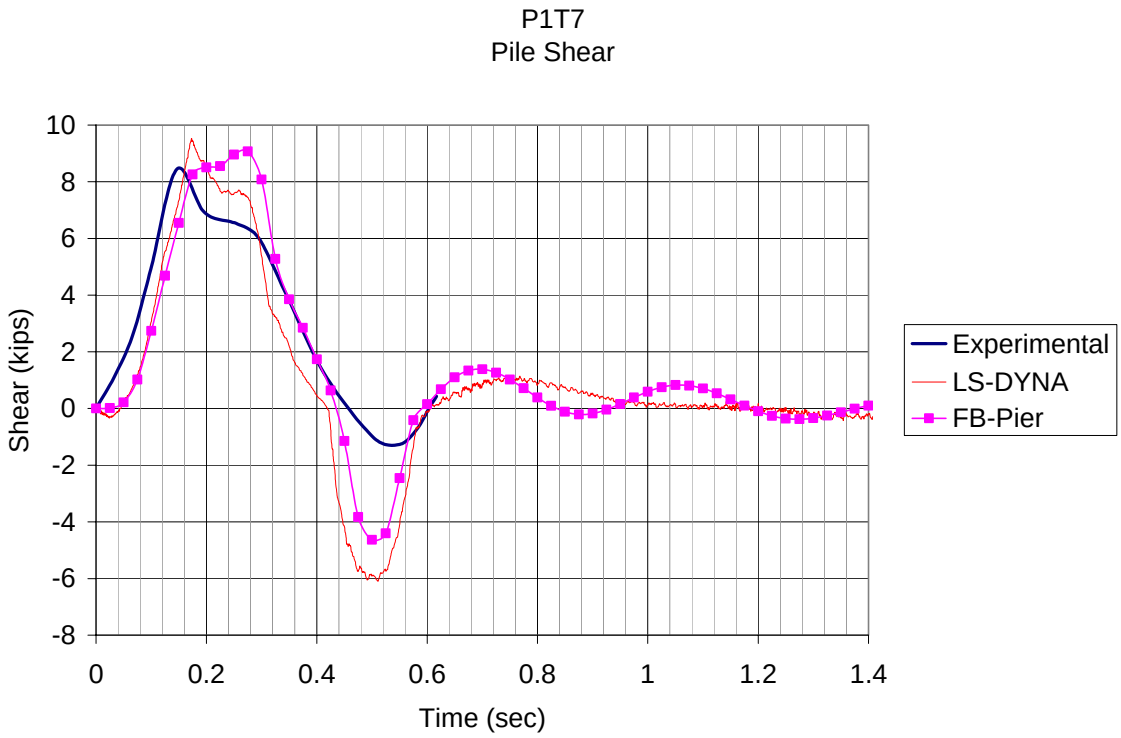

Figure 4.19 Predicted and Measured Experimental Pile Head Shear

CHAPTER 5
CONCLUSIONS AND RECOMMENDATIONS

5.1 Background

It has been observed that at least one serious vessel collision occurs with a bridge every year. For example, in September 2001, a barge collided with the Queen Isabella Causeway Bridge in South Padre Texas collapsing 3 spans. Subsequently, in May 2002, an errant barge tow struck the interstate I-40 Bridge in Webbers Falls, Oklahoma, resulting in the loss of fourteen lives.

The current AASHTO procedure for vessel collision defines an equivalent static load on a bridge based on kinetic energy (mass and velocity) of a moving barge for a specific waterway. Since the loading is a static force, other dynamic forces, i.e., inertia and damping are not considered. Depending on the duration of impact, particle velocities, accelerations, and size of soil-structure mass, dynamic resistance may be significant. Of interest are dynamic resistances provided by the soil-structure system below the vessel impact zone.

Besides recording and quantifying the dynamic forces within the soil-structure system, there is strong interest in identifying the capability of existing time-domain finite element software in modeling soil-structure response subject to vessel impact. In terms of soil properties, the traditional P-y lateral and T-z axial soil properties are required, along with viscous damping properties, as well as soil mass effects need to be quantified.

To characterize the dynamic soil-structure resistances, the Florida Department of Transportation (FDOT) decided to monitor and model a full-scale barge-bridge collision. The bridge, St. George Island Causeway (Florida State Road 300) near Apalachicola, Florida was selected for this study because of its size, shape and foundation layout. Specifically, the main pier was a reinforced concrete structure, composed of a pile cap, two large square pier columns, and a lateral stiffened shear wall. The width of each pier column at the point of barge impact was 6 ft. The mud-line footing consisted of a single concrete pile cap (21 ft. wide, 39 ft. long, 5 ft. thick), underlain by a concrete tremie seal (24 ft. wide, 42 ft. long, and 6 ft. thick) with forty steel HP 14x73 piles down to elevation –60 ft.

This part of the research was broken into 3 separate areas: 1) field instrumentation, and monitoring of Pier 1S; 2) reduction of field instrumentation data from multiple vessel impacts; and 3) time domain analysis of the barge-bridge impact with FB-MultiPier and LS-DYNA software. As part of the field instrumentation in order to improve the analysis of dynamic soil-structure interaction, insitu tests [Standard Penetration (SPT), Cone Penetration (CPT), Dilatometer (DMT), and Pressuremeter (PMT)] were performed at the site. The latter was used to quantify soil stratigraphy, soil properties, as well as direct assessment of lateral P-y, and axial T-z soil resistance. A summary of major findings in each category follows.

5.2 Site Description, Field Instrumentation, and Impact Data

Presented in Figure 5.1 is a plan view of the final insitu testing, and field instrumentation layout for Pier 1S, one of the main channel piers at St George Island Causeway Bridge. A total of 9 insitu tests (SPT, CPT, DMT & PMT) were conducted around Pier 1S (see Chapter 2.2). Based on the insitu tests, 8 soil layers as shown in

Figure 5.2 were identified for Pier 1S. A Layer of Sandy-Shell, underlain by alternating layers of silt, clays and sands were found, Table 5.1. Properties of each layer based on all of the insitu data (i.e., SPT, CPT, DMT, and PMT) were developed and are identified in Table 5.1. Besides soil properties (i.e., strength and Moduli), P-y representation from insitu data (e.g., PMT) were predicted (Fig. 2.6) and compared with field impact results (Fig. 3.14).

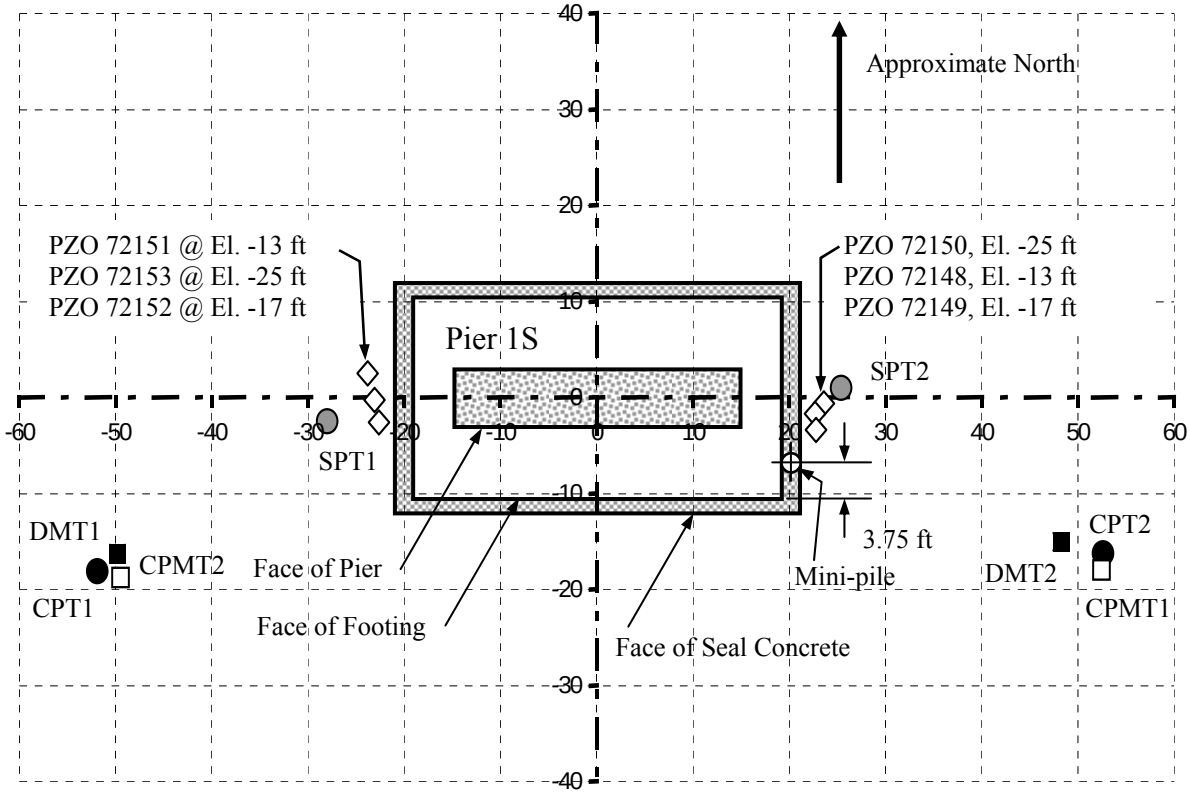

Figure 5.1 Plan View of Pier 1S Borings, Soundings, and Instrumentation

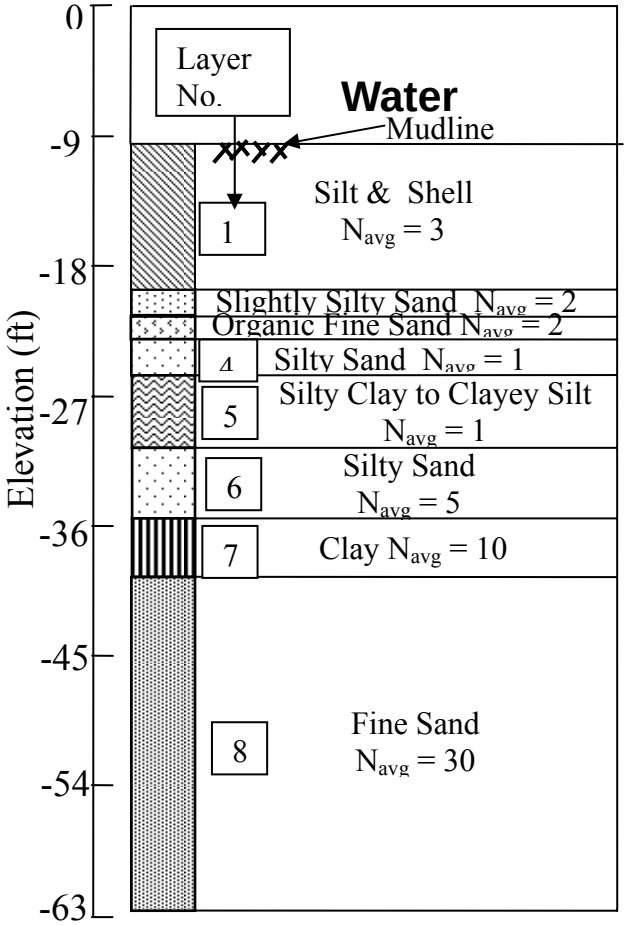

Figure 5.2 Soil Stratigraphy for Pier 1S

Table 5.1 Soil Layer Description and Properties

Layer	Soil Type	SPT N	Elev. (ft)	ϕ_{avg} (deg)	Unit Weight (pcf)	Subgrade (kcf)	Undrained Strength (psf)	Strain ε_{50} at 50%	Shear Mod. G (ksi)	Poisson' Ratio	Vert. Shear Fail. (psf)
1	Loose Silt and Shell	3	9-20	27	97	43	104	0.02	0.632	0.3	840
2	Slightly Silty Sand	2	20-21	34	106.3	35	NA	NA	1.075	0.3	564
3	Organic Fine Sand	2	21-22		104.3	NA	574	0.02	0.145	0.37	480
4	Silty Sand	2	22-25	31	109.6	51	NA	NA	2.043	0.3	564
5	Silty Clay to Clayey Silt	3	25-30		97	NA	331.3	0.02	0.096	0.2	840
6	Silty Sand	5	30-35	29	109	77	NA	NA	4.730	0.3	1374
7	Clay	10	35-40		99.5	NA	370.7	0.07	0.095	0.35	1629
8	Fine Sand	30	40-63	35	125.3	224	NA	NA	23.276	0.37	1269

In order to monitor lateral stress during the barge impact, 6 total stress gages and pore pressure transducers were placed in front and behind the cap and seal (see Fig 5.1). The lateral stress gages were very useful in identifying the change in horizontal stress acting on the pile cap and seal. For instance, Figure 5.3 shows the change in the lateral stress in front of the pile cap and seal from barge impact P1T7.

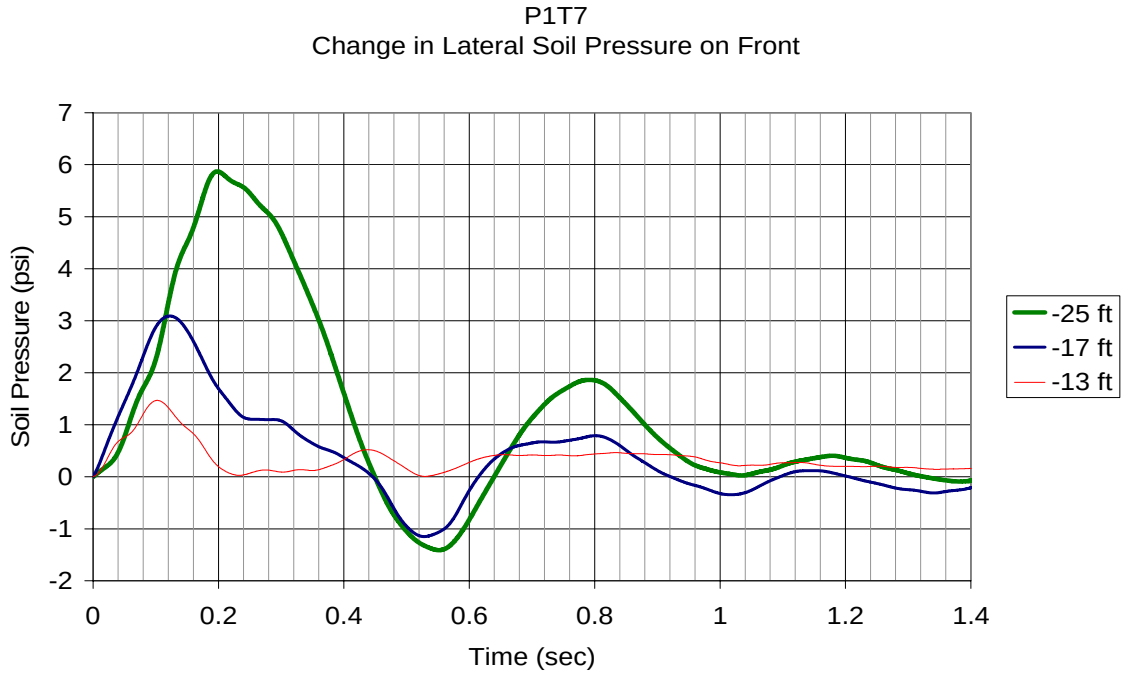

Figure 5.3 Changes in Stresses on Front of Cap and Seal for P1T7

To recover the dynamic pile soil-structure interaction within the group, the project installed a 8.625" steel pipe, i.e., ZW drill casing with a steel reinforcement cage, and high-strength grout, Fig 5.4. The composite pile was designed to match the flexure stiffness of an individual HP 14x73 pile used beneath Pier 1S.

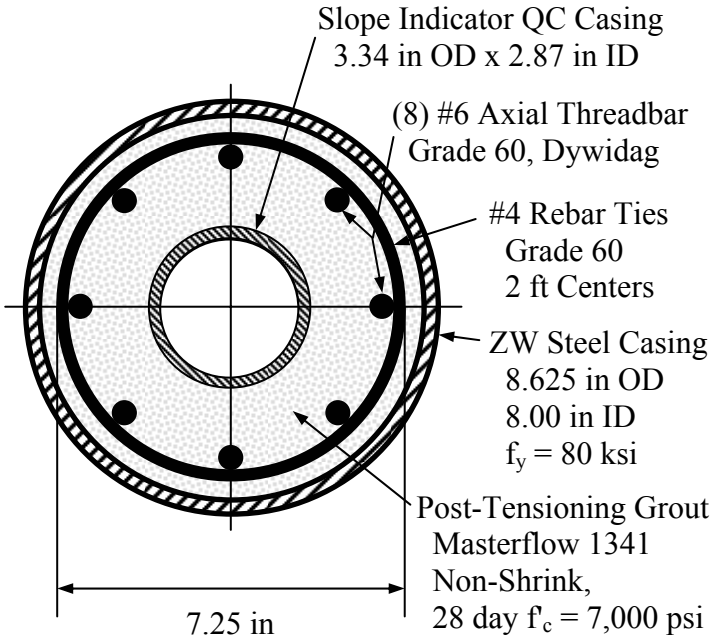

Figure 5.4 Cross-Section of ZW Mini-Pile

Cast within the high strength grout at various elevations along the mini-pile (see Fig. 5.5) were pairs of strain gages. The gages, were monitored with a National Instruments Data Acquisition System (2000 samples per second) for three of the barge impacts. Shown in Figure 5.6 is the strain gage output from a pair at the bottom of the concrete seal during one of the vessel impacts, P1T7, Figure 5.7. The strains were converted to moments along the length of the mini-pile by moment curvature relationship established from laboratory 3-point load testing on an instrumented section of the mini-pile.

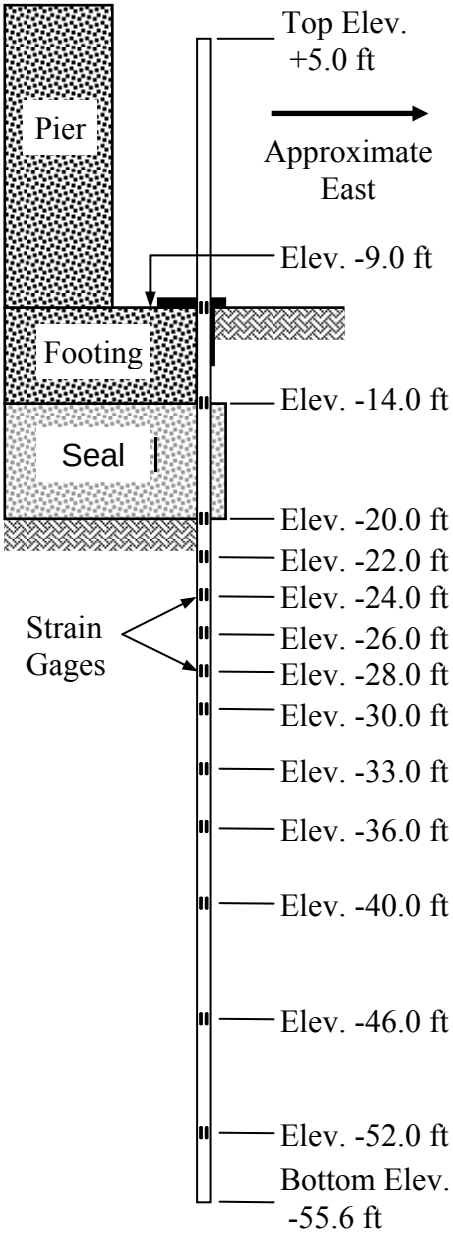

Figure 5.5 Elevations of Strain Gages in Mini-Pile

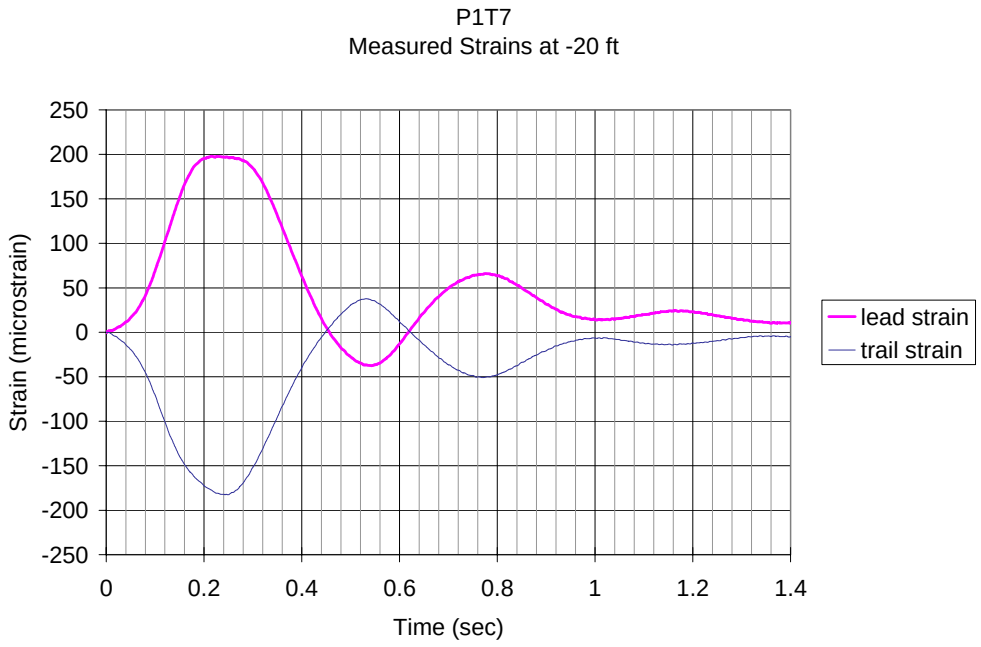

Figure 5.6 Paired Strains at -20 ft for P1T7

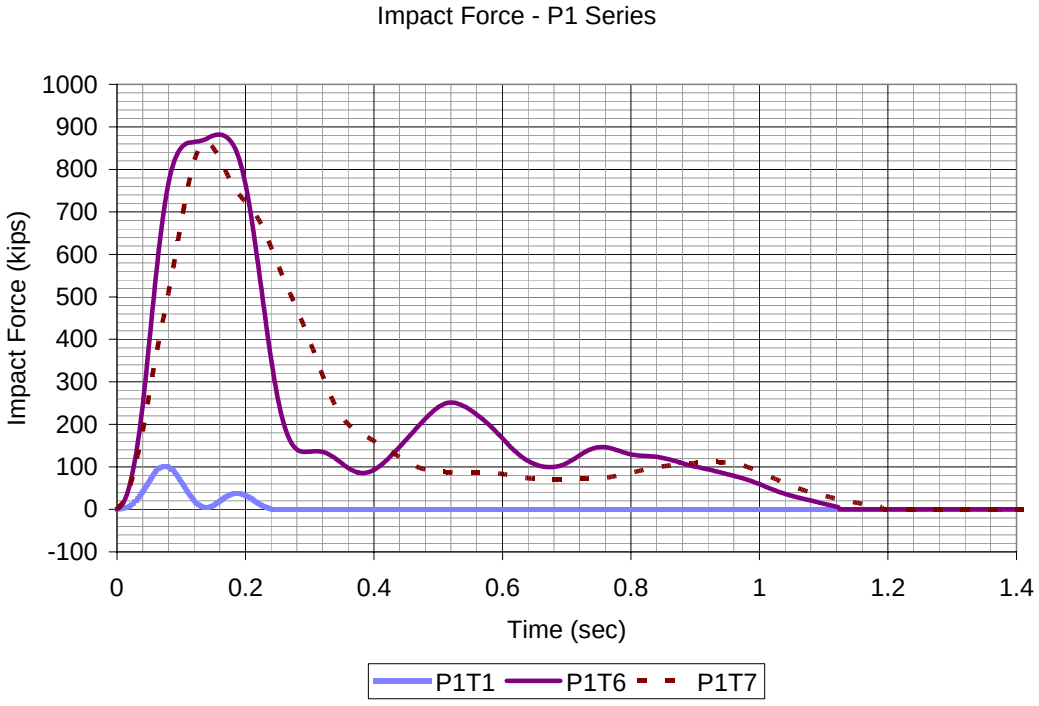

Figure 5.7 Measured Dynamic Impact Forces on Pier Shear Wall

5.3 Experimental Dynamic Soil-Structure Interaction

Using the instrumented strain data for the mini-pile, the rotations, deflections, moments, shears along the length experimental pile were determined for each of the vessel impacts, Fig. 5.7. For instance, Figure 5.8 shows the deflected shape of the mini-pile for multiple time steps for impact P1T7. Figure 5.9 shows the deflection of the pile head, and shear wall as a function of time for impact P1T7.

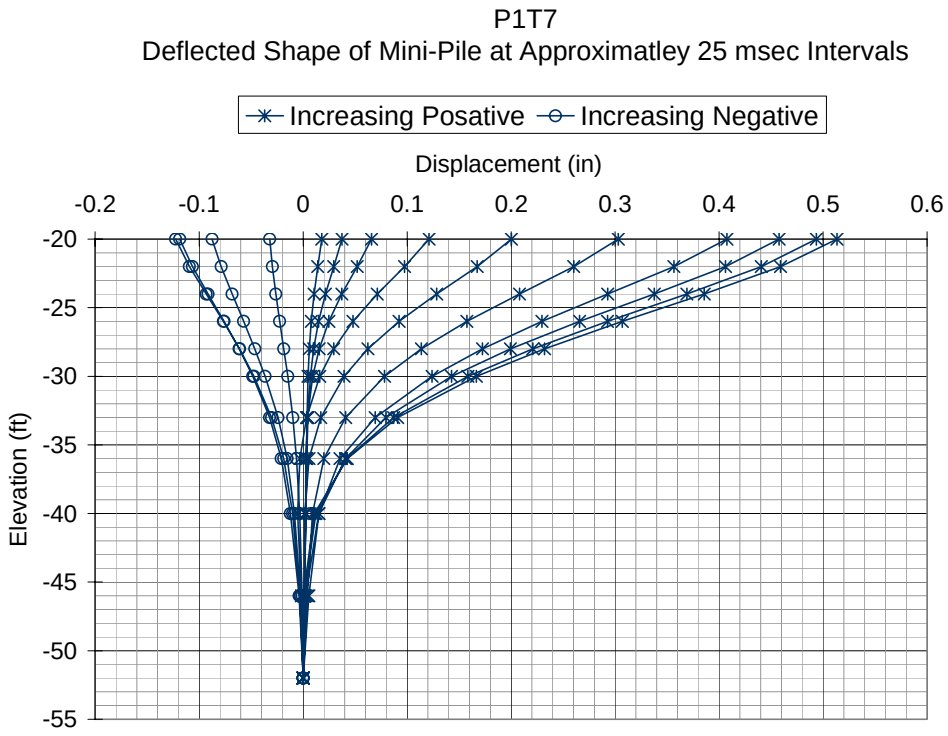

Figure 5.8 Deflected Shapes of Mini-Pile for P1T7

Of strong interest is the distribution of shear along the length of the pile for a specific deflected shape, Fig. 5.8. Specifically, if the shear distribution at a particular depth was differentiated, the soil resistance, P (Force/Length) may be assessed.

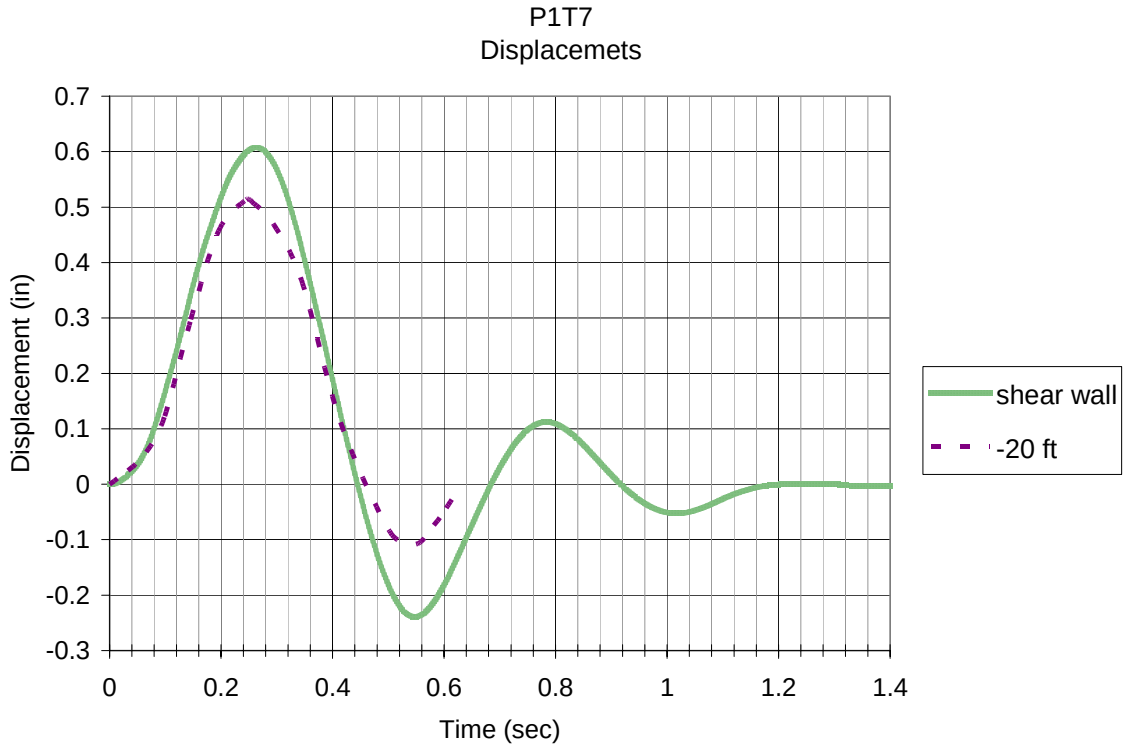

Figure 5.9 P1T7 Displacements

Shown in Figure 5.10 is an example of the dynamic soil resistance (Force/Length) at specific depth (Elev. -20 ft) as a function of pile displacement. The resistance, Fig. 5.10, is cyclic in nature due to the pile motion, i.e., back and forth; however of interest is the shape of the resistance. Evident is the resistance builds with lateral displacement up to 0.3in.; however after 0.3in, the resistance diminishes to less than ½ of its maximum value. Evident from Fig. 5.9, the velocity of the pile is a maximum at this time (slope = 0), suggesting significant damping resistance within the soil-structure system at this displacement and time. Fig. 5.10, suggest damping resistance equal to or slightly greater than the static value.

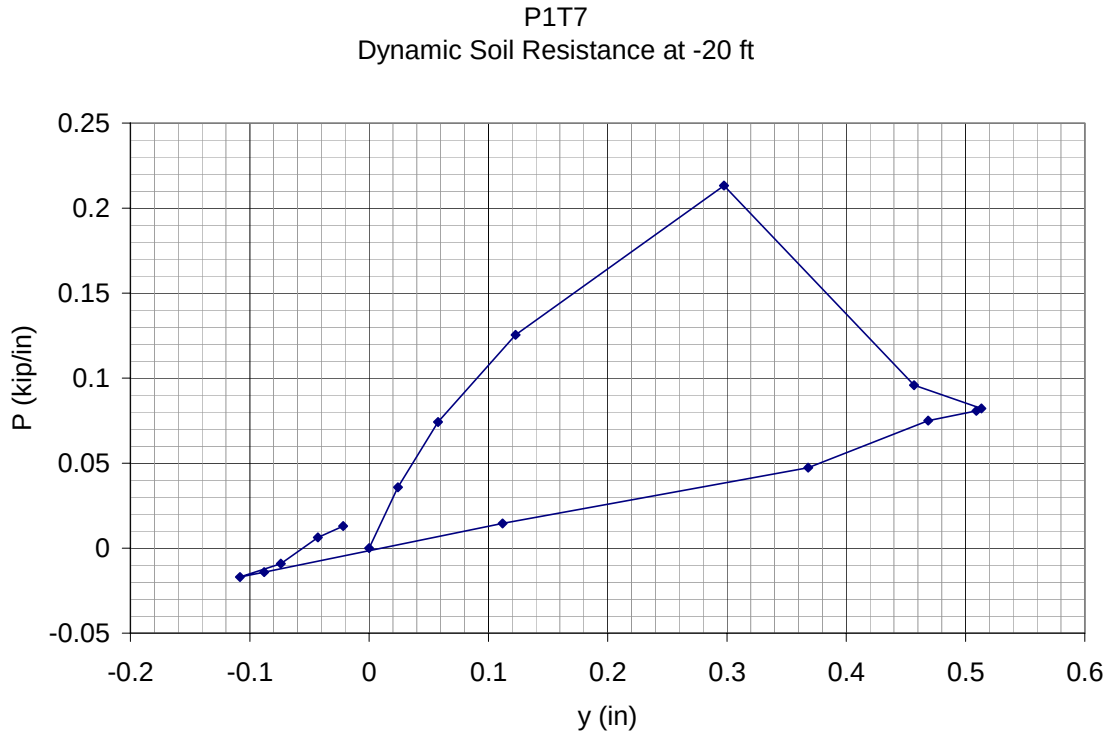

Figure 5.10 Dynamic Soil Resistance on Mini-Pile at Elev. -20ft for P1T7

Multiplying the total stress gages times the surface area they act for the front and rear of the pile cap and seal resulted in the soil resistance Figure 5.11, for impact P1T7. This figure shows the total dynamic soil resistance (i.e., inertia, damping and static) in front and behind the pile cap and seal from Elev. –11ft to –20ft. Evident from this figure is that the soil dynamic resistance is zero at zero pile cap & seal displacements, Fig. 5.9, suggesting the soil is either stationary or possibly moving with the pile-cap structure. The numerical analysis, Fig. 4.6, suggested the soil mass does not move or is stationary. Consequently, the soil resistance is provided through either damping or static resistance.

Figure 5.11 Resultant Forces on Cap and Seal for P1T7

5.4 Time Domain Analysis of Soil-Structure Interaction

A FB-MultiPier time domain analysis of Pier 1S was performed for barge impact P1T7. The model, Figure 5.12, consisted of 40 14x73 H piles, a 5' concrete cap, a shear wall and 2 concrete piers with a pier cap. The 6' thick concrete tremie seal, Fig. 5.5, was modeled with concrete beam elements arranged in a cross-bracing pattern, Fig. 5.12. The static soil resistance from the ground surface down to the bottom of the concrete seal, Elev. –20ft, i.e., Layer 1: Fig. 5.2 was characterized with Reese-Cox P-y curve based on soil properties from Table 5.1. The damping resistance required for a time domain analysis for layer 1 was characterized with viscous dashpots, Fig. 5.12. The required viscous damping parameter, c, was obtained using a Smith damping approach. That is, Smith damping coefficient, js, ($0.1 < js < 0.6$) or a value of 0.1 (granular soils) was

multiplied the static lateral resistance of the pile, Ru for a specific layer. Ru was determined as the ultimate lateral resistance from the P-y curve at the center of the layer times the thickness of the layer, i.e., 11'. Since the viscous damping parameter, c, is for a single pile which is located in a group arrangement, the total viscous representation of the group was adjusted through the P-Y multipliers recommended in the literature. The latter resulted in a total viscous damping, c, of 45 kip-sec/in. The dynamic resistances of the other layers, Fig. 5.2, were set equal to the experimental mini-pile values. Note, this was the only way to handle the damping, Fig. 5.10, since the version of FB-MultiPier at time of analysis did not allow dashpots along the pile.

Analysis of vessel impact P1T7, Fig. 5.7, resulted in the predicted shear wall and bottom seal motion shown in Figure 5.13. Comparison of measured and predicted displacement time histories of the shear wall and bottom of seal concrete (i.e., top of piles) show good correlation for both amplitude and period of motion. Similar comparisons of measured and predicted pile displaced shapes (section 4.2.2.1) and pile head shears (section 4.2.2.2) were completed.

Also of interest are the predicted vs. measured soil resistance acting on the pile cap and seal as a function of time, Fig. 5.14. Evident from this figure, initial resistance is due to damping (high velocity), which diminishes and is picked up by static resistance. Based on Figures 5.13 and 5.14, the damping assumptions, and distributions seem reasonable; however it is recommended that further testing (single piles and groups) for different soils and loading conditions be performed for further validation and development.

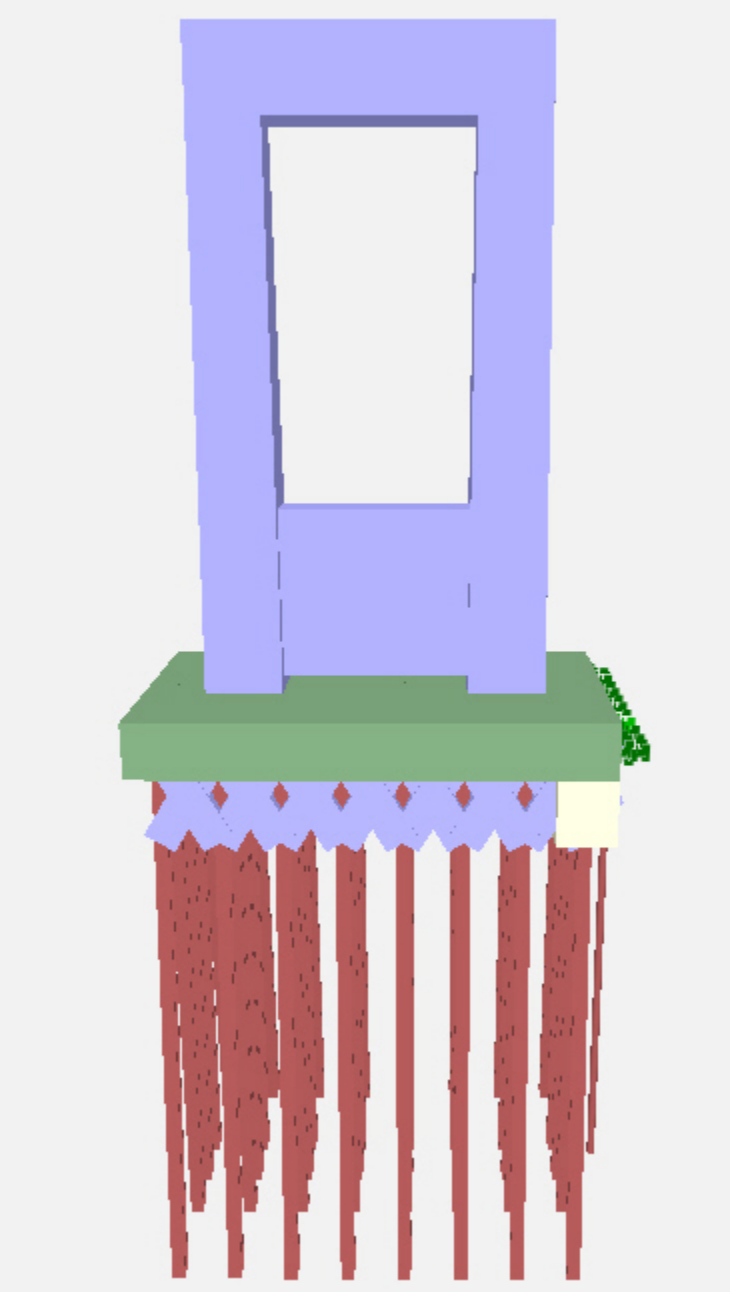

Figure 5.12 FB-MultiPier Depiction of Pier 1S

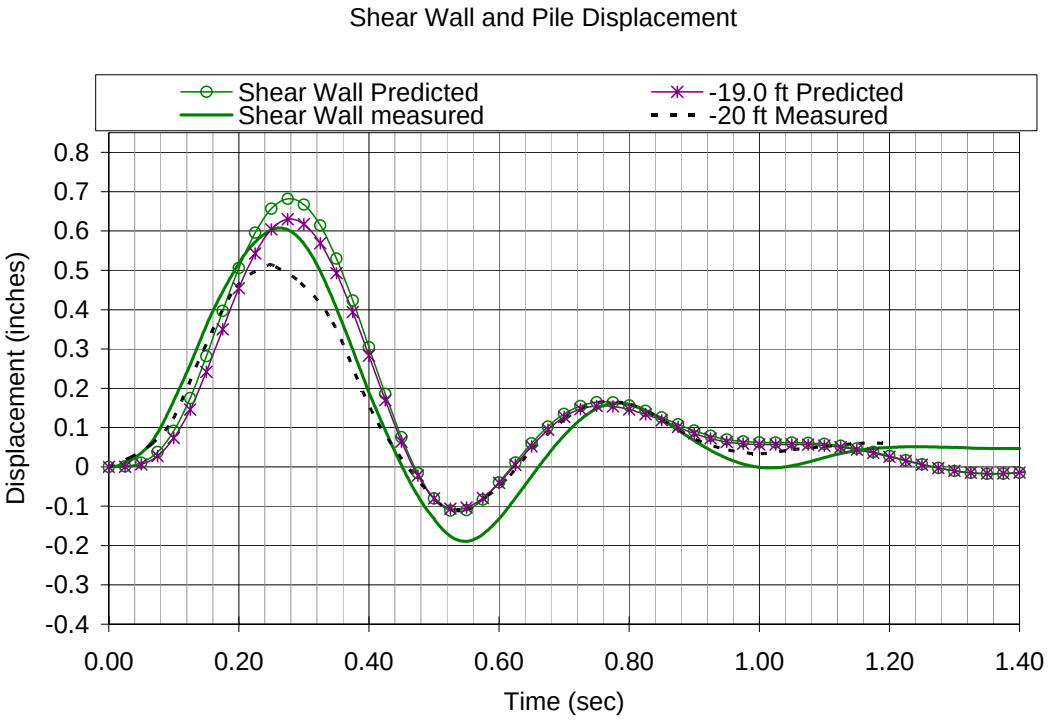

Figure 5.13 FB-MultiPier Predicted and Measured Displacements

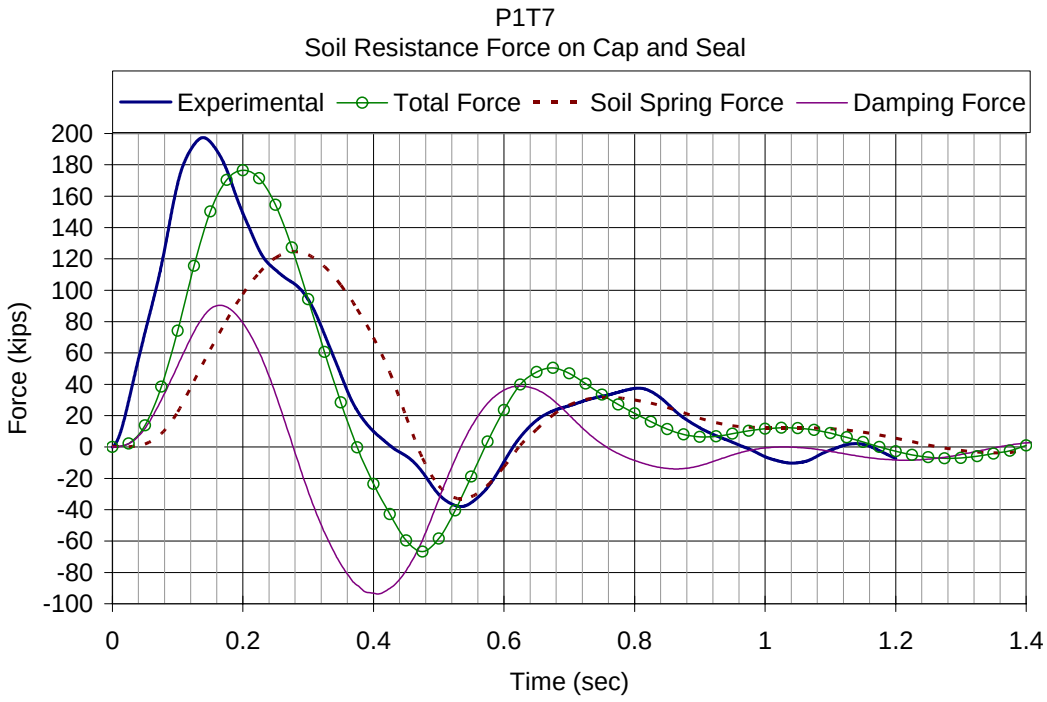

Figure 5.14 Lateral Soil Force on Cap and Seal

Shown in Figure 5.15 are the total forces acting on the cap and seal during barge impact P1T7. The measured applied load is compared with predicted inertia, damping and static resistance of the soil around the cap and seal, as well as the dynamic resistance from the underlying piles. Note the pile shear includes both static and damping resistance in a fifty/fifty split. Evident from Fig. 5.15, the inertia then damping, followed by static resistance is the order of mobilization. At the peak-applied load, 864 kips at 0.15 sec, approximately 70% of the resistance is due to dynamic resistances, i.e., inertia, and damping. Obviously, the latter forces would not be considered in a static analysis, i.e., current AASHTO vessel collision guideline. The analysis strongly supports the use of time domain analysis, which assesses substructure component velocity and acceleration determination. However, it is highly recommended that further testing of individual pile, bents, and pier group configurations be modeled and field tested for validation purposes.

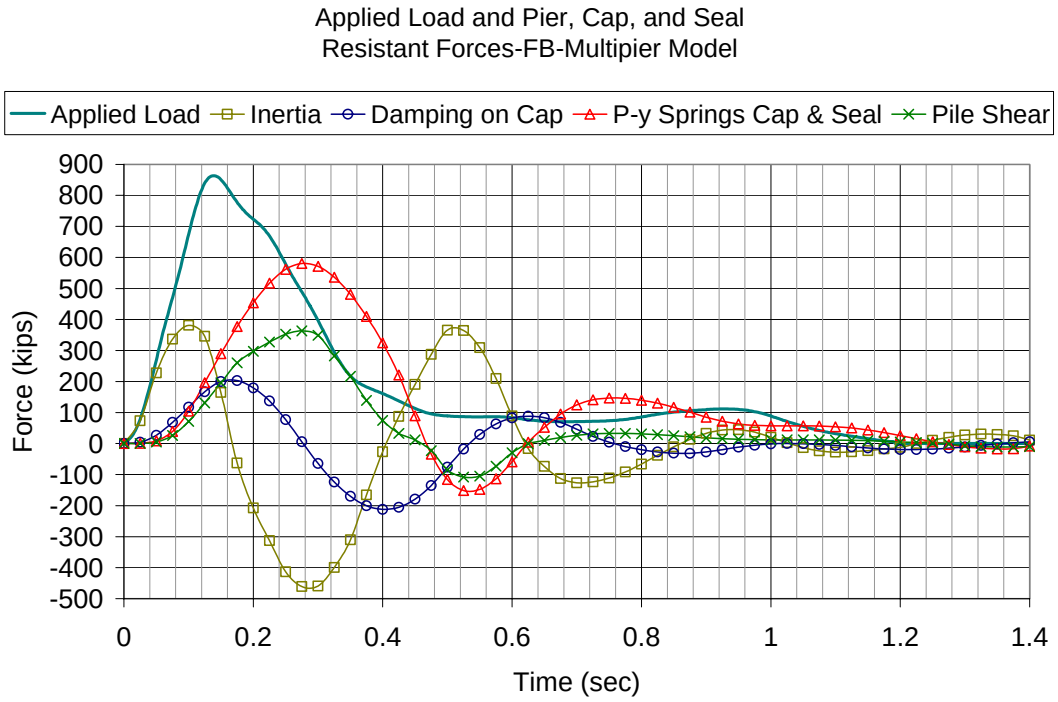

Figure 5.15 Total Forces Acting on the Pile Cap: Inertia, Damping, and Static Resistance

APPENDIX A
INSITU SOIL TEST DATA

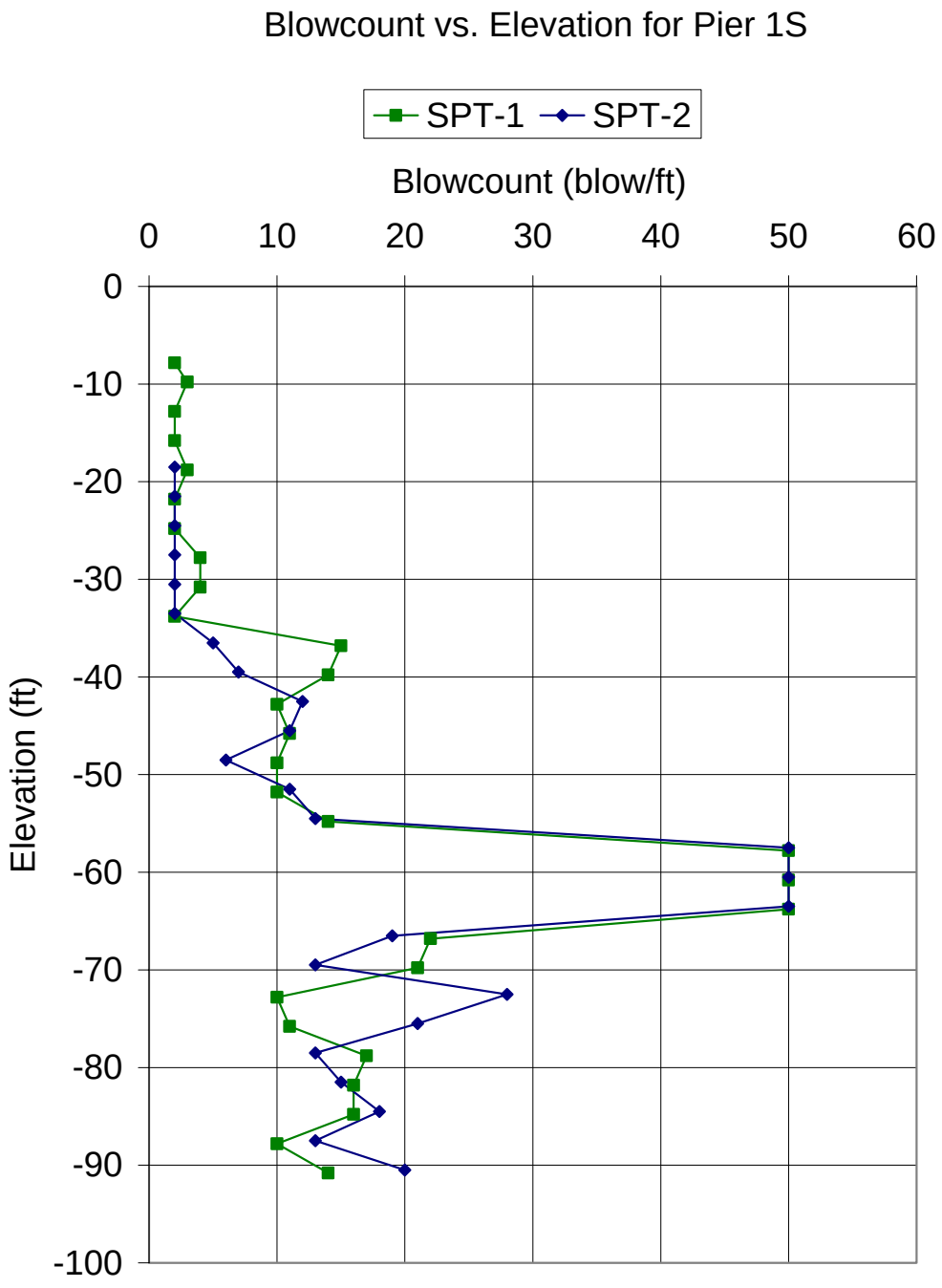

Figure A-1 Pier 1S SPT Blowcount versus Elevation

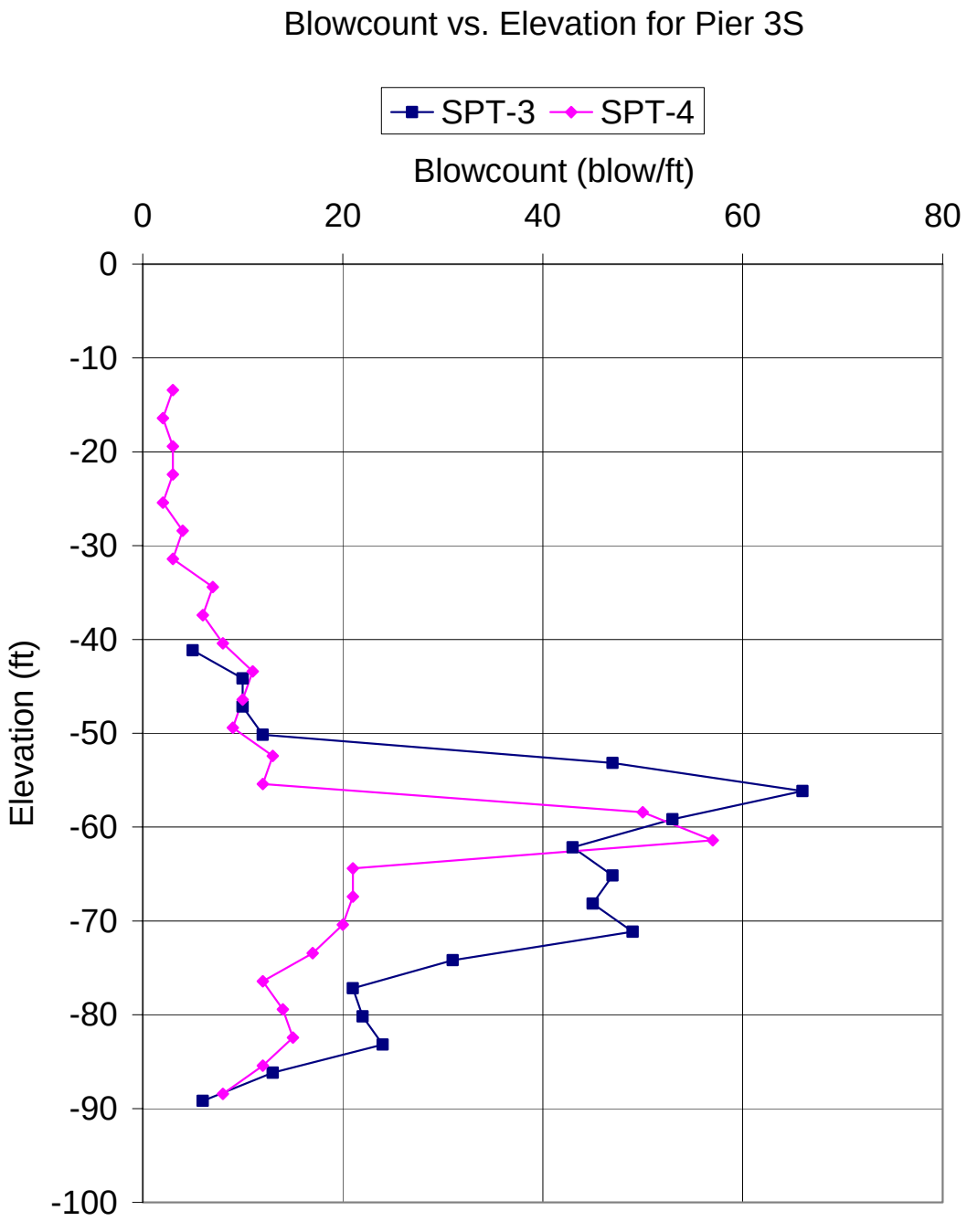

Figure A-2 Pier 3S SPT Blowcount versus Elevation

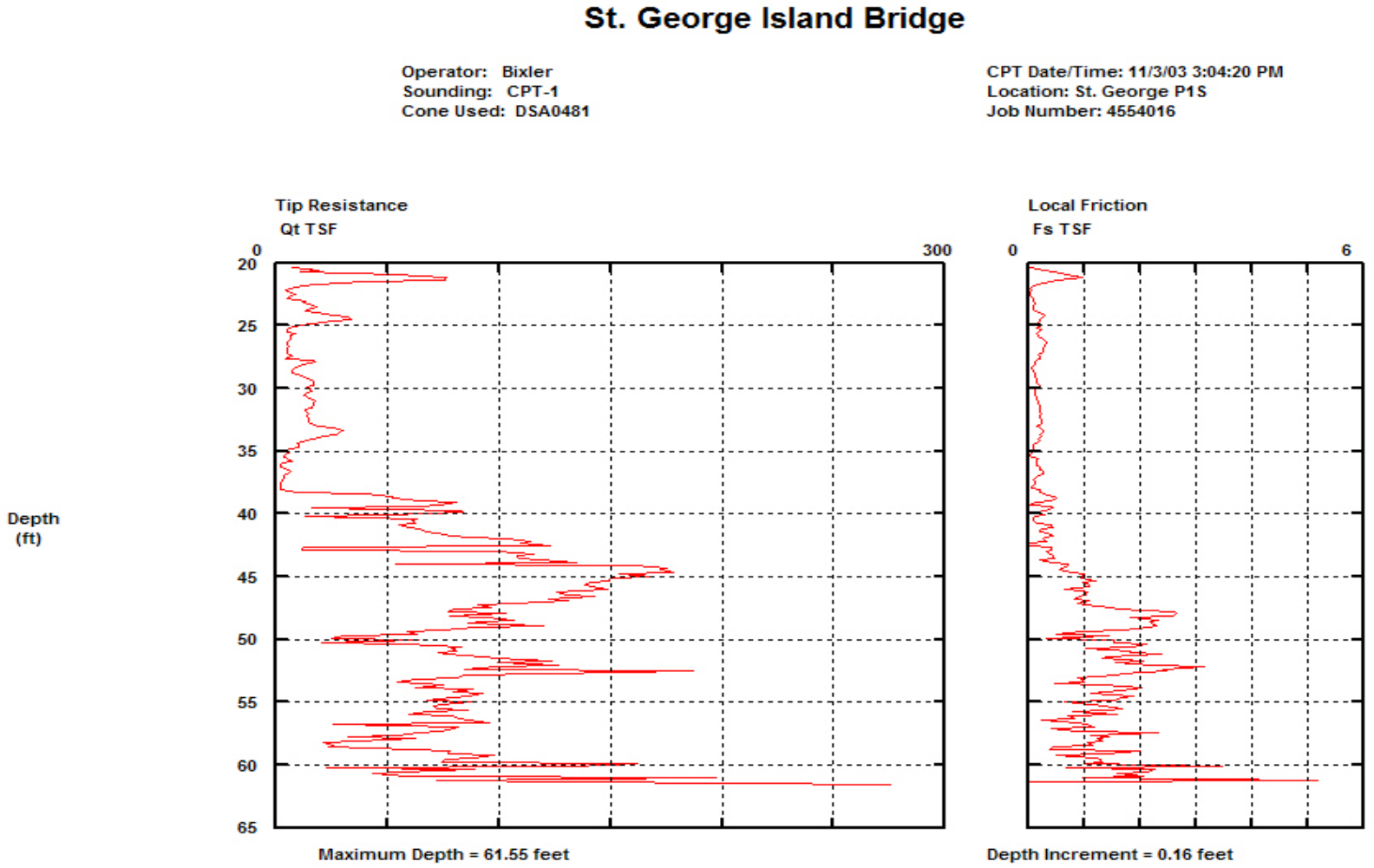

Figure A-3 CPT-1 Tip Resistance and Local Friction Profiles

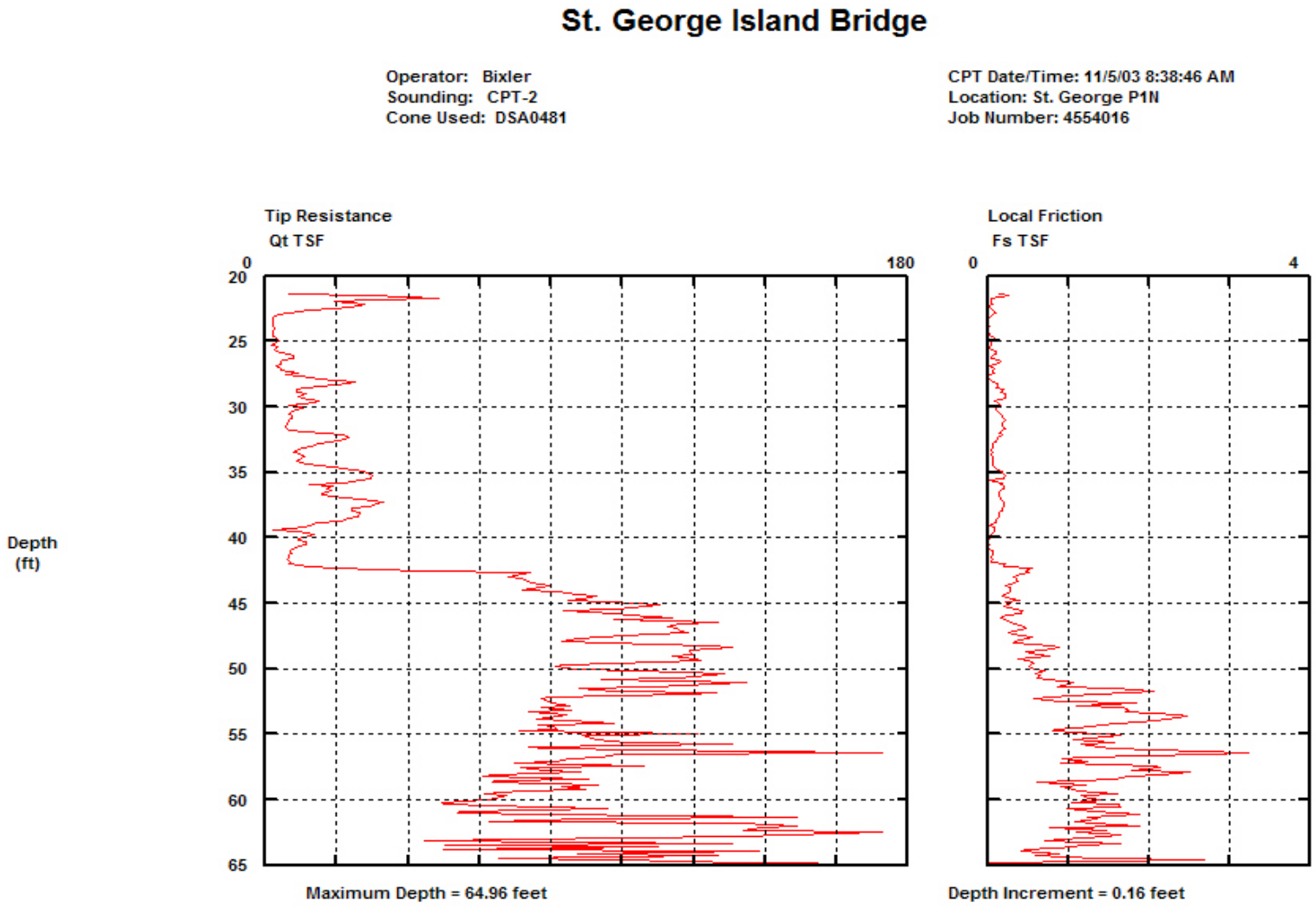

Figure A-4 CPT-2 Tip Resistance and Local Friction Profiles

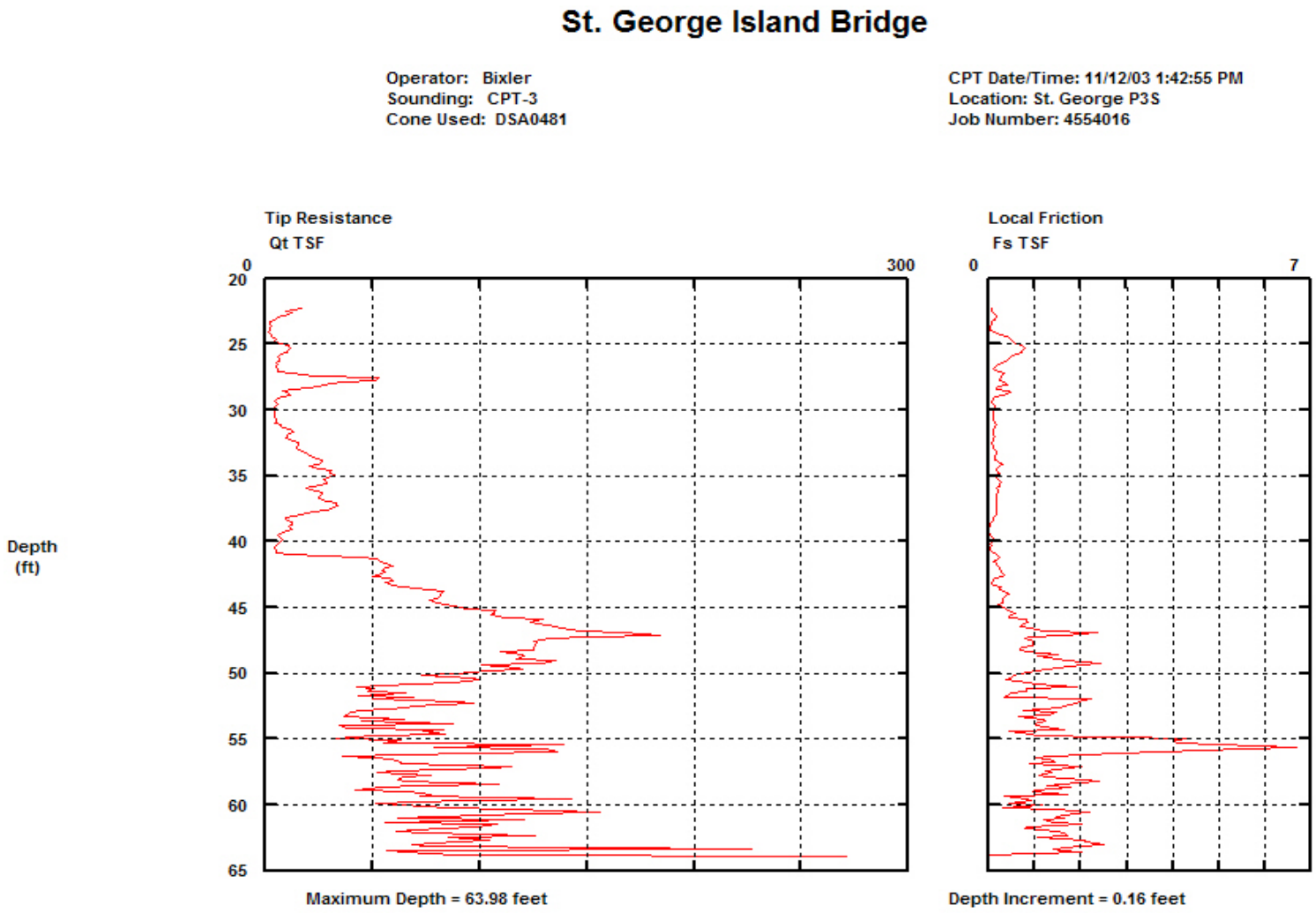

Figure A-5 CPT-3 Tip Resistance and Local Friction Profiles

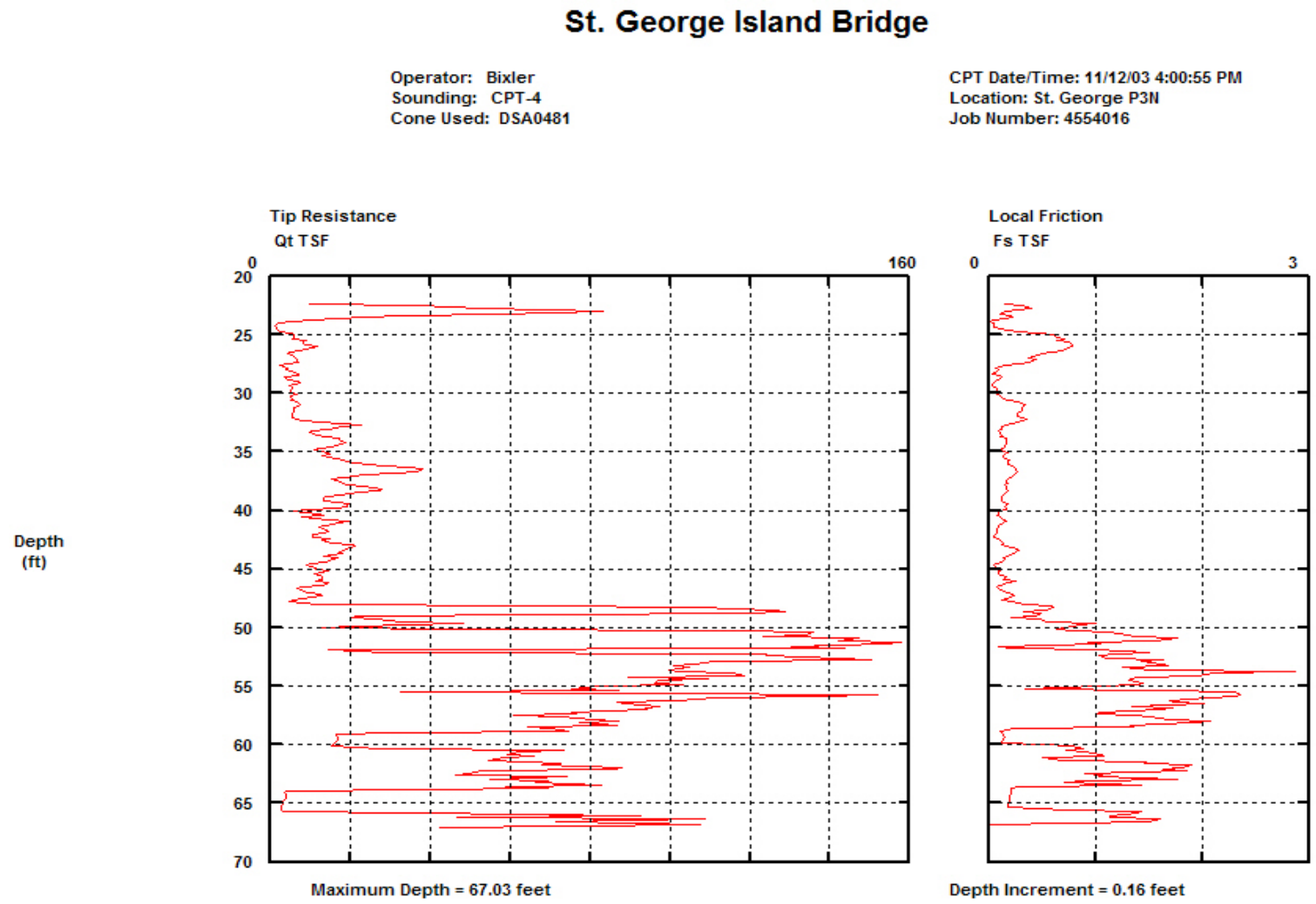

Figure A-6 CPT-4 Tip Resistance and Local Friction Profiles

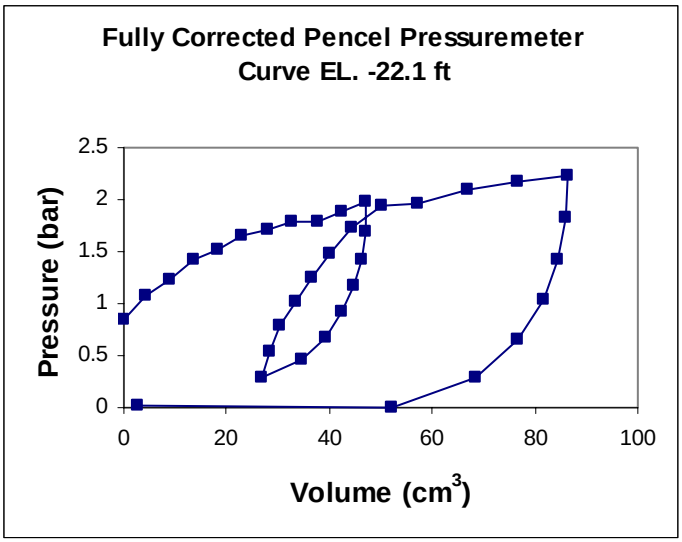

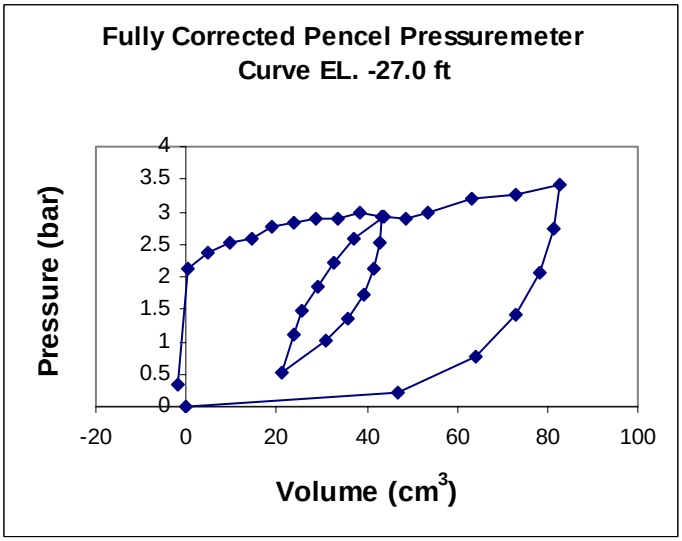

Figure A-7 CPMT-1 Curves

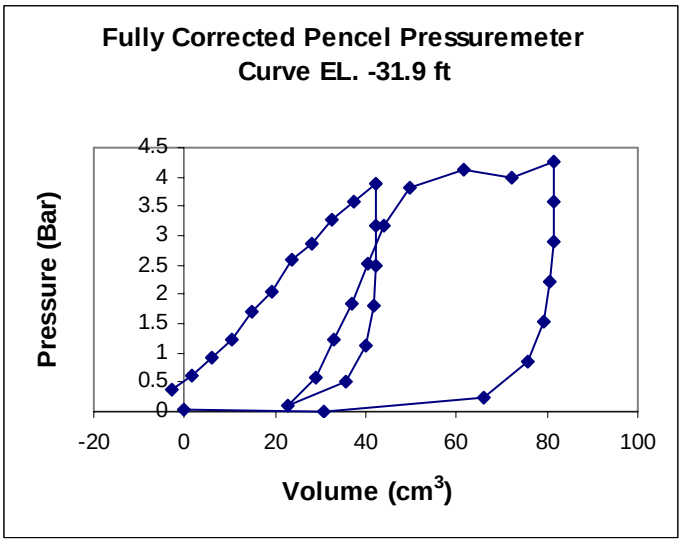

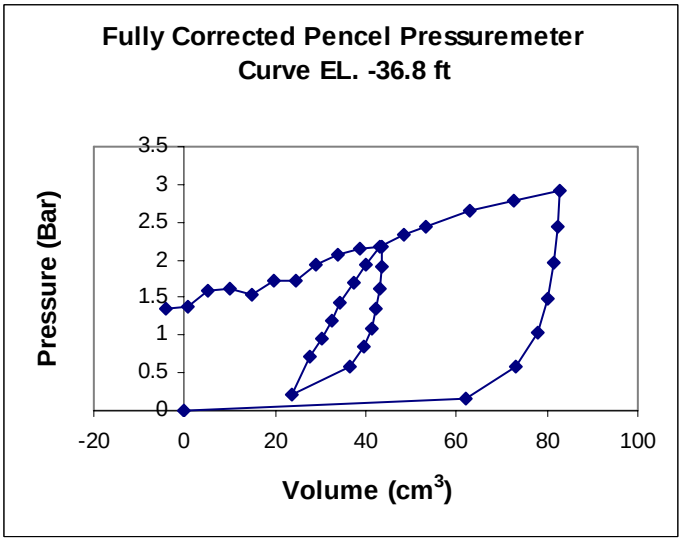

Figure A-8 CPMT-1 Curves

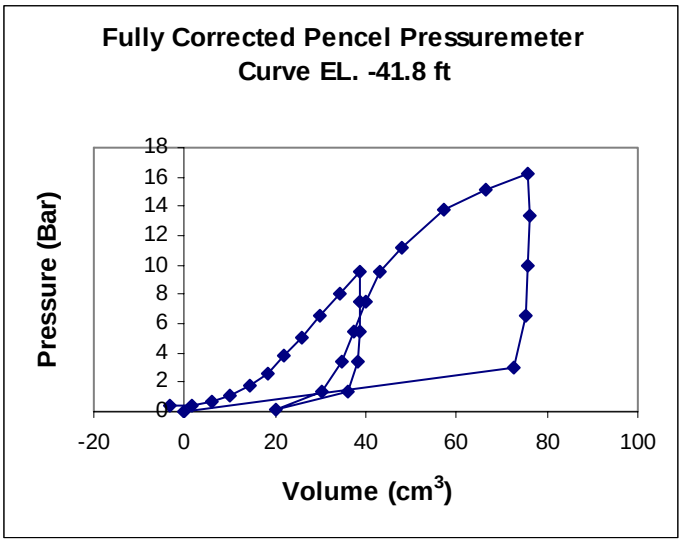

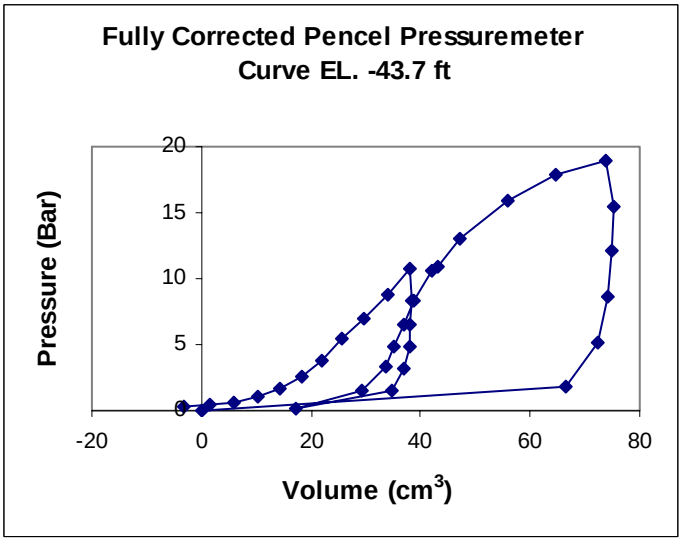

Figure A-9 CPMT-1 Curves

Table A-1 DMT-1 Data

Location:	**P1S**					
Sounding#:	**DMT1**					
SP#:				**Vented=**	**-0.01**	**bars**
GSE=	**0**	**ft**		**dA avg=**	**0.11**	**bars**
GWE=	**0**	**ft**		**dB avg=**	**0.55**	**bars**

Depth (m)	Depth (ft)	Elev (ft)	Thrust (N*100)	A (bars)	B (bars)	C (bars)
5.01	16.43781	-16.43781	22	1.05	2.21	
5.21	17.09401	-17.09401	31	1.03	2.23	
5.41	17.75021	-17.75021	27	1.14	1.95	
5.61	18.40641	-18.40641	19	0.96	1.6	
5.81	19.06261	-19.06261	24	0.91	1.61	
6.01	19.71881	-19.71881	43	0.95	1.58	
6.21	20.37501	-20.37501	55	0.94	1.54	0.42
6.41	21.03121	-21.03121	84	0.92	1.48	0.5
6.61	21.68741	-21.68741	94	0.83	1.52	0.4
6.81	22.34361	-22.34361	132	0.757	1.5	0.47
7.01	22.99981	-22.99981	116	0.96	1.95	0.55
7.21	23.65601	-23.65601	104	1.56	2.62	0.8
7.41	24.31221	-24.31221	104	2.25	4.16	1.08
7.61	24.96841	-24.96841	106	2.43	4.24	1.05
7.81	25.62461	-25.62461	124	3.03	4.57	1.42
8.01	26.28081	-26.28081	200	2.91	8.13	0.53
8.21	26.93701	-26.93701	190	1.41	3.36	0.54
8.41	27.59321	-27.59321	240	1.82		
8.61	28.24941	-28.24941	150	1.55	4.21	0.61
8.81	28.90561	-28.90561	138	1.48	2.96	1.15
9.01	29.56181	-29.56181	200	1.2	2.33	0.55
9.21	30.21801	-30.21801	200	1.13	1.97	
9.41	30.87421	-30.87421	150	1.34	1.88	0.63
9.61	31.53041	-31.53041	122	1.52	2.98	1.64
9.81	32.18661	-32.18661	210	1.54	3.44	0.68
10.01	32.84281	-32.84281	240	1.46	3.45	0.58
10.21	33.49901	-33.49901	230	1.74	6.29	0.71
10.41	34.15521	-34.15521	220	1.71	3.55	0.78
10.61	34.81141	-34.81141	170	2	3.61	0.8
10.81	35.46761	-35.46761	150	2.24	3.5	1.15
11.01	36.12381	-36.12381	180	2.44	3.5	1.3
11.21	36.78001	-36.78001	150	2.54	5.14	1
11.41	37.43621	-37.43621	330	3.24	11.55	0.74

Table A-1 Continued

11.61	38.09241	-38.09241	310	3.44	12.8	0.9
11.81	38.74861	-38.74861	280	2.84	8.52	0.93
12.01	39.40481	-39.40481	310	2.67	9	0.95
12.21	40.06101	-40.06101	315	3.77	11.7	
12.41	40.71721	-40.71721	360	4.5	14.3	0.88
12.61	41.37341	-41.37341	438	5.45	17.6	
12.81	42.02961	-42.02961	480	6.95	22.8	1.02
13.01	42.68581	-42.68581	580	7.74	25.2	
13.21	43.34201	-43.34201	570	7.24	24.8	1
13.41	43.99821	-43.99821	562	8.55	24.5	
13.61	44.65441	-44.65441	505	5.72	16.6	1.04
13.81	45.31061	-45.31061	410	5.1	14.4	
14.01	45.96681	-45.96681	395	3	8.02	
14.21	46.62301	-46.62301	400	5.6	22.8	1.06
14.41	47.27921	-47.27921	350	3.63	10.5	
14.61	47.93541	-47.93541	380	12.1	31.4	0.72
14.81	48.59161	-48.59161	320	3.8	7.64	
15.01	49.24781	-49.24781	420	10.9	34.4	0.8
15.21	49.90401	-49.90401	420	6.33	22.4	
15.41	50.56021	-50.56021	420	3.67	5.5	
15.61	51.21641	-51.21641	360	4.94	11.6	0.8
15.81	51.87261	-51.87261	360	5.82	20.4	
16.01	52.52881	-52.52881	330	10.5	34	1.05
16.21	53.18501	-53.18501	320	6.83	15.6	
16.41	53.84121	-53.84121	290	3.1	9.2	
16.61	54.49741	-54.49741	280	2.65	8.61	1
16.81	55.15361	-55.15361	280	3.25	6.7	
17.01	55.80981	-55.80981	300	2.37	7.67	
17.21	56.46601	-56.46601	320	2.67	5.42	1.33
17.41	57.12221	-57.12221	400	2.68	16.5	
17.61	57.77841	-57.77841	500	2.35	3.86	1.1
17.81	58.43461	-58.43461	700	2.96	28.3	1.2

Table A-2 DMT-2 Data

Location:	**P1S**				
Sounding #:	**DMT2**				
SP#:			**Vented=**	**0**	**bars**
GSE=	**0**	**ft**	**dA avg=**	**0.1**	**bars**
GWE=	**0**	**ft**	**dB avg=**	**0.74**	**bars**

Depth (m)	Depth (ft)	Elev (ft)	Thrust (N*100)	A (bars)	B (bars)	C (bars)
5.02	16.47062	-10.19	24.5	0.75	2.46	
5.22	17.12682	-10.8462	39	0.76	2.3	
5.42	17.78302	-11.5024	35	1	1.9	
5.62	18.43922	-12.1586	33	1.12	2.03	0.59
5.82	19.09542	-12.8148	55	1.18	2.13	0.6
6.02	19.75162	-13.471	54	1.25	2.72	
6.22	20.40782	-14.1272	62	1.49	2.88	0.48
6.42	21.06402	-14.7834	110	1.56	3.16	0.4
6.62	21.72022	-15.4396	150	2.32	3.57	0.5
6.82	22.37642	-16.0958	140	1.52	3.04	
7.02	23.03262	-16.752	130	1.44	2.54	0.64
7.22	23.68882	-17.4082	120	1.85	3.24	0.84
7.42	24.34502	-18.0644	130	2.03	4.3	0.73
7.62	25.00122	-18.7206	130	2.84	4.57	
7.82	25.65742	-19.3768	130	3.14	4.88	1.4
8.02	26.31362	-20.033	150	3.09	4.62	
8.22	26.96982	-20.6892	180	2.31	7.42	0.58
8.42	27.62602	-21.3454	200	1.85	4.44	
8.62	28.28222	-22.0016	180	1.98	3.82	0.7
8.82	28.93842	-22.6578	180	1.94	4.96	
9.02	29.59462	-23.314	170	1.8	4.96	0.57
9.22	30.25082	-23.9702	150	2.38	6.21	
9.42	30.90702	-24.6264	170	2.44	5.82	1.3
9.62	31.56322	-25.2826	120	2.52	6.02	
9.82	32.21942	-25.9388	130	1.93	5.73	0.69
10.02	32.87562	-26.595	160	3	9.36	0.7
10.22	33.53182	-27.2512	110	2.67	7.62	
10.42	34.18802	-27.9074	100	2.14	3.56	
10.62	34.84422	-28.5636	100	2.23	4.03	0.85
10.82	35.50042	-29.2198	150	2.95	4.74	
11.02	36.15662	-29.876	170	3.51	5.54	1.5
11.22	36.81282	-30.5322	150	3.12	5.6	1.2
11.42	37.46902	-31.1884	280	4.38	13.5	0.74

Table A-2 Continued

11.62	38.12522	-31.8446	290	5.24	15.9	
11.82	38.78142	-32.5008	230	3.37	11.6	0.83
12.02	39.43762	-33.157	260	3.67	13.2	
12.22	40.09382	-33.8132	270	3.12	11.6	
12.42	40.75002	-34.4694	300	2.92	12.9	0.88
12.62	41.40622	-35.1256	310	5.86	17.9	
12.82	42.06242	-35.7818	360	2.95	13.8	0.96
13.02	42.71862	-36.438	430	5.82	20.1	0.95
13.22	43.37482	-37.0942	450	5.64	21	
13.42	44.03102	-37.7504	520	5.73	20.4	0.97
13.62	44.68722	-38.4066	450	3.44	11.4	
13.82	45.34342	-39.0628	420	6.32	23.9	0.9
14.02	45.99962	-39.719	410	3.58	11.4	
14.22	46.65582	-40.3752	400	4.84	22.8	0.98
14.42	47.31202	-41.0314	400	5.05	21.8	
14.62	47.96822	-41.6876	380	2.37	6.12	1
14.82	48.62442	-42.3438	330	8.32	26	
15.02	49.28062	-43	440	2.14	5.82	
15.22	49.93682	-43.6562	340	3.08	9	0.98
15.42	50.59302	-44.3124	400	2.28	6.26	
15.62	51.24922	-44.9686	430	3.98	12.6	1.03
15.82	51.90542	-45.6248	390	2.13	3.68	
16.02	52.56162	-46.281	320	2.32	9.6	1.25
16.22	53.21782	-46.9372	310	1.76	3.38	
16.42	53.87402	-47.5934	270	2.9	10.2	
16.62	54.53022	-48.2496	270	2.3	5.05	1.85
16.82	55.18642	-48.9058	240	4.48	17.06	1.45
17.02	55.84262	-49.562	390	9.45	18.02	
17.22	56.49882	-50.2182	400	10	33.4	1.1
17.42	57.15502	-50.8744	440	2.9	15.7	
17.62	57.81122	-51.5306	450	2.48	7.56	1.35
17.82	58.46742	-52.1868	720	5.62	59.3	1.18

Table A-3 DMT-3 Data

Location:	**P3S**				
Sounding #:	**DMT3**				
SP#:			**Vented=**	**-0.01**	**bars**
GSE=	**0**	**ft**	**dA avg=**	**0.24**	**bars**
GWE=	**0**	**ft**	**dB avg=**	**0.32**	**bars**

Depth (m)	Depth (ft)	Elev (ft)	Thrust (N*100)	A (bars)	B (bars)	C (bars)
4.6	15.0926	-15.0926	28	1.11	2.63	
4.8	15.7488	-15.7488	25	0.73	1.42	
5	16.405	-16.405	13	1.08	1.74	
5.2	17.0612	-17.0612	0.2	1.12	1.7	
5.4	17.7174	-17.7174	6	0.97	1.57	
5.6	18.3736	-18.3736	27	1.84	2.73	0.6
5.8	19.0298	-19.0298	130	2.26	5.13	
6	19.686	-19.686	100	2	3.63	
6.2	20.3422	-20.3422	46	1.44	2.32	0.46
6.4	20.9984	-20.9984	64	1.8	4.02	0.38
6.6	21.6546	-21.6546	102	2.33	5.1	
6.8	22.3108	-22.3108	150	2.42	3.93	
7	22.967	-22.967	85	2.38	3.52	1.2
7.2	23.6232	-23.6232	81	2.83	3.7	
7.4	24.2794	-24.2794	71	2.81	4.93	0.63
7.6	24.9356	-24.9356	90	2.33	7.21	
7.8	25.5918	-25.5918	130	2.21	7	
8	26.248	-26.248	95	2.39	8.44	0.47
8.2	26.9042	-26.9042	91	2.13	6.23	
8.4	27.5604	-27.5604	81	2.5	6.14	0.44
8.6	28.2166	-28.2166	85	2.28	6.83	
8.8	28.8728	-28.8728	99	1.73	3.12	
9	29.529	-29.529	75	2.21	6.32	0.48
9.2	30.1852	-30.1852	92	2.78	7.13	
9.4	30.8414	-30.8414	98	2.63	8.25	0.5
9.6	31.4976	-31.4976	75	2.16	4.68	
9.8	32.1538	-32.1538	95	1.98	3.8	0.58
10	32.81	-32.81	58	1.98	2.73	
10.2	33.4662	-33.4662	39	2.44	3.84	1.08
10.4	34.1224	-34.1224	26	2.04	2.86	
10.6	34.7786	-34.7786	61	2.56	7.21	0.68
10.8	35.4348	-35.4348	220	2.98	11.9	
11	36.091	-36.091	220	3.64	11.39	0.85

Table A-3 Continued

11.2	36.7472	-36.7472	220	3.06	10	
11.4	37.4034	-37.4034	230	3.42	12.05	0.77
11.6	38.0596	-38.0596	270	3.24	11.1	
11.8	38.7158	-38.7158	400	4.91	14.1	0.81
12	39.372	-39.372	460	5.83	19.1	0.8
12.2	40.0282	-40.0282	480	7.33	29.1	
12.4	40.6844	-40.6844	440	7.92	26.3	0.83
12.6	41.3406	-41.3406	420	6.47	28.1	
12.8	41.9968	-41.9968	360	2.57	7.39	
13	42.653	-42.653	370	2.8	14.3	1
13.2	43.3092	-43.3092	400	4.82	18.3	
13.4	43.9654	-43.9654	320	2.96	28	
13.6	44.6216	-44.6216	320	3.82	15.2	1.6
13.8	45.2778	-45.2778	320	5.28	28.6	
14	45.934	-45.934	320	2.24	6.45	
14.2	46.5902	-46.5902	320	3.36	12.8	1.08
14.4	47.2464	-47.2464	320	6.72	17.6	
14.6	47.9026	-47.9026	280	3.83	10.1	
14.8	48.5588	-48.5588	330	2.47	16.6	
15	49.215	-49.215	370	4.74	12.8	1.1
15.2	49.8712	-49.8712	320	5.66	18	
15.4	50.5274	-50.5274	280	4.12	12.9	1.2
15.6	51.1836	-51.1836	340	3.63	16	
15.8	51.8398	-51.8398	300	10.4	28.8	1.12
16	52.496	-52.496	350	7.62	17.4	
16.2	53.1522	-53.1522	320	3.86	21.1	0.8
16.4	53.8084	-53.8084	300	3.23	11.8	
16.6	54.4646	-54.4646	320	3.63	9.35	
16.8	55.1208	-55.1208	460	5.43	23.1	1.3
17	55.777	-55.777	720	13.4	43.6	1.1

Table A-4 DMT-4 Data

Location:	**P3S**				
Sounding #:	**DMT4**				
SP#:			**Vented=**	**-0.09**	**bars**
GSE=	**0**	**ft**	**dA avg=**	**0.23**	**bars**
GWE=	**0**	**ft**	**dB avg=**	**0.21**	**bars**

Depth (m)	Depth (ft)	Elev (ft)	Thrust (N*100)	A (bars)	B (bars)	C (bars)
5.16	16.92996	-16.92996	44	1.51	3.92	
5.36	17.58616	-17.58616	12	1.23	1.79	
5.56	18.24236	-18.24236	8	1.39	2.41	0.28
5.76	18.89856	-18.89856	34	1.92	3.42	
5.96	19.55476	-19.55476	410	2.63	4.96	
6.16	20.21096	-20.21096	200	2.53	3.81	
6.36	20.86716	-20.86716	120	1.64	2.47	
6.56	21.52336	-21.52336	120	1.27	3.57	0.37
6.76	22.17956	-22.17956	220	2.18	3.99	
6.96	22.83576	-22.83576	200	1.9	3.29	0.77
7.16	23.49196	-23.49196	190	2.15	3.39	
7.36	24.14816	-24.14816	190	2.69	4.11	
7.56	24.80436	-24.80436	160	3.06	4	1.69
7.76	25.46056	-25.46056	150	2.9	4.55	
7.96	26.11676	-26.11676	260	2.08	6.4	0.58
8.16	26.77296	-26.77296	250	2.28	5.63	
8.36	27.42916	-27.42916	240	2.09	6.5	0.62
8.56	28.08536	-28.08536	230	1.65	3.75	
8.76	28.74156	-28.74156	240	2.15	6.28	
8.96	29.39776	-29.39776	220	2.2	4.92	0.6
9.16	30.05396	-30.05396	280	1.87	4.1	
9.36	30.71016	-30.71016	200	1.9	3.45	
9.56	31.36636	-31.36636	240	1.42	2.09	0.69
9.76	32.02256	-32.02256	200	1.78	2.85	
9.96	32.67876	-32.67876	190	1.6	2.85	0.7
10.16	33.33496	-33.33496	200	1.9	3.4	
10.36	33.99116	-33.99116	190	1.85	3.65	0.87
10.56	34.64736	-34.64736	200	1.88	2.85	
10.76	35.30356	-35.30356	150	2.2	3.85	
10.96	35.95976	-35.95976	200	2.05	4.05	0.85
11.16	36.61596	-36.61596	190	2.17	3.4	
11.36	37.27216	-37.27216	160	2.15	3.8	0.92
11.56	37.92836	-37.92836	170	2.2	3.38	

Table A-4 Continued

11.76	38.58456	-38.58456	160	3.2	4.83	
11.96	39.24076	-39.24076	180	4.25	6	2.48
12.16	39.89696	-39.89696	260	4.35	5.75	
12.36	40.55316	-40.55316	250	3.12	4.65	
12.56	41.20936	-41.20936	250	2.48	3.5	0.98
12.76	41.86556	-41.86556	370	3.2	5.32	
12.96	42.52176	-42.52176	340	2.3	3.05	0.97
13.16	43.17796	-43.17796	440	3.28	10.9	
13.36	43.83416	-43.83416	580	7.08	20.2	1.02
13.56	44.49036	-44.49036	550	5.3	15.1	
13.76	45.14656	-45.14656	550	5.65	17.8	0.93
13.96	45.80276	-45.80276	510	4.75	17.5	
14.16	46.45896	-46.45896	480	3.98	11.2	0.92
14.36	47.11516	-47.11516	660	2.85	6.25	
14.56	47.77136	-47.77136	520	4.85	15.3	0.9
14.76	48.42756	-48.42756	580	4.55	10.6	
14.96	49.08376	-49.08376	500	5.45	16.8	
15.16	49.73996	-49.73996	450	2.75	6.35	1.25
15.36	50.39616	-50.39616	480	3.35	13.5	
15.56	51.05236	-51.05236	580	2.6	8.75	
15.76	51.70856	-51.70856	440	4.15	13.8	1.05
15.96	52.36476	-52.36476	400	2.12	3.75	
16.16	53.02096	-53.02096	260	2.05	8.2	1.25
16.36	53.67716	-53.67716	340	2.05	3.78	
16.56	54.33336	-54.33336	280	2	2.8	
16.76	54.98956	-54.98956	280	2.02	3.25	1.35
16.96	55.64576	-55.64576	340	13.8	33.2	
17.16	56.30196	-56.30196	600	2.25	5.77	1.4
17.36	56.95816	-56.95816	300	2.17	6.78	
17.56	57.61436	-57.61436	750	2.68	9.9	1.28

APPENDIX B
VESSEL IMPACT TEST DATA

P1T6 Data

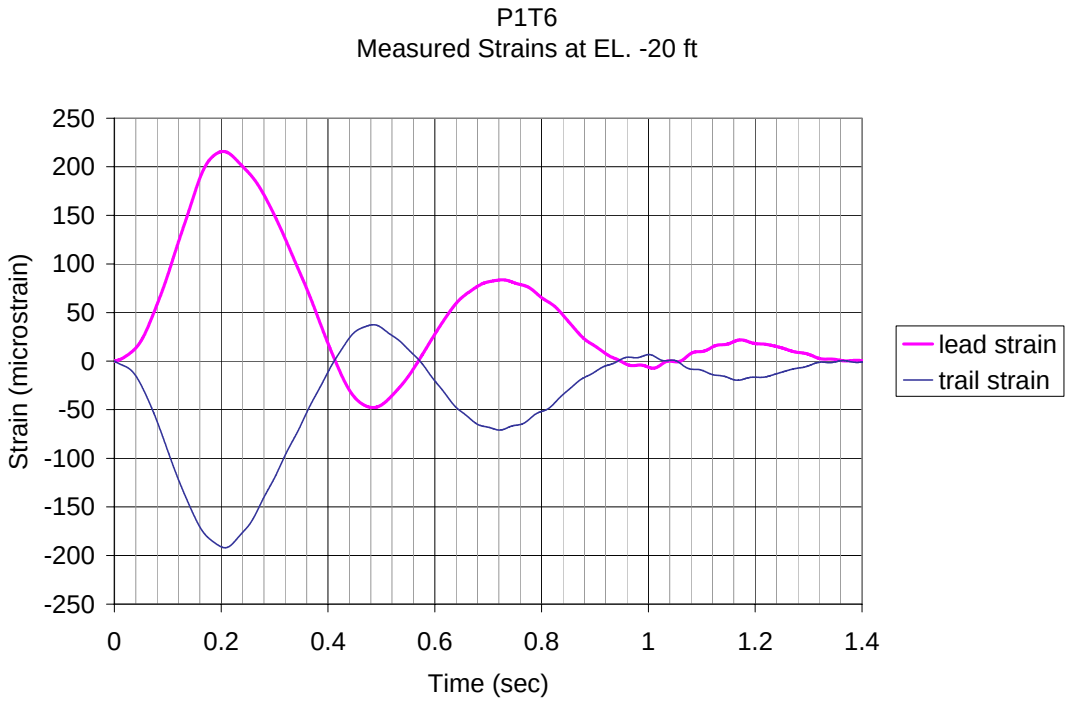

Figure B-1 P1T6 Measured Strains at Elevation -20.0 ft

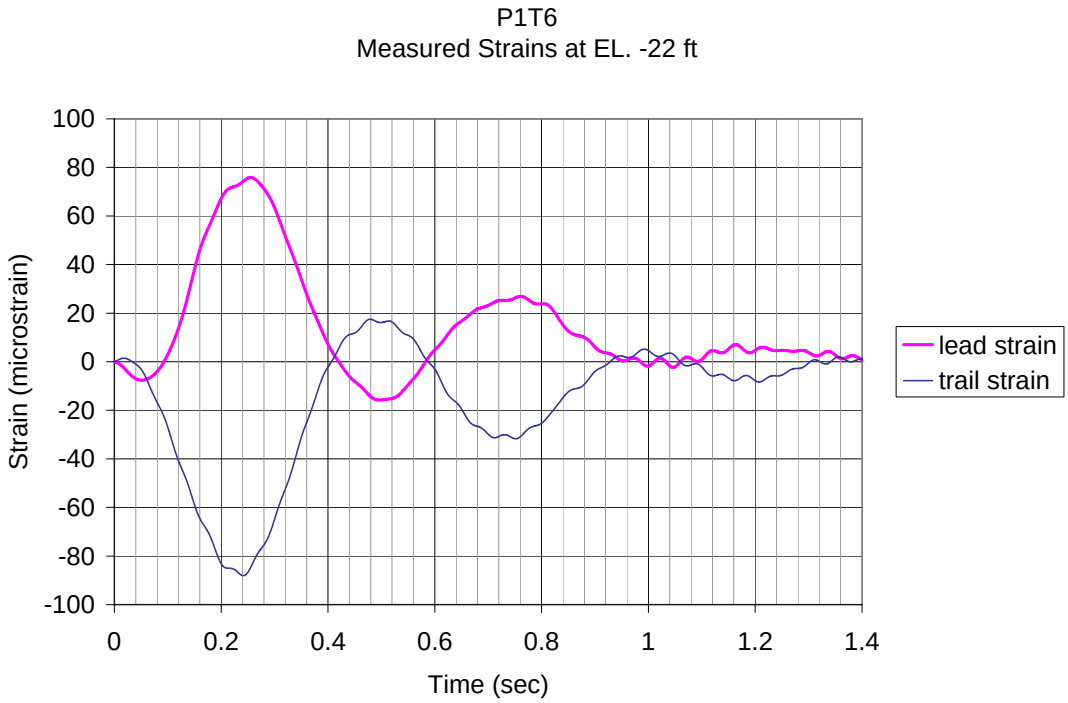

Figure B-2 P1T6 Measured Strains at Elevation -22.0 ft

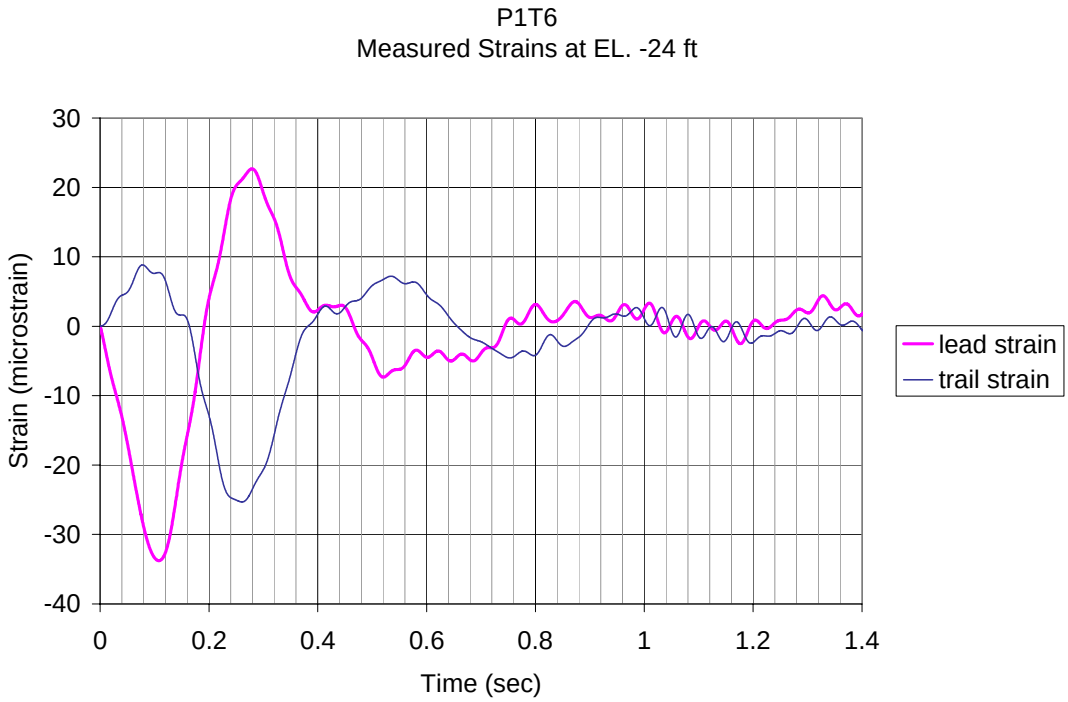

Figure B-3 P1T6 Measured Strains at Elevation -24.0 ft

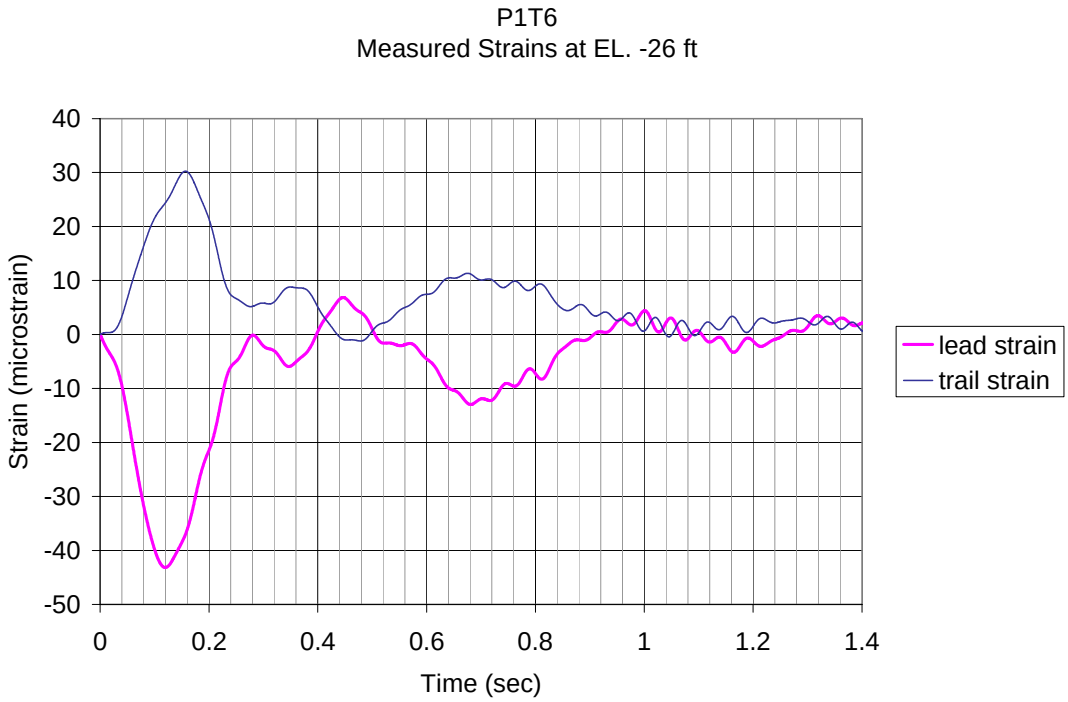

Figure B-4 P1T6 Measured Strains at Elevation -26.0 ft

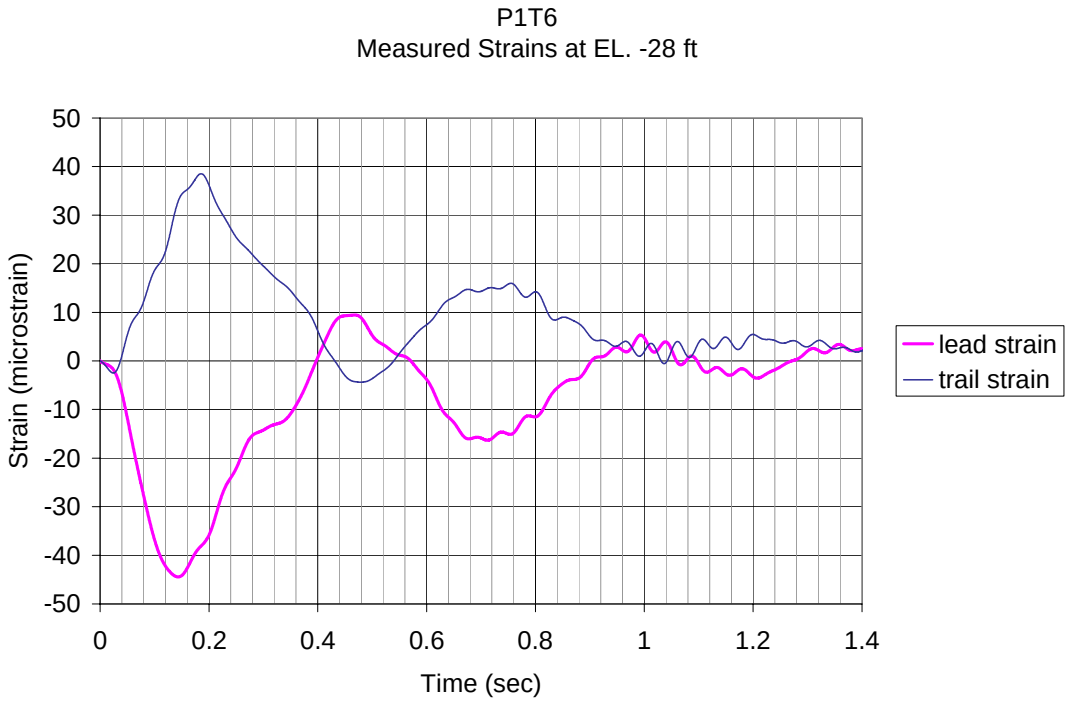

Figure B-5 P1T6 Measured Strains at Elevation -28.0 ft

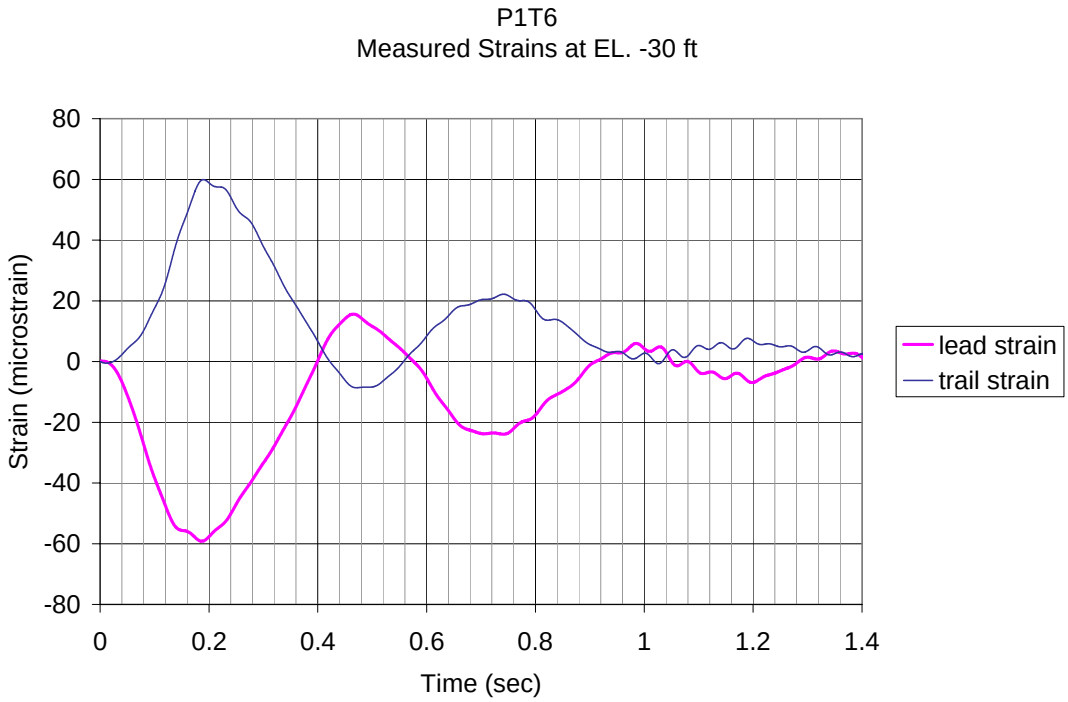

Figure B-6 P1T6 Measured Strains at Elevation -30.0 ft

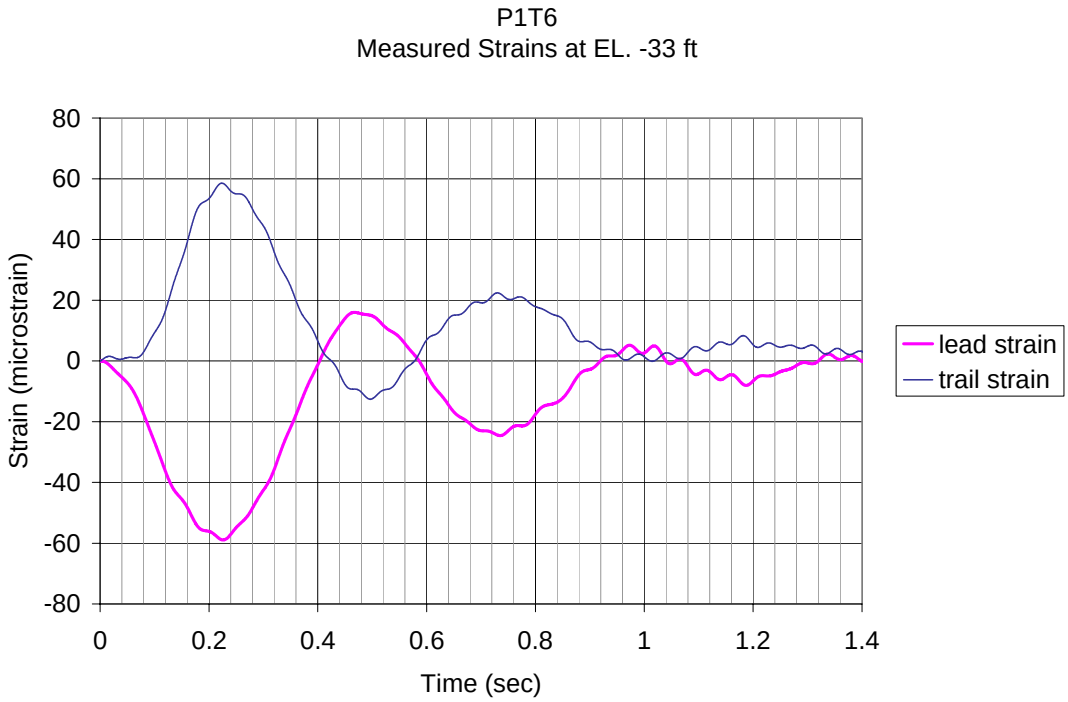

Figure B-7 P1T6 Measured Strains at Elevation -33.0 ft

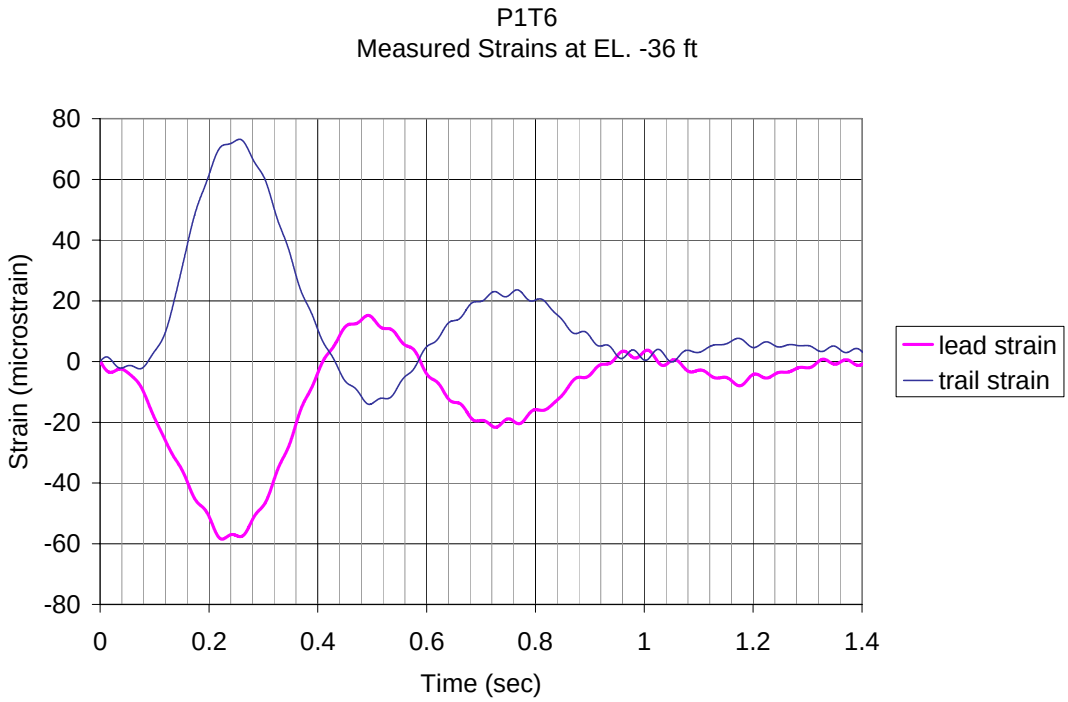

Figure B-8 P1T6 Measured Strains at Elevation -36.0 ft

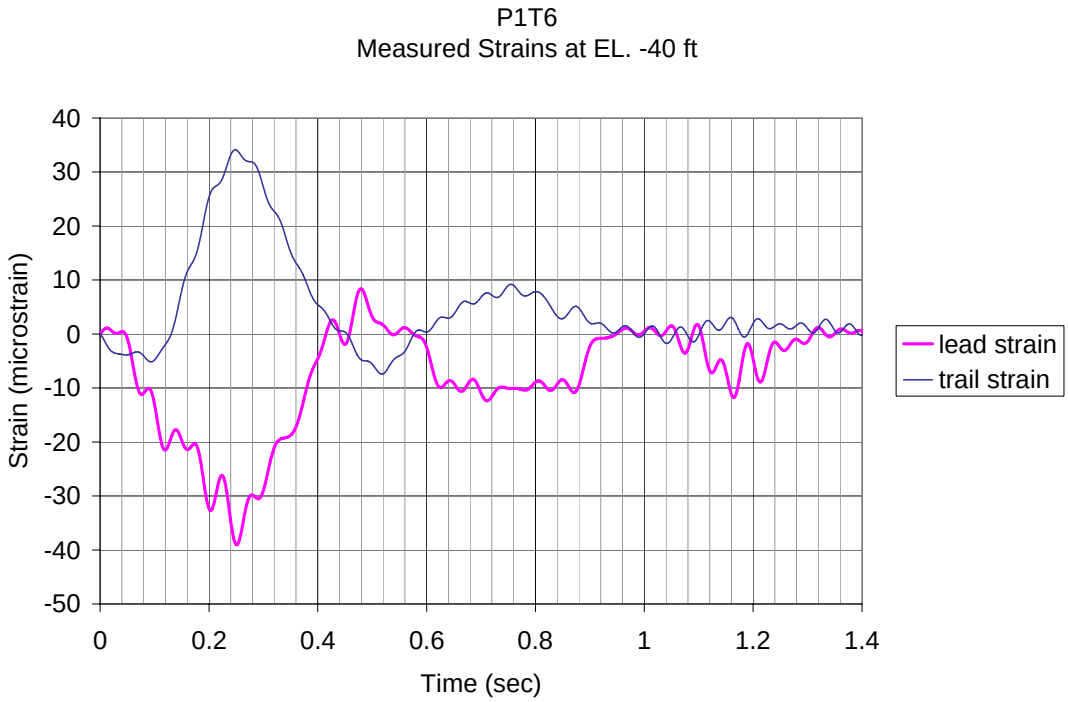

Figure B-9 P1T6 Measured Strains at Elevation -40.0 ft

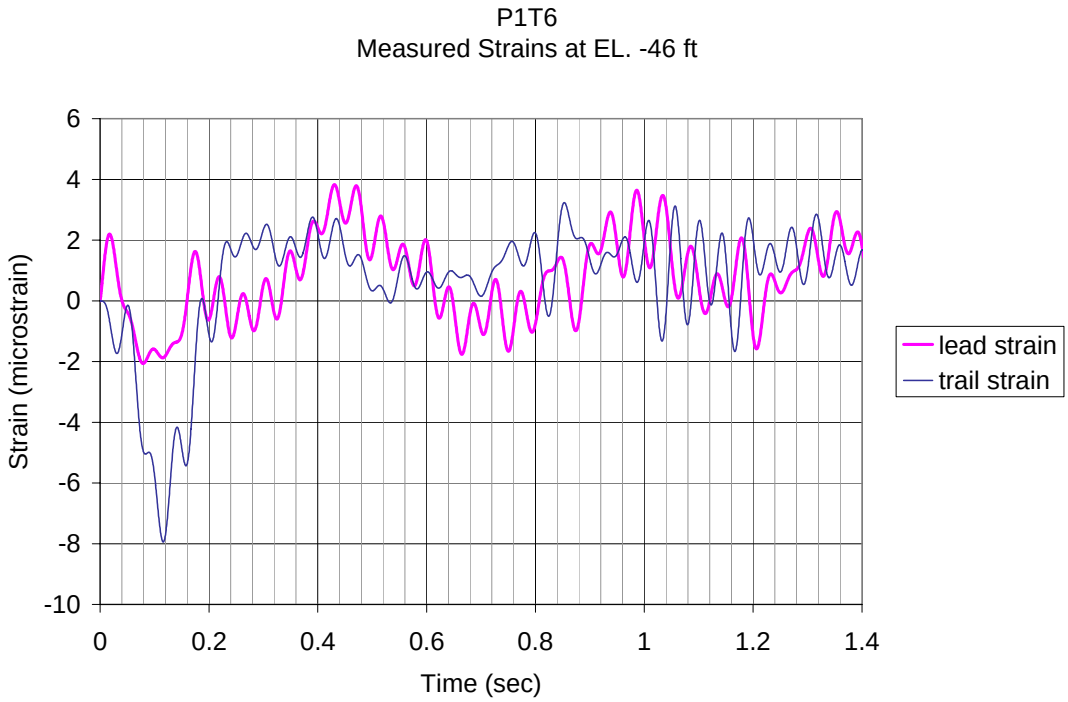

Figure B-10 P1T6 Measured Strains at Elevation -46.0 ft

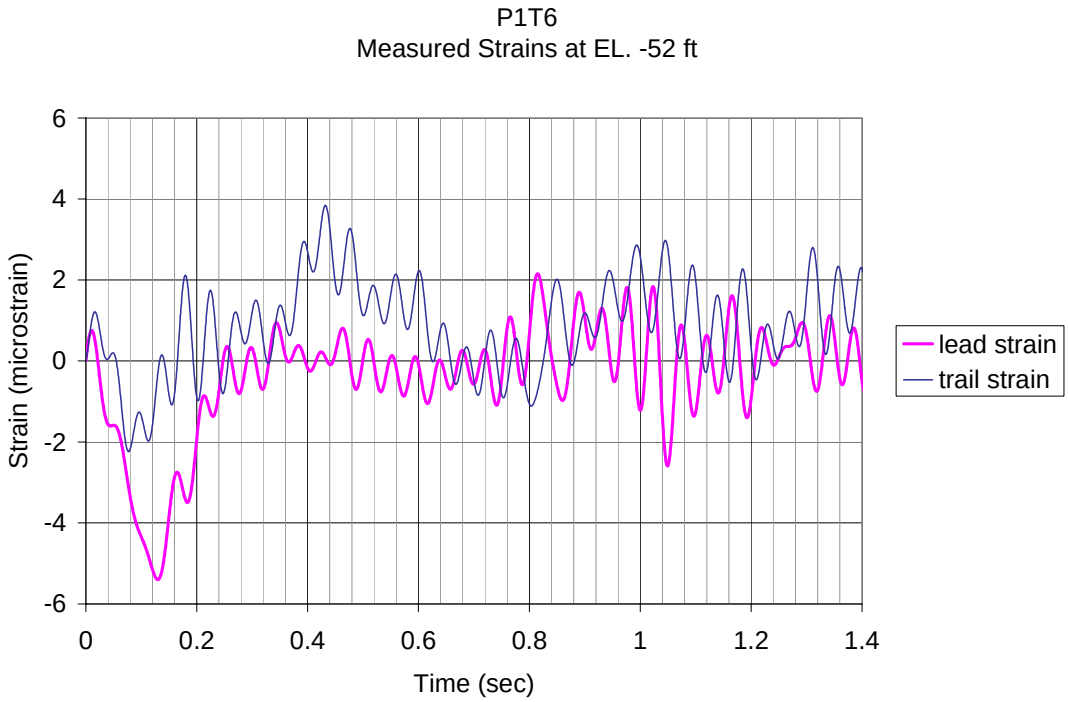

Figure B-11 P1T6 Measured Strains at Elevation -52.0 ft

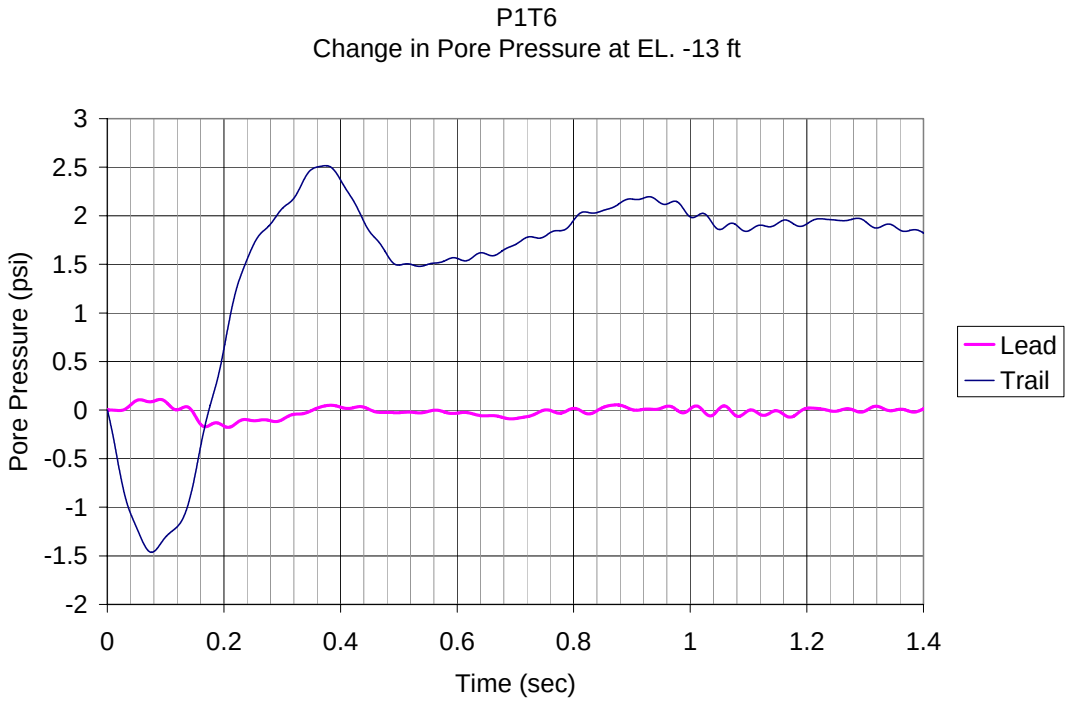

Figure B-12 P1T6 Change in Pore Pressure at Elevation -13.0 ft

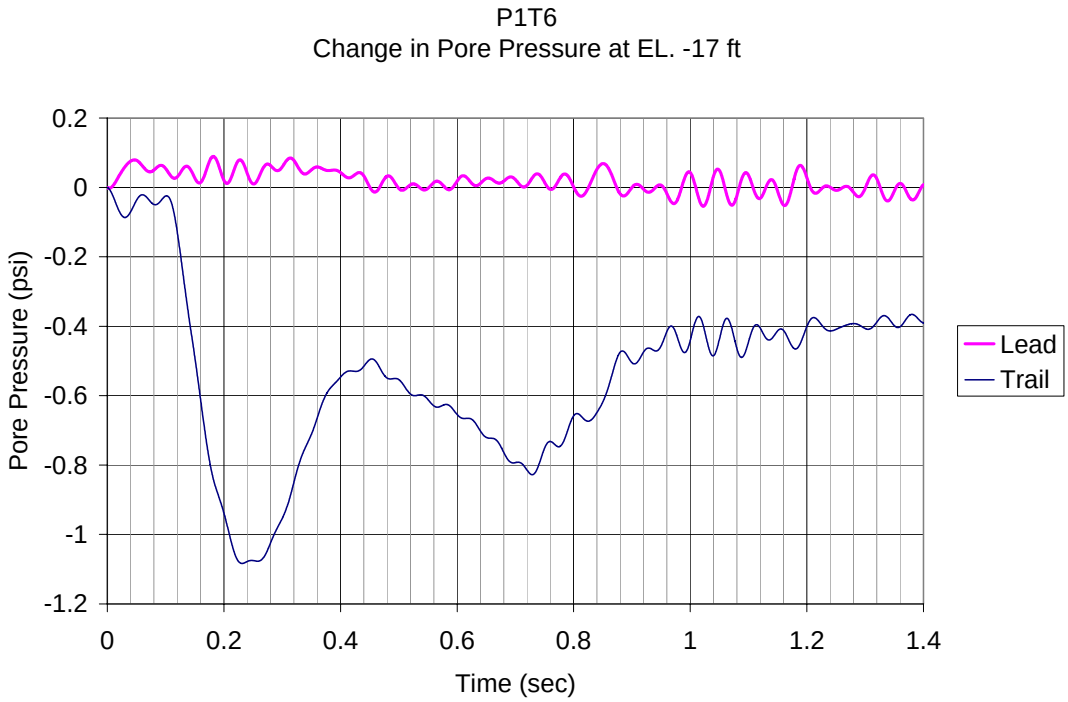

Figure B-13 P1T6 Change in Pore Pressure at Elevation -17.0 ft

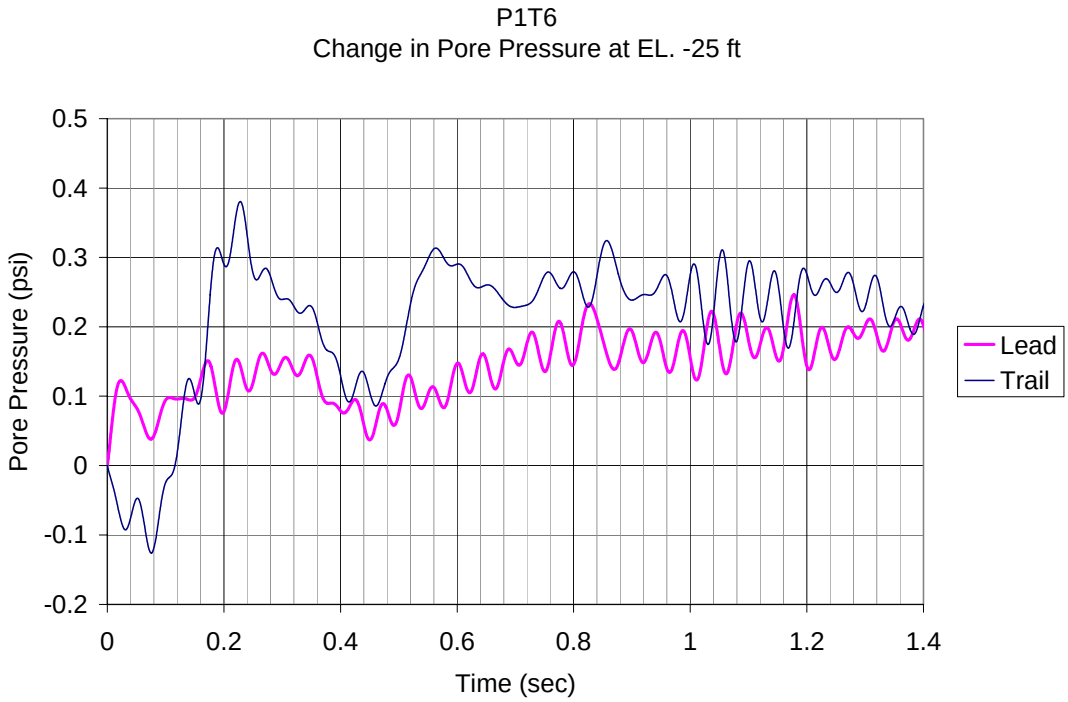

Figure B-14 P1T6 Change in Pore Pressure at Elevation -25.0 ft

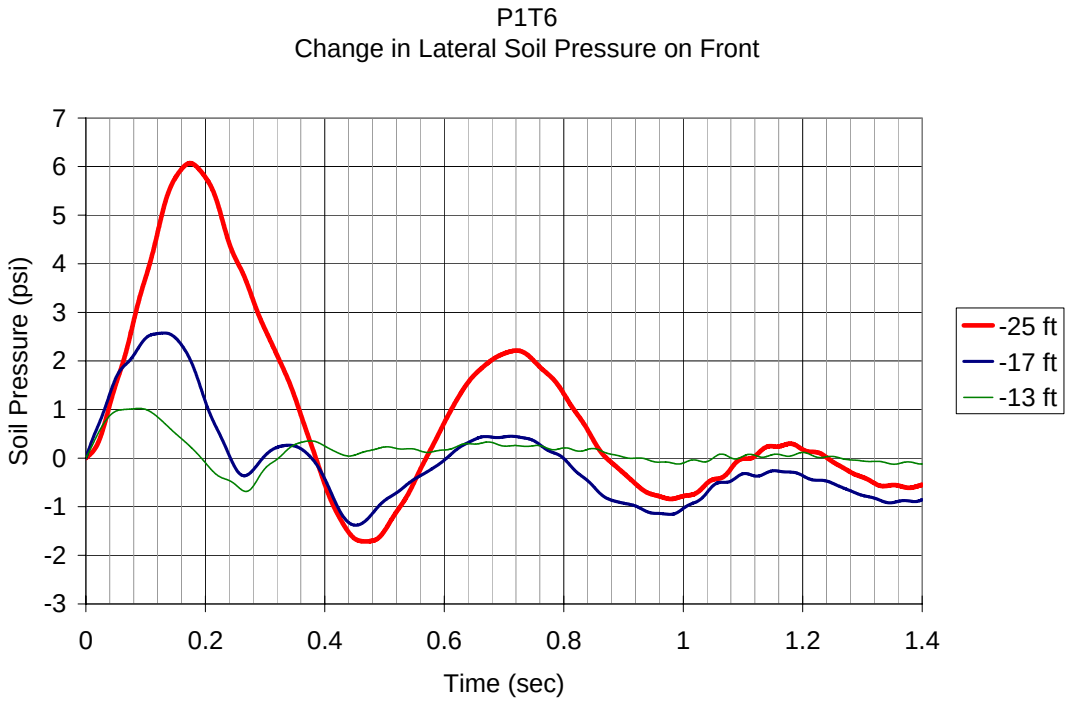

Figure B-15 P1T6 Change in Lateral Soil Pressure on Front

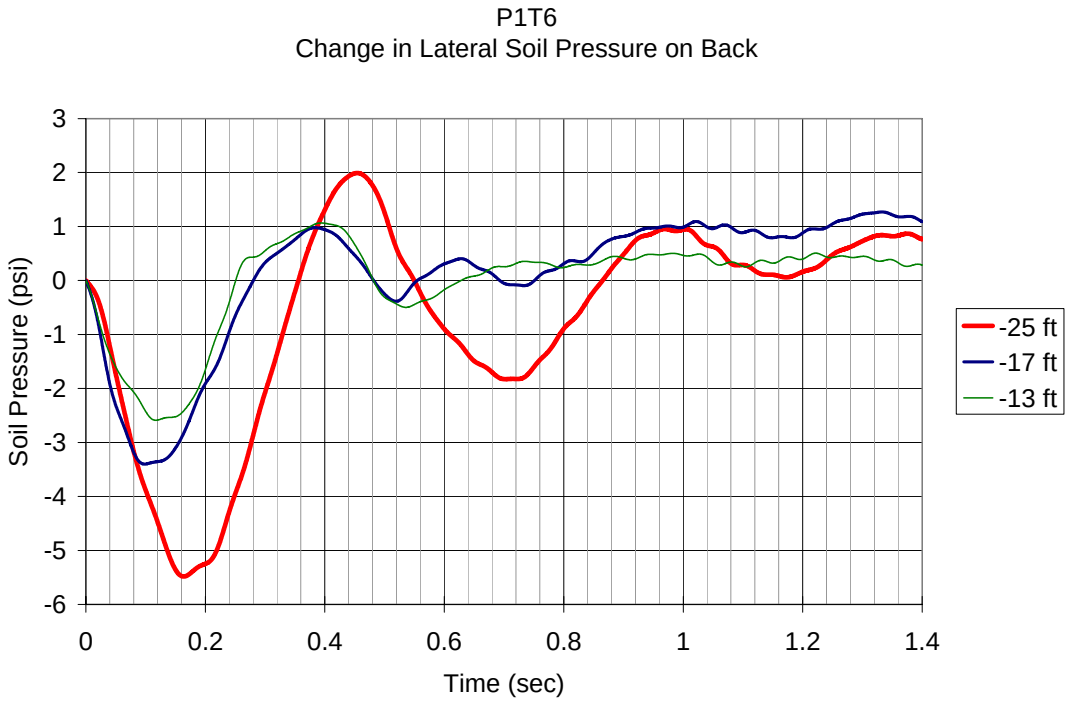

Figure B-16 P1T6 Change in Lateral Soil Pressure on Back

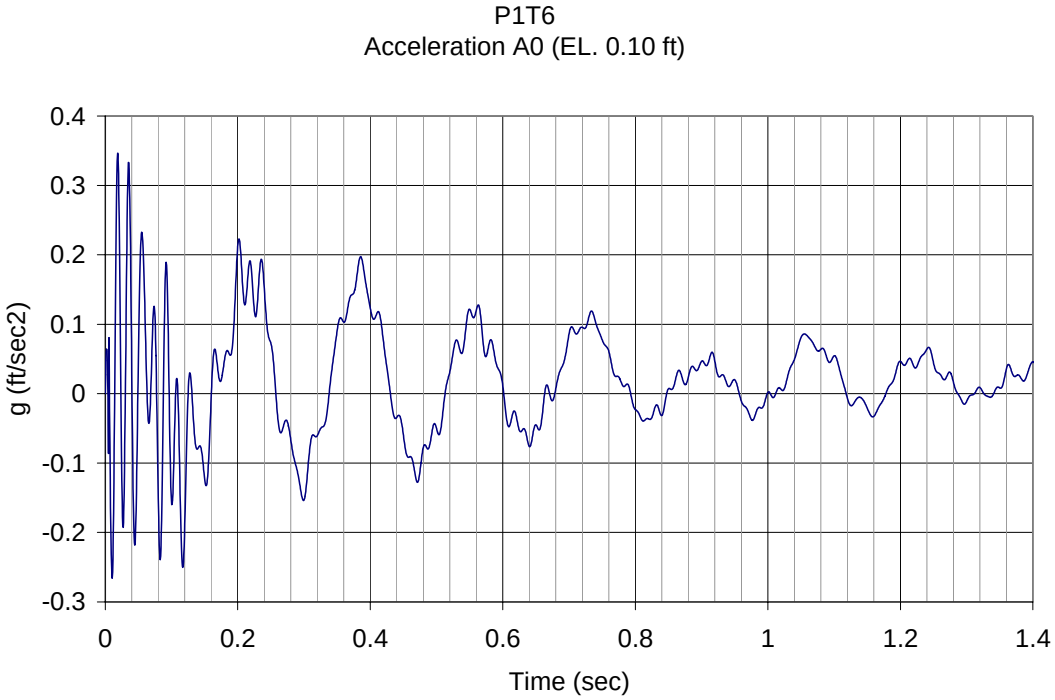

Figure B-17 P1T6 Acceleration Record for Accelerometer A0

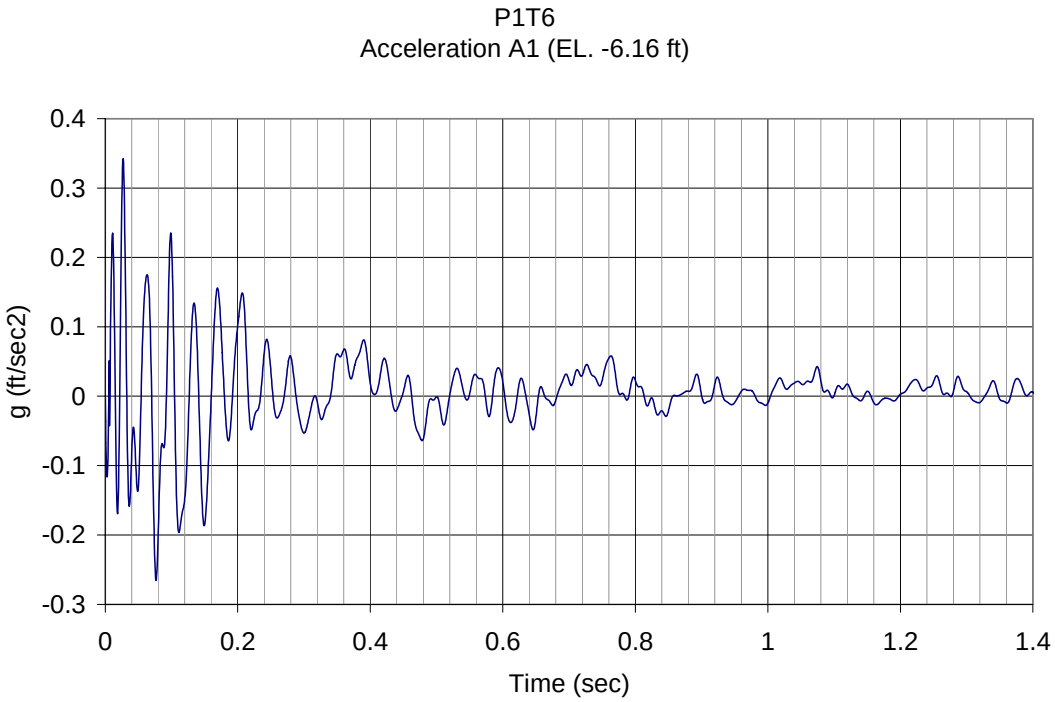

Figure B-18 P1T6 Acceleration Record for Accelerometer A1

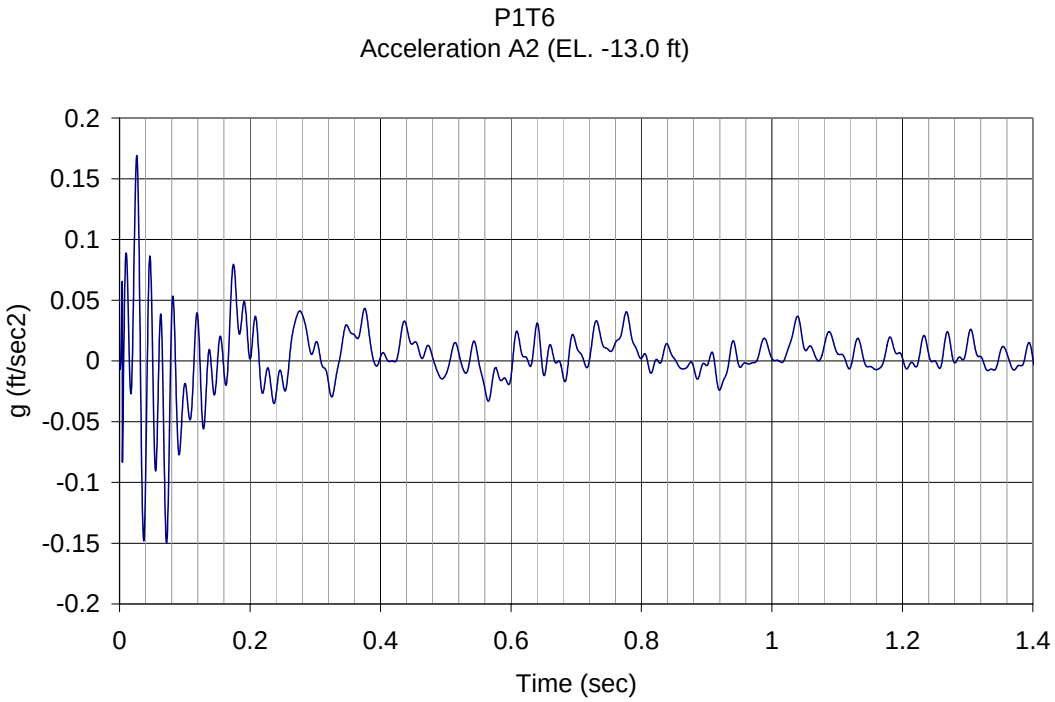

Figure B-19 P1T6 Acceleration Record for Accelerometer A2

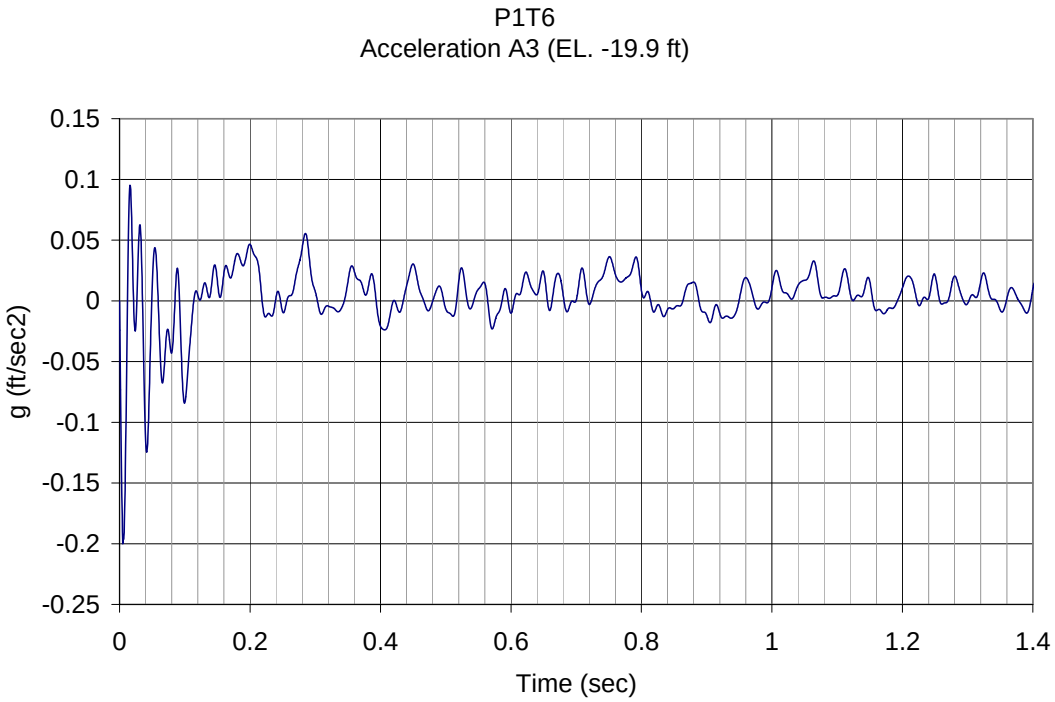

Figure B-20 P1T6 Acceleration Record for Accelerometer A3

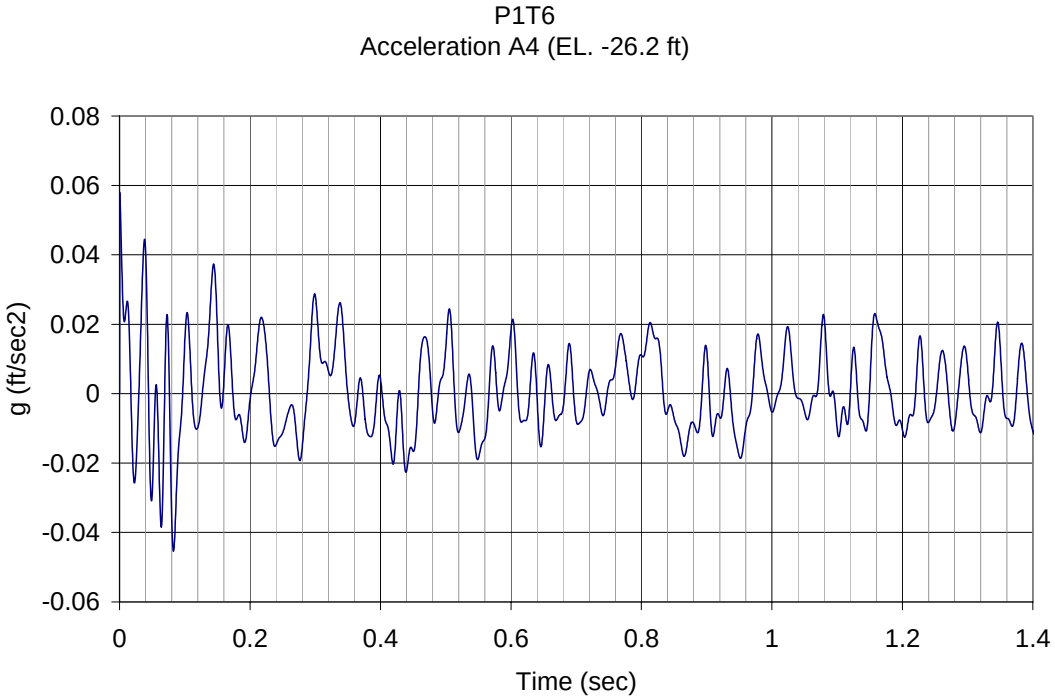

Figure B-21 P1T6 Acceleration Record for Accelerometer A4

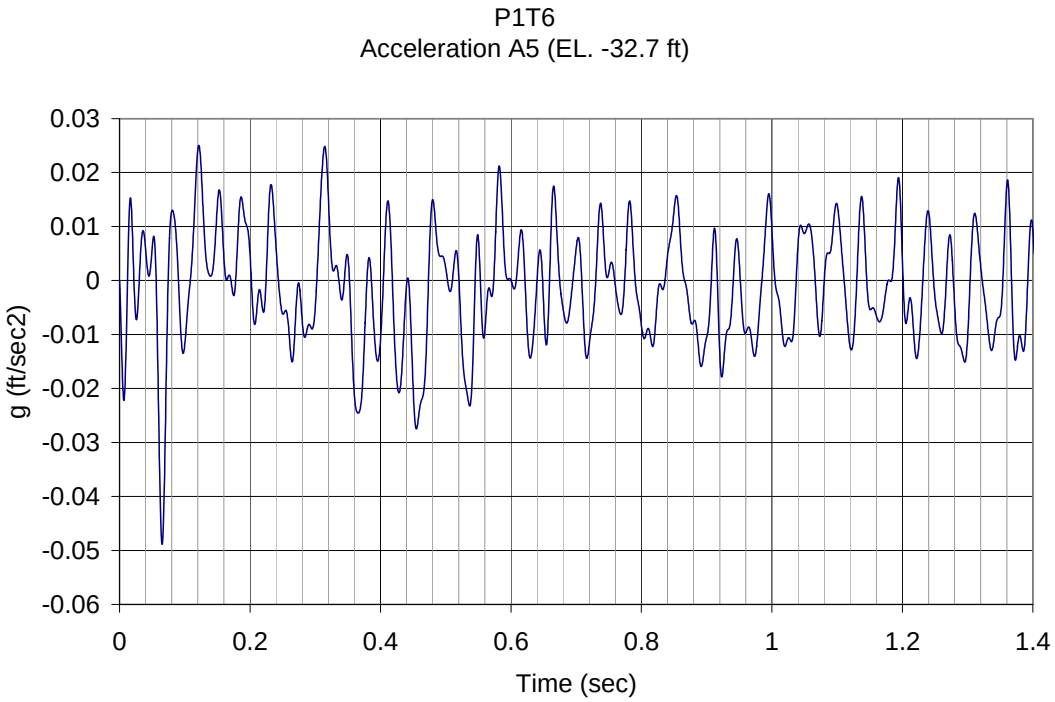

Figure B-22 P1T6 Acceleration Record for Accelerometer A5

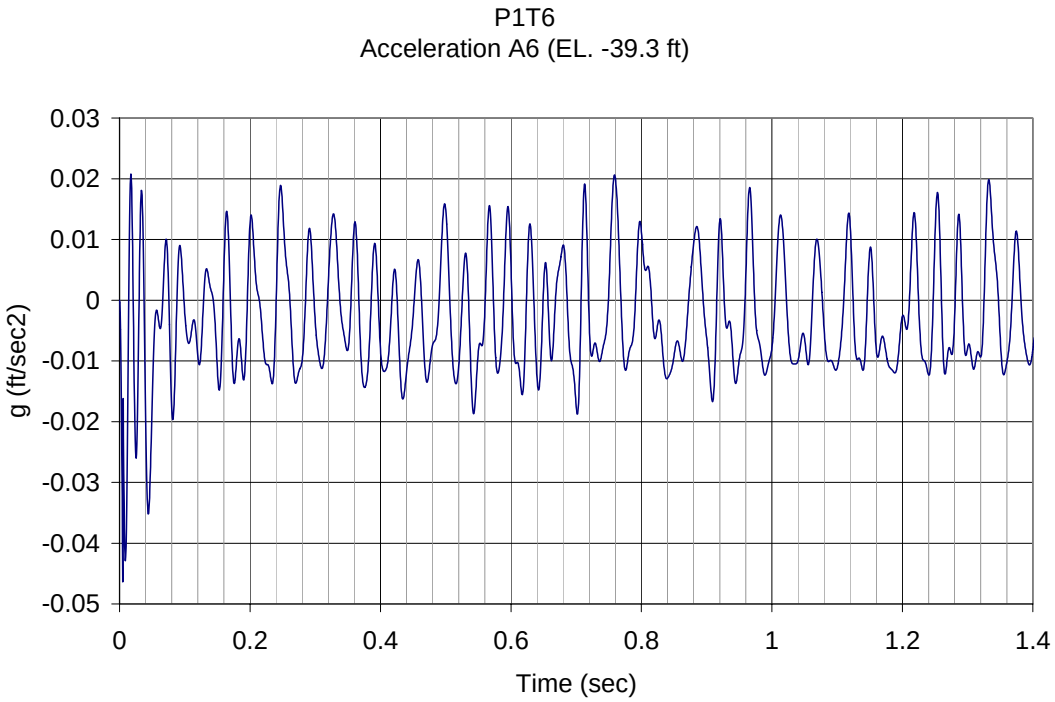

Figure B-23 P1T6 Acceleration Record for Accelerometer A6

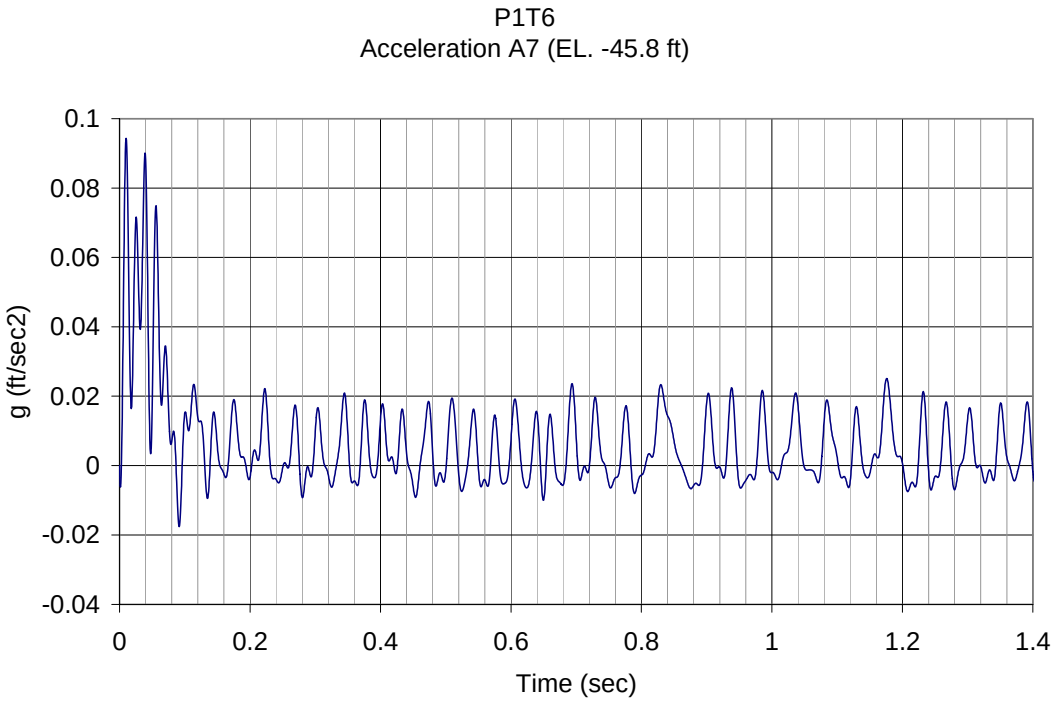

Figure B-24 P1T6 Acceleration Record for Accelerometer A7

P1T7 Data

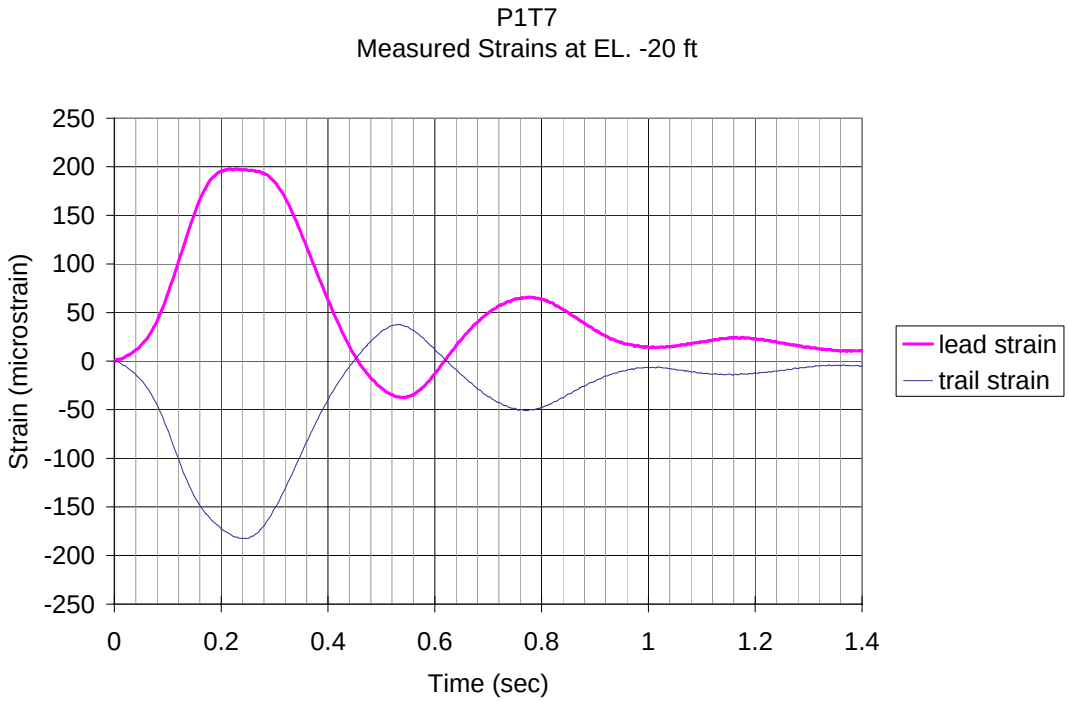

Figure B-25 P1T7 Measured Strains at Elevation -20.0 ft

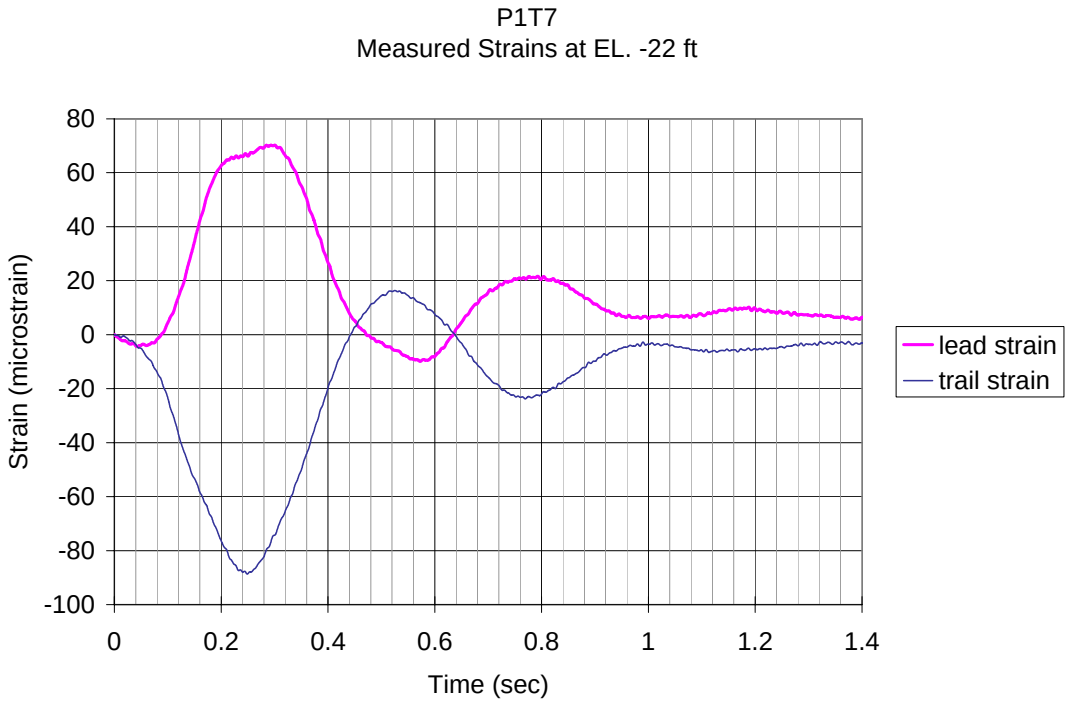

Figure B-26 P1T7 Measured Strains at Elevation -22.0 ft

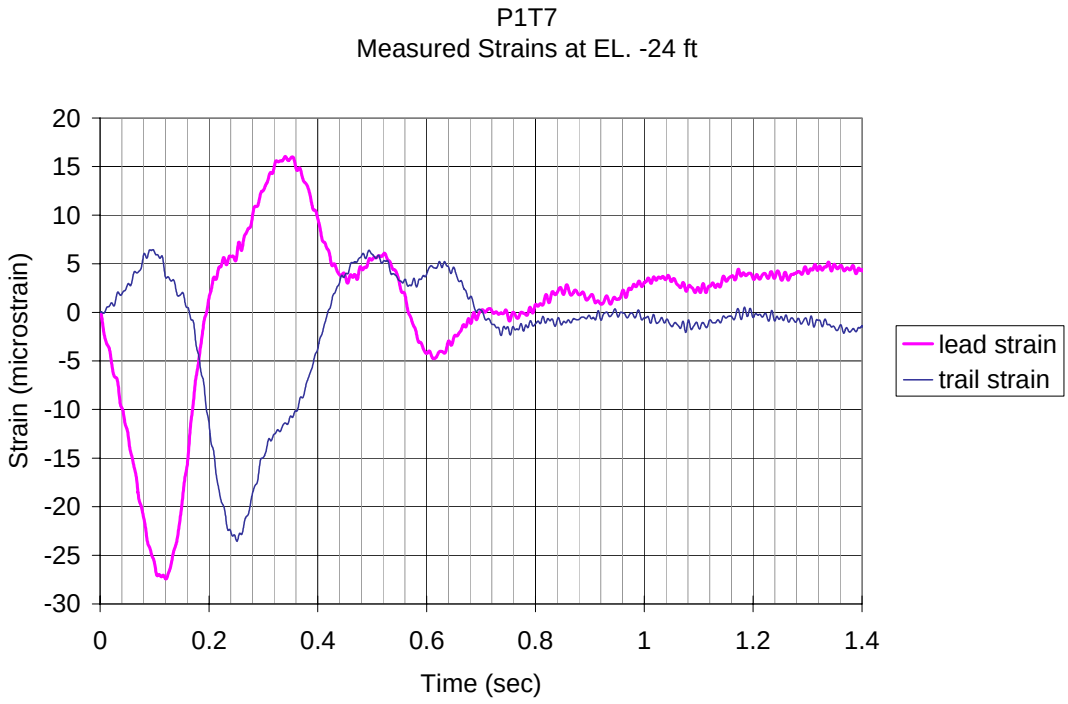

Figure B-27 P1T7 Measured Strains at Elevation -24.0 ft

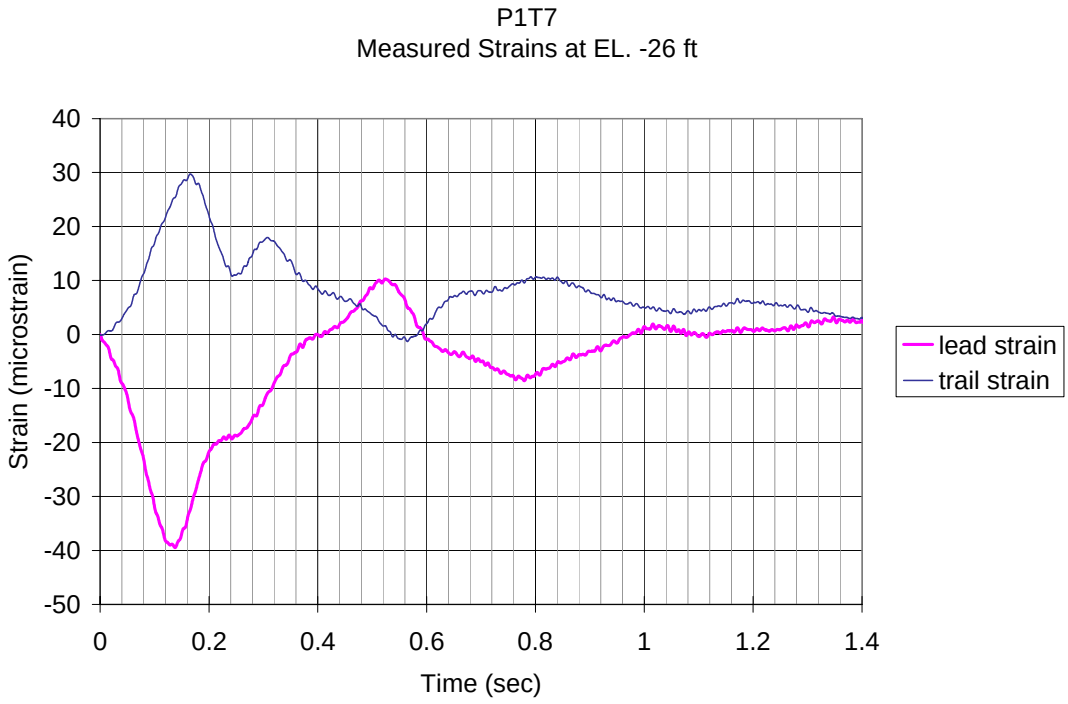

Figure B-28 P1T7 Measured Strains at Elevation -26.0 ft

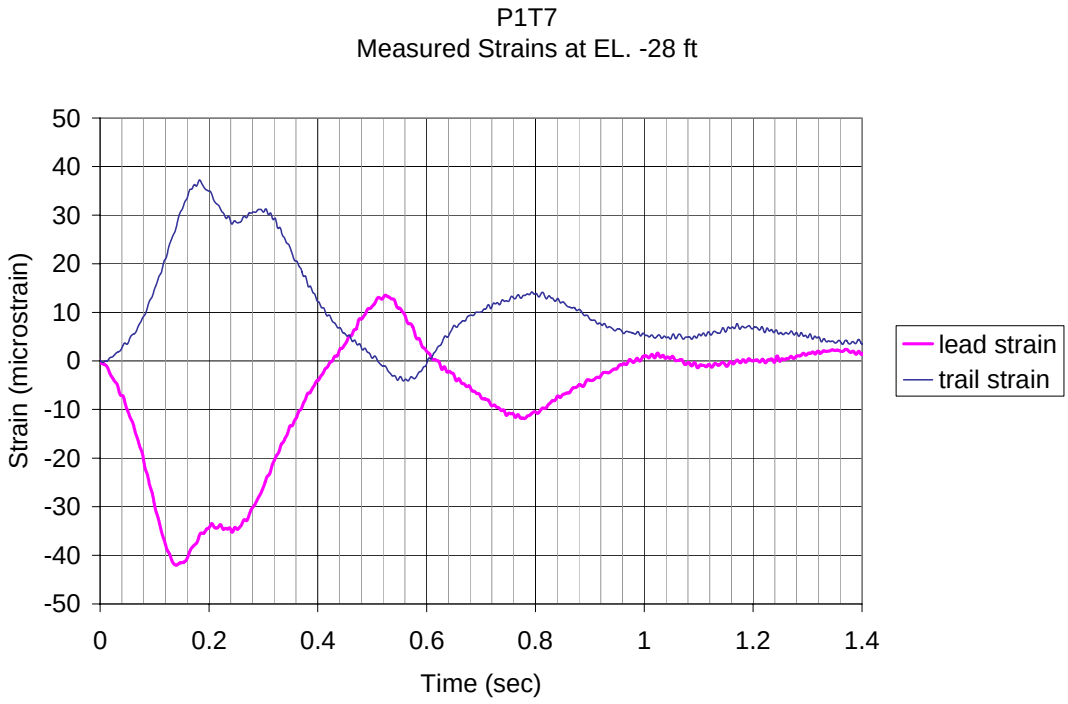

Figure B-29 P1T7 Measured Strains at Elevation -28.0 ft

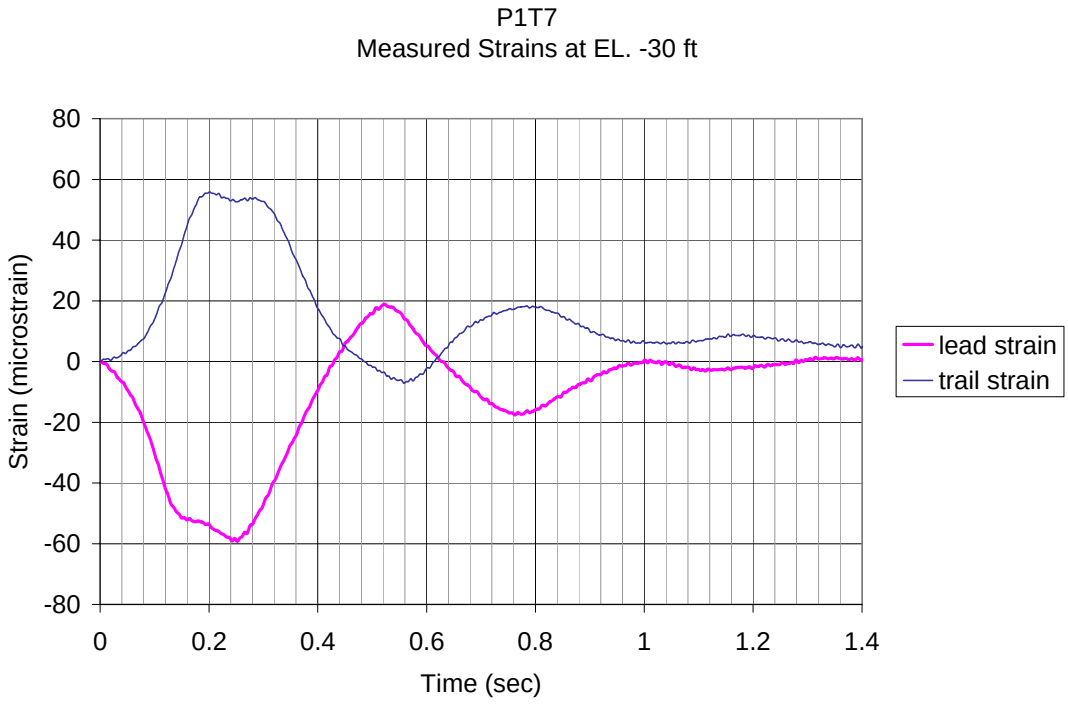

Figure B-30 P1T7 Measured Strains at Elevation -30.0 ft

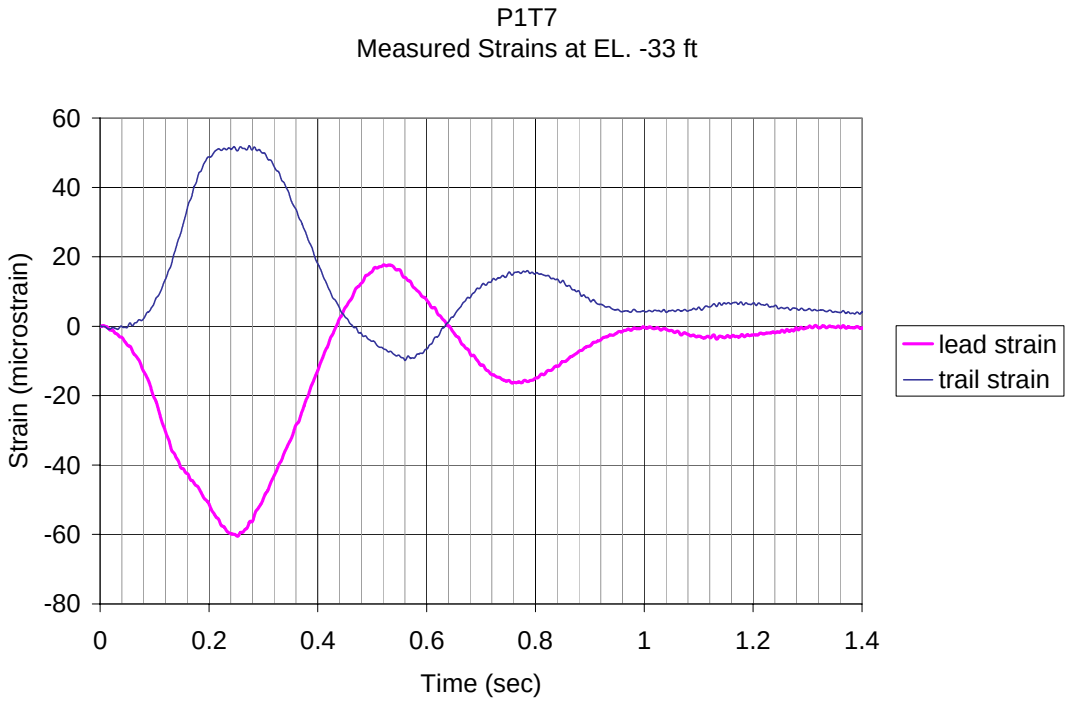

Figure B-31 P1T7 Measured Strains at Elevation -33.0 ft

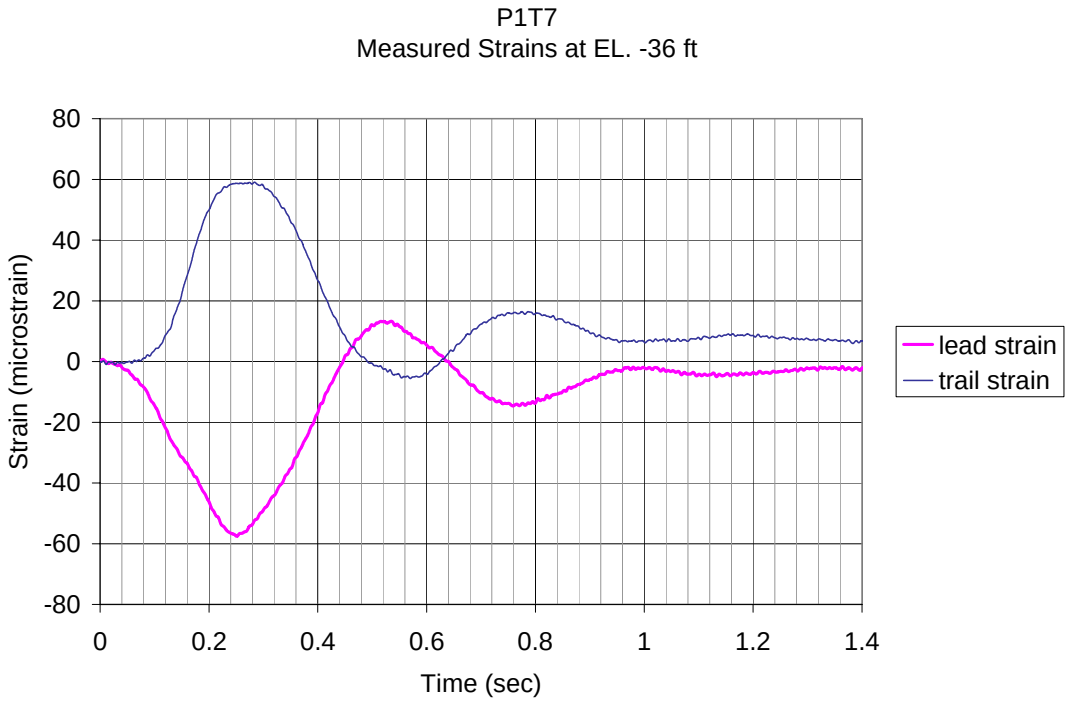

Figure B-32 P1T7 Measured Strains at Elevation -36.0 ft

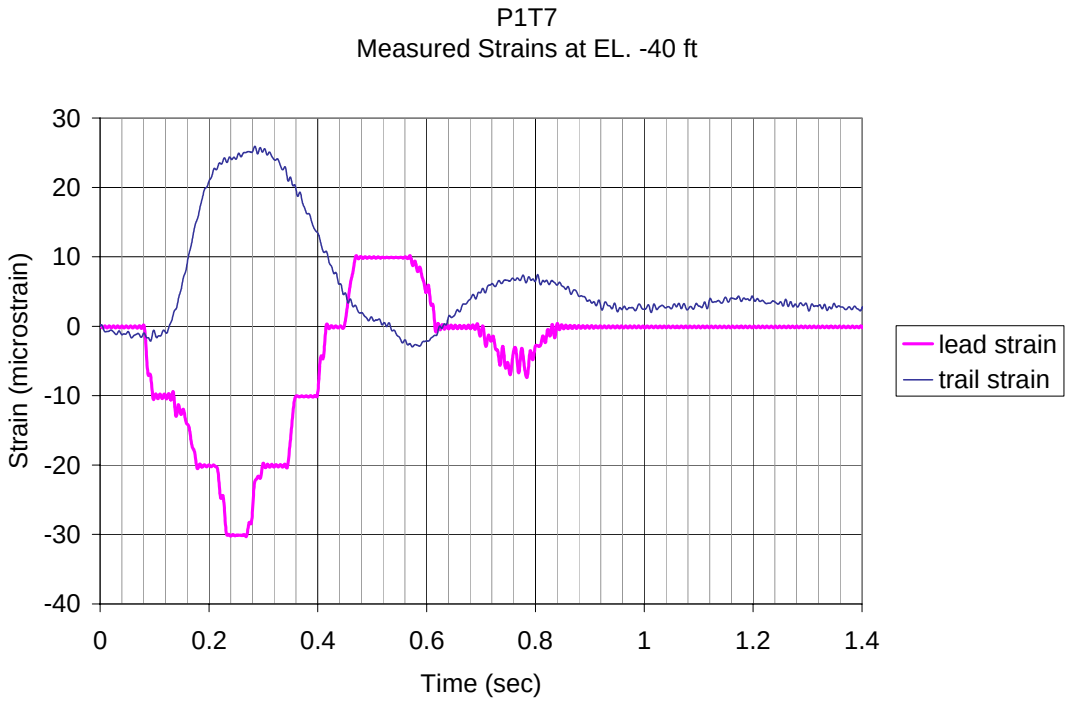

Figure B-33 P1T7 Measured Strains at Elevation -40.0 ft

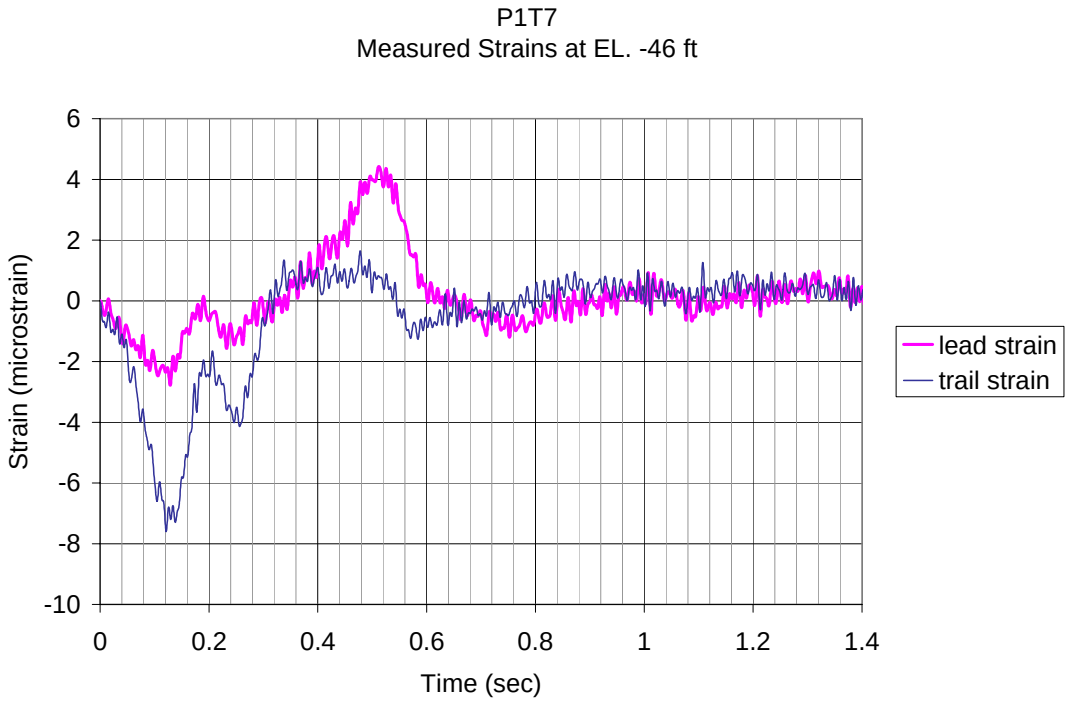

Figure B-34 P1T7 Measured Strains at Elevation -46.0 ft

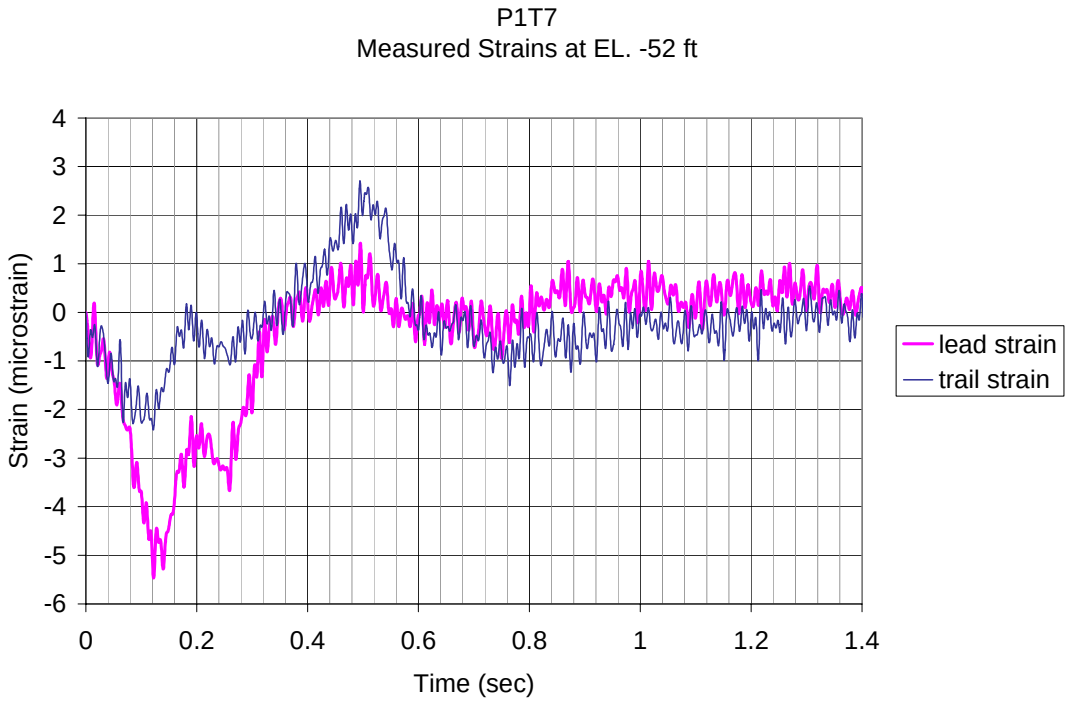

Figure B-35 P1T7 Measured Strains at Elevation -52.0 ft

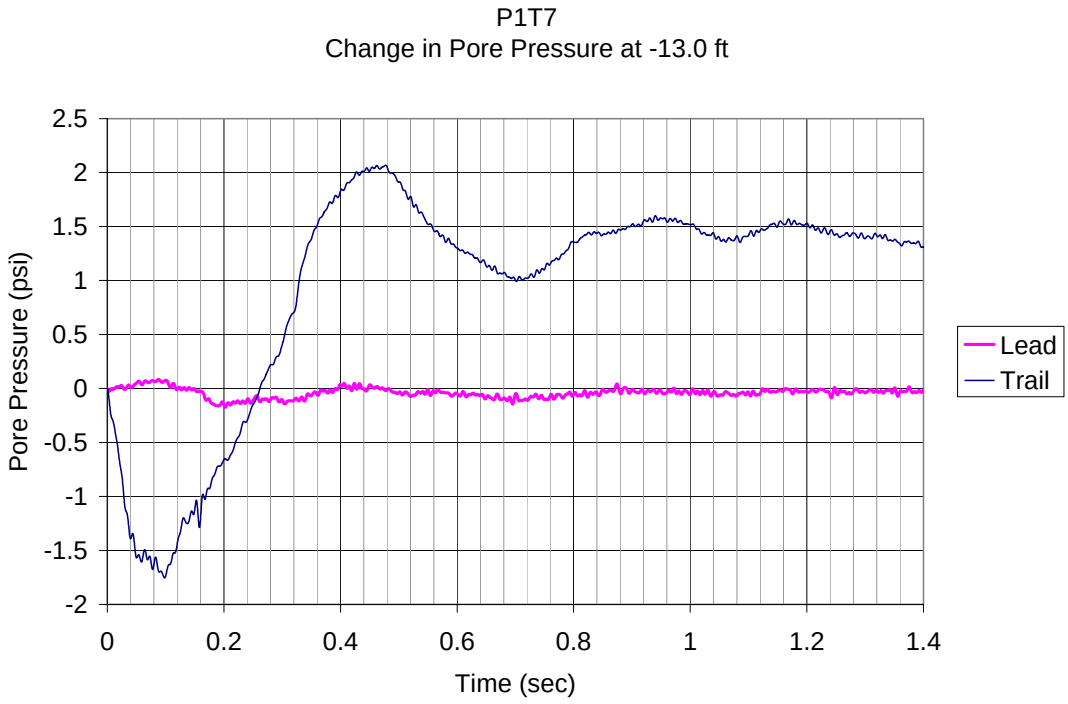

Figure B-36 P1T7 Change in Pore Pressure at Elevation -13.0 ft

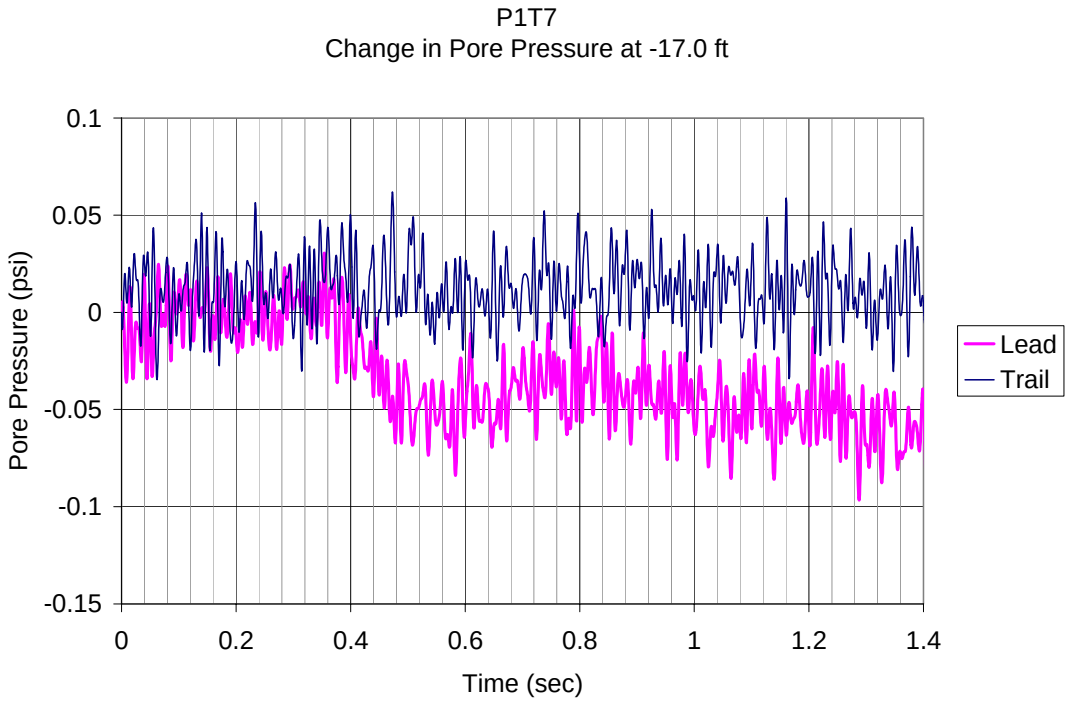

Figure B-37 P1T7 Change in Pore Pressure at Elevation -17.0 ft

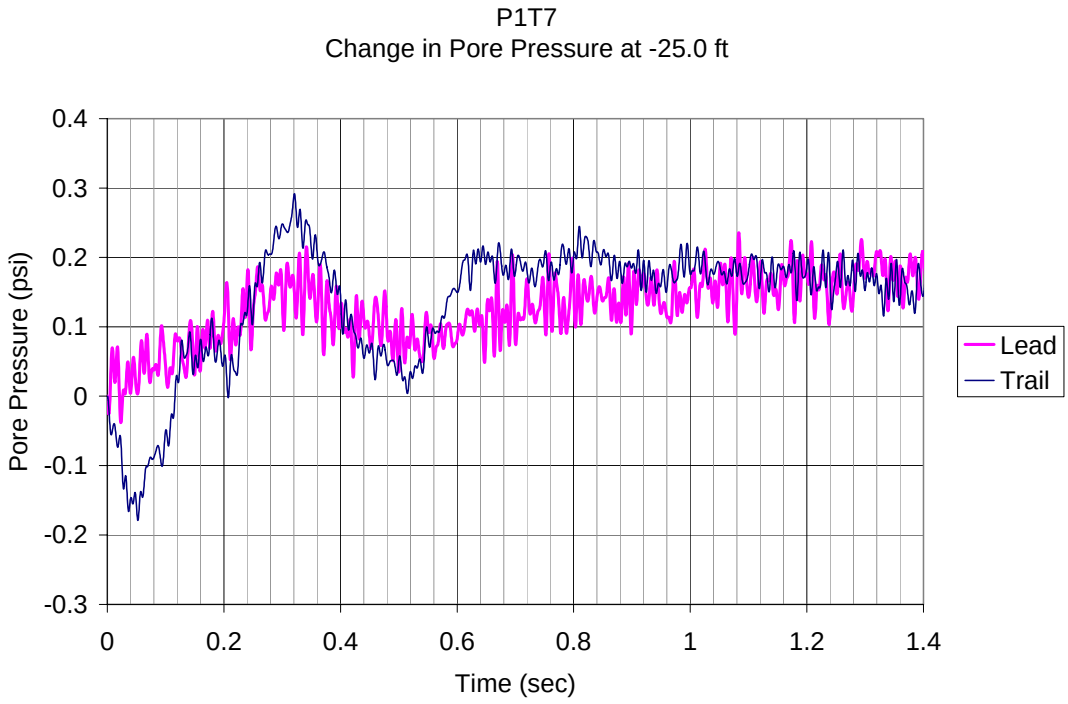

Figure B-38 P1T7 Change in Pore Pressure at Elevation -25.0 ft

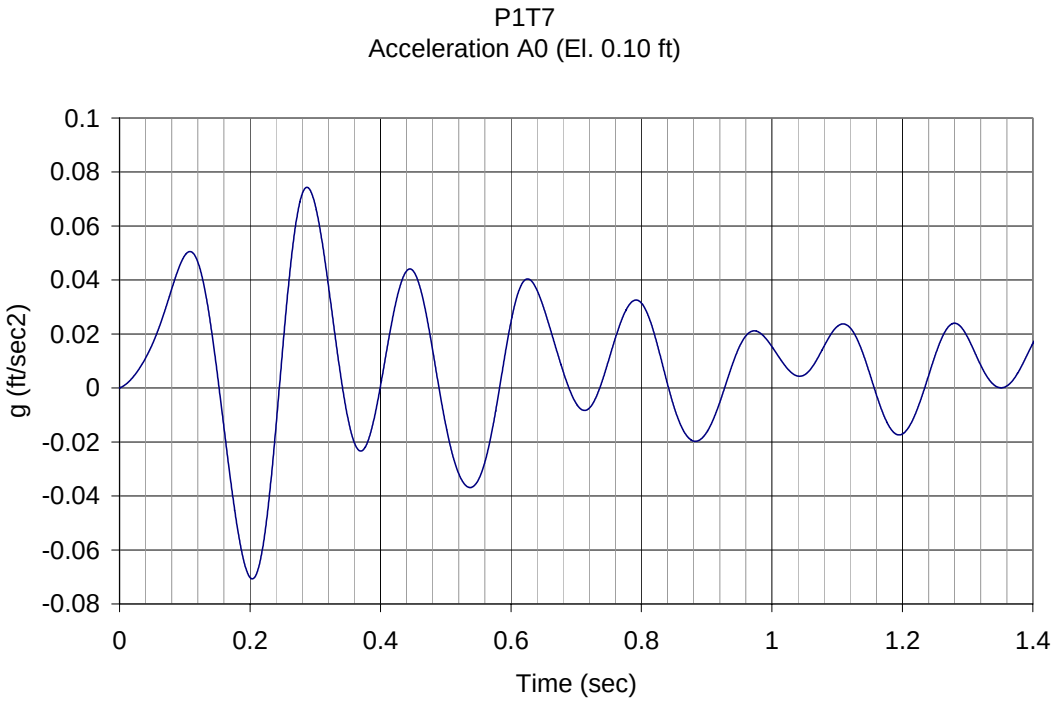

Figure B-39 P1T7 Acceleration Record for Accelerometer A0

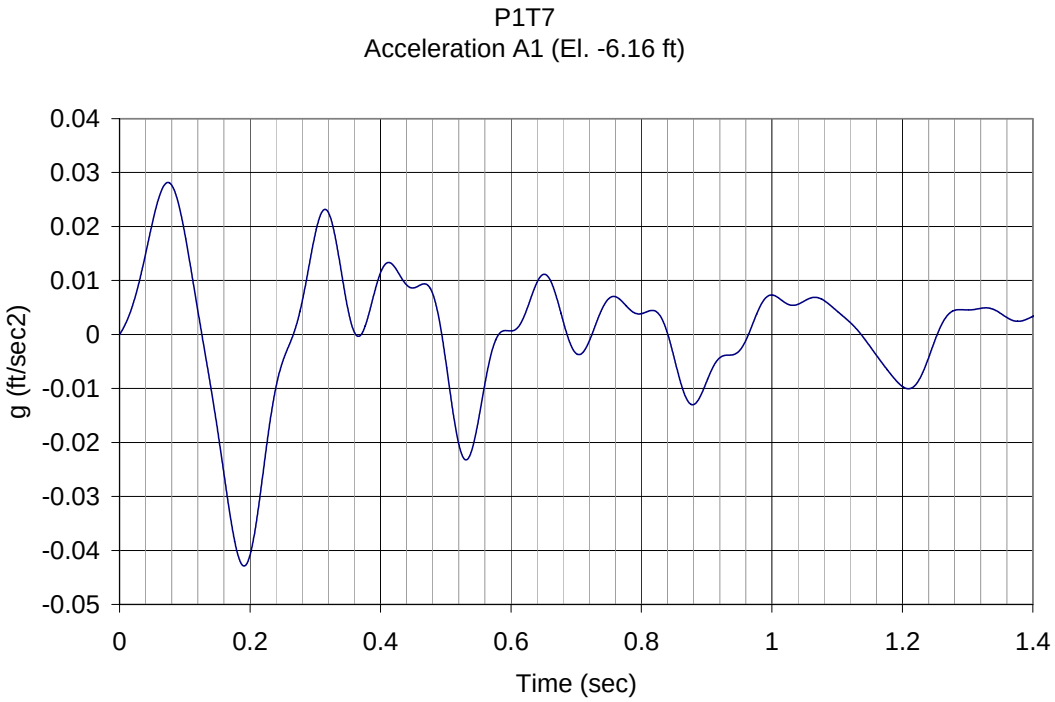

Figure B-40 P1T7 Acceleration Record for Accelerometer A1

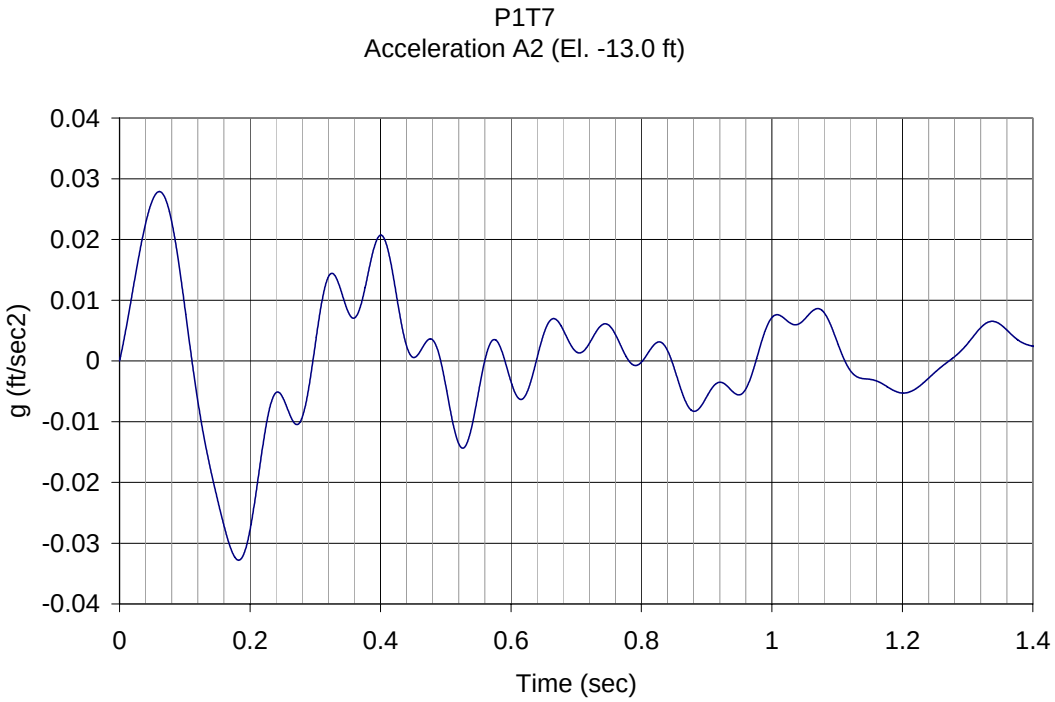

Figure B-41 P1T7 Acceleration Record for Accelerometer A2

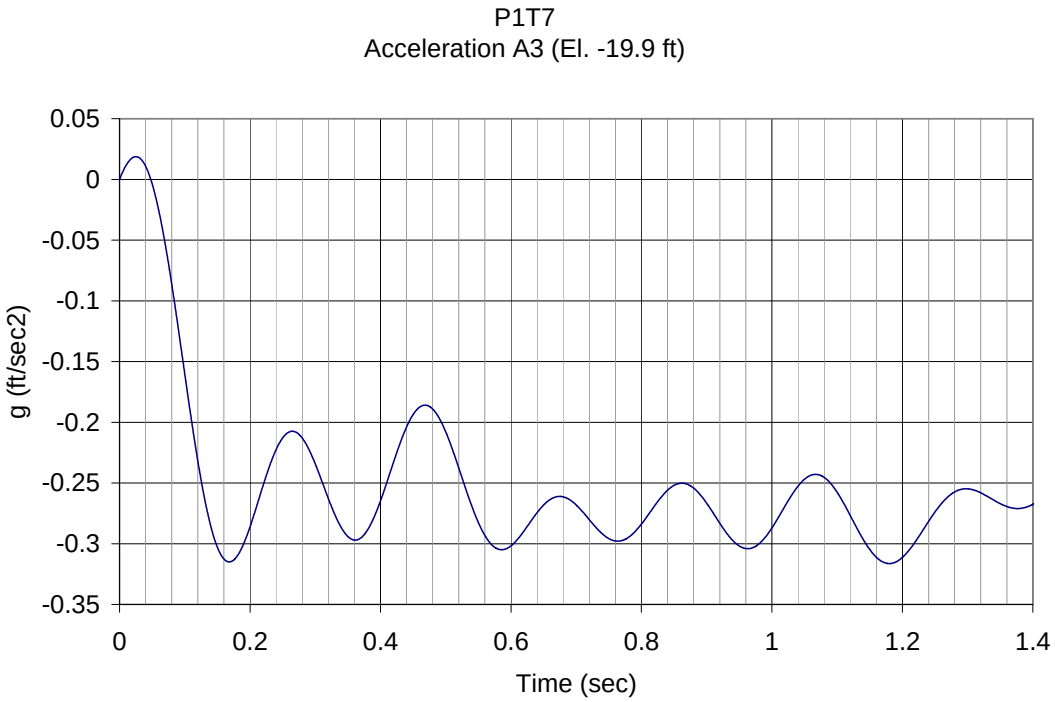

Figure B-42 P1T7 Acceleration Record for Accelerometer A3

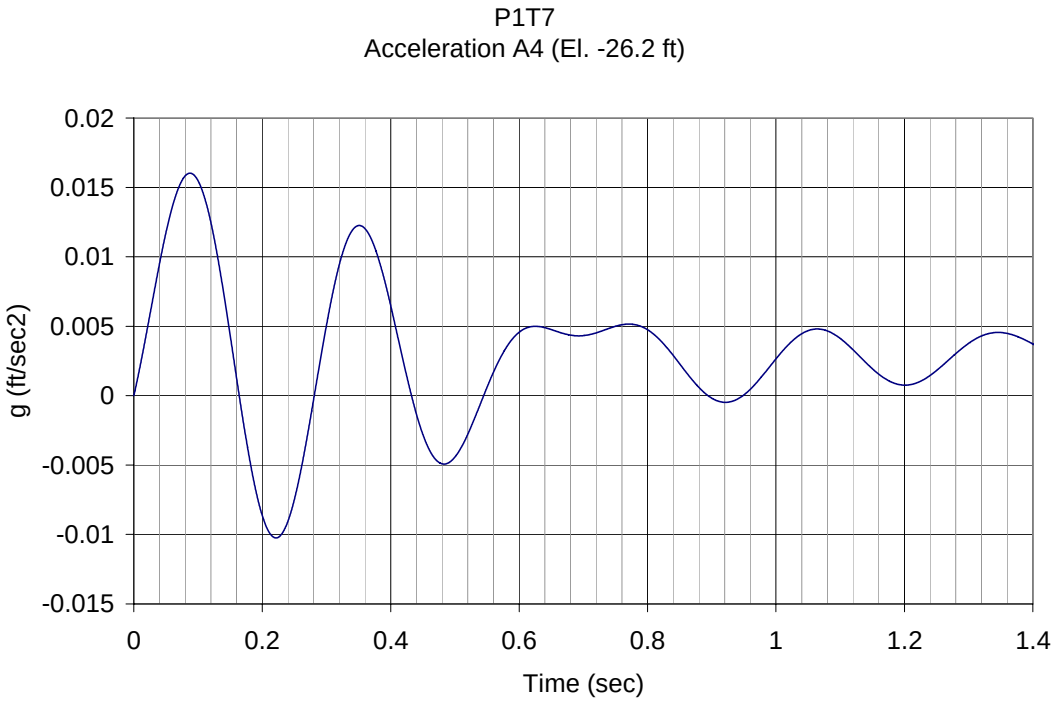

Figure B-43 P1T7 Acceleration Record for Accelerometer A4

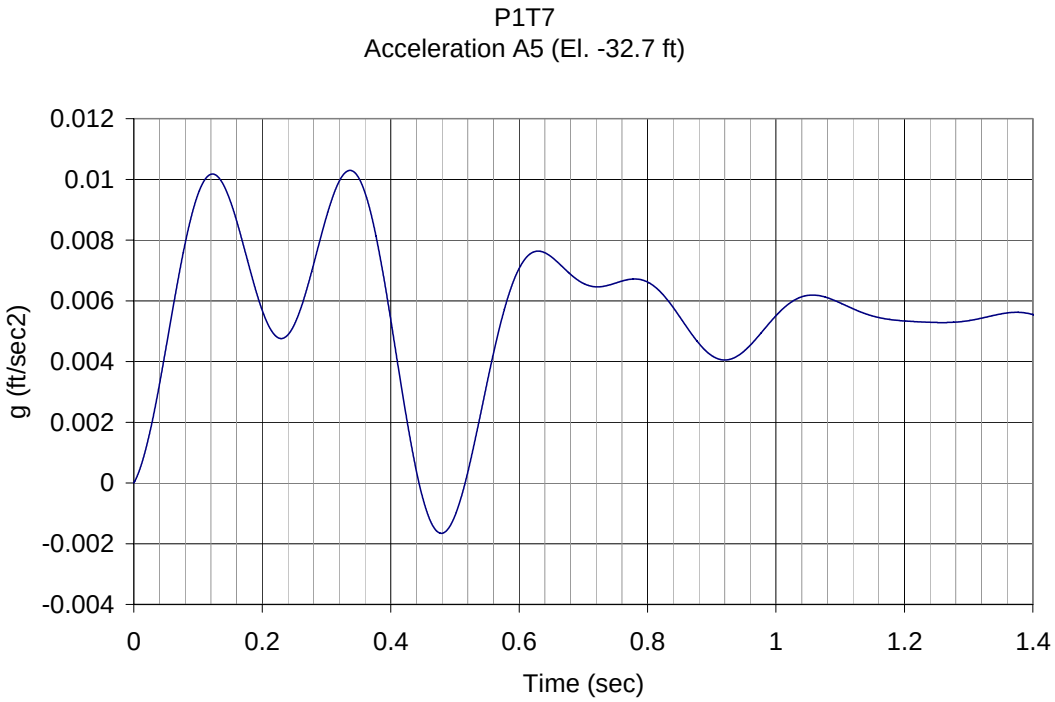

Figure B-44 P1T7 Acceleration Record for Accelerometer A5

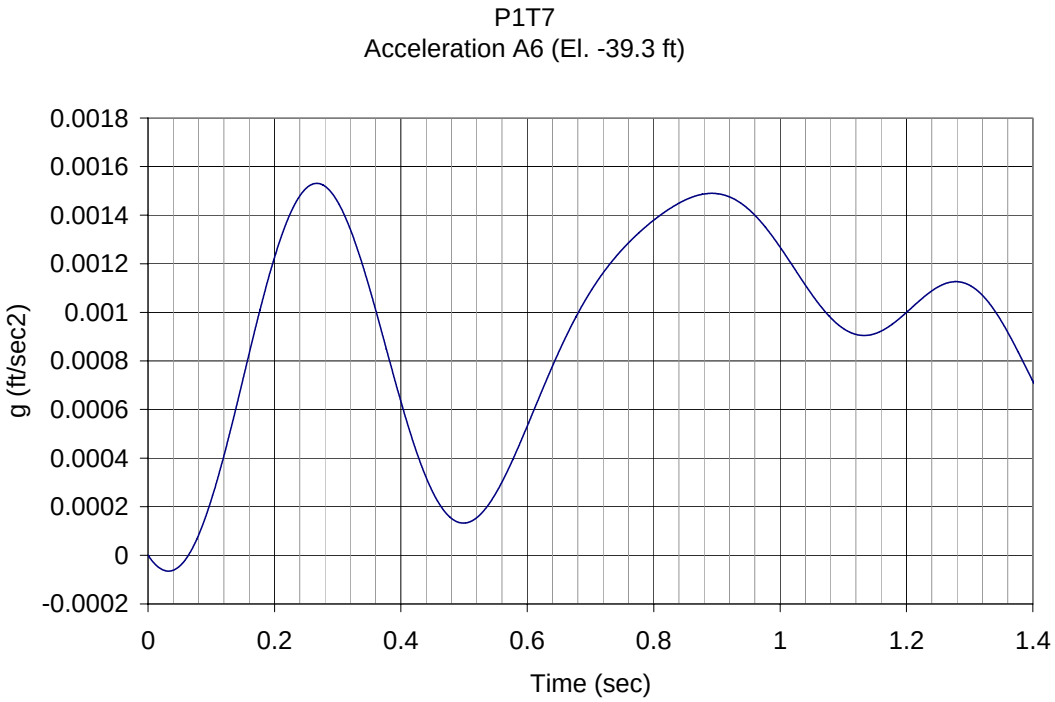

Figure B-45 P1T7 Acceleration Record for Accelerometer A6

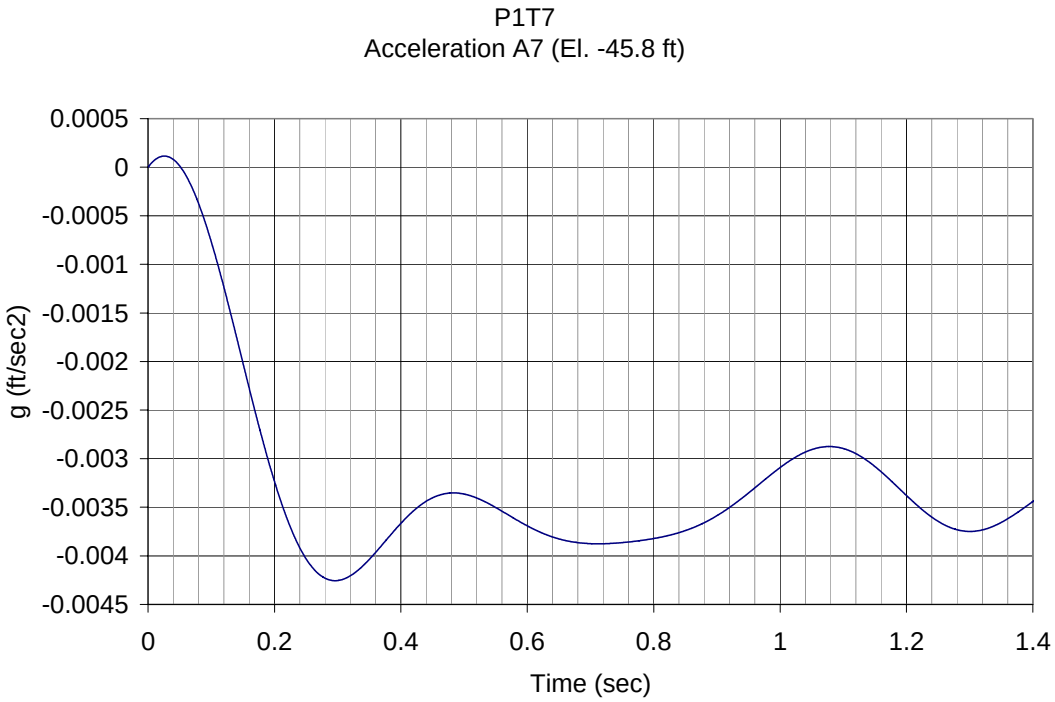

Figure B-46 P1T7 Acceleration Record for Accelerometer A7

Back Computed Dynamic P-y Curves for P1T7

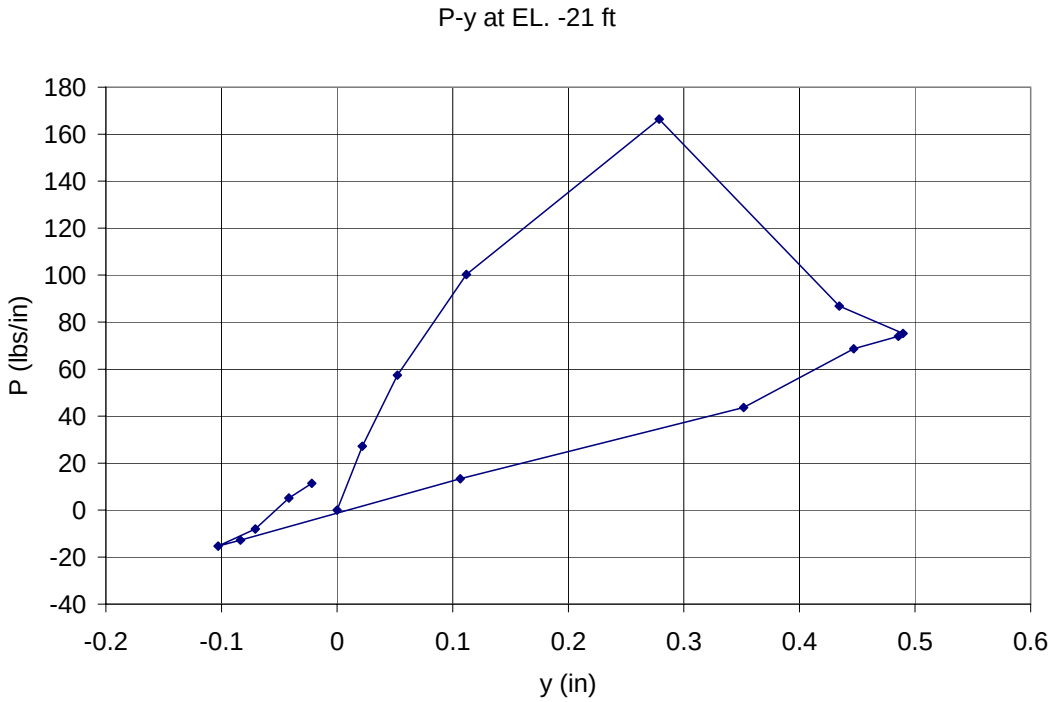

Figure B-47 Back Computed P-y Curve at Elevation -21.0 ft

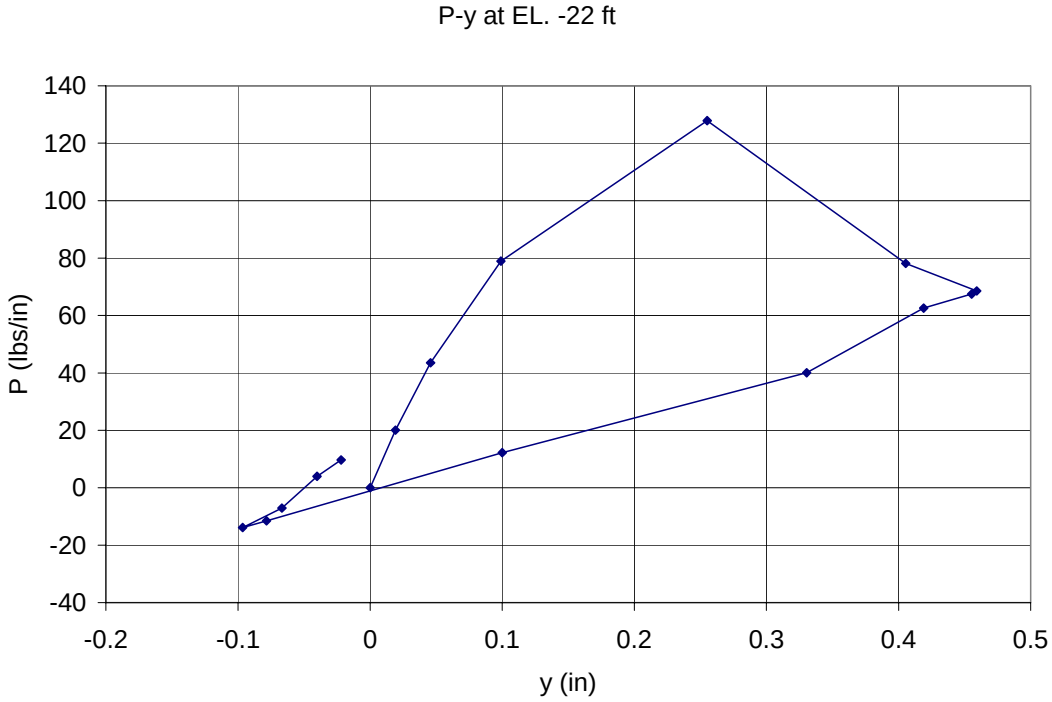

Figure B-48 Back Computed P-y Curve at Elevation -21.0 ft

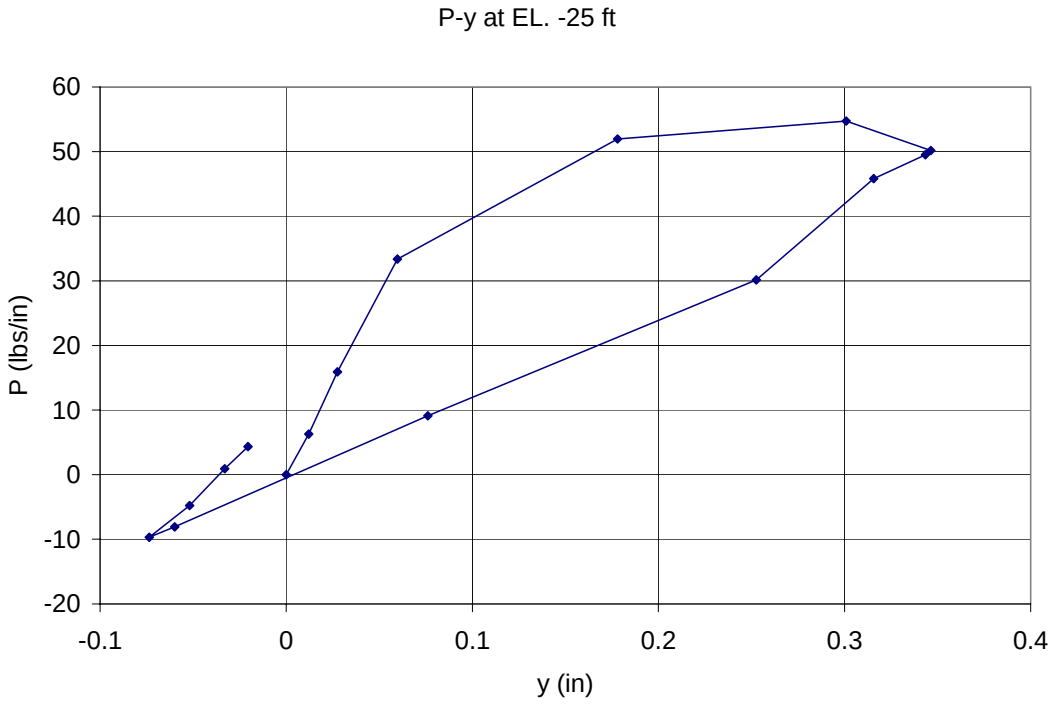

Figure B-49 Back Computed P-y Curve at Elevation -21.0 ft

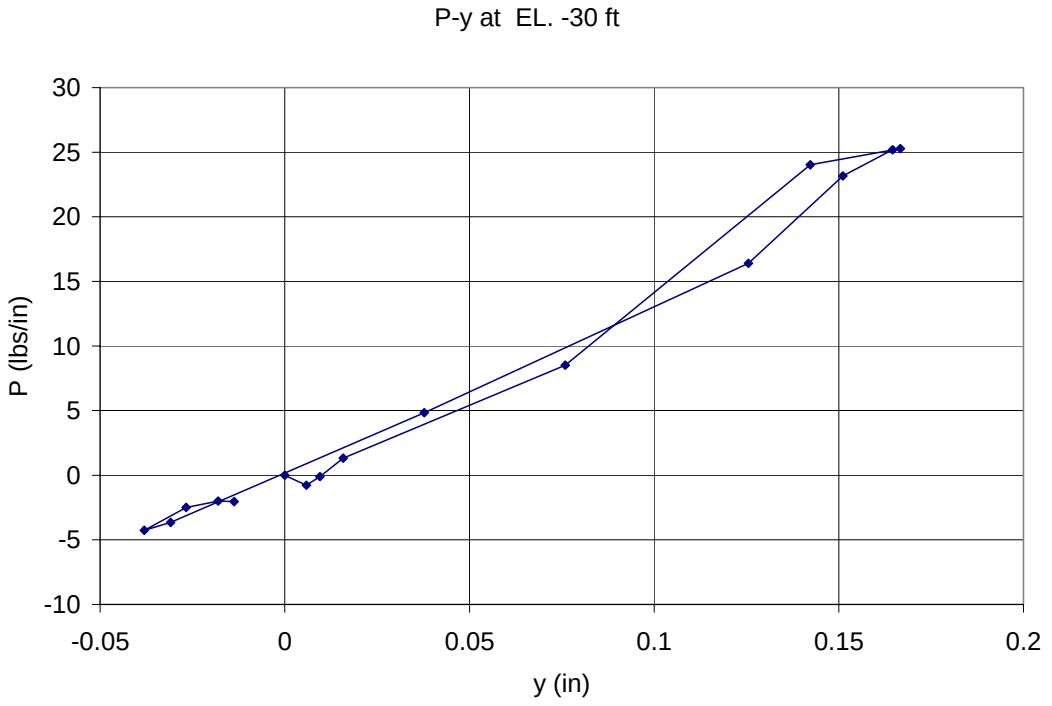

Figure B-50 Back Computed P-y Curve at Elevation -21.0 ft

LIST OF REFERENCES

American Association of State Highway and Transportation Officials (AASHTO), *Guide Specification and Commentary for Vessel Collision Design of Highway Bridges*, Washington, D.C., 1991.

Bowles, J. E., *Foundation Analysis and Design*, 5th Edition, McGraw Hill, New York, 1996.

Brown, D.A., O'Neill, M.W., Hoit, M., McVay, M.C., El Naggar, M.H., Chakraborty, S., *Static and Dynamic Lateral Loading of Pile Groups*, NCHRP Report No. 461, Washington D.C., 2001.

Coduto, D., *Foundation Design: Principles and Practices*, 2nd Edition, Prentice Hall, Englewood Cliffs, 2001.

Consolazio, G.R., R.A. Cook, A.E. Biggs, D.R. Cowan, L. Bui, and H.T. Bollman. *Barge Impact Testing of the St. George Island Causeway Bridge:Final Report*. Structures Research Report, Engineering and Industrial Experimental Station, University of Florida, Gainesville, Florida, 2005.

Coyle, H.M., Gibson, G.C., "Empirical Damping Constants for Sands and Clays," *Journal of the Soil Mechanics and Foundations Division*, ASCE, Vol. 96, No. SM3, 1970, pp. 949-965.

Das, B. M., *Fundamentals of Soil Dynamics*, Elsevier Publishing Co., Inc, New York, 1983.

Electrical Power Research Institute, *Manual on Estimating Soil Properties for Foundation Design*, EPRI, Prepared by Cornell University, Ithaca, New York, 1990.

Florida Department of Transportation, *FB-MultiPier Users Manual*, FDOT, Tallahassee, 2005.

Gazates, G., Dobry, R., "Horizontal Response of Piles in Layer Soils," *Journal of Geotechnical Engineering*, ASCE, Vol. 110, No. 1, 1984, pp. 20-40.

Habibagahi, K. and Langer, J. A., "Horizontal Subgrade Modulus of Granular Soils," *Laterally Loaded Deep Foundations: Analysis and Performance, ASTM STP.835*, J. A. Langer, E. T. Mosley, and C. D. Thompson, Eds., American Society for Testing and Materials, 1984, pp. 21-34.

Knott M., Z. Prucz, Vessel Collision Design of Bridges, *Bridge Engineering Handbook*, Edited by W.F. Chen and L. Duan, CRC Press, Boca Raton, FL, 1999, pp. 60-1 – 60-18.

Larsen O.D. *Ship Collision with Bridges: The Interaction between Vessel Traffic and Bridge Structures, Structural Engineering Document 4*. International Association for Bridge and Structural Engineering, IASBE-AIPC-IVBH, Zurich, Switzerland, 1993.

Leet, K., Bernal, D., *Reinforced Concrete Design*, 3rd Ed., McGraw Hill, New York, 1997.

McVay, M.C., Alvarez, V., Zhang, L., Perez, A., and Gibson, A., *Estimating Driven Pile Capacities During Construction*, Final Report to Florida Department of Transportation, State Job No. 99700-3600-119, Contract No. BB-349, October 2002.

McVay, M.C., Shang, T., and Casper, R., "Centrifuge Testing of Fixed Head Laterally Loaded Battered and Plum Pile Groups in Sand," ASTM, *Geotechnical Testing Journal*, GTJODJ, Vol. 19, No. 1, March 1996, pp. 41-50.

Marchetti, S., "In Situ Test by Flat Dilatometer," Proceedings of American Society of Civil Engineers, *ASCE Journal of the Geotechnical Engineering Division*, Vol. 106, No.GT3, March 1980, pp. 299-321.

Mayne, P. W. and Martin, G. K., "Commentary on Marchetti Flat Dilatometer Correlations in Soils," *Geotechnical Testing Journal*, GTJODJ, Vol. 21, No.3, September 1998, pp. 222-239.

Niraula, L., *Development of Modified T-z Curves for Large Diameter Piles/Drilled Shafts in Limestone for FB-Pier*, Master's Thesis, The University of Florida, 2004.

Peck, R. B., Hanson, W. E., and Thornburn, T. H., *Foundation Engineering*, John Wiley and Sons, New York, 1974.

Reese, L.C., Cox, W.R., and Koop, F.D., "Analysis of Laterally Loaded Piles in Sand," Paper No. OTC 2080, *Proceedings of the Fifth Annual Offshore Technology Conference*, Houston, Texas, 1974.

Reese, L. C., and Wang, S., *Comp624P-Laterally Loaded Pile Analysis Program for the Microcomputer Version* 2.0, USDOT Publication No. FHWA-SA-91-048, August 1993.

Robertson, P. K., and R. E. Campanella, "Interpretation of Cone Penetration Tests: Part 1: Sand," *Canadian Geotechnical Journal*, Vol. 20, No.4, November 1983, pp. 718-733.

Robertson, P.K., Campanella, R.G., Brown, P.T., Grof, I., and Hughes, J.M., "Design of Axially and Laterally Loaded Piles Using In Situ Tests: A Case History," *Canadian Geotechnical Journal*, Vol. 22, No. 4, 1985, pp.518-527.

Ruestra, P., *Prediction and Evaluation of a Laterally Loaded Pile Group*, Master's Thesis, The University of Florida, 1996.

Terzaghi, K. and Peck, R.B., *Soil Mechanics in Engineering Practice*, 2nd Ed., John Wiley and Sons, New York, 1967.